Potential of Synthetic Aperture Radar backscatter for monitoring volcanic eruptions

Edna Warsame Dualeh

Submitted in accordance with the requirements for the degree of
Doctor of Philosophy

The University of Leeds
School of Earth and Environment

September 2022

The candidate confirms that the work submitted is their own, except where work which has formed part of jointly authored publications has been included. The contribution of the candidate and the other authors to this work has been explicitly indicated below. The candidate confirms that appropriate credit has been given within the thesis where reference has been made to the work of others.

The work in Chapter 2 is adapted from an accepted publication to the *Journal of Geophysical Research: Solid Earth*:

Dualeh, E.W., Ebmeier, S.K., Wright, T.J., Albino, F., Naismith, A., Biggs, J., Ordoñez, P.A., Boogher, R.M. & Roca, A. (2021). Analyzing Explosive Volcanic Deposits From Satellite-Based Radar Backscatter, Volcán de Fuego, 2018. *Journal of Geophysical Research: Solid Earth*, 126(9), p.e2021JB022250.

As first author on this work, E.W. Dualeh, undertook the data processing, setting up method and analysis. I also produced all figures and wrote the manuscript for submission. S.K. Ebmeier (University of Leeds) acquired funding for the project and along with T.J. Wright (University of Leeds) provided guidance and suggestions throughout the project. F. Albino (University of Bristol) produced the pre- and post-eruption DEM of Volcán de Fuego (Albino et al., 2020). A. Naismith (University of Bristol) provided us with background information about Volcán de Fuego and the 2018 eruption and put us in contact with the local observatory (A. Roca). J. Biggs (University of Bristol) acquired initial funding. P.A. Ordoñez, R.M. Boogher & A. Roca (INSIVUMEH) provided ground-based insight to the eruption and monitoring. SAR data was provided through the CEOS Volcano Demonstrator. All co-authors provided comments on the manuscript.

The work in Chapter 3 of the thesis is being written up as a manuscript to be submitted in Autumn 2022 under the title:

Dualeh, E.W., Ebmeier, S.K., Wright, T.J., & Poland, M.P. (In Prep.) Tools for interpreting Synthetic Aperture Radar backscatter during effusive eruptions: The 2010–2013 eruptions at Pu‘u ‘Ō‘ō Crater, Hawai’i.

As the first author, E.W. Dualeh, processed and analysed the data, wrote the manuscript and produced all the figures. S.K. Ebmeier (University of Leeds), provided suggestions on work and provided comments on draft. T.J. Wright (University of Leeds) provided suggestions on work. M.P. Poland (Yellowstone Volcano Observatory) provided expert knowledge on the volcano and eruptions examined. The SAR data was provided through the Hawaiian Volcanoes Supersite.

The work in Chapter 4 of the thesis is a manuscript that will be submitted to the journal *Earth and Planetary Science Letters* in September 2022:

Dualeh, E.W., Ebmeier, S.K., Wright, T.J., Poland, M.P., Grandin R., Stinton A.J. & Camejo-Harry M. (Submitted). Rapid Pre-explosion Increase in Dome Extrusion Rate at La Soufrière, St. Vincent Quantified from Synthetic Aperture Radar Backscatter. *Earth and Planetary Science Letters.*

As first author on this work, E.W. Dualeh, co-coordinate the tasking of the COSMO-SkyMed imagery, conceptualisation of project, processed SAR data, method development and testing. I also produced all figure and wrote manuscript. S.K. Ebmeier (University of Leeds) helped coordinate SAR data tasking, and along with T.J. Wright (University of Leeds) provided input on the project concept and on the method development. M.P. Poland (Yellowstone Volcano Observatory) provided input on volcanological context. R. Grandin (Institut de Physique du Globe de Paris) produced the high resolution pre-eruption DEM of the volcano. A.J. Stinton (Montserrat Volcano Observatory) provided the ground-based observations and photogrammetry measurements. M. Camejo-Harry (University of Oxford) was our key UWI-SRC contact who provided background context and knowledge of La Soufrière, St. Vincent and the 2021 eruption. SAR data was provided through the CEOS Volcano Demonstrator. All co-authors provided comments on the manuscript.

Acknowledgements

It might have taken me longer than planned but I finally made it! The last few years have been all over the place (for everyone). There are so many people who have helped and supported me throughout my PhD journey. As you know I am not really the best at expressing my thoughts or emotions but hopefully I manage to get some of my gratitude across.

First, I would like to thank my supervisors Dr. Susi Ebmeier and Prof. Tim Wright. I feel so very lucky to have had such amazing supervisors who gave me the chance to work in such an interesting field and supported me throughout. Thank you for sharing your immense knowledge on everything SAR and volcano related! I would also like to thank Dr. Mike Poland for being so approachable and helpful, even when I forgot to email for months.

My PhD was funded by an underspent ESA Living Planet Fellowship to SKE (awarded 2015) and the School of Earth and Environment, University of Leeds. I was also a member of the Centre for Observation and Modelling of Earthquakes, Volcanoes and Tectonics (COMET), which provided me with the opportunity to connect with researchers across the U.K. Thank you to all the people who I have had the luck of working with over during my PhD.

Secondly, thank you to all my fellow PhD students and IGT staff for the chats and discussion over coffee or lunch and making my time in Leeds so memorable. To Emma, Vickie and Carissa, for constantly reminding me why I like geology and being my number one cheerleaders. A big thank you to my family, although we are scattered all over the place you all have always offered me endless support and encouragement. Thank you for listening to me practice a presentation for the hundredth time, letting me moan about the internet speed and just letting me be myself. And finally, to James, for listening to my endless babble on all things SAR, for reading through everything I wrote, and in general for always being there and supporting me. I promise I won't be sleeping on my dreams.

Thank you so much to everyone!

Abstract

Radar backscatter has been shown to be useful for observing volcanic eruptions, especially for remote or dangerous eruptions, as it is not limited by access to the volcano or cloud-coverage. Currently it is still being less widely used for volcano monitoring than radar phase measurements. This is in part because of the ambiguity in the interpretation of backscatter signals: there is not always a simple link between the magnitude or signal of the backscatter and the physical properties of the fresh volcanic deposits. In this thesis, I present three case studies (1) the 2018 explosive eruption of Volcán de Fuego, Guatemala, (2) the 2011–2013 effusive eruptions from Pu‘u ‘Ō‘ō Crater, Kīlauea, Hawai‘i, and (3) the 2021 dome growth at La Soufrière, St. Vincent and using a range of SAR sensors (COSMO-SkyMed, TerraSAR-X, Sentinel-1, and ALOS) demonstrate how radar backscatter can be used to monitor volcanic eruptions and quantify the changes to the ground surface.

Radar backscatter is dependent on the scattering properties of the ground surface (i.e., surface roughness, local incidence angle, and dielectric properties). All of which can be altered during a volcanic eruption and provide information about specific deposits and processes. The pyroclastic density currents and lahars during the 2018 eruption of Volcán de Fuego and the emplacement and development of lava flows in 2010–2013 in Hawai‘i were dominated by changes in the surface roughness. I identify deposits and variations within these based on their different morphologies, calculating the lengths of flows and areas affected by the eruptions. Where a deposit is emplaced over a period of multiple SAR acquisitions, I can map the progression and development of the deposit through time. While the backscatter signals associated with the eruptions in Hawai'i and Volcán de Fuego were dominated by changes to the surface roughness, backscatter changes during dome growth at St. Vincent were dominated by changes in the local incidence angle. The analysis at La Soufrière is therefore driven by this gradient-dominated signal, which provided the opportunity to extract topographic profiles from the SAR backscatter.

I test different SAR backscatter method to increase the signal-to-noise ratio and improve the identification of SAR backscatter change related to volcanic deposits. I found that using a combination of (1) spatial filters, (2) extended timeseries, (3), ra-

diometric terrain corrections, and (4) understanding the pre-eruption land cover work to improve the signal, but depends on the type of deposit and volcanic setting. Further, the addition of supplementary datasets (e.g., high-resolution DEM, rainfall data, pre-eruption land cover) are important when interpreting backscatter changes.

Through the three case studies, I demonstrate the ways backscatter can be used to understand and monitor a range of volcanic eruption styles. I highlight a number of quantitative volcanic outcomes (e.g., flow lengths, deposit thicknesses, areas and volumes), a variety of SAR methods (e.g., change difference, extended timeseries, flow mapping, pixel offset tracking) and corrections (e.g., radiometric terrain correction, satellite dependency).

Contents

List of Figures

List of Tables

Nomenclature

List of acronyms

ALI	Advanded Land Imager
ALOS-1	Advanced Land Observing Satellite-1
ALOS-2	Advanced Land Observing Satellite-2
ARIA-SG	Advanced Rapid Imaging and Analysis Singapore
ASI	L'Agenzia Spaziale Italian
AVO	Alaska Volcano Observatory
CEOS	Committee on Earth Observation Satellites
CSG	COSMO-SkyMed Second Generation
CSK	COSMO-SkyMed
DBSCAN	Density-Based Spatial Clustering of Applications with Noise
DEM	Digital Elevation Model
EMS	Emergency Management Service
EO-1	Earth Observing-1
EOS-RS	Earth Observatory of Singapore - Remote Sensing
ERP	Effective Radiated Power
ERS	European Remote Sensing
ERZ	East Rift Zone
ESA	European Space Agency
gamma-MAP	gamma Maximum-A-Posteriori
GEO	Group on Earth Observation
GNSS	Global Navigation Satellite System
GPS	Global Positioning System
GSNL	Geohazard Supersites and Natural Laboratory initiative
HH	Horizontal transmitted–Horizontal received
HRWS	High Resolution Wide Swath
HV	Horizontal transmitted–Vertical received
HVO	Hawaiian Volcano Observatory
IfSAR	airborne Interferometric Synthetic Aperture Radar

InSAR	Interferometric Synthetic Aperture Radar
INSIVUMEH	Instituto Nacional de Sismologia, Vulcanologia, Meteorologia e Hidrologia
IW	Interferometric Wide
JAXA	Japan Aerospace Exploration Agency
JERS	Japanese Earth Resources Satellite
LERZ	Lower East Rift Zone
LiDAR	Light Detection and Ranging
LOS	Line-Of-Sight
MR	Morphological Reconstruction
MultiGAS	Multi-component Gas Analyzer System
NEMO	National Emergency Management Organisation
NISAR	NASA-ISRO SAR
NOAA	National Oceanic and Atmospheric Administration
PALSAR	Phased Array L-band Synthetic Aperture Radar
PC1	First Principal Component
PCA	Principal Componment Analysis
PDC	Pyroclastic Density Currents
RCM	RADARSAT Constellation Mission
RCS	Radar Cross Section
RGB	Red Green Blue
RISAT	Radar Imaging Satellite
RMS	Root-Mean-Square
RMSE	Root-Mean-Square Error
S1	Sentinel-1
SAOCOM	Satélite Argentino de Observación Con Microondas
SAR	Synthetic Aperture Radar
SCM	SAR Coherence Mapping
SLAR	Side-Looking Airbourne Radar
SMU	Soufrière Monitoring Unit
SRTM	Shuttle radar Topography Mission
TROPOMI	TROPOspheric Monitoring Instrument
TSX	TerraSAR-X
UAV	Unmanned Aerial Vehicle
USGS	United States Geological Survey
UTC	Universal Time Coordinated
UV	Ultraviolet Radiation
UWI-SRC	University of the West Indies Seismic Research Centre
VH	Vertical transmitted–Horizontal received
VT	Volcano-tectonic
VV	Vertical transmitted–Vertical received

List of symbols

A	Surface area
β_0	Backscatter coefficient in slant-range (Radar Brightness)
d	Data Vector
δ	Pixel Spacing
Δ_H	Radar shadow height shift
$\Delta\phi$	Interferometric phase
D_{max}	Maximum crater depth
D_o	Antenna directivity
ε	Relative height
f_a	Absorbed power by scatterer
G	Design matrix
γ_0	Backscatter coefficient perpendicular to satellite line of sight
G_t	Antenna Gain
G_{ts}	Gain in the direction of the receiver
h	Height
I	Intensity
k	Calibration constant
K^2	Laplacian Scale Factor
r	Rate of lava flow recovery
λ	Wavelength of the transmitted energy
∇^2	Laplacian Smoothing Operator
ϕ	Angle between feature and satellite line of sight
P or ρ	Power density
R	Range distance
s	Variance
σ	Radar Cross Section
σ_0	Backscatter coefficient
θ	Satellite Incidence Angle
t	Time
W	Width

Chapter 1

Introduction

Volcanic eruptions have the ability to completely alter the ground surface surrounding the volcano, and pose hazards to those who live near them. In part, as a result of the nutrient rich soils that commonly surround volcanoes, it has been estimated that over 800 million people in over 86 countries live within 100 km of an active volcano (Loughlin et al., 2015). These populations are at risk from a range of a volcanic processes that span a wide spatial area, including the eruption of lava flows, pyroclastic flows and ash. There have been more than 300,000 deaths since the 17^{th} century have been attributed to volcanic disasters (Tilling, 2008) and the continued growth of the global population means that the risk to humans from volcanoes will further increase as exposure increases. The human and economic loss caused by volcanoes motivates volcanologists to try and better understand volcanic processes by observing and monitoring volcanic systems. Systematic monitoring of volcanoes gives an insight into how volcanoes behave and improve hazard assessments and models to protect the populations living on the volcano.

Historically, volcanic eruptions have been shown to be almost always preceded by a period of unrest (Tilling, 2008). Geophysical and geochemical methods are used to gather data and track various parameters, including seismicity and ground deformation, of a volcano. Long-term collection of this type of data can be used to establish a baseline of volcanic behaviour, and any divergences from this baseline provides an indication of a changing system and possibly volcanic unrest. Understanding the variations from the baseline can be used to help identify precursory activity and reduce the risk to the human population (e.g., improved warning systems and zonation maps). Despite the clear importance of monitoring volcanic activity for hazard assessment, a majority of volcanoes either lack proper ground-based monitoring or are not monitored at all (Sparks et al., 2012).

The increase in the number of Earth Observation satellites in recent decades has

made systematic monitoring of volcanoes possible on both regional and near-global scales (e.g., Massonnet et al., 1995). Active satellite-based sensors, such as Synthetic Aperture Radar (SAR), provide their own source of illumination allowing for ground surface observations over large geographical areas (e.g 40 - 200 km, depending on sensor) at any time of the day, including nights (Bürgmann et al., 2000). The short wavelengths (X-band 2.4-3.75 cm, C-band 3.75-7.5 cm, L-band 15-30 cm) used by the sensors do not strongly interact with moisture in the atmosphere, therefore SAR imagery is not limited by meteorological cloud coverage. However, the interaction with the atmosphere does introduce delays in the SAR phase signal used in interferometry. This provides SAR with an advantage over passive remote sensing senors with respect to observing and monitoring processes, particularly at tropical volcanoes.

This thesis focuses on the applicability of the lesser used SAR backscatter to observe and monitor on-going volcanic eruptions and examine the variation in backscatter signals associated with the diverse range of volcanic processes and deposits. The eruptions used as case studies are; the explosive 2018 eruption of Volcán de Fuego, which was characterised by pyroclastic flow deposits and post-eruption reworking of material by lahars, the 2011–2013 lava lake and flows from Pu‘u ‘Ō‘ō crater, Hawai‘i and the 2021 dome growth at La Soufrière, St. Vincent before the eruption transitioned from effusive to explosive. The remainder of this chapter is divided into three sections (1) an introduction to SAR theory, sensor parameters and influences and associated corrections (Section 1.1), (2) the use of SAR backscatter in volcano monitoring (Section 1.2), which describes previous volcanic case studies, methods used, and other SAR products, and (3) the main aims and structure for the thesis (Section 1.3).

1.1 Synthetic Aperture Radar (SAR)

In volcanology SAR, the reflectivity of the ground surface has been described with various terms such as, radar amplitude (e.g., Wadge et al., 2002; Arnold et al., 2018), backscattering intensity (e.g., Di Traglia et al., 2018; Wadge et al., 2012), backscatter (e.g., Carn, 1999; Saepuloh et al., 2015a) or a combination of these terms. However they all represent the same property, the normalized radar cross sections or the backscatter coefficient, σ_0. To measure the reflectivity of the ground surface the SAR sensor emits a microwave pulse towards the earth's surface and measures the portion of the signal that is backscattered towards the sensor.

1.1.1 The Radar Equation

In this section, I outline the basic derivation of the radar equation and what are the contributing variables. There are many books and papers that delve into the physics, implementation and development of radar systems, for comprehensive descriptions of

radar theory can be found in Tomiyasu (1978) and Keysight Technologies (2018). The fundamental relationship between the radar characteristics, the imaged target and the received signal at the satellite can be expressed by the radar equation. In radar physics the ratio between the incident (I_r) and received (I_i) signal intensity is described using the Radar Cross Section (RCS) σ. The RCS assumes that all of the energy that the target intercepts is scattered uniformly or isotropically and is expressed in m^2,

$$\sigma = \frac{I_r}{I_i} 4\pi R^2 \qquad [\mathrm{m}^2] \tag{1.1}$$

The RCS represents the physical properties of the scatterer and the signal is influenced by surface roughness, local gradient and dielectric properties as well as the satellite parameters (e.g., wavelength). This combination of factors results in a signal that can be difficult to interpret. A calibrated SAR image, which has been normalized by the size of the area reflecting the energy back towards the satellite is referred to as the backscatter coefficient, σ_0, or the normalised RCS is written as

$$\sigma_0 = \frac{\sigma}{A_\sigma} \qquad [\frac{\mathrm{m}^2}{\mathrm{m}^2}] \tag{1.2}$$

where A_σ is the area illuminated by the satellite (i.e., the surface area covered by a pixel).

Derivation of Radar Equation

The radar equation represents the conversion from the transmitted power into the power signal received at the antenna. It demonstrates the relationship between the radar system characteristics, the target or scatterer, and the received signal at the satellite. It can be applied for mono- (e.g., SAR) or bi-static radar systems and be used to determine the received power from a point and an extended target. The transmitter emits a pulse of high-frequency energy. For an isotropic radiator under ideal conditions the transmitted power is propagated uniformly in all directions from the source (i.e., transmitter). This power can be directed in one direction using the antenna gain to increase the power density in that direction and focus the radar pulse toward the target. At the scatter (Fig. 1.1a), this power density can be expressed as,

$$S_s = \frac{P_t G_t}{4\pi R_t^2} \qquad [\mathrm{Wm}^{-2}] \tag{1.3}$$

where P_t is the total power transmitted, G_t the antenna gain and the range, R_t from the transmitter antenna to the target. As the power is distributed uniformly over a sphere around the antenna there is an associated reduction in the power density, shown by the spreading factor, $\frac{1}{4\pi R^2}$. The combination of $P_t G_t$ is more commonly known as

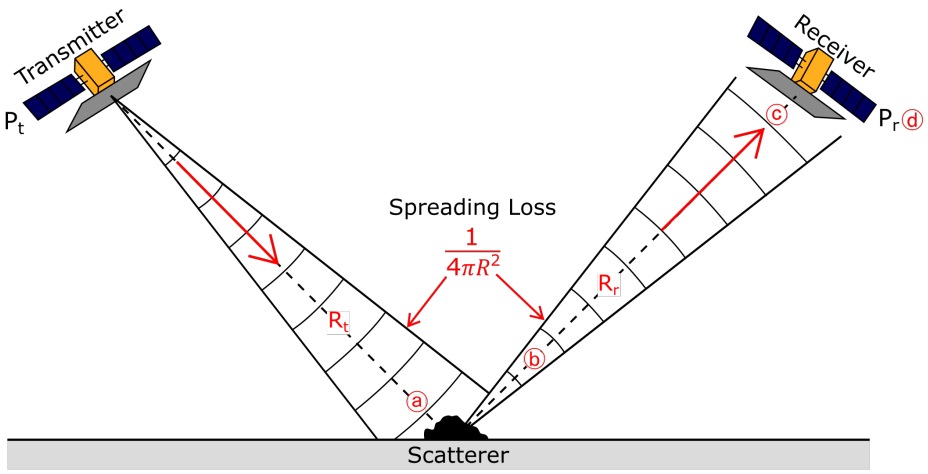

Figure 1.1: Schematic of the geometry for a bistatic radar system showing the power emitted from the transmitter (P_t), being received (a) and scattered (b) by a surface scatterer back towards the receiver (c), which measures the final power received (P_r) from the ground scatterer (d).

the effective radiated power (ERP) and corresponds to the power in the centre of the beam.

The total power intercepted by the scatterer can be calculated by multiplying the power density at the scatterer, S_s, with the effective area of the scatterer, A_{rs} (i.e., $P_{rs} = S_s A_{rs}$, [W]). Unless the scatterer is a perfect isolater some of the received power is absorbed, f_a. Thus the reradiated power by the scatterer (Fig. 1.1b), P_{ts} directed towards the receiver can be expressed by,

$$P_{ts} = P_{rs}(1 - f_a)G_{ts} \qquad [\mathrm{W}] \tag{1.4}$$

where G_{ts} is the gain in the direction of the receiver. By expanding eq. 1.4, we can combine all the terms associated with the scatter into a single variable known as the radar cross section (RCS), σ. Demonstrated here,

$$P_{ts} = (S_s A_{rs})(1 - f_a)G_{ts} = \left(\frac{P_t G_t}{4\pi R_t^2}\right)[A_{rs}(1 - f_a)G_{ts}] = \frac{P_t G_t \sigma}{4\pi R_t^2} \qquad [\mathrm{W}] \tag{1.5}$$

The observation geometry, the shape and composition of the scatterer alter the RCS value.

The power density at the receiver, S_r (Fig. 1.1c), can be expressed in similar terms as the power density at the scatterer since the pulse encounters the same condition. The power density yielded at the receiver is given by,

$$S_r = \frac{P_{ts}}{4\pi R_r^2} \qquad [\mathrm{Wm}^{-2}] \tag{1.6}$$

with the range between the scatterer and the receiver antenna shown as R_r. Similar to at the scatterer, the power received at the antenna (Fig. 1.1d) is dependent on the power density at the receiver, S_r and the effective antenna aperture, A_e (i.e., $P_r = S_r A_e$, [W]). The effective antenna aperture is based on the antenna's geometric area and efficiency and has to be considered to account for the loss in power at the receiver. The total power received at the antenna is therefore given by:

$$P_r = \frac{P_t G_t A_e \sigma}{(4\pi)^2 R^4} \qquad [\mathrm{W}] \tag{1.7}$$

Until now we have considered the transmitted and reflected waves separately, which is the case for a bistatic system (Fig. 1.1). For a monostatic system, such as SAR, the range from the transmitter to the scatterer, R_t and the range from the scatterer towards the receiver, R_r, are the same. Therefore, we can combine these to simplify the equation.

Antenna Gain Function

The power density of an isotropic system, as described above, decreases rapidly as distance from the antenna increases. The radar system is altered to emit its pulses as a beam, which allows the power density to be increased in that direction. The beam concentrates the power in the direction of the antenna and reduces the signal in all other directions (Fig. 1.2)

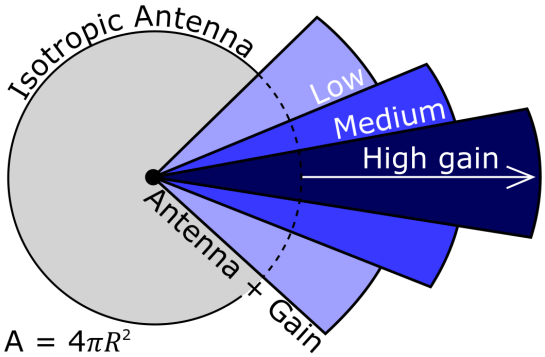

Figure 1.2: Simplified schematic illustrating the comparison between an isotropic antenna system and an antenna with gain.

A narrow beamwidth represents a high antenna gain whereas a wide beamwidth indicates a low antenna gain. The antenna gain is a dimensionless parameter which does not create any energy but rather diverts, directs or concentrates the energy. The gain function is a directional feature that is defined as,

$$G_t = \rho D_o \tag{1.8}$$

where ρ is the antenna efficiency which represents the actual losses in power that are due to the antenna itself (e.g., through manufacturing faults, imperfections etc.). Antenna directivity, D_o is the ratio between the power density in the direction where the antenna is focusing most of the power and the power density of the isotropic antenna with the same total power of transmission. A directivity of 1 (or 0 dB) is indicative of an antenna that emits power uniformly in all directions (i.e., an isotropic antenna). The maximum directivity,

$$D_o = \frac{4\pi A_a}{\lambda^2} \tag{1.9}$$

estimates the maximum possible gain for a physical aperture area (A_a) for an antenna. The antenna gain in combination with the effective aperture ($A_e = \rho A_a$) and the antenna gain function can be rewritten as,

$$G_t = \frac{4\pi A_e}{\lambda^2} \tag{1.10}$$

where λ is the wavelength of the transmitted energy (i.e., satellite wavelength). Using the equation 1.10, we can rewrite the radar equation (eq. 1.7) in terms of the antenna gain for a monostatic radar system.

$$P_r = \frac{P_t G_t^2 \lambda^2 \sigma}{(4\pi)^3 R^4} \tag{1.11}$$

1.1.2 Principles of SAR

The active nature of SAR imagery may give it an advantage over passive sensors. However, because of how and what it measures, SAR data is more complex to process and interpret than other dataset, such as optical imagery.

A SAR image is acquired in radar geometry, which is expressed in terms of range and azimuth direction (Fig. 1.3). Azimuth, or along-track direction, corresponds to the direction the satellite is travelling in. The range direction is perpendicular to the azimuth direction and progressively increases from the near- to the far-range.

The resolution of SAR images is determined by differences in these directions, which makes it different from Real Aperture radars (i.e., SLAR, Side Looking Airborne Radar). The range resolution for both SAR and SLAR is inversely proportional to the systems bandwidth and incidence angle. However, the azimuth resolution of SAR systems are based on the aperture synthesis concept, also known as Doppler Beam

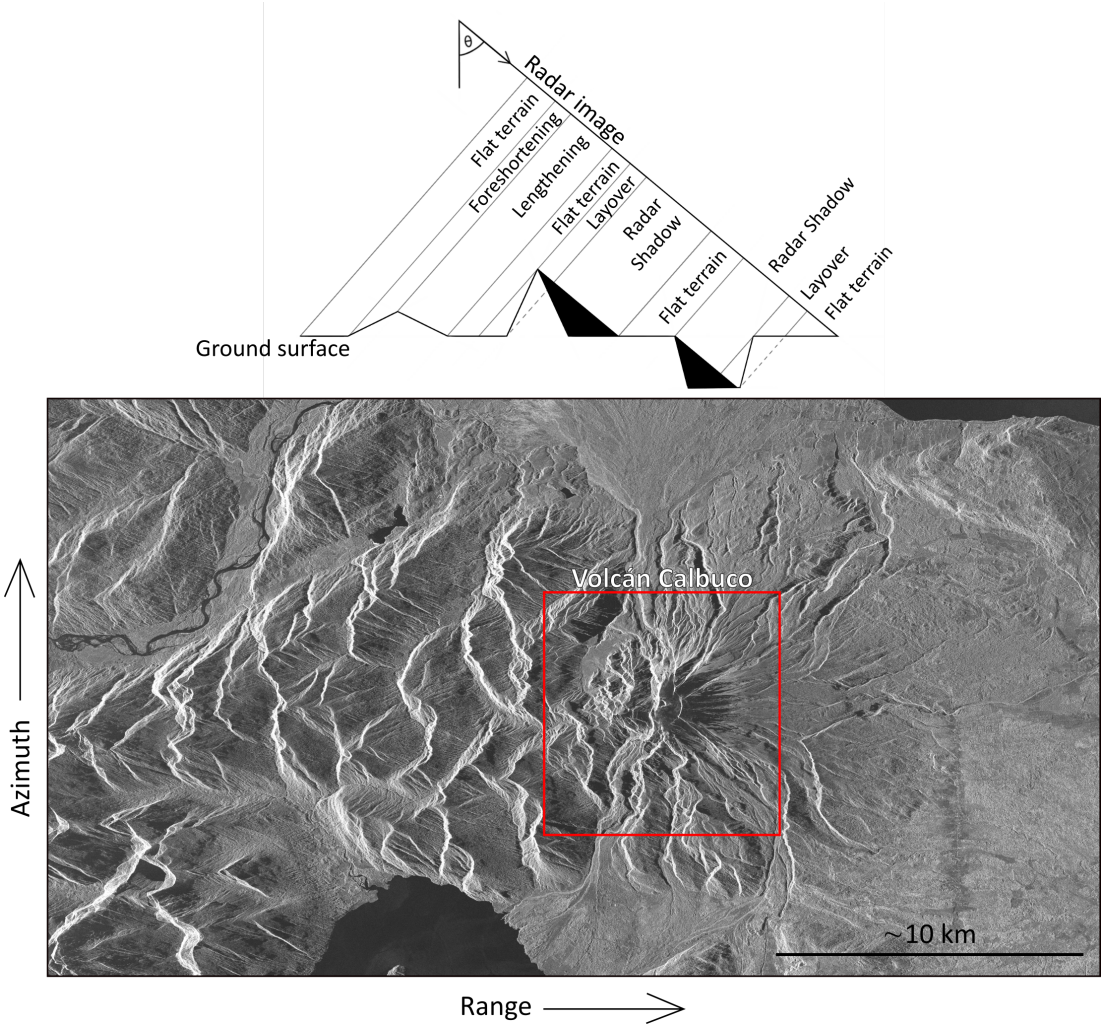

Figure 1.3: Schematic of satellite viewing geometry that demonstrates how the ground surface appears as the result of the side-looking nature of the satellite and how distortions (i.e., radar shadow and layover) are formed. Schematic modified from (Pinel et al., 2014). The bottom image shows a SAR backscatter image in radar geometry of the ice-capped Calbuco Volcano, Chile, acquired by TerraSAR-X satellite. The skewed nature of the mountains on the left-hand side of the image demonstrates the distortions introduced by the side-looking nature of the radar sensor.

Sharpening, which was first introduced by Carl Wiley in 1951 (Sherwin et al., 1962; Wiley, 1985). Using the motion of the SAR sensor on the satellite and multiple consecutive pulses, a single target on the ground surface produces shifted doppler signals that simulates a larger effective antenna length.

However, it is important to note that the spatial resolution of a SAR image is not the same as the pixel spacing. The spatial resolution is the minimum distance that can be distinguished between two point targets with similar reflective strength (Woodhouse et al., 2011). For SAR, the spatial resolution is determined by the aspect of the system (range by azimuth). Due to the side-looking nature of SAR satellites, the range

resolution increases between the near- and far-field as the incidence angle increases. The pixel spacing, or grid spacing, of a SAR image is uniform across the image and generally is smaller than the spatial resolution. This oversampling means that adjacent pixels are influenced by similar signals. For example, the spatial resolution for the Sentinel-1 interferometric wide (IW) swath mode is 2.7–3.5×22 m (range×azimuth) but the SAR images have a pixel spacing of 2.3×14.1 m (ESA, 2022). Multi-looking the data increases the pixel spacing of the image.

Current SAR sensors show a large range in spatial resolution, ranging from 0.5 m (e.g., ICEYE, TerraSAR-X staring spotlight) up to 100 m (e.g., ALOS ScanSAR). The range in the resolution for SAR data is due to the specific design of the sensor to either maximise the image resolution (e.g., Spotlight) or the spatial extent of the scene (e.g., Stripmap, ScanSAR). To avoid ambiguities between points on either side of the satellite that would have the same doppler shift and travel times, SAR sensors face sideways, imaging the ground surface at an angle.

This side-looking nature of the satellite introduces distortions within the backscatter images (Fig. 1.3). Surfaces that face towards the sensor will appear foreshortened, the amount of foreshortening depends on the satellite incidence angle (θ) and the gradient of the slope. When the gradient of the slope is larger than the incidence angle, then the top of the features is closer to the sensor and gets imaged before the bottom, this is known as a layover. Similarly, slopes facing away from the satellite are lengthened, until the gradient becomes greater than the incidence angle and casts a radar shadow, an area where the sensor cannot image (Hanssen, 2001; Pinel et al., 2014).

Satellite	Band	Frequency (GHz)	Wavelength (cm)	Repeat cycle (days)	Number of Satellites
COSMO-SkyMed (CSK)	X	9.7	3.1	1-16	4*
TerraSAR-X (TSX)	X	9.7	3.1	11	1
ICEYE	X	9.7	3.1	-	16
Sentinel-1 (S1)	C	5.4	5.6	6-12	2*
ALOS-1/2	L	1.3	23.6	46/14	1/1

Table 1.1: Select SAR satellite and overview of system parameters that are used within this thesis. *Note that CSK3 was decommissioned in May 2022 and Sentinel-1b stopped transmitting in Dec. 2021

The radar backscatter is a function of the satellite observation parameters (i.e., polarisation, wavelength and incidence angle) and the surface scattering properties (i.e., surface roughness, local incidence angle and dielectric properties). The scattering characteristics of a surface feature is a combination of all these parameters, which makes it very complex to interpret and understand changes in radar backscatter signals.

SAR sensors transmits signals within the microwave spectrum (1 GHz to 100 GHz), which has been subdivided into frequency bands (Hanssen, 2001). Satellite-based SAR sensors have generally used the lower frequency bands (Ku- to L-band). Due to the availability of the data, X-, C-, and L-band have been the main wavelengths, λ, used for monitoring volcanoes (Table. 1.1). This range of frequencies has shown advantages for observing volcanic activity in different parts of the world (e.g., L-band for tropical volcanoes with dense vegetation coverage, Saepuloh et al., 2010; Solikhin et al., 2015), and over small and widespread spatial extents. The wavelength of the satellite determines the penetration depth and the relative roughness of the target for that particular sensor. Longer wavelengths (e.g., L-Band) will have longer penetration depths, allowing them to image through tree crowns. However, the penetration depth of a material is also correlated to its moisture content, with a dry soil having a deeper penetration depth and a lower backscatter signal than a wet soil.

Radar polarisation determines the orientation of the electric field components of the wave. SAR sensors tend to use linear polarisation configurations that relate to the emitted and received radiation and have either single- (e.g., HH, VV, HV or VH), such as COSMO-SkyMed (HH), dual- (e.g., HH and HV or VV and VH), such as Sentinel-1 (VV and VH) or quad-polarisation (i.e., transmitting and receiving both H- and V-polarised waveforms, ALOS-2) capacities. This satellite parameter strongly control the backscatter signal observed by a specific sensor. However, unlike the surface scattering properties, these will remain constant across the whole scene.

Volcanic eruptions change the ground surface through the emplacement or removal of material. This thesis therefore focuses on examining changes to the radar backscatter signal related to change to the surface scattering properties over time. These scattering properties all contribute and interact to the final observed signal. The roughness of a surface depends on the wavelength and incidence angle of the satellite. A sensor considers a surface as 'rough' based on the Rayleigh criterion,

$$\Delta h > \frac{\lambda}{8 \cos \theta} \tag{1.12}$$

where h is the mean height of the surface variation, λ is the SAR wavelength and θ the incidence angle. Next, the local incidence angle, which depends on the sensors incidence angle. This means that slopes facing towards the satellite appear brighter than the same slope facing away. And last, the dielectric properties of the ground surface, which is a measure of the electric properties of the material and is strongly dependent on the moisture content. In radar backscatter an increase in moisture will cause an increase in the scattering properties of the target. The ground surface can be changed significantly during a volcanic eruption due to the emplacement and removal of material, which changes all three surface scattering parameters that control radar

backscatter signals. We can therefore use backscatter to observe and understand these changes.

1.1.3 Speckle and Radiometric Terrain Correction

When examining radar backscatter signal, we have to be aware of speckle, which is the constructive and destructive interference from individual scatters within a pixel. Speckle can produce changes in the backscatter signal for a pixel that in reality remained stable between acquisitions. Therefore, when examining the changes in radar backscatter associated with volcanic eruption, speckle can obscure signals making it difficult to interpret. Downsampling, or multi-looking, can improve the quality of the SAR image by reducing speckle at the cost of the resolution of the image. Since multi-looking averages the signal of surrounding pixels there can still be residual speckle present in the image. Depending on the type of process being examined (e.g., lava dome growth), multi-looking might be an adequate filter. Alternative or further corrections can be done using various spatial filtering methods or speckle filters. These methods generally focus on attempting to (1) reduce speckle, (2) preserve edge features, and (3) retain textural information. Some examples of speckle reduction filters are median, Lee-Sigma, Gamma-MAP and Frost (Frost et al., 1982; Lopes et al., 1993; Lee et al., 1994).

The backscatter coefficient for a distributed target is described as the backscatter ratio for a given reference area (Raney et al., 1994). The backscatter coefficient σ_0, represents the scattering properties normalised to the ground surface. There are three reference areas that are used in SAR to calibrate the backscatter coefficient. When the reference area is defined in the slant-range plane is called β_0. β_0 is commonly referred to as the radar brightness and is considered the basic calibration of the reflectivity of a distributed target. It does not require information about the incidence angle. More commonly, σ_0 or the normalized radar cross section, is used to calibrate SAR images. As shown in equation 1.5, σ_0 accounts for the incidence angle and uses a horizontal plane based on an ellipsoid model as the reference area. If the reference area is perpendicular to the satellite's line of sight then the backscatter coefficient is calibrated as γ_0 (Fig. 1.4).

Unlike the radar brightness, σ_0 and γ_0 take the incidence angle of the satellite into account. Without addition information these are both based on an ellipsoid ground model. A radiometric terrain correction (e.g., Small, 2011; Frey et al., 2012) addresses the issues introduced by the side-looking nature of the satellite. By incorporating a Digital Elevation Model (DEM) into processing it is possible to correct and mask out geometric distortions (e.g., radar shadows) and adjust the 'brightness' introduced by variations in local incidence angle (e.g., foreshortened areas). Small, 2011 showed that using a pixel-area based integration for the radiometric terrain correction produced the

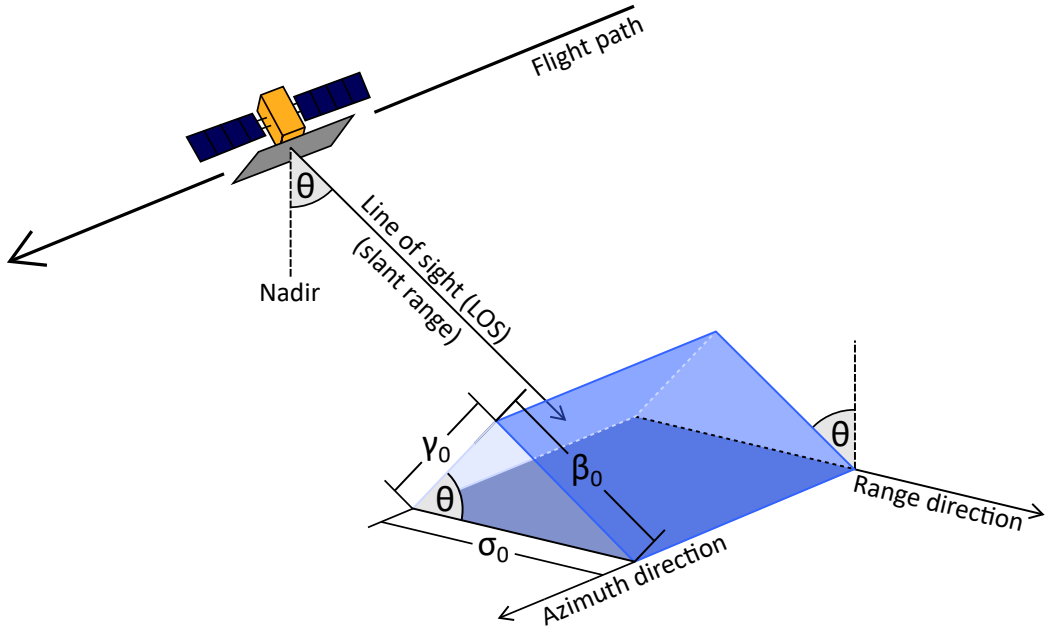

Figure 1.4: Schematic showing the relationship between geometric areas of the different backscatter coefficients, β_0, σ_0 and γ_0. These areas are used to normalise the Radar Cross Section. Figure based Small (2011).

best calibration and that using normalisation areas rather than directly using the local incidence angles better captures the backscatter measurements.

Radiometric terrain corrections are particularly useful in areas with moderate relief or where surface roughness dominates the scattering properties as here the topography induced distortions can be reduced. Larger distortions, such as radar shadows, cannot be corrected as these areas have no observed backscatter values. Doing a radiometric terrain correction can allow for better comparison between acquisitions from different geometries (Meyer et al., 2015).

1.2 SAR for Volcano Monitoring

In the last two decades there have been multiple studies (Table 1.2) that have used SAR amplitude as a means to identify, monitor and examine various types of volcanic processes and products. SAR amplitude has been used to assess dome growth and monitor the stability during ongoing eruptions when, due to weather conditions, ground-based and optical imagery could not (e.g., Wadge et al., 2011; Pallister et al., 2013). Lava flow extents have been mapped using SAR backscatter (Wadge et al., 2002; Wadge et al., 2012; Goitom et al., 2015; Arnold et al., 2017; Di Traglia et al., 2018), and radar shadows have been used to calculate variations in lava lake height (Barrière et al., 2018; Moore et al., 2019), flow thicknesses and effusion rates (Wadge et al., 2012; Arnold et

al., 2017).

Effusive eruptions generally show high magnitude changes in backscatter in relation to the emplacement and development of the deposits. Lava flows cause large variations to the ground surface with a systematic spatial extent helping to map the extent and path of the flow (e.g., Goitom et al., 2015). Following the initial emplacement, SAR backscatter can help identify changes related to the development of morphological structures (e.g., channels, Dumont et al., 2018) or cooling down over time. Lava flows with higher silica content tend to produce thicker flows, forming steep walled edges that due to the side looking nature of the satellite produce radar shadows and can be used to observe the relative change in heights of these features (e.g., Wadge et al., 2012; Arnold et al., 2017).

Volcanic deposits associated with explosive eruptions (i.e., pyroclastic density currents and lahars) are more challenging to identify and to measure in radar backscatter. These deposits are generally spatially confined by the underlying topography, following, infilling and overtopping drainage systems down the flanks of the volcano. Major pyroclastic density currents have been identified both in single backscatter images (Carn, 1999) and using multi-image composites (Wadge et al., 2011).

Finer and more widespread explosive volcanic deposits (i.e., ash) produce subtle changes in the radar backscatter that are not bound by the underlying topography. Four studies have identified ash deposits (Wadge and Haynes, 1998; Goitom et al., 2015; Meyer et al., 2015; Arnold et al., 2018) and show that the backscatter signals are strongly related to the pre-existing surface roughness and whether ash infills and smooths the surface on the scale of the satellite wavelength, or changes a specular reflecting surface (e.g., ice) to one that scatters diffusely (e.g., Arnold et al., 2018).

In the last decade the use of SAR backscatter has steadily increased, with more case studies and methods being published. There has also been an increase in the use for near real-time monitoring with many recent eruptions (Fig. 1.5) using SAR backscatter to either supplement (Fig. 1.5a) or provide first observations (Fig. 1.5b) of an eruption. However, it is important to note that the term near real-time monitoring represents a longer time frame in comparison to other disciplines, such as seismology where data can be acquired and examined continuously during or within minutes of an eruption. The main limitation for using SAR data for volcano monitoring is the timing of the acquisition with respect to the acquisition and subsequent sampling rate.

1.2.1 SAR Backscatter Methods

There have been numerous studies that have used various radar backscatter methods to examine volcanic eruptions (Table 1.2). The simplest and most widespread approach has been to use single radar backscatter image (Fig. 1.6) to identify deposits and

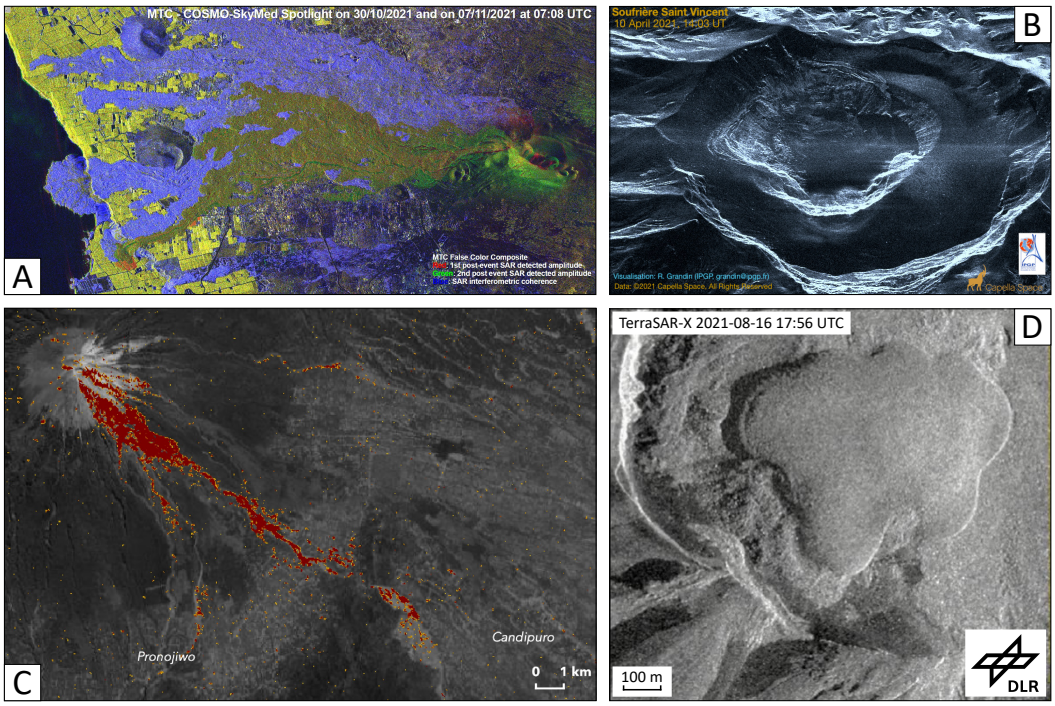

Figure 1.5: Examples of SAR images and products used in near-real time monitoring during volcanic eruptions. (a) COSMO-SkyMed RGB images of the Cumbre Vieja lava flows, La Palma 2021, (b) single Capella SAR image of the newly formed crater during the eruption at La Soufrière, St. Vincent 2021, (c) pyroclastic density current deposits mapped out using Sentinel-1 imagery related to the eruption of Semeru, Indonesia 2021, and (d) continuous monitoring of the lava dome growth at the remote Great Sitkins, Alaska 2021. Full published products can be found in Appendix A.

structures (e.g., Carn, 1999; Carr et al., 2007; Wang and Wright, 2012; Arnold et al., 2017; Walter et al., 2019a). The benefit of using single radar backscatter images is that it does not require multiple images from the same sensor or track. Whilst radar backscatter signals can be complex to interpret, large changes (e.g., flow emplacements or crater collapses) are relatively easy to identify. However, understanding how the ground surface has changed and what caused the change are useful observations for monitoring and understanding an eruption. The interpretation of changes in radar backscatter could be missed when solely using single radar backscatter images.

To observe the changes in radar backscatter, it is common to calculate the change (e.g., through differences or ratios, Fig. 1.6) between a pair of radar backscatter images. These methods bring out areas where the radar backscatter has changed or remained the same between the two images. In addition, RGB change difference maps (Fig. 1.6, Wadge et al., 2011) have been used as a tool to aid in the visualisation of these change maps, by highlighting increases, decreases, and unchanged areas with distinct colours. Change difference maps have been sucessfully used to identify pyroclastic flow deposits

(e.g., Wadge and Haynes, 1998; Wadge et al., 2011; Saepuloh et al., 2015a), lahars (e.g., Wadge et al., 2011), the emplacement of lava flows (e.g., Goitom et al., 2015; Di Traglia et al., 2018), changes in their effusion rate (e.g., Wadge et al., 2012) and ashfall (e.g., Meyer et al., 2015; Arnold et al., 2018). More detail of previous SAR backscatter case studies and what methods they applied are summarised in Table 1.2.

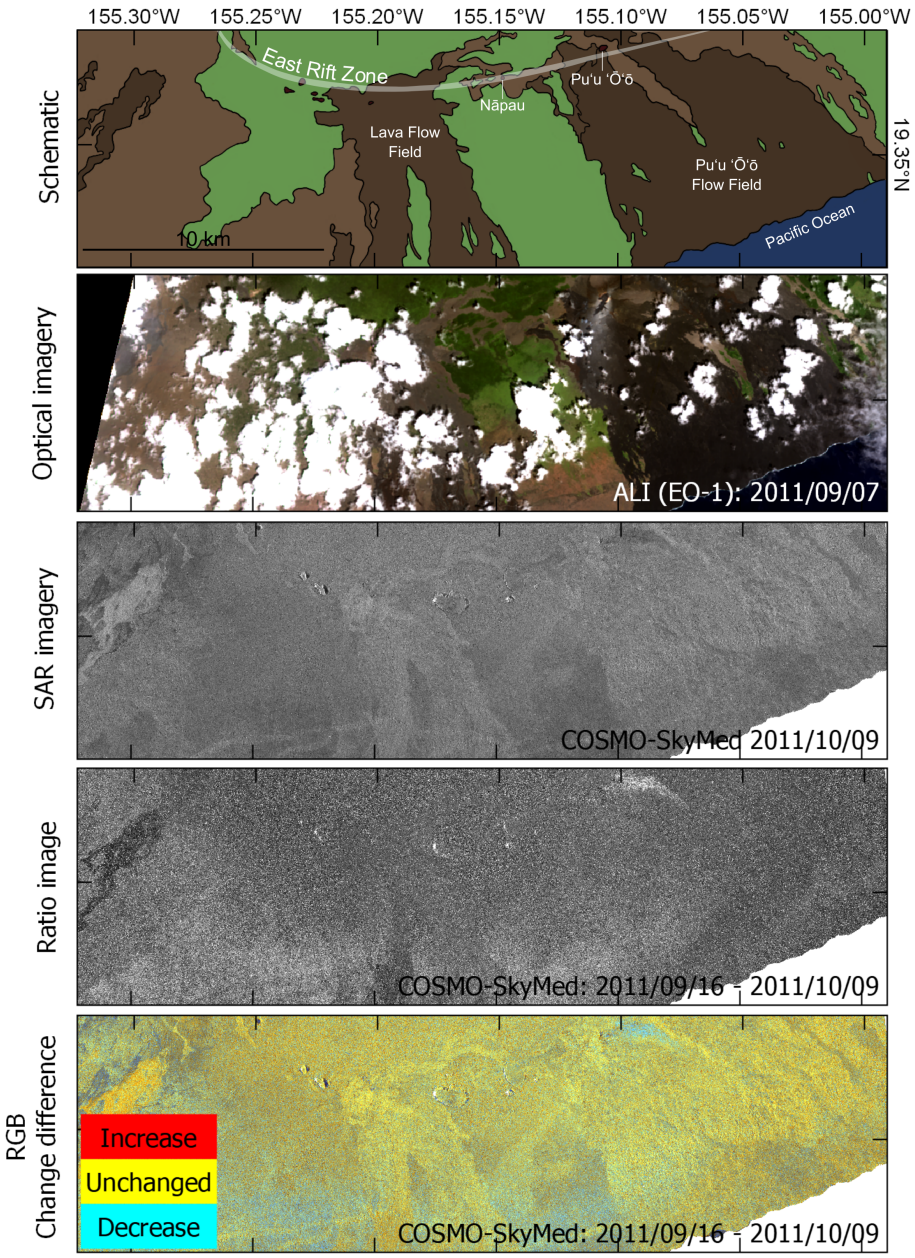

Figure 1.6: The East Rift Zone, Hawai'i shown in (a) simple cartoon, (b) optical imagery from the Earth Observing-1 (EO-1) Advanced Land Imager (ALI) in 2011, (c) SAR backscatter image acquired by COSMO-SkyMed (CSK), (d) ratio and (e) RGB image showing the changes in SAR backscatter between two images spanning the September 2011 eruption of Pu'u 'Ō'ō.

Table 1.2: Summary of previous case studies using SAR backscatter to examine volcanic deposits. Main methods used are (1) examining single backscatter images, (2) pairwise comparison of two backscatter images (e.g., differencing, normalisation, ratios etc.), (3) visualisation method using multiple backscatter images (e.g., RGB change difference) and (4) measuring heights using radar shadows.

	Region	Volcano	Time-span	Process	SAR Methods applied	Reference
Explosive eruptions	Alaska	Okmok	2008	Ash	Ratio Image	Meyer et al., 2015
	East Java		1995	Pyroclastic flow Lahars Lava Dome	Single Image	Carn, 1999
	Ecuador	Cotapaxi	2015	Ash	Single Image	Arnold et al., 2018
	Eritrea	Dubbi	1861	Tephra Pumice Lava Flows	Single Image Composite Image (Optical)	Wiart et al., 2000
	Iceland	Grímsvötn Caldera	1861	Ash	Single Image (Values)	Scharrer et al., 2007
	Indonesia	Cotapaxi	2015	Crater morphology	RGB change difference	Arnold et al., 2018
		Merapi	1996–2006	Pyroclastic flow	Single Image Ratio Image	Saepuloh et al., 2010
			2010	Lava Dome Pyroclastic flow	Single Image Ratio Image	Jousset et al., 2012
				Pyroclastic flow Lahar	Ratio Image Image segmentation	Bignami et al., 2013
				Lava Dome	Single Image	Saepuloh et al., 2013
				Pyroclastic flow	Single Image Ratio Image	Saepuloh et al., 2015a
				Pyroclastic flow Lava Dome	Single Image	Pallister et al., 2013

Explosive eruptions	Indonesia	Merapi	2010	Pyroclastic flow Tephra	Single Image Ratio Image	Solikhin et al., 2015
			2013	Lava Dome Phreatic explosions	Single Image RGB change difference	Walter et al., 2015
		Sinabung & Merapi	2007–2010	Lava Dome	Single Image	Saepuloh et al., 2015b
		Anak Krakatau	2018	Crater Collapse	Single Image Composite image (coherence)	Babu and Kumar, 2019
				Flank collapse	Single Image	Walter et al., 2019a
						Williams et al., 2019
			2018–2019	Growth and collapse	Single Image (Indexing)	Xiang et al., 2022
	Italy	Stromboli	2018–2021	Strombolian eruption	Single Image RGB change difference	Corradino et al., 2021
	Japan	Mt. Unzen	1991–1995	Pyroclastic flow Lahar	Difference Image	Terunuma et al., 2005
	Mexico	Volcán de Colima	2013	Lava dome	Single Image Composite Image	Walter et al., 2019b
	Montserrat	Soufrière Hills	1996	Pyroclastic flow Ash	Composite Image	Wadge and Haynes, 1998
			1996–1999	Pyroclastic flow Lava dome	Ratio Image	Wadge et al., 2002
			2008–2010	Pyroclastic flow Lava dome Lahars	Single Image RGB change difference Radar shadow	Wadge et al., 2011
	Philippines	Pinatubo	1993	Lahars	Single Image	Chorowicz et al., 1997

					RGB change difference	
	Tonga	New Late'iki	2019	Surtseyan eruption	Single Image Unsupervised classification	Plank et al., 2020
Effusive eruptions	Alaska	Westdahl	1991–1992	Lava flows	Single Image	Lu et al., 2004
			1978–1995	Lava flows	Single Image Composite Image	Dean et al., 2002
		Mt. Cleveland	2011–2012	Lava Dome	Single Image	Wang et al., 2015
	Alaskan & Aleutian			General observation Lava flow Debris flow	Single Image	Rowland et al., 1994
	Chile	Puyehue-Cordon Caulle	2011	Lava flows	Single Image RGB change difference	Bignami et al., 2014
	Colombia	Nevado del Ruiz	2015–2021	Lava dome	Single Image	Ordoñez et al., 2022
	Democratic Republic of the Congo	Nyiragongo	2016–2017 2002–2021	Lava lake fluctuations	Radar Shadow	Barrière et al., 2018 Barrière et al., 2022
	Ecuador	El Reventador	2011–2016	Lava flows Lava dome	Single Image Radar Shadow	Arnold et al., 2017
			2012–2016	Lava flows	RGB change difference Radar Shadow	Arnold et al., 2019
	Eritrea	Nabro	2011	Tephra Lava flows	Single Image Normalised difference Radar shadow	Goitom et al., 2015
	Ethiopia	Erta Ale	2017	Lava lake fluctuations	Radar shadow	Moore et al., 2019
	Iceland	Holuhraun	2014–2015	Lava flows	Single Image	Dumont et al., 2018 Pedersen et al., 2017

Effusive eruptions	Italy	Stromboli	2010–2014	Lava flows	RGB change difference Slope failure	Di Traglia et al., 2018
	Kamchatka	Tolbachik	2012–2013	Lava flows	Single Image RGB change difference	Kubanek et al., 2017
		Bezymianny	2016–2017	Lava dome	Single Image RGB change difference	Mania et al., 2019
		Shiveluch	2018–2019	Lava dome	Single Image	Shevchenko et al., 2021
	Papua New Guinea	Bagana	2010–2011	Lava flows	Single Image Radar shadow	Wadge et al., 2012
		Kadovar	2018–2019	Slope failure Lava dome Lava flows	Single Image RGB change difference	Plank et al., 2019
	Global			Lava dome	Single Image Difference Image	Chaussard, 2017
Others	Iceland	Katla	1994–1996	Geothermal	Single Image (Profiles)	Scharrer et al., 2008
	Alaska	Shishaldin	2019–2020	Cone Growth	Topography extraction	Angarita et al., 2022
		Mt. Cleveland	2011–2012	Lava dome		
	Costa Rica	Arenal	2011–2013	Slope Failure	RGB change difference	Ebmeier et al., 2014
	Global			Volcanic flow maps	RGB Composite (Coherence)	Poland, 2022

1.2.2 Differential Interferometric SAR

With the increase of SAR data over the last three decades, Interferometric Synthetic Aperture Radar (InSAR) has become a significant tool in volcano monitoring to measure ground displacement. I will outline the basics of InSAR processing, however comprehensive descriptions of InSAR processing and applications in volcanology can be found in Hanssen (2001) and Lazecký et al. (2020).

InSAR calculates the difference in the phase component between two SAR acquisitions to measure the change in range between the satellite and the ground surface (e.g., Pinel et al., 2014; Ebmeier et al., 2018; Pritchard et al., 2018). Through the combination of two SAR images, InSAR can be used to measure relative ground displacement based on changes in SAR phase between two acquisitions. However, shifts in radar phase are not unique to surface displacement $\Delta\phi_{def}$, in the direction of the satellite's line-of-sight (LOS). The interferometric phase $\Delta\phi_{InSAR}$, is expressed as,

$$\Delta\phi_{InSAR} = \Delta\phi_{def} + \Delta\phi_{DEM} + \Delta\phi_{orb} + \Delta\phi_{atm} + \Delta\phi_{noise} \tag{1.13}$$

which demonstrates to various influence that contribute to the phase shift between acquisitions. $\Delta\phi_{DEM}$ and $\Delta\phi_{orb}$ represent the DEM and orbital errors, which remain after correcting for the influence of the topography and flattening of the phase that were introduced by the satellite geometry. The influence of the topography is corrected for using estimates based on a DEM and the perpendicular baseline. $\Delta\phi_{atm}$ is the shift in phase introduced by different atmospheric delays (mainly due to water vapour) for the two acquisitions and $\Delta\phi_{noise}$ corresponds to other sources of errors unaccounted for (e.g., thermal noise). The atmospheric delays can be mitigated through various approaches, such as generic topography-correlated atmosphere patterns or more advanced correction models based on weather models (e.g., Yu et al., 2018). The resulting interferogram is 'wrapped', meaning that the phase shift is cyclical, ranging between 0–2π and appear as interference fringes. The interferograms are then 'unwrapped', to estimate the cumulative phase change in the satellite LOS (Hanssen, 2001).

Radar Coherence

Phase coherence represents the similarity, or correlation, between the two acquisitions. The magnitude of the coherence is calculated for every pixel using the values from neighbouring pixels in both acquisitions (Hanssen, 2001). Phase coherence ranges from 0 to 1, where 0 represents complete decorrelation between the acquisitions. The main causes of incoherence in an interferogram are (1) spatial, (2) thermal, and (3) temporal decorrelation (Zebker and Villasenor, 1992). Spatial decorrelation correlates to changes in the satellite position between the two images. Higher levels of incoherence are observed with larger baseline. Thermal decorrelation is related to the noise from

the sensor itself. The most common cause for incoherence, is temporal decorrelation or changes to the surface scattering over time. To accurately resolve for the shift in radar phase, the scattering properties of the ground surface need to remain stable between acquisitions. Therefore, either rapid changes to the surface scattering properties or over extended periods of time between acquisition will likely be incoherence. Vegetation, precipitation and landslide are some of the causes for incoherence (e.g., Zebker and Villasenor, 1992; Scott et al., 2017; Burrows et al., 2020). To calculate ground deformation using InSAR, high coherence is preferred. However, the emplacement and development of volcanic deposits will cause the loss of coherence between images. These changes in phase coherence have been used to map out volcanic deposits (e.g., Lava flows, Dietterich et al., 2012). In this thesis, I use loss and recovery of coherence as a complimentary dataset to SAR backscatter.

1.3 Thesis Aims

The aim of this thesis is to investigate the use of SAR backscatter to observe, identify and quantify various volcanic eruptive deposits through time. I will use a variety of methods to examine difference types of signals (e.g., roughness or local gradient dominated) to understand eruption deposits and processes. With the aim to test how SAR backscatter can be used as a 'main' dataset to provide information about an eruption not only as a subsection or to confirm other observations. My specific objectives for this thesis are as follows,

1. Explore what SAR backscatter methods are best suited for the identification of a range of volcanic deposits (e.g., pyroclastic flow, lahars, lava flows)
2. Exploiting dense high-resolution SAR datasets to improve the SAR backscatter signal-to-noise ratio to allow for better identification of volcanic deposits
3. Extract quantitative measurements of topographic changes related to volcanic activity seen in SAR backscatter imagery

1.3.1 Thesis Structure

In this thesis, I will use SAR backscatter to identifying explosive volcanic deposits and their development through time dominated by changes to the surface roughness (Volcán de Fuego, Guatemala; Chapter 2), examine the emplacement and development of lava flows and lakes over multiple years that permanently changes the surface roughness (Kīlauea, Hawai'i; Chapter 3), and quantify dome growth through the alteration of the local gradients (La Soufrière, St. Vincent; Chapter 4). In Chapters 2–4, I use plural pronouns (e.g., we, us, our etc.) as these chapters are part of joint-author work that have either been published or are currently being prepared for publication. The

breakdown of co-author contribution has been explicitly stated on pages iii-iv. The rest of this section provides a outline of the subsequent chapters in this thesis.

- In chapter 2, I examine in detail the changes in SAR backscatter for the explosive 2018 eruption at Volcán de Fuego. I show how various methods help in the identification of different eruption processes and deposits and illustrate the importance of understanding the underlying surface topography and properties, the influence of rainfall, and topographic corrections. I also show the difference that high- and low- resolution SAR backscatter imagery has on these results. This chapter has been published in the *Journal of Geophysical Research: Solid Earth*, (Dualeh et al., 2021).

- In Chapter 3, I delve into a multiyear dataset of high-resolution CSK SAR backscatter images to monitor the effusive eruption at Kīlauea Volcano, Hawai‘i between 2010–2013. I identified and corrected for a satellite dependency present in the CSK constellation that obscured the subtle changes in SAR backscatter. Using this corrected dataset, I was able to automatically map out lava flow emplacement and attempted to examine cooling of the lava flow post-emplacement. In addition to the activity on the lava field, I calculated changes in height for Pu‘u ‘Ō‘ō crater and examine variations in lava lake activity.

- In Chapter 4, I develop a method to extract lava dome volumes and extrusion rates from SAR backscatter from multiple sensors (TerraSAR-X, COMSO-SkyMed and Sentinel-1). I apply this method to the dome growth phase during the 2021 eruption of La Soufrière, St. Vincent. Through the combination of multiple SAR sensors, I was able to observe variations in extrusion rate prior to the transition from the effusive dome growth phase to the explosive phase. This chapter has been written up as a paper to be submitted to *Earth and Planetary Science Letters*.

- In Chapter 5, I summarise the outcomes from the different case studies with respect to improvements to monitoring volcanic eruptions using SAR backscatter, quantifying topography changes and improving the signal to noise ratio. I then go on to discuss the future of SAR backscatter and how certain methods could be optimised for volcano monitoring.

Chapter 2

Radar backscatter analysis of explosive volcanic deposits from the June 2018 eruption of Volcán de Fuego, Guatemala

Satellite radar backscatter has the potential to provide useful information about the progression of volcanic eruptions when optical, ground-based, or radar phase-based measurements are limited. However, backscatter changes are complex and challenging to interpret: explosive deposits produce different signals depending on pre-existing ground cover, radar parameters and eruption characteristics.

In this chapter, we use high temporal- and spatial-resolution backscatter imagery to examine the emplacement and alteration of pyroclastic flows, lahars, and ash from the June 2018 eruption of Volcán de Fuego, Guatemala, drawing on observatory reports and rain gauge data to ground truth our observations. We use dense timeseries of backscatter to reduce noise and extract deposit areas. Backscatter decreases where six flows were emplaced on 3 June 2018. In B. Las Lajas, we measured a 11.9-km-long flow that altered an area of 6.3 km^2 and used radar shadows to estimate a thickness of 10.5 $\pm$2 m in the lower sections. The 3 June eruption also changed backscatter over an area of 40 km^2, consistent with ashfall. We use transient patterns in backscatter timeseries to identify nine periods of high lahar activity in Barranca Las Lajas between June and October 2018. We find that the characterisation of subtle backscatter signals associated with explosive eruptions is assisted by (1) radiometric terrain calibration, (2) speckle correction, and (3) consideration of pre-existing scattering properties. Our observations demonstrate that SAR backscatter can capture both the emplacement and subsequent alteration of a range of explosive products, allowing the progression of an

explosive eruption to be monitored.

2.1 Introduction

During an explosive volcanic eruption, monitoring can be impeded by both cloud coverage and damage to instrument networks. However, satellite-based Synthetic Aperture Radar (SAR) images are unaffected by cloud and can provide frequent observations of the progression of an eruption. While measurements from differential Interferometric Synthetic Aperture Radar (InSAR) are increasingly widely used for volcano monitoring (e.g., Fournier et al., 2010; Pritchard et al., 2018; Ebmeier et al., 2018), radar backscatter from individual SAR images (e.g., Wadge et al., 2011; Wadge et al., 2012) has been under-exploited. Backscatter changes can be high magnitude and obvious (e.g., dome collapse, Pallister et al., 2013), or very subtle (e.g., ash dispersion, Arnold et al., 2018). The interpretation of SAR backscatter for volcanology is challenging because there is no simple relationship between the magnitude or sign of backscatter change and the physical properties of fresh volcanic deposits. Backscatter signals from explosive deposits are particularly difficult to interpret because their thickness varies over several orders of magnitude and because of their tendency to be rapidly eroded.

We use imagery spanning the 3 June 2018 eruption of Volcán de Fuego to investigate the potential of backscatter for monitoring explosive eruptions. We characterise the backscatter changes associated with pyroclastic flows, lahars, ash and investigate post-emplacement reworking by water and numerous lahars over a four month period.

2.1.1 Synthetic Aperture Backscatter

Radar backscatter, σ, is the proportion of the transmitted electromagnetic pulse that the ground surface directs back towards the satellite. For an area with multiple scatterers, the backscatter coefficient (σ°) is the radar cross section (σ) normalised by the area illuminated by the satellite (A) and expressed as,

$$\sigma^\circ = \frac{4\pi R^2 \rho_R}{\rho_T A} \tag{2.1}$$

where ρ_T and ρ_R are the power density transmitted from the satellite antenna towards the Earth and returned to the satellite sensor respectively, and R is the distance or range between sensor and target. σ° is sensitive to changes in the satellite parameters (local incidence angle, wavelength λ and polarisation) and the scattering properties of the ground. Variables including surface roughness, local slope, and dielectric properties combine to determine the scattering properties of the ground surface. Erupted material may alter one or all of these scattering properties, which are also affected by independent non-volcanic processes such as rainfall, producing complex backscatter signals.

2.1.2 The 2018 Eruption of Volcán de Fuego, Guatemala

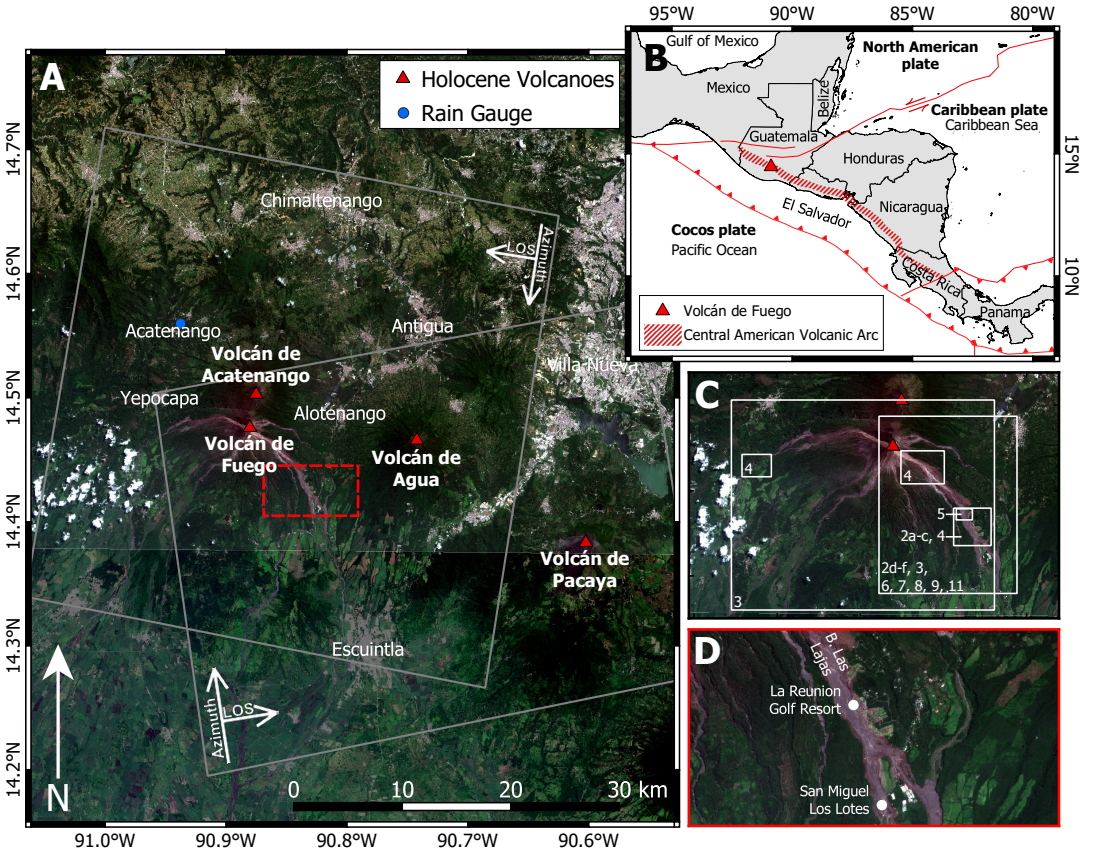

Figure 2.1: (a) Map of Volcán de Fuego showing the footprint of COSMO-SkyMed tracks and look direction (white rectangle), with (b) location of Fuego within Guatemala. (c) spatial extents used for subsequent figures in this article are shown by white outlines with corresponding figure number and (d) names of settlements and notable locations. (Basemap: 11 Nov. 2018 and 04 July 2018, Copernicus Sentinel-2 data)

Volcán de Fuego (3763 m a.s.l.) is the southernmost and currently most active crater of the Fuego-Acatenango volcanic complex in Guatemala, located ∼ 40 km southwest of the capital, Guatemala City. Since the first written record of activity at Fuego in 1524, the volcano has had ∼ 60 subplinian eruptions (Global Volcanism Program, 2005) separated by long periods of intermittent Strombolian activity, making it one of the most active volcanoes in Central America. Periods of high activity at Fuego are characterised by frequent Strombolian eruptions, producing short lava flows (100s m), lahars and ash explosions (Patrick et al., 2007; Lyons et al., 2010). These periods are interspersed with high magnitude explosive eruptions, known as paroxysms (Martin and Rose, 1981). These paroxysms are short lived (∼ 24 - 48h) eruptions that produce longer lava flows (100s - 1000s m), pyroclastic flows, and are able to produce and sustain an eruptive column. Volcán de Fuego is monitored by INSIVUMEH (Instituto

Nacional de Sismología, Vulcanologia, Meteorologia e Hidrología), who are responsible for monitoring and communication on natural hazards, including volcanic activity to the government and private sector.

The current period of activity started in 1999 (Lyons et al., 2010) with eruptive intensity increasing in 2015 (Naismith et al., 2019). The 3 June eruption was an unusually large paroxysm (Naismith et al., 2019), with much longer pyroclastic flows and activity that increased in intensity during the eruption. The eruption began on 3 June 2018 at 06:00 local time with frequent strong summit explosions accompanied by pyroclastic flows and a plume that reached up to 17.5 km a.s.l (Pardini et al., 2019). The first pyroclastic flows were emplaced on the western flanks of the volcano. By 14:00 local time, pyroclastic flows had descended six drainage ravines on the east and west flanks. These included multiple flows inside Barranca Las Lajas (Fig. 2.1). Most of the pyroclastic flows were restricted to the upper flanks of Fuego. However, the series of pyroclastic flows in B. Las Lajas extended over 12 km from the summit, longer than all the other flows, and buried the town of San Miguel Los Lotes (Fig. 2.1d), killing several hundreds of people. Official numbers report 332 people missing as a result of the eruption, although the death toll could be as high as 2,900 people (Naismith et al., 2020).

The eruption ended after 16 hours, when activity was reduced to an ash column of $\sim 4,500$ m a.s.l (INSIVUMEH, 2018c) and weak to moderate explosions at the summit. Over the following days activity level remained high, with multiple pyroclastic flows recorded on the 5^{th}, 7^{th}, 8^{th} and 12^{th} June, dominantly on the east flank of Fuego. Interaction between the freshly deposited material and high levels of rainfall resulted in frequent lahars: INSIVUMEH reported 65 lahars between 3 June and 1 July 2018.

2.1.3 SAR Backscatter Dataset

COSMO-SkyMed (CSK) is a constellation of four X-band (3.1 cm) satellites, with a 2 x 3 metres pixel dimensions in radar geometry in stripmap mode. We used 62 HH-polarised acquisitions from an ascending (H4-0B) and descending (H4-03) track between January and October 2018. This time frame includes a typical Fuego paroxym in February 2018, the unusually large 3 June 2018 paroxysm, the three months prior to the 3 June paroxysm that were uncharacteristically quiet compared to recent activity and the four months after the eruption that encompassed smaller pyroclastic flows, multiple lahars and the transition from the dry to wet season. The wet season lasts between April and September, with a pause in rainfall during July, known as the canicula. Acquisition intervals range from 1 to 8 days, with an average perpendicular baseline between images of 690 m (ranging from 6 to 1890 m).

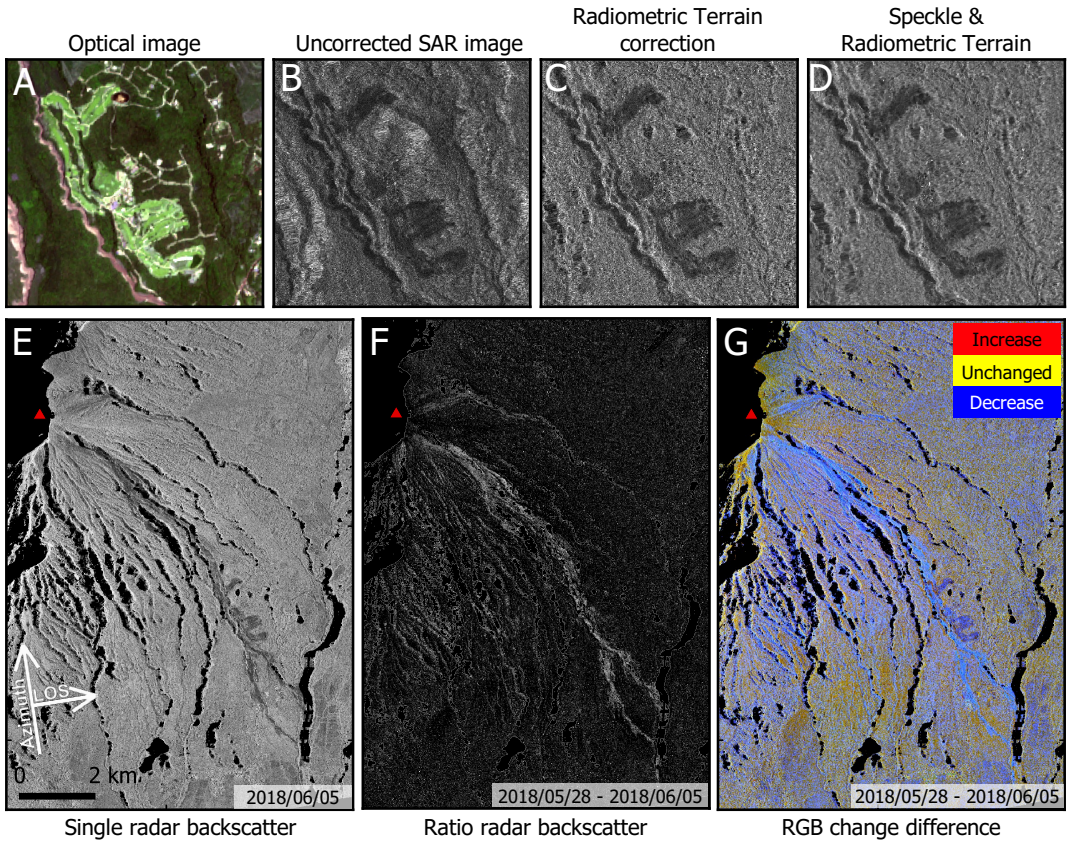

Figure 2.2: La Réunion golf course in (a) Sentinel-2 optical imagery (20-04-2018), (b-c) backscatter corrections and (e-g) visualisation methods applied to ascending CSK images. (b) uncorrected single backscatter image (2018-06-05) over the La Réunion golf course, (c) with a radiometric terrain correction and (d) with a radiometric terrain correction and a 5 x 5 pixel Gamma-*MAP* speckle correction. (e) single backscatter image showing the 3 June 2018 eruption, (f) ratio and (g) RGB change difference of pre- and post-eruption backscatter. Location of the scene is shown in Fig. 2.1c.

Corrections and Calibrations

We produced full resolution geocoded backscatter images using the GAMMA remote sensing software (Werner et al., 2000), with all images resampled to the geometry of a common date to facilitate comparison. Slopes facing towards or away from a side-looking SAR sensor will appear in radar images to be either foreshortened or lengthened respectively. If the slope's gradient is steeper than the radar incidence angle, returns from the top of the slope reach the satellite before those from the bottom, producing a layover effect. Similarly, steep slopes facing away from the satellite cast a shadow, from which no information is scattered back to the SAR sensor. To mitigate the impact of topography on backscatter we do a terrain-based radiometric calibration (Fig. 2.2c) using 10 m resolution digital elevation models (DEMs), constructed from pairs of TanDEM-X bistatic images acquired on 18/10/2015 and 09/08/2018 (Albino et

al., 2020). The radiometric terrain correction uses the DEM to increase the accuracy of the pixel area estimation used in the normalisation of the backscatter coefficient. The calibration also reduces the sensitivity to the incidence angle by normalising the backscatter coefficient by the cosine of the incidence angle (Small, 2011; Meyer et al., 2015).

Speckle, the constructive and destructive interference from individual scatters within a pixel, causes backscatter changes even in pixels that would otherwise remain stable between acquisitions. Speckle in SAR images can obscure signals in backscatter and complicate the data interpretation. We applied a 5×5 pixel adaptive Gamma-*MAP* filter, which reduces speckle while attempting to preserve structural and textural features in the radar data (Lopes et al., 1993). We found that this filter preserved the sharp boundaries of the fresh pyroclastic flow deposits and man-made structures (e.g., golf course, Fig. 2.2d) whilst reducing the speckle allowing for better comparison between acquisitions.

2.2 SAR Backscatter Analysis of the June 2018 Fuego Eruption

We describe the characteristics of the major explosive deposits from the June 2018 eruption as they appear in SAR backscatter, first using simple approaches, before establishing generalisable techniques for deposit identification and then exploring the potential for automated mapping. We use the ratio of two backscatter images (Fig. 2.2f) to emphasise areas that have changed (Wadge et al., 2002), and use RGB composites for visualisation (Fig.2.2g, Wadge et al., 2011) where we display the later date in the red band, the earlier date in the green band and their ratio in blue. Increases in backscatter therefore appear magenta, and are mostly associated with the ground has becoming rougher due to the emplacement of the pyroclastic flow (e.g., pyroclastic flow deposits around the La Réunion golf course, lower B. Las Lajas, Fig. 2.2g). Decreases in radar backscatter appear cyan, and are largely associated with smoothing between acquisitions (e.g., Upper B. Las Lajas, Fig. 2.2g). Areas that do not change between acquisitions (e.g., 10 km southwest from Fuego's summit, Fig. 2.2g) appear yellow.

The major pyroclastic flow that descended B. Las Lajas during the 3 June 2018 eruption caused an overall decrease in backscatter (Fig. 2.3). There is a broad zone of backscatter change near the summit, which narrows as flows are funnelled into drainage channels. Here material is removed, reworked and moved downslope before being deposited, blanketing the ground surface (Albino et al., 2020). The fresh blanket reduces the backscatter (blue, Fig. 2.4a) by making the ground smoother on the scale of the X-band radar wavelength (i.e. CSK, 3.1 cm). However, in the middle of the pyroclastic flow path in B. Las Lajas there is a 60 m wide channel-like feature where backscatter

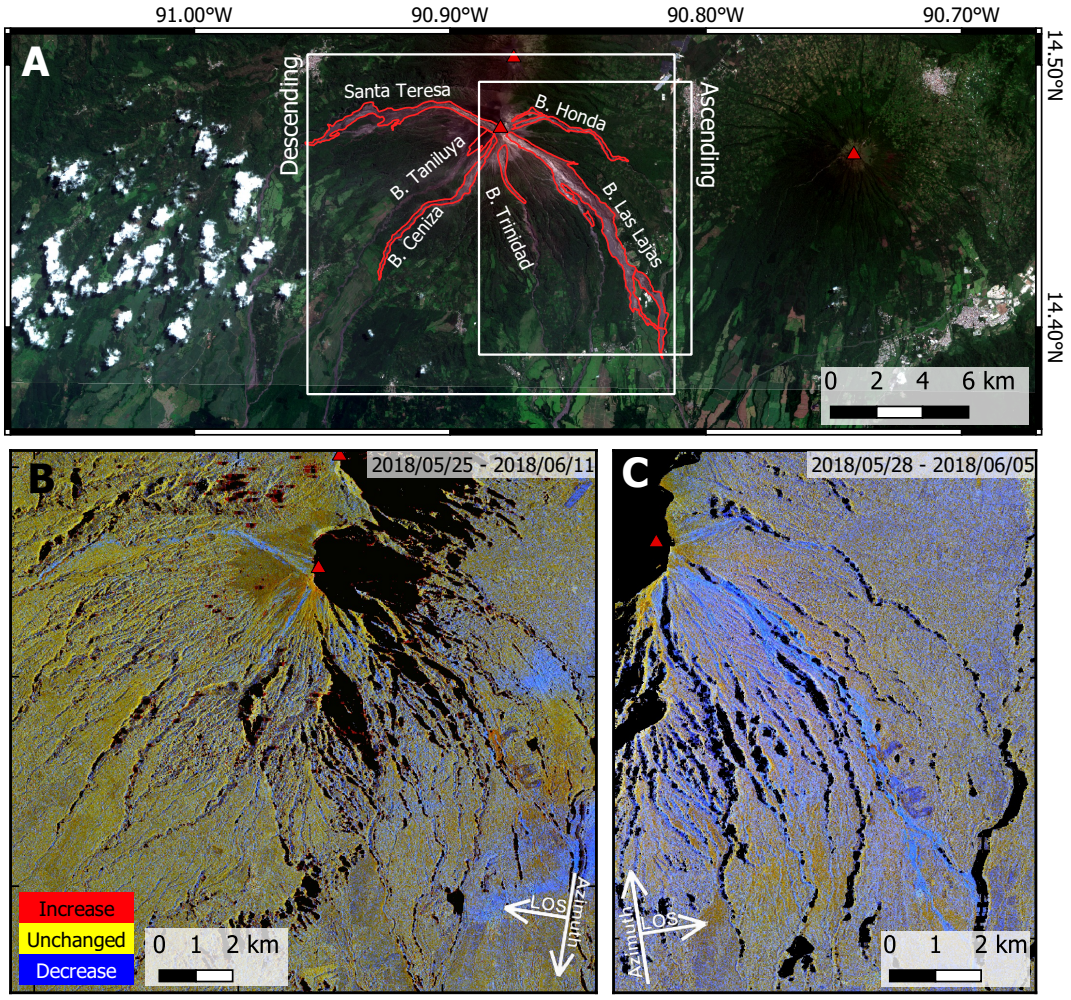

Figure 2.3: a) Map of the main drainage systems on Fuego affected by the 3 June 2018 eruption, as seen RGB change difference image using (b) ascending and (c) descending track showing backscatter changes in B. Honda and B. Las Lajas on the east flank and B. Santa Teresa, B. Taniluya and B. Ceniza on the west flank. Location of the scene is shown in Fig. 2.1c.

increases (red, Fig. 2.4a). Where the pyroclastic flow has overtopped the drainage channel, the changes in backscatter depend strongly on the scattering properties of the previous surface cover resulting in complex change patterns in the lower drainage systems (e.g., dense vegetation or bare rock, Fig. 2.4). Where a pyroclastic flow removes vegetation the ground becomes smoother and the contribution of volumetric scattering is removed, resulting in a decrease in backscatter (e.g., forested area south of B. Santa Teresa, Fig. 2.4b). Backscatter change patterns differ for ascending and descending CSK tracks where the pyroclastic flow interacted with vegetation or buildings (e.g., La Réunion golf course, Fig. 2.4c), because scattering properties vary depending on the angle from which an object is viewed.

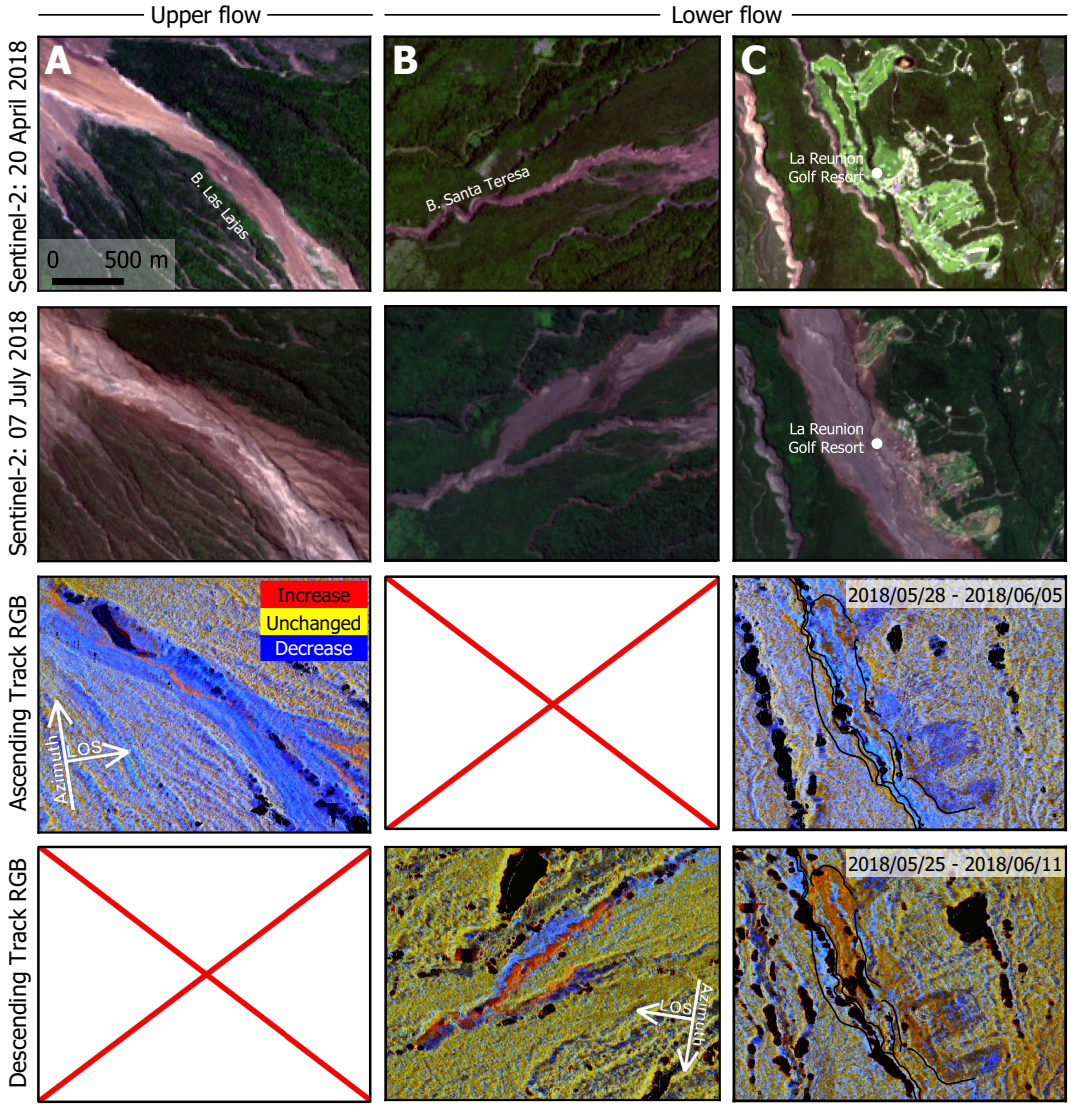

Figure 2.4: Backscatter changes associated with the 3 June 2018 eruption in different sections of the drainage systems. Pre- and post-eruption optical imagery and ascending CSK RGB image of (a) eastern summit area affected by pyroclastic flows in B. Las Lajas and (b) the lower section of B. Santa Teresa showing the 3 June pyroclastic flow infilling and overtopping the drainage system. Blue and red overlays indicate the increases and decreases in backscatter observed from the RGB images. (c) Pre- and post-eruptive optical imagery, descending and ascending CSK RGB images over the La Réunion golf course and B. Las Lajas showing backscatter changes correlated with different satellite look direction and incidence angle. Location of the scene is shown in Fig. 2.1c.

2.2.1 Multiple Image Backscatter Analysis

Changes in backscatter images between two dates can be noisy, and impacted by non-volcanic effects such as changes in moisture levels. We consider background noise present in backscatter images to include variations introduced by speckle, which has no temporal or spatial structure; instrument noise, which may have temporal structure,

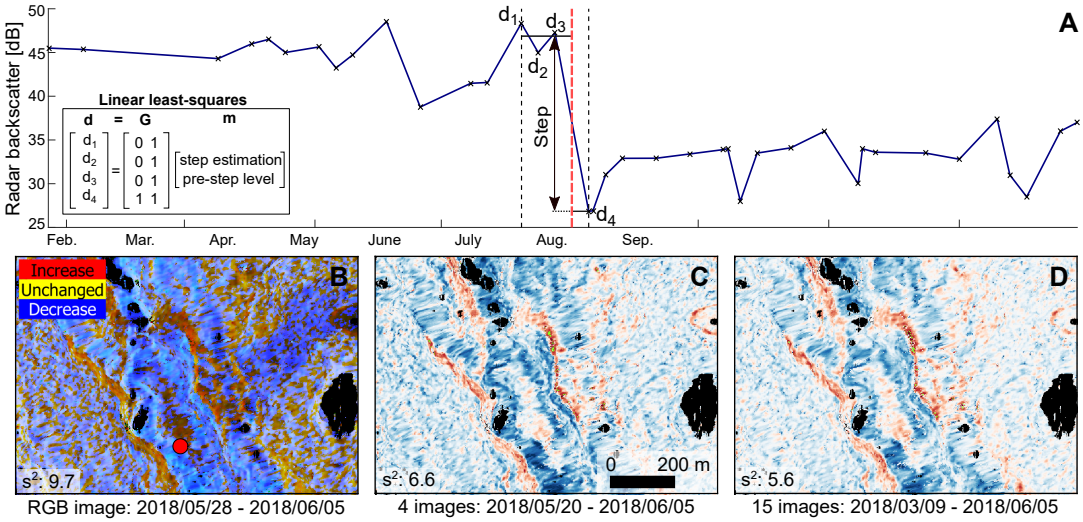

Figure 2.5: (a) Timeseries of single pixel (red dot in B) spanning the 3 June 2018 eruption (red dashed line) showing an acquisition time range (black dashed line) containing four images and the backscatter step calculated using the equation shown where 'd' is the backscatter values and 'G' is the design matrix. The zoomed-in images over a section of 3 June 2018 PDC deposits in B. Las Lajas show the changes in backscatter between 2018/05/28 - 2018/06/05 as (b) a RGB change difference image, (c-d) a 4- and 15-image step estimation, with variance (s^2) of background labelled. Location of the scenes is shown in Fig. 2.1c.

and changes to the ground surface unrelated to the volcanic eruption (e.g., moisture level), which can be spatially and temporally correlated. Using our temporally dense dataset we can solve for the step associated with changes in backscatter that occur on a particular date, placing no constraint on whether the step should be positive or negative. Using a pixel-by-pixel least squares inversion (Fig. 2.5a), we found that at least four images were required to see an improvement in the sharpness of flow edges when comparing to the ratio between two backscatter images. This method allowed for better identification of flow boundaries (Fig. 2.5c,d), and lower magnitude changes that were not visible in RGB ratio images (Fig. 2.6c). The variance of backscatter change was reduced by 31% when using a total of four rather than two images, and the addition of more dates reduced the variance even further to 42% for 15 images.

To refine our map of the 3 June 2018 eruption deposits, we make a step estimate using 14 backscatter images before the eruption and one after to avoid contamination by later flows, slope movements, and erosion. We also observe broad, low magnitude spatially correlated backscatter increases and decreases on the southern flank of Fuego associated with the 3 June 2018 and not apparent at any point before the eruption (Fig. 2.6c). The association only with the date of the main eruption, distinct spatial correlations in backscatter magnitude and sign, and limited extent are consistent with a major ash fall event rather than with changes due to rainfall. We therefore attribute it

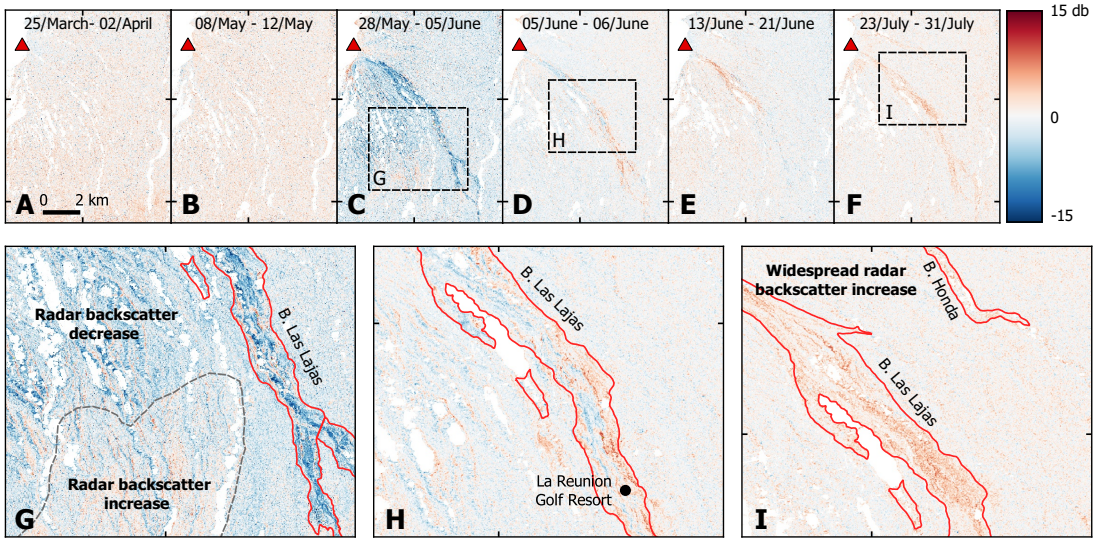

Figure 2.6: Step estimation (locations shown in Fig. 2.1c) each using four acquisition dates spanning 12–24 days in total showing (a-b) backscatter variations prior to 3 June 2018 eruption, (c) the emplacement of the 3 June 2018 pyroclastic flows and ash deposits and (d-f) post-eruption emplacement of new deposits, alteration and interaction with rainfall. (g-i) detailed sections of backscatter alteration seen post-eruption.

to ash emplaced on 3 June 2018 that was rapidly removed during the first rainfall event that occurred on the 5 June. Over densely vegetated areas of the flank the ash causes a decrease in backscatter whereas on agricultural land there was an increase (Fig. 2.6g). Reports of ash associated with the 3 June 2018 eruption suggest ash was deposited in almost every direction for about six days, with fine ash deposits extending as far as 40 km towards the northeast (INSIVUMEH, 2018b), however backscatter signals appear to be more limited.

2.2.2 Identification of Explosive Deposits

Flow Mapping

The mapping of new flows is important to track eruption progression, update hazard assessments and protect the local communities. We can manually extract flow shapes from backscatter data, but this is both subjective and requires a longer time than may be realistic during future ongoing eruptions. We therefore test a semi-automated approach that exploits the changes in our backscatter step estimations (Fig. 2.7a). We consider unsupervised classification to be an appropriate approach because suitable training data is unlikely be available for a particular volcano and specific deposits type before an eruption.

We use image segmentation methods aiming to keep extraction as simple as possible, and to limit the number of subjective decisions. We employ a morphological

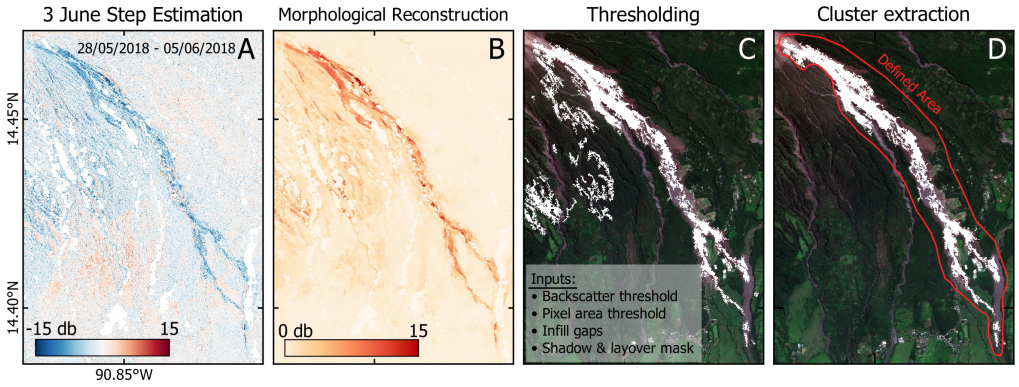

Figure 2.7: Semi-automatic method used to extract flow areas and lengths from (A) a four month step estimation using 15 CSK SAR acquisitions from 5 February to 5 June 2018 to extract the 3 June 2018 PDC in B. Las Lajas. (B) Morphological Reconstruction (MR) applied to step estimation image, then using (C) multiple thresholds to clear up clusters before (D) selection of clusters associated with specific flows based on drainage location and cluster pattern after thresholds. Location of the scene is shown in Fig. 2.1c.

reconstruction (MR) on our step estimations prior before thresholding the image to extract large changes in backscatter associated with the emplacement of flows (Fig. 2.7b). MR uses a marker image based on the backscatter values to preserve object shapes whilst reducing noise (e.g., Lei et al., 2018), and we use a structuring element (10 - 20 pixels wide) in order to selectively reconstruct features with the characteristic spatial scales of flow deposits. We then apply a backscatter threshold (1.5 - 3 db for the 3rd June flows), a pixel area threshold (removing groups < 7000 m^2) and fill in any small, closed gaps within the flow using a gap size threshold (Fig. 2.7c). We retain larger complete gaps because they could possibly reflect real flow path structures. Lastly, we select and remove larger pixel clusters that are not associated with the emplaced flow (e.g., signals from the ash deposits) to extract the final flow shape (Fig. 2.7d).

We used this semi-automatic approach to estimate the areas altered by pyroclastic flows during the 3 June eruption (Table 2.1). Areas extracted semi-automatically from backscatter imagery were 40 - 90 % lower than those found manually (Table 2.1), with the biggest differences for smaller flows (e.g., B. Taniluya) where the backscatter signals are more difficult to differentiate from the surrounding noise. Estimates from the semi-automatic method are minima, because low magnitude backscatter changes, such as flow edges, overlaps with other deposits (e.g., ash) were not captured, especially near the summit or where the flows were relatively narrow. Areas estimated from optical imagery were also consistently larger than those from the SAR imagery, perhaps because very thin deposits can have a minimal impact on backscatter values for some types of land cover.

Table 2.1: Lengths and area measurements of Fuego drainage systems (location Fig. 2.1a) affected by the 3 June 2018 pyroclastic density currents extracted manually and semi-automatically from the step estimation backscatter and from optical imagery (Sentinel-2, 2018/07/04).

	Honda	Las Lajas	Ceniza	Taniluya	Seca	Trinidad
SAR Flow Length (km)	6.4	11.9	8.3	1.8	9.1	> 2.5
[1]Length (km)	-	11.7	8.5	-	9.0	-
SAR area, Manual (km^2)	1.2	6.3	1.7	0.5	2.9	> 0.6
SAR area, Semi-automatic (km^2)	0.4	4.0	0.2	-	1.1	-
SAR Percentage decrease (%)	83.3	39.7	88.2	-	62.1	-
Optical area, Manual (km^2)	1.4	7.4	1.8	1.2	3.7	1.2

[1]Measurements cited from Escobar Wolf, R. and Ferres, D. (2018) .

Deposit thicknesses from Radar Shadow

Radar shadows are the product of the side-looking satellites when the slope casting the shadow is steeper than the satellite incidence angle. The width of the radar shadow can be used to measure the height, h, of the feature casting the shadow using (e.g., Arnold et al., 2018),

$$h = W_{range} \cos\theta \tag{2.2}$$

W_{range} is the width of the radar shadow in the range direction in satellite radar geometry, θ is the radar incidence angle (Fig. 2.8). Changes in the radar shadow width can be used to calculate the thickness of volcanic material that infills valleys. When the feature casting the radar is at an angle (ϕ) to the range direction, Arnold et al. (2017) indicates that this method only works when $\phi \leq 45°$ to calculate accurate height measurements.

Shadows produced by the side-looking satellite radar can be used to estimate the changes in heights of the feature that cast them, (e.g., Arnold et al., 2018). However, this relies on the geometry of topographic features relative to satellite look direction, and only in the lower sections of B. Las Lajas (Fig. 2.8) were we able to use radar shadow to calculate a flow thickness of 10.5 $\pm$2 m for the freshly emplaced 3 June 2018 pyroclastic flow.

Exploiting Full Backscatter Timeseries

Backscatter changes during an eruption may be subtle, complicated by multiple events (e.g., lahar flows) or develop slowly over an extended period of time (e.g., erosional

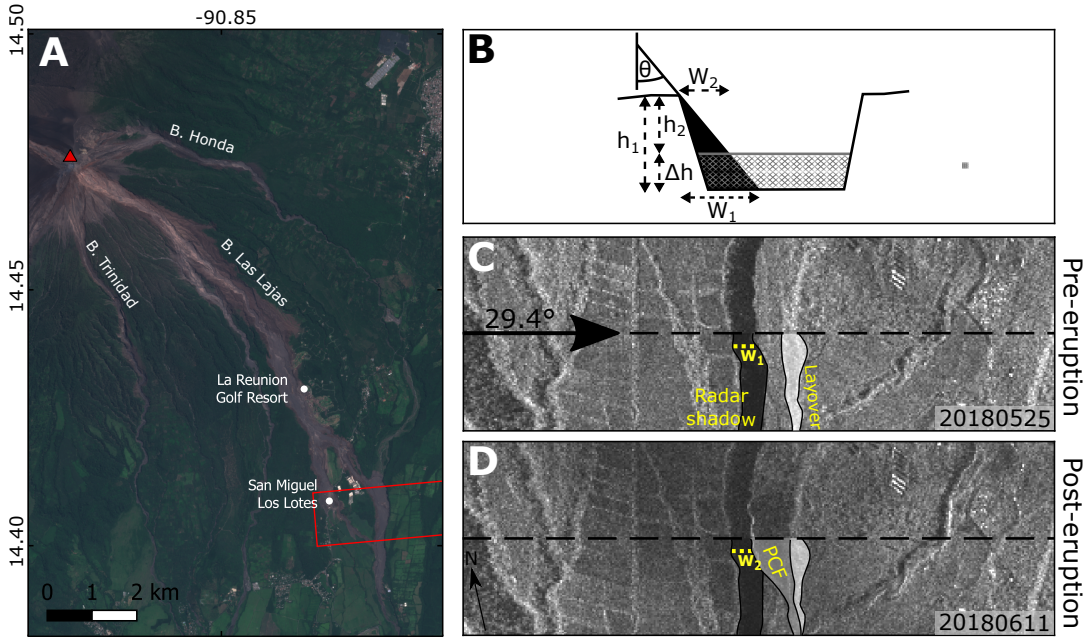

Figure 2.8: (a) Sentinel-2 imagery of the east flank of Fuego showing places (e.g., drainages and towns) in white. (b) Schematic of radar shadow method for measuring pyroclastic flow deposit thicknesses within a wide infilling valley. h_1 and h_2 are the pre- and post-eruption valley heights respectively, and Δh is the difference between h_1 and h_2, W_1 and W_2 are the width of the radar shadow pre- and post-eruption and θ is the radar incidence angle. (c-d) are annotated descending CSK images (red box in (a)) showing the change in radar backscatter after the emplacement of the 3 June 2018 pyroclastic flow in B. Las Lajas.

processes). To examine these types of signals, we calculate the changes in backscatter for a particular area for all possible date combinations in our dataset (producing backscatter change grids: Fig. 2.9). These highlight temporal structures that allow us to distinguish between long-term processes (e.g., erosion and material settling) and abrupt changes that correlate to specific volcanic events (e.g., lahars).

Prior to the 3 June 2018 eruption, backscatter variations were minimal for all parts of B. Las Lajas (Fig. 2.9d-h). The 3 June pyroclastic flows caused high magnitude changes that were strongly dependent on pre-existing scattering properties (e.g., compare the valley and the golf course in Fig. 2.9d and f). Backscatter changes on fresh pyroclastic deposits between pairs of images after the 3 June 2018 eruption show more complexity, and highlight structures not easily recognisable in the individual change difference images (e.g., Fig. 2.6). To distinguish between gradual erosion and re-working by lahars, we compare backscatter change grid patterns to rainfall data from the El Platana rain gauge (Fig. 2.1c, 1578 m a.s.l.; 14.56°N, 90.94°W). We found that episodes of complex changes in backscatter coincided with periods of high rainfall and matched periods of reported lahars from the INSIVUMEH bulletins.

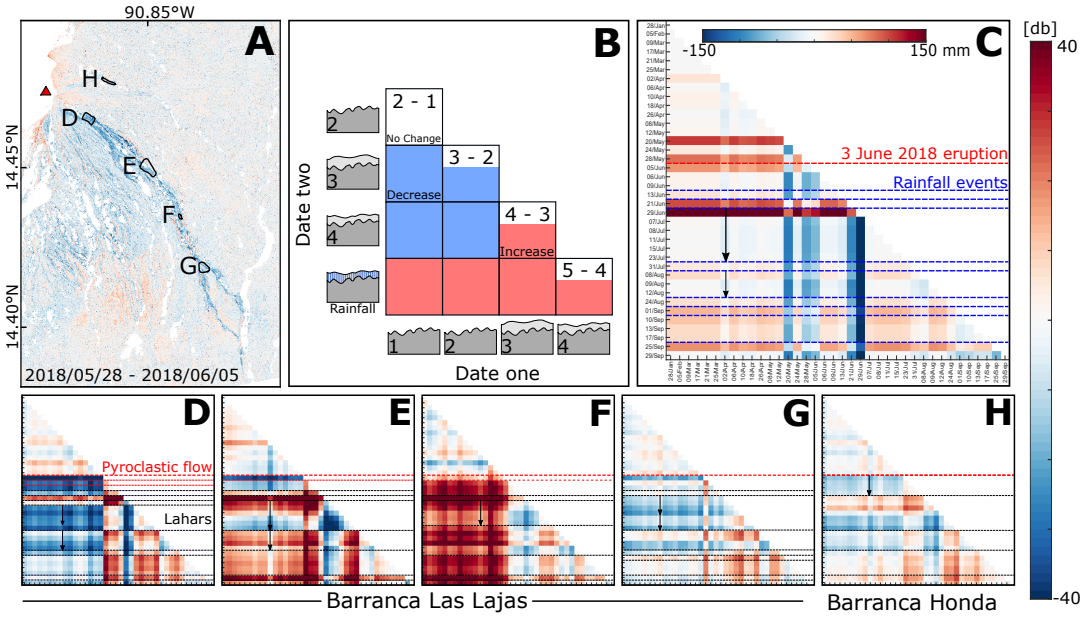

Figure 2.9: Backscatter change grid to show long term patterns in dataset. (A) shows the locations of each backscatter change grid (Location of the scene is shown in Fig. 2.1c.) (B) Schematic showing a simplified example of how a backscatter change grid is constructed. Each square represents the difference in backscatter produced from the two ground surface cartoons. The whole grid represents all possible pair combinations in the dataset. (C) Rainfall data shown as a grid from rain gauge located 11km northwest of Fuego, location indicated on Fig. 2.1a. (D-H) backscatter change grids for areas along the length of B. Las Lajas and B. Honda drainage system and in overtopped deposits. Red line indicates 3 June 2018 eruption and pyroclastic flows, black line shows changes in backscatter attributed to lahar activity and blue line show changes attributed to rainfall.

The lack of rainfall during July at Fuego (Fig. 2.9c) allowed material to settle and resulted in gradual decrease in backscatter (29 June and 23 July, arrows in Fig. 2.9d-g). The next major rainfall after these drying periods are marked both by abrupt changes in backscatter in the drainage channels and by scene-wide increases in backscatter (Fig. 2.6f, i) with higher magnitudes in both the newly deposited volcanic material and the agricultural land towards the south and southeast of Fuego. When the subsurface goes from dry to wet, radar penetration into the ground decreases and there is less interaction with deeper scatterers, increasing the influence of the near-surface scatterers and returning more radiation towards the satellite. We speculate that backscatter change is higher magnitude over the looser fresh volcanic material and agricultural fields because these hold moisture better than the surrounding vegetation.

2.2.3 Phase Coherence of Flow Deposits

Interferometric phase coherence is very sensitive to changes in surface properties due to volcanic deposits (e.g., Wadge et al., 2002; Dietterich et al., 2012). A pixel's phase comprises contributions from all the individual scatterers within it, and its phase coherence can be estimated from the correlation between phases for a group of pixels. Exposed bed rock, roads, or any stable structure will result in high coherence values, whereas features that change between acquisitions, such as vegetation or rockfall, will cause low coherence. Both the time span between acquisitions and satellite perpendicular baseline may be proportional to the degree of phase decorrelation.

We estimate coherence by assessing the correlation of 3×3 grids of pixels for selected areas along the 3 June 2018 pyroclastic flow in B. Las Lajas using all possible image pairs within our dataset. The large perpendicular baseline range of CSK images, average of 690 m between acquisitions, results in very high geometric decorrelation and many images that are entirely incoherent. By plotting the perpendicular baseline against the average coherence we identify a perpendicular baseline threshold of >700 m at Fuego, beyond which we lose coherence except where the temporal baseline is especially low (e.g., one day interferograms).

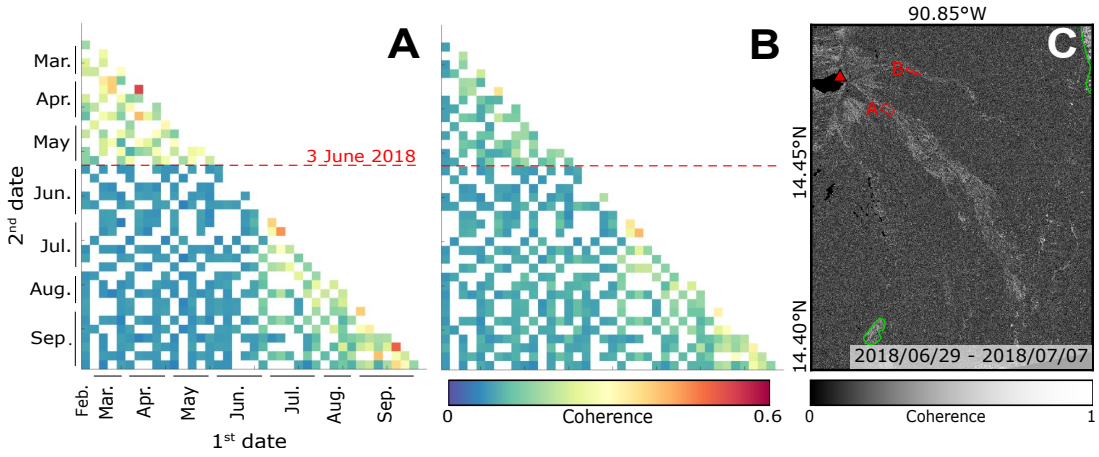

Figure 2.10: Radar coherence matrix for the upper sections in (a) B. Las Lajas and (b) Honda for areas shown in red in (c) coherence image (D and H, Fig. 2.9a) showing the complete loss of coherence associated with the 3 June 2018 pyroclastic flow, the short-term reappearance at the end of June and the return to pre-eruption coherence levels by September 2018. Coherence matrix represent the same temporal scale with white squares representing perpendicular baselines >700 m. High coherence that correlates to towns and agricultural fields outlined in green.

Coherence over Fuego is very low with only ∼ 7% of the 100 km^2 around B. Las Lajas and Honda showing a coherence over 0.5, even for perpendicular baseline <700 m. High coherence is limited to towns and some agricultural fields (Fig. 2.10c), while dense vegetation and steep slopes lead to low coherence on the volcano. Prior to the

June eruption, the drainage systems on the volcano flanks showed higher coherence but the emplacement of the pyroclastic flow on 3 June 2018 resulted in a sudden loss of coherence (Fig. 2.10). In B. Las Lajas, the complete loss of coherence lasted for approximately a month before higher coherence values reappear. These higher coherence values in July 2018 correspond to the break in the rainy season and temporary pause in lahar activity (Fig. 2.11a). Post-July the coherence drops slightly as the increased number of lahars slowly reworked the material in B. Las Lajas. The scattering properties gradually stabilise during September 2018 and return to the pre-eruption coherence levels. Similar trends are visible in B. Honda (Fig. 2.10b) demonstrating the strong correlation between lahar activity, rainfall and coherence levels.

2.3 Discussion

2.3.1 3 June 2018 Explosive Deposits

Six drainage systems at Fuego showed changes in backscatter as the result of pyroclastic flows on 3 June 2018 (Fig. 2.3), as described in the INSIVUMEH special bulletins (INSIVUMEH, 2018c). These newly emplaced pyroclastic flows follow the pre-existing drainage down the flanks of the volcano (Fig. 2.3). Our measurements show that the multiple flows in B. Las Lajas extend up to 11.9 km from the summit, altering a total area of 6.3 km^2 (Table 2.1) with flow thicknesses of up to 10.5 $\pm$2 m in the lower sections of the drainage where the flow accumulated against the valley edge. Our thickness estimate compares well with topographic increases of 12 m derived from TanDEM-X data (Albino et al., 2020) for the lower portions of B. Las Lajas. Overall, the flow lengths we measured from the backscatter (Table 2.1) were within 0.2 km of ground-based measurements (Escobar Wolf, R. and Ferres, D., 2018). Near the summit the flows funnelled into different drainage systems reduced the surface roughness. The narrow band of backscatter increase we observe in B. Las Lajas, Fig. 2.4b) is likely to be caused by local increases in cm-scale roughness associated with a central higher energy flow, transporting a wider range of material than in the surrounding channel. These localised increases in backscatter correlate roughly with the collapse and transitional facies described in Albino et al. (2020), where material was dominantly removed. Although changes in local slope caused by the incision of a small higher energy inner channel, could also cause bands of backscatter increase, there is no indication of a new channel in the post-eruption backscatter image (05/06/2018). Further down the drainage system, deposits were generally bounded by the channel wall and the backscatter changes are associated with different stages of valley infill and in some areas overtopping (Fig. 2.4b).

An approximately 40 km^2 wide area on the southern flank of Fuego showed subtle changes in backscatter that we attribute to ashfall from the initial 3 June 2018 eruption

(Fig. 2.6c, g). These changes are apparent only in the co-eruptive step estimation images (Section 2.2.1), which reduced the background backscatter noise. The origin of this change is unclear, but we attribute the backscatter decrease to the emplacement of a layer of ash, rather than the removal of leaves from vegetation, since this would produce long-term changes in backscatter that we do not observe. The impact of this ash layer on the backscatter images was short-lived and completely disappears from all other post-eruption images, which were acquired after the first major post-eruption rainfall.

Following the 3 June 2018 eruption, the backscatter remained low within B. Las Lajas (Fig. 2.6d, h, 2.9d, e). This low backscatter was concentrated to the upper slopes of B. Las Lajas, extending downslope within a defined channel (Fig. 2.6h) within the 3 June flow deposits. This backscatter pattern coincides with two smaller pyroclastic flows observed by INSIVUMEH on the 5 June 2018 (INSIVUMEH, 2018a; INSIVUMEH, 2018d).

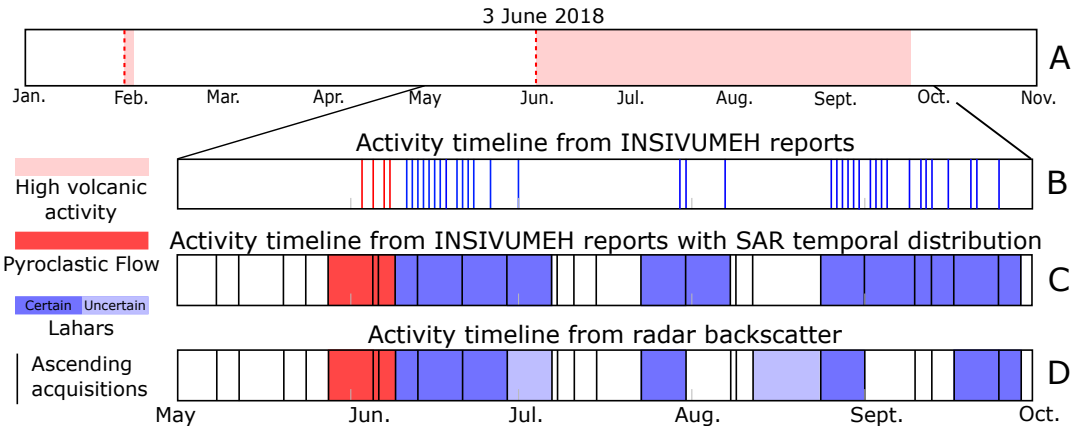

Figure 2.11: Timelines showing activity the various activity in B. Las Lajas. (a) shows the periods of volcanic activity in 2018 at Fuego, (b) the daily processes in B. Las Lajas as reported by INSIVUMEH, (c) the activity reported from the INSIVUMEH bulletins from the shown in the same time steps as the SAR acquisition, and (d) the timeline of volcanic activity derived from backscatter.

During June and then between August to September, Fuego had periods of high lahar activity (Fig. 2.11), which appeared as both increases and decreases in our backscatter change grid depending on the conditions and location of the lahar. We used the INSIVUMEH reports to ground truth our identification of lahar activity, and found good agreement between backscatter and field observations. From June to September 2018, we identified nine possible periods of lahar activity in B. Las Lajas from backscatter alone, two of which produced small, spatially discontinuous changes or do not correlate with a major rainfall event. A period that we flagged as lahar activity with high uncertainty in June and July in B. Las Lajas was confirmed by in-situ observations recorded in INSIVUMEH reports (e.g., INSIVUMEH, 2018e). However,

there were three periods with lahars reported by INSIVUMEH in September that are not clear from our backscatter analysis. This could be because flows were narrower or shorter, or missed by our choice of areas selected for our backscatter change grid. It is also possible that their erosional and depositional impact on the backscatter was minimal. Further, we potentially observed a period of lahar activity in B. Las Lajas between 12-24 August 2018 (Fig. 2.11) that was not reported by INSIVUMEH, but showed spatially correlated changes in backscatter throughout B. Las Lajas.

2.3.2 Identification of Volcanic Products from Backscatter

Here we discuss the approaches that were most successful for studying explosive eruption deposits at Fuego, including the potential for automatic extraction of flow shapes.

Mitigating Sources of Noise

Backscatter changes caused by explosive volcanic products may be low magnitude, small in spatial extent and differ according to scattering properties of the pre-existing land cover and topography. Interpreting backscatter therefore requires some knowledge of both pre-event scattering properties (e.g., inferred from radar, optical or ground-based imagery) and pre-existing topography (from a global, or preferably local, DEM). Maximising signal to noise ratio is also critical, and can be achieved by mitigation of noise in the backscatter.

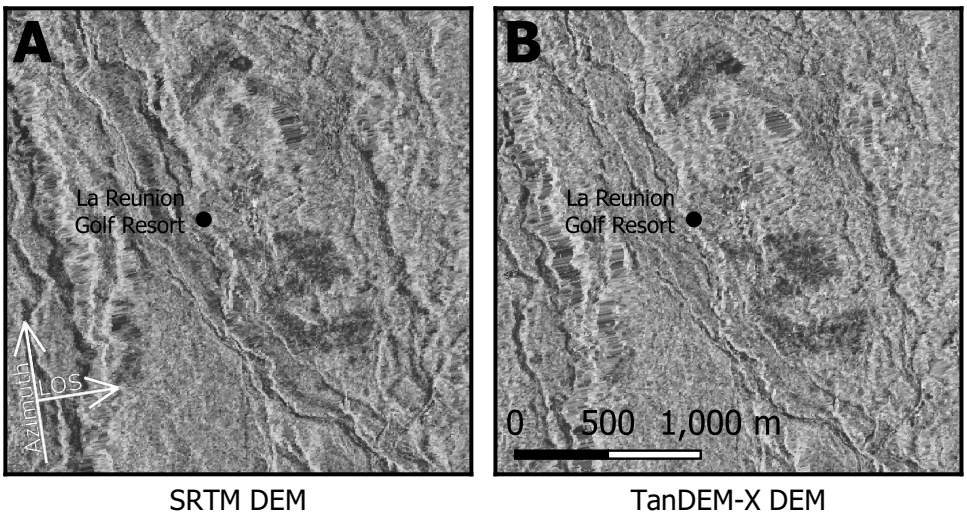

Figure 2.12: Ascending CSK radar backscatter image (05/06/2011) using (a) SRTM DEM (30 m, 11/02/2000) and (b) the TanDEM-X derived DEM (10 m, 08/09/2018) as input for the radiometric terrain correction. Variations in radar backscatter between the different DEM corrections are visible in the B. Las Lajas drainage pattern (east of La Reunion) and the topography (west of La Reunion).

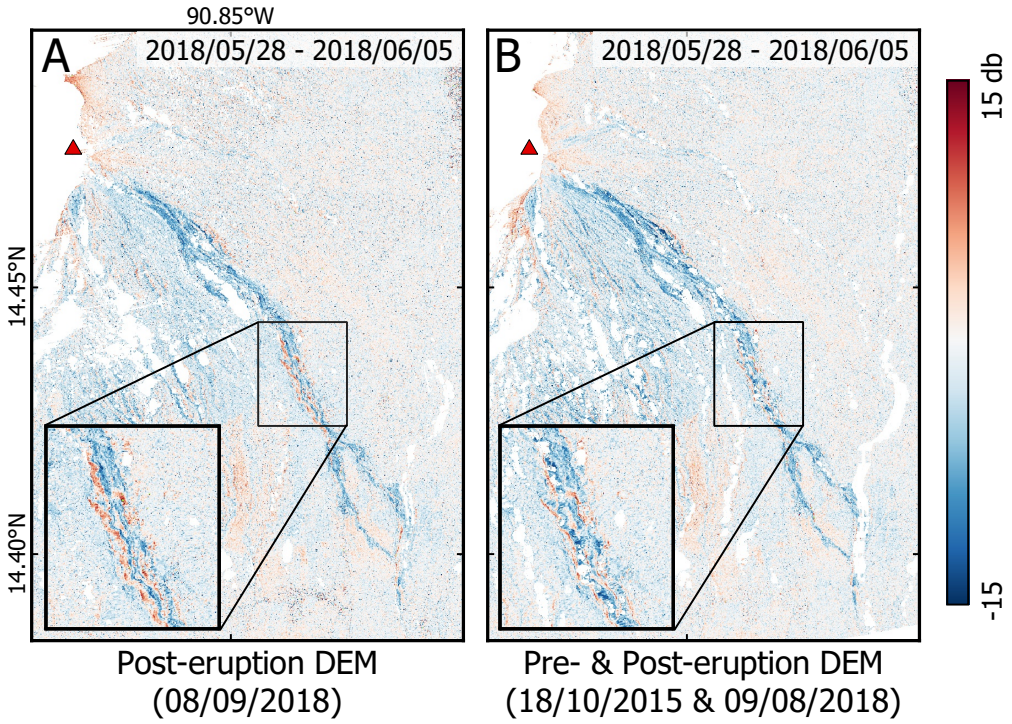

Figure 2.13: Step estimation images constructed from 15 CSK SAR acquisitions from 05 February to 05 June 2018 over B. Las Lajas showing the differences in backscatter signals when using (a) a single DEM for all acquisitions and (b) using a pre- and post-eruption DEM in the radiometric terrain correction. Location of the scene is shown in Fig. 2.1c

Applying a radiometric terrain correction to the Fuego dataset reduced distortions from the steep topography allowing us to make backscatter change measurements on the steeper slopes near Fuego's summit. The high-resolution TanDEM-X-derived DEMs (10 m, 18/10/2015 and 09/08/2018) were better able to correct distortions than SRTM (30 m, 11/02/2000) (Fig. 2.12). Using both a pre- and post-eruption DEM for our analysis also minimised errors associated with differences between topography at the time of each SAR image and the DEM used for correction (especially the local gradient and location of drainage channels) (Fig. 2.13). Even with a radiometric terrain correction, major differences in the satellite geometry still affect the backscatter change if the scattering mechanisms vary with incidence angle. For example, trees produce very different scattering signals depending on whether radar encounters the crown or the trunk first. This effect may account for the differences in backscatter change pattern that we observe between different tracks with different incidence angles in some locations (Fig. 2.4c). Without the application of an adaptive filter, speckle can mask shapes and structures of the explosive volcanic deposits (Fig. 2.2d). The adaptive Gamma-*MAP* filter (Lopes et al., 1993) improved our analysis of the backscatter changes for all methods. In our step estimation images the speckle filter made the transition be-

tween flow and surrounding areas sharper, reducing the background variance by 7% and making the subtle changes in backscatter, such as ash (Fig. 2.6c, g), more easily distinguishable. For major changes such as those caused by the eruptions on 3 June, the single backscatter and change difference RGB images are sufficient to identify the main deposits. However, solving for a step in backscatter using longer timeseries (>30 days) and more images improved both our mapping of flow boundaries, and allowed identification of more subtle changes in backscatter (e.g., ash fall).

Identification of Explosive Deposits in Backscatter

In general, the significant changes to backscatter due to pyroclastic flows are limited to drainage channels and surroundings, with the sign of backscatter change dependent on radar wavelength, flow roughness and pre-eruption scattering properties. It may take the backscatter a few days, months, or years to return to pre-eruption levels of backscatter (e.g., for vegetation to grow back where it was completely removed). However, backscatter can also remain permanently altered and never return to the values it had before the eruption (e.g., complete restructure of drainages systems).

Backscatter signatures of major pyroclastic flows have been identified at Soufrière Hills Volcano, Montserrat using TerraSAR-X (X-band) (Wadge et al., 2011) and the 2010 Merapi eruption with ALOS-PALSAR (L-band) (Solikhin et al., 2015). For Fuego (Fig. 2.4) and Soufrière Hills Volcano, decreases in backscatter were associated with pyroclastic surge deposits blanketing and overtopping drainage channels. However, pyroclastic surge deposits at Merapi caused an increase in the backscatter, perhaps because at Merapi darker forest was removed and covered by high energy, bright surge deposits. There are also similarities in backscatter patterns within flows at different eruptions. At Fuego and Soufrière Hills Volcano, narrow bands of increased backscatter occur in the middle of surge deposits (e.g., Fig 2.4a), which we attribute to fresh block and ash deposits, including larger, up to metre-scale blocks that dominate the backscatter signal. However, the 2010 Merapi eruption, a narrow band of decreased backscatter was observed in the centre of the flow where the most energetic flows were deposited. The differences between observations at Merapi, Fuego and Montserrat are consistent with the different roughness lengths scales to which L-band (λ = 23 cm) and X-band (λ = 3.1 cm) radar are sensitive. The Rayleigh Criterion, $\Delta h > \frac{\lambda}{8cos(\theta)}$, provides a material size threshold of whether a surface is appears 'rough' (bright) or 'smooth' (dark) in backscatter. For X-band, objects <0.4 cm appear smooth while for L-band objects <3.6 cm will appear smooth. This means that material between 0.4–3.6 cm will produce different backscatter signals at L- and X-band wavelengths.

Lahars produce much more subtle signals in backscatter limited to active drainages and freshly deposited material. Distinguishing between the sudden changes caused by a lahar and more gradual erosion is particularly challenging using non-continuous im-

agery. The addition of rainfall data provides some constraint on when lahars are more likely to have occurred. The use of dense SAR timeseries with short revisit times is also critical. The Fuego lahars produce both increases and decreases in backscatter at different positions within the flow. In general, the upper sections of drainages are dominated by erosion, reducing the backscatter, while surface roughness increases downslope as larger blocks are deposited. Multiple lahars of different sizes and magnitude may occur during the several days between SAR acquisitions so that the backscatter change patterns do not represent a single change to the ground but are due to multiple events. The backscatter change caused by a lahar is also sensitive to the timing of rainfall; high rainfall closer to the second acquisition produces a higher magnitude change than if it were close to first acquisition and the ground had time to dry out. Although backscatter signals from lahars are superficially similar to those from gradual erosion and deposition in any image pair, we found that we could identify lahar signals at Fuego by finding turning points in backscatter sign in the timeseries (Fig. 2.9) and comparing their timing to high rainfall events (Fig. 2.9c).

The backscatter changes associated with the emplacement of ash from 3 June eruption are much more widespread than either the pyroclastic flows or lahars. In general, backscatter signals from ash reach their maximum close to the eruptive vent of the volcano and are characterised by short-lived changes. The sign of the change is dependent on the pre-eruption land cover, the moisture content of the ground and the ash, whether the deposit coats the ground or is thick enough to remove or destroy vegetation. Although ash deposits are spatially systematic, they may produce only very small magnitude variations in backscatter, difficult to differentiate from background noise. Therefore, reliable corrections for noise (e.g., speckle) are necessary, especially as the impact of ash on SAR backscatter (e.g., the impact of thickness variations, morphology, dielectric properties, etc) is poorly understood. At Fuego we measure both an increase and decrease in backscatter caused by ashfall over different surfaces, but at Nabro (June 2011, Goitom et al., 2015) the pre-eruption land cover was a uniform semi-arid environment, resulting in a decrease in backscatter signal linked to topographic smoothing. For both Fuego and Nabro eruptions, backscatter changes related to ash were dominated by changes in the surface roughness. However, the ash at Cotapaxi, Ecuador (August 2015, Arnold et al., 2018) had a high moisture content producing an increase in backscatter and masking any decrease in surface roughness. Although ash fallout can be easily observed in backscatter at some eruptions (e.g., Nabro, Eritrea, Goitom et al., 2015), there is a trade-off between the different influences factors contributing to the SAR signal. Depending on the magnitude of the backscatter change and land cover, the emplacement of a deposit (e.g., ash) can produce a much more subtle change in backscatter, such as seen for the 2018 Fuego eruption. In these cases, longer timeseries are more adept at extracting these types of signals.

Potential for Automated Flow Shape Extraction

While our study of the 2018 Fuego eruption is retrospective, analysis of backscatter has great potential as a tool to track the progression of an eruption, especially where visual observations are limited. We assess the accuracy of the areas and lengths generated by our semi-automatic approach (section 2.2.2) by comparing them to measurements extracted manually from backscatter (Table 2.1) and optical imagery (i.e. Sentinel-2, 2018/07/04, Table 2.1). For B. Las Lajas the semi-automatically identified area was ∼38% smaller than through manual extraction, while smaller flows where backscatter variations were not significantly different to the background noise (e.g., B. Taniluya) showed up to ∼85% difference. Using smaller MR structuring elements and lower thresholds allowed us to extract some of these flow shapes, reducing these values too far resulted in false positives especially in areas where the surrounding variations were large (e.g., summit or ash on south flank). False positives were also associated with overlapping deposit distributions, signals from volcanic ash on the southern flank merged with changes associated to the flow in B. Trinidad and upper sections of B. Las Lajas in June 2018 (Fig. 2.6c). Our use of a morphological operators and image segmentation limited bias in the identification of flows. However, the semi-automatic method was less effective where backscatter changes were low magnitude (e.g., B. Honda, Fig. 2.3c), where changes were similar to the level of background noise, or where the boundaries showed gradual transitions (false negatives).

The flow areas measured from optical imagery (Table 2.1) were larger for all drainages than seen in the backscatter images. This may be because the first SAR image that was acquired two days post eruption, while the first completely cloud free Sentinel-2 optical image was acquired over a month later on the 4 July 2018 and captures multiple events, not seen in the SAR image pair. Further, some deposits (e.g., overtopped deposits in lower B. Seca, Fig. 2.4b) visible in the optical imagery either do not change the radar scatterers enough to cause a difference in backscatter (e.g., very thin layers), or different signal contributions (e.g., from roughness and moisture) cancel each other out. For example, the backscatter would show a decrease for a rough surface becoming smoother and an increase for a dry surface becoming wet. A rough, dry surface that changes to a smooth wet one may produce minimal backscatter change. A deposit that produces changes in all contributing factors: local slope, centimetre-scale roughness, and moisture, produces a very complicated change pattern, with the potential for some flow sections to produce minimal or non-observable change signals.

2.3.3 Application to Explosive Volcanoes Globally

The high spatial resolution and temporal density provided by CSK SAR images are ideal for analysis of explosive volcanic eruptions using backscatter. However, CSK is a commercial constellation and although it has a good volcano background mission, it is

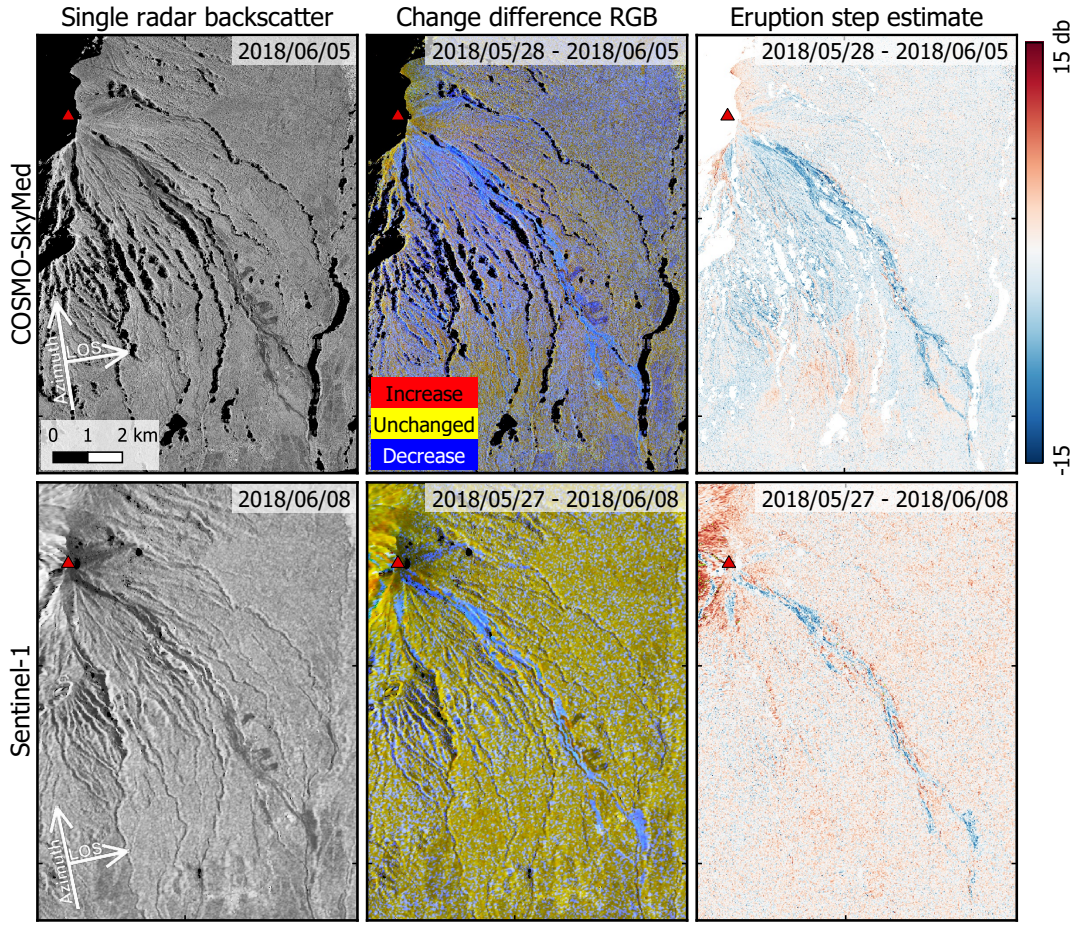

Figure 2.14: Comparison of S1 and CSK backscatter methods for the 3 June 2018 pyroclastic flow in B. Las Lajas. A radiometric terrain correction and speckle filters were applied to both S1 (using the SRTM 30 m DEM and a 3×3 pixel window) and CSK (using the TanDEM-X derived 10 m DEMs and a 5×5 pixel window). Location of the scene is shown in Fig. 2.1c

not free or open, although it is available to observatory and research scientists through programmes such as the CEOS Volcano Demonstrator. We therefore also examine the applicability of the methods we developed here by applying them to freely available C-band (5.6 cm) data from the Sentinel-1 (S1) satellite constellation, which provides global open access imagery with a resolution of 4×20 m.

The major 3 June 2018 eruption at Fuego produced fundamentally similar signals in both CSK and S1 data, which both captured changes in all affected drainage systems (Fig. 2.14). The pyroclastic flows in B. Trinidad (not reported in the INSIVUMEH eruption reports), which was partially masked in the CSK images due to the incidence angle, is clearer in the S1 imagery. The S1 change difference and step images showed overall similar shapes and temporal trends for the pyroclastic flows deposits, although

the lower resolution does not capture the finer detail seen in the CSK data, (e.g., complexity around La Réunion golf course and the overtopping at San Miguel Los Lotes). The longer repeat time for the S1 data also results in the aliasing of more events in the step estimates, and thus masks or reduces changes associated with transient processes. Nevertheless, the global availability of Sentinel-1 data allows for frequent (6-12 day) observation and interpretation of explosive volcanic eruptions.

The initial removal of dense forest and vegetation around Fuego by 3 June 2018 eruption (Albino et al., 2020) meant that the eruption changed the surface scatters considerably when it was removed, after which changes were more subtle. Although tropical vegetation produced very low interferometric phase coherence at Fuego, in other settings (e.g., Dietterich et al., 2012), phase coherence would provide an independent comparison to flow extent maps derived from backscatter. The 3 June eruption, occurred following a few months of low volcanic activity, allowing us to build up a good baseline of backscatter variations due to moisture changes and other sources of noise before the eruption. When the eruption occurred, this allowed us to distinguish the change in backscatter associated the emplacement of fresh material.

Backscatter is most useful to examine explosive volcanic eruption in areas where there is substantial change the ground surface, for example where deposits are extensive and the volcanoes topography is significantly altered. Eruptions where ash and pyroclastic flows cover or remove dense vegetation will also produce strong backscatter changes. Similarly, eruptions that occur after long non active periods will more likely show large magnitude backscatter changes than a volcano that is continuously erupting.

2.4 Conclusion

We provide a thorough application of multiple backscatter methods to examine explosive volcanic deposits of the 2018 activity of Volcán de Fuego, Guatemala. We use SAR backscatter to map six drainages affected by pyroclastic flows (Table. 2.1) during the 3 June 2018 eruption accompanied by backscatter changes associated with ashfall. The major flow in B. Las Lajas showed an extent of 11.9 km from the summit covering an area of 6.3 km^2 and with a thickness up to 10.5 $\pm$2 m in the lower section, where we could use radar shadows to observe valley infilling. The backscatter signals associated with the B. Las Lajas deposits showed increases related to the block and ash deposits within the channel and wider spread decreases in backscatter linked to the flow surge. Between June and September 2018, we observed two more pyroclastic flows in B. Las Lajas and, with additional information from local rainfall data and INSIVUMEH reports, nine periods of potential high lahar activity.

We demonstrate that solving for a step change in backscatter from a timeseries improved signal to noise ratio and aided the identification of explosive volcanic deposits.

Our use of timeseries of backscatter change show temporal patterns that have potential to differentiate between lahars and more gradual post-eruption erosion processes.

This work demonstrates the suitability of SAR backscatter for monitoring the progression of explosive eruptions and the subsequent alteration of their deposits. We demonstrate the extraction of quantitative information from backscatter in the presence of noise, as well as the identification of pyroclastic flows, lahars and ash. This case study shows the potential of the backscatter datasets to provide useful observations and measurements for volcano monitoring when optical, radar phase or ground-based observations are limited.

Chapter 3

Tools for interpreting Synthetic Aperture Radar backscatter during effusive eruptions: The 2010–2013 eruptions at Pu‘u ‘Ō‘ō Crater, Hawai‘i

Synthetic Aperture Radar (SAR) backscatter is known to be sensitive to the products of effusive eruptions, especially lava flows, but is currently less widely used for volcano monitoring than radar phase measurements. In part, this is because of the complexity of the data interpretation for backscatter: there is not a simple link between the magnitude or sign of the change in backscatter and the physical properties of the fresh volcanic deposits. However, SAR backscatter has some advantages over the use of optical or infrared instruments for near real-time monitoring because it does not depend on cloud-free days or solar radiation. It is also sensitive to some different physical processes from phase coherence change, for example, capturing post-emplacement changes to lava flows.

In this chapter, we present a retrospective SAR backscatter analysis of Kīlauea's lava lake and lava flows emplaced during 2011 and 2013 from Pu‘u ‘Ō‘ō crater, examining the potential to track the emplacement and progression of lava flows and lava lake changes. This period is characterised by three very different eruptions; the Kamoamoa Fissure Eruption (Episode 59, March 2011), a breakout in August 2011 (Episode 60) and the Peace Day flow (Episode 61, September 2011), which was accompanied by inflation and collapse events at Pu‘u ‘Ō‘ō crater. Using a simple model for backscatter change, we map the emplacement of multiple lava flows, and examine how post-emplacement

flow cooling is captured by backscatter timeseries. In Pu‘u ‘Ō‘ō crater, we test the geometrical and morphological limitations of using radar shadows to extract accurate height measurements and compare patterns in the lava lake SAR backscatter signal to lava lake activity.

We also demonstrate the use of principal component analysis to reduce noise in the backscatter and allow for easier identification of volcanic activity in SAR backscatter timeseries. Our in depth analysis of the 2011–2013 effusive eruptions at Pu‘u ‘Ō‘ō crater demonstrated how SAR backscatter can be used to monitor effusive volcanic eruptions, especially when other datasets are limited or unavailable.

3.1 Introduction

Effusive volcanic eruptions can completely reshape the Earth's surface, building new topography and resurfacing the surrounding landscape. Tracking the progression of an effusive eruption is an essential part of monitoring as it can provide an understanding of how an eruption is developing over time and help forecast possible hazards associated with a developing flow field. However, monitoring ongoing eruptions can be impeded by the accessibility to the volcano, extent of the eruption, resources, and cloud coverage. Various satellite-based remote sensing datasets have demonstrated means to monitor active lava flows to overcome these ground-based hazards. Optical (e.g., Lu et al., 2004; Head et al., 2013) and thermal (e.g., Wright et al., 2004; Patrick et al., 2017) have been used to map effusive deposits (e.g., lava flows). However, both these datasets depend on having a direct view of the volcano (i.e., cloud free). Active sensors, such as Synthetic Aperture Radar images, can provide frequent systematic observations over the ongoing eruption as the sensors are unaffected by cloud coverage or solar illumination. Over the last decades SAR imagery has been used more frequently for monitoring effusive eruptions. Lava flows have been mapped using radar phase coherence, as the emplacement of the flows can cause a sudden loss of coherence (e.g., Zebker et al., 1996; Dietterich et al., 2012; Moore et al., 2019) and using bistatic SAR imagery to calculate topographic changes between two dates (e.g., TanDEM-X, Poland, 2014; Arnold et al., 2017). SAR backscatter is still under-exploited for monitoring effusive eruptions. In the past, single radar backscatter images have been used to visualise the emplacement of lava flows (e.g., Castro et al., 2016; Arnold et al., 2017; Kubanek et al., 2017) and measure relative heights using cast radar shadows (e.g., Arnold et al., 2017; Barrière et al., 2018; Moore et al., 2019). Other studies have used changes in the radar backscatter through time to map the flow fields (Goitom et al., 2015; Dumont et al., 2018) and observe changes in effusion rate (e.g., Wadge et al., 2012). Poland (2022) demonstrated the strength of combining SAR backscatter images with coherence produce flow maps regardless of the initial surface condition. Further, SAR backscatter has been used to differentiate between different flow morphology (Di Traglia et al., 2018; Tolometti

et al., 2022).

The emplacement and development of lava flows can be very simple going straight from emplacement to cooling. However, they can be much more complex processes with different morphological structures, including multiple active branches and transitions between channels, levees, and tubes (Cashman et al., 2013; Dietterich and Cashman, 2014; Tolometti et al., 2022). Understanding the flow dynamics and behaviour (e.g., active fronts, flow path, and flow velocity) is important for hazard assessment needed for eruption response. SAR backscatter has the potential to be a source of important information about the initial emplacement, subsequent development and cooling. SAR backscatter is not a differential dataset meaning that each image captures the eruption at that moment in time, and even when we lose coherence as the flow is emplaced, the SAR backscatter continues to capture information about the changes to the flow surface. In this chapter, we examine the long-term changes in radar backscatter to understand (1) the dynamics of an active lava lake, and (2) what information we can gain from backscatter about the emplacement and development of lava flows.

At Kīlauea volcano, the extensive geological (e.g., camera observations, flow maps), geophysical (e.g., deformation, seismic, gravity) and geochemical (e.g., gas emissions, geochemical analysis) monitoring data are collected by the Hawaiian Volcano Observatory (HVO) and collaborators. In addition to the comprehensive ground-based measurements, satellite-based observations (e.g., optical, thermal, SAR) of the volcanoes are frequently acquired as part of the permanent Hawaiian Volcano Supersite organised by the Group on Earth Observation (GEO) Geohazard Supersites and Natural Laboratory initiative (GSNL). The Supersite is a platform to aid with distribution of this archive of ground- and satellite-based data. This diversity in the dataset makes the Kīlauea an ideal case study to explore different SAR backscatter method because this allows comparison to ground-based observations and measurements. Here, we explore the potential of SAR backscatter for examining the changes in lava lake activity, and mapping out the emplacement and development of lava flows during 2011–2013.

3.1.1 The 2011–2013 Eruptions of Pu‘u ‘Ō‘ō Crater

Kīlauea volcano, (Fig. 3.1), had continuous lava lake activity the summit caldera between 2008–2018, coinciding with the 35 year long (1983–2018) eruption of Pu‘u ‘Ō‘ō on the East Rift Zone (ERZ), which produced 4.4 km^3 of lava (Neal et al., 2019). The ERZ eruptions are characterised by periods of lava flow and lava lake activity (Orr et al., 2015). The lava lake level at the summit showed strong correlation with local deformation and with activity at Pu‘u ‘Ō‘ō (2008-2018, Patrick et al., 2019a; Patrick et al., 2019b). After the last major eruption on the Lower East Rift Zone (LERZ) in 2018, activity ceased until a lava lake returned to the summit caldera at the end of 2020 and has continued on and off until present. Measurements during the recent eruptions

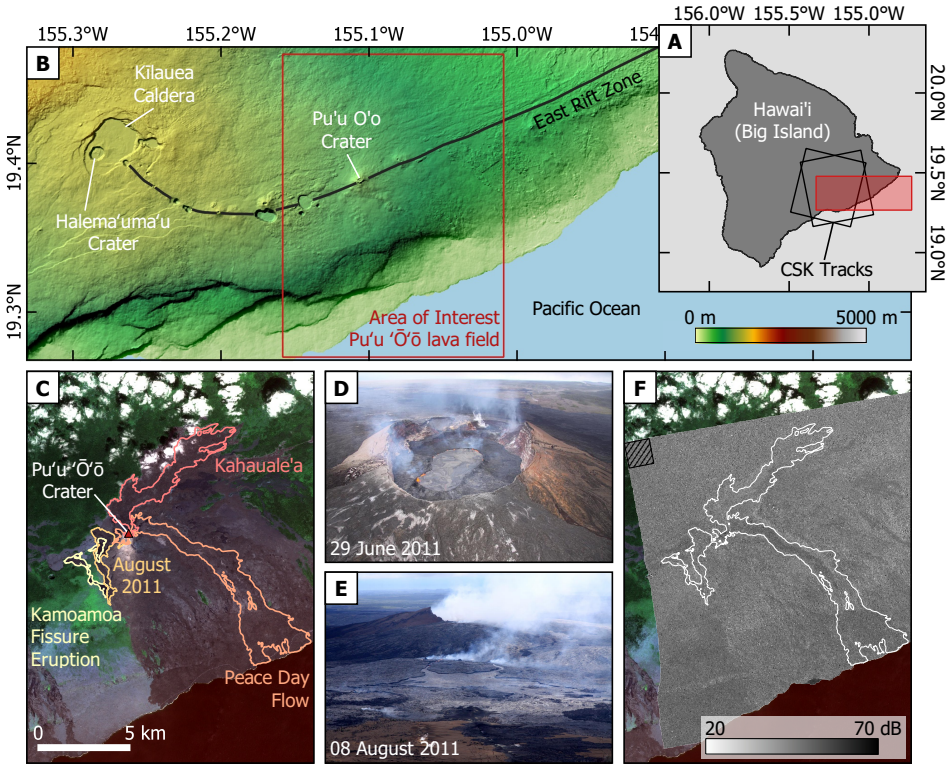

Figure 3.1: Map of Kīlauea volcano, Hawai'i. (a) Big Island of Hawai'i, with COSMO-SkyMed (CSK) tracks indicated by black rectangles and location of (b) in red rectangle. (b) Kīlauea volcano and the East Rift Zone, showing location of Pu'u 'Ō'ō crater. (c) Sentinel-2 image (24-12-2017) showing Pu'u 'Ō'ō crater (location shown in b) and the 2011–2013 lava flow outlines and names based on HVO flow field maps. Photos taken by HVO of (d) a perched lava lake in Pu'u 'Ō'ō crater (HVO, 2011b) and (e) August 2011 lava flow with Pu'u 'Ō'ō in background (HVO, 2011c). (f) COSMO-SkyMed image (04-12-2011) over the Pu'u 'Ō'ō lava field showing a section of the Peace Day Flow (darker backscatter values in white outline). Stripped black box represents the area used to produce Fig. 3.2a.

at Kīlauea have shown the pressurisation of Pu'u 'Ō'ō crater leading up to periods of new eruptions (2007, 2011, 2014 and 2018), demonstrating that there is a hydraulic connection between the summit and the East Rift Zone and the magma source (Orr et al., 2015; Patrick et al., 2019a).

In early 2011, volcanic activity moved back from the ERZ to Pu'u 'Ō'ō crater following an eruption at an established vent 2 km downrift that had been active since 2007, called Episode 58 by the USGS. The activity during the following year at Pu'u 'Ō'ō was divided into three episodes marking different eruptions, the Kamoamoa fissure eruption (Episode 59) in March 2011, a rapid lava flow breakout in August 2011 (Episode 60) and the Peace Day lava flow (Episode 61) in September 2011.

Prior to the Kamoamoa eruption in March 2011 there were several months of pre-

cursory activity at the summit caldera (e.g. inflation and rising of lava lake), increased seismicity in the upper ERZ and rising of the Pu‘u ‘Ō‘ō crater lava lake (Orr et al., 2015). The culmination of this activity resulted in the collapse of Pu‘u ‘Ō‘ō crater by ∼80 m in ∼4 hours on the 5 March 2011. This collapse at Pu‘u ‘Ō‘ō correlates to a drop in the lava lake of 143 m at Halema’uma’u, the summit caldera. Between 5-9 March 2011 lava broke out as north-eastward propagating fissures about 2 km southwest of Pu‘u ‘Ō‘ō crater towards Napau crater. At the end of the eruption on 9 March 2011, two fissure systems had formed extending for over 2 km and were made up of five to six fissures each (Orr et al., 2015). Following the Kamoamoa eruption, the East Rift Zone was quiet until lava returned to the recently collapsed crater of Pu‘u ‘Ō‘ō on 26 March 2011. From March to August 2011 the crater steadily filled up and eventually overflowed.

On 3 August 2011, lava erupted from the lower west flank of Pu‘u ‘Ō‘ō draining the lava lake within the crater and resulting in the collapse of the newly built up Pu‘u ‘Ō‘ō crater. The flow was rapidly emplaced in a sheet-like fashion with field measurements suggesting that up to 25% of the flow volume was emplaced during the first 3h (Poland, 2014). The mean dense-rock equivalent time-averaged discharge rate of lava was ∼8 m^3s^{-1} from the 3-15 August 2011. Although, with much higher short term effusion rates during the first few hours before rapidly decreasing after the lava lake was drained (Poland, 2014). The flow became inactive on 15 August, and there was a hiatus of activity at Pu‘u ‘Ō‘ō of five days before lava reappeared infilling the crater.

By 10 September lava began to overflow Pu‘u ‘Ō‘ō crater again and continued to do so until a small fissure opened on 21 September near the top of the northeast flank. This breakout would feed the Peace Day flow, which carried lava towards the southeast over the Pu‘u ‘Ō‘ō flow field towards the ocean for the next two years, until mid-2013. During this eruption, the activity on the ERZ was relatively stable, concentrated on the Peace Day flow. The lava flow developed its own lava channel and tube system and by November 2012 had persistent ocean entry points. The Peace Day flow was abandoned in November 2013 almost a year after another flow, Kahauale’a Flow, started propagating from Pu‘u ‘Ō‘ō toward the northeast at the beginning of 2013 (Orr et al., 2015).

The 2011–2013 eruptions covered a variety of effusive eruption features, including multiple inflation and collapses events of Pu‘u ‘Ō‘ō crater, persistent lava lakes and three very different types of lava flows. During 2011, we can observe the short-lived fissure eruption (Kamoamoa Fissure Eruption), a rapidly emplaced sheet-like lava flow (August 2011) and a typical Hawaiian long-term lava flow (Peace Day Flow) active from 2011–2013 that formed a complex system with multiple ocean entry points, lava channels and tubes. Further, these lava flows were emplaced on both the old lava flows

and entered into the surround vegetation, making it an interesting time period to test various SAR backscatter methods on. In addition, not only are the target lava flows and crater activity varied and complex, there is also a temporally dense high-resolution COSMO-SkyMed dataset to examine the effusive activity with.

3.2 Data Processing and Analysis

We used 137 and 105 ascending and descending COSMO-SkyMed (CSK) X-band (3.1 cm) images from August 2010 to December 2013 to examine the effusive deposits and processes that characterised the eruptions at Pu‘u ‘Ō‘ō Crater, Kīlauea, Hawai‘i (Fig. 3.1). The CSK data used were acquired by the Italian Space Agency (L'Agenzia Spaziale Italian, ASI) and is available through the Hawaiian Volcanoes Supersite. CSK is a constellation satellite system made up of four satellites following the same orbit with a repeat cycle of 16 days for each satellite. Repeat intervals range from 1 to 8 days. We use the GAMMA remote sensing software (Werner et al., 2000) to process the CSK SAR images at full resolution (3×2 m). For the dataset, we have a range of 1 to 32 days between acquisitions for 2010–2013, with an average of 7 days between acquisitions.

The side-looking nature of the satellite introduces distortions in the SAR backscatter. To mitigate these distortions and correct the saturation based on their local incidence angle, we apply a radiometric terrain correction (Small, 2011; Meyer et al., 2015) using a high-resolution (5 m) digital elevation model (DEM) constructed from airborne interferometric SAR (IfSAR) data collected between 16–23 October 2005 by the National Oceanic and Atmospheric Administration, NOAA (NOAA Office for Coastal Management, 2022). Depending on the application of the SAR backscatter, we filter our date using the 10×10 boxcar filter (i.e., spatial averaging) to further mitigate the speckle contribution. If we are examining smaller features (e.g., Pu‘u ‘Ō‘ō lava lake) we do not apply this filtering to prioritise the resolution.

The radar backscatter, σ_0 represents the proportion of the emitted electromagnetic pulse scattered back towards the satellite for a single pixel surface area, A. Conventionally, radar backscatter is expressed in dB, σ°_{dB}, to account for its high dynamic range, and σ°_{dB} can be written as,

$$\sigma^{\circ}_{dB} = 10 \log_{10} \left(\frac{4\pi R^2 \rho_R}{\rho_T A} \right) \tag{3.1}$$

where R is the distance between the sensor and target, ρ_T is the power density $[Wm^{-2}]$ scattered by the sensor, and ρ_R the power density $[Wm^{-2}]$ received by the target. Radar backscatter is controlled by changes both in the satellite parameters (e.g., local incidence angle, wavelength λ and polarisation) and the scattering properties of the ground (Meyer et al., 2019). These scattering properties are a combination of surface

roughness on the scale of the satellite wavelength, local incidence angle, and dielectric properties.

Effusive activity, such as lava flows and lakes, alter either one or multiple of these scattering properties. For examples, the emplacement of a fresh lava flow on an older eroded flow surface produces a smoother surface or the build up of levees would change the local gradient over time. Along with other independent non-volcanic processes (e.g., rainfall) and contributions of multiple scatterers within a single pixel, the resulting radar backscatter signal is complex.

3.2.1 Correction for Satellite Dependency in SAR Backscatter

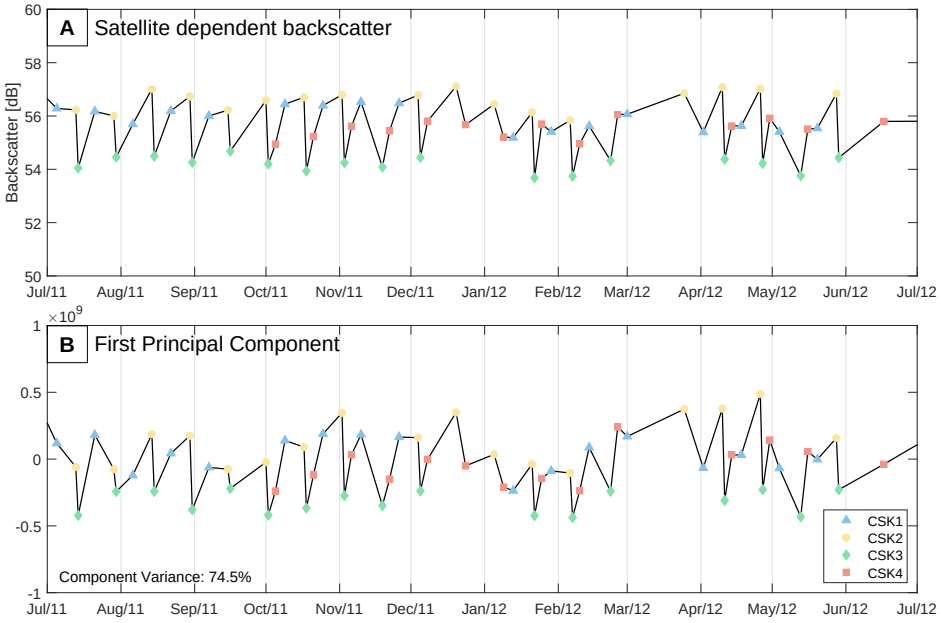

Figure 3.2: COSMO-SkyMed radar backscatter timeseries of (a) for vegetated area (striped square in Fig. 3.1f) showing the strong correlation between CSK satellite and backscatter signal and (b) the first principal component for the dataset between July 2011 and July 2012 correlated to each CSK satellite.

In the Hawai‘i CSK dataset, in areas where we expect no significant changes in radar backscatter through time, such as vegetation or over the old flow field, we observe a repetitive pattern in the radar backscatter. This pattern correlates with which CSK satellite in the constellation acquired that image (Fig. 3.2), but not with other satellite properties (e.g., incidence angle or perpendicular baseline, Fig. B.1). We speculate that this systematic pattern associated with the sensor constellation could be introduced during the data acquisition and calibration, by damage or changes to the sensor of one or more satellites, which then introduces errors in the calibration factors applied to the data during processing.

To mitigate this variation in the radar backscatter, we use principal component

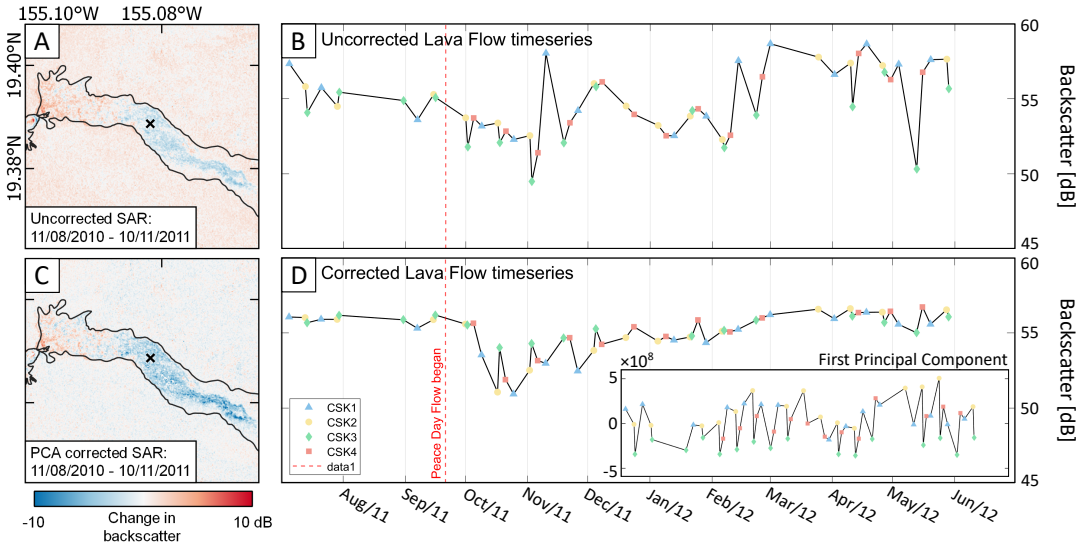

Figure 3.3: Comparison over the Peace Day Flow for the uncorrected and PCA-corrected COSMO-SkyMed dataset. Step estimation images produced using method described in Section 2.2.1 showing the early stage of the Peace Day Flow using 68 acquisitions (a) uncorrected CSK images, and (b) PCA-corrected CSK images, spanning a total of 456 days and calculating the changes in radar backscatter at the beginning of November 2011. Black outline represents the complete Peace Day flow field made from the published HVO maps. Timeseries for the same single pixel (cross in a) for (b) uncorrected, and (d) PCA-corrected radar backscatter over the Peace Day Flow showing the improvement in the signal following the removal of the first principal component (PC1) from the dataset (PC1 shown in insert on d).

analysis (PCA) to isolate and remove this repetitive pattern (Fig. 3.2a). For the PCA, we use the whole image for all 137 CSK images. Our first principal component for the ascending dataset (taking the whole of all 137 images, Fig. 3.2b) closely resembles the pattern of the satellite dependency (Fig. 3.2a) we observed and accounted for ∼75% of the variance in the dataset.

The removal of the first principal component from the CSK dataset, produced much more useful radar backscatter timeseries. From these we could easily identify the changes associated with the emplacement of the lava flow (Fig. 3.3) and we found that the variance of timeseries not affected by volcanic flows reduced by approximately 87% (e.g., vegetation, Fig. B.2). Correcting the satellite dependent component to backscatter is therefore critical for mapping out the emplacement of lava flows (Fig. 3.3a) identifying flow boundaries and structures.

3.3 The 2011 Pu‘u ‘Ō‘ō Crater

A small number of SAR backscatter studies have focused on lava lake activity. Barrière et al. (2018) and Moore et al. (2019) used changes in radar shadows width to extract

lava lake fluctuations at Nyiragongo and Erta Ale respectively and interpret these in terms of pressure changes to the shallow plumbing system. Here we aim to examine the limitations to the radar shadow method, and understand variations in radar backscatter signals related to lava lake activity.

In 2011, Pu‘u ‘Ō‘ō crater hosted numerous active lava lakes (surface expression of an open-vent volcano) and passive (or lava pond; where lava pools in a topographic depression away from active vent) lava lakes (Tilling, 1987; Lev et al., 2019). The appearance of the lava lake correlated with the inflation and collapses seen during this period (Patrick et al., 2019a). We observe episodes of lava infilling Pu‘u ‘Ō‘ō Crater, frequent outbreaks of lava from active lava lakes, which either pool on crater floor or form small flows, construction of levees elevating the lava lake above the crater floor and periods of multiple lava lakes active simultaneously.

3.3.1 Potential for Automatic Detection of 2011 Lava Lake

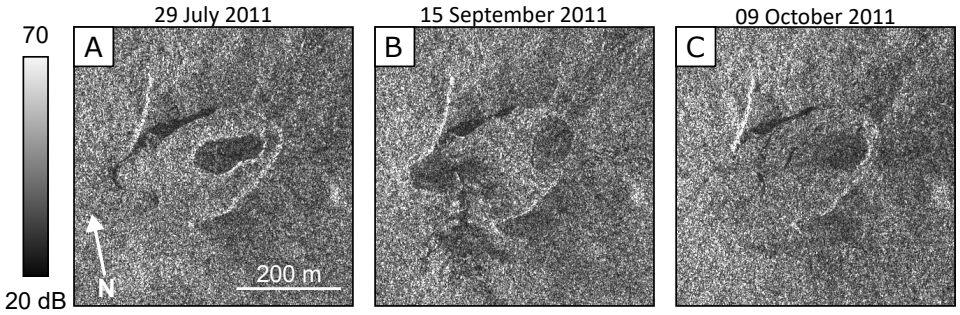

Figure 3.4: Single CSK backscatter images of the Pu‘u ‘Ō‘ō lava lake on in 2011 showing (a) a perched lava lake, (b) contained lava lake in northeast and outbreak from second lava lake in southwest of Pu‘u ‘Ō‘ō crater and (c) short-lived lava lake.

The scattering properties of a lava lake in the radar backscatter images is dominated by the surface roughness. In the 2011 Hawai‘i dataset, the lava lake and fresh lava generally had low radar backscatter values (Fig. 3.4). We interpret low σ_0 values as the smooth lava lake surface that reflects the majority of the SAR pulse away from the satellite. Using the 2011 lava lake, we investigate how backscatter varies with the presence of different lava lake features (e.g., source of lava, surface cooling and crustal plate formation) and to test potential for automatic extraction of area. The 2011 lava lake is a good example to test this because it was almost continuously monitored through other sources (e.g., webcam imagery, thermal imagery, SO_2 emissions, seismicity, GPS Orr et al., 2015). We compare lava lake activity as recorded by webcam and thermal imagery to backscatter values and patterns. We also explore the most appropriate method to extract the shape of the lava lake from radar backscatter, which could be useful contribution to real-time monitoring. Due to the size of Pu‘u ‘Ō‘ō crater and its lava lakes, we prioritise the resolution of the SAR imagery (over

noise reduction) to maintain detail in the lava lake surface. We therefore use the full resolution dataset without any correction (1.3×2.1 m range by azimuth spacing), this does mean we reintroduce the satellite dependency, as this correction relied on a spatial filter to improve the identification of satellite-related dependency (PC1 goes from 25% to 75% after applying a 10×10 boxcar). However, we were doing analysis on individual images rather than a temporal comparison of SAR backscatter values so we do not consider the variation between satellite as a limiting factor.

When there is a lake present, we observe a wider distribution of backscatter values across the crater with a lower peak or even a bi-modal distribution. In these cases, it is possible to apply a threshold to determine the shape of the lake (Fig. 3.5a). However, in some images where the lava lake is known to be present radar backscatter values are very similar over the lake to the rest of the crater. We expect the lava lake to increase in radar backscatter when the surface becomes rougher, as activity slows or a crust is formed.

We explore a method to automatically extract the areas of the a lava lake (Fig. 3.5b). To do this, we apply a morphological reconstruction (MR; Vincent, 1993) to our images before applying multiple simple thresholds. MR has been used to improve fuzzy c-mean clustering (e.g., Lei et al., 2018) by preserving object boundaries and reducing noise to optimize the distribution characteristics of the data. After applying the MR to our images they are much clearer, grouping together similar pixels based on their spatial distribution. In comparison to other filtering methods (e.g., direct application of threshold, k-means clustering) we applied to Pu‘u ‘Ō‘ō crater, MR showed better results for further image clustering and segmentation. After the MR, we use a sequence of masks and thresholds to identify the lava lake as follows. We first apply a crater mask, so that possible lava lake pixels can only be flagged within the crater. This mask means that this method does not identify when a lava lake overtops or produces a lava flow that goes out of the crater. The second mask we apply is a radar shadow mask, to avoid areas of low SAR backscatter being misidentified as lava lakes. Following the two masks, we apply a sequence of thresholds to the MR cluster outputs (Fig. 3.5b), as follows:

1. A combined threshold
   This identifies all the large clusters (>1000 pixels) that have a mean SAR backscatter (<51 dB). We do this as we expect the majority of the active lava lakes to cover a relatively large area, with low SAR backscatter values in comparison to the rougher surfaces of the bare rock in the surrounding crater. This threshold aims to remove all groups that either have very high radar backscatter levels or are too small.

2. A SAR backscatter threshold
   However, the first threshold only identifies large areas with low SAR backscatter values. We know that the lava lakes at Pu‘u ‘Ō‘ō can be relatively small. We therefore combine the first thresholds with a second SAR backscatter threshold and apply it the the original MR cluster output, so that cluster that satisfy either threshold (1) or (2) remain. This second requirement does not have an area

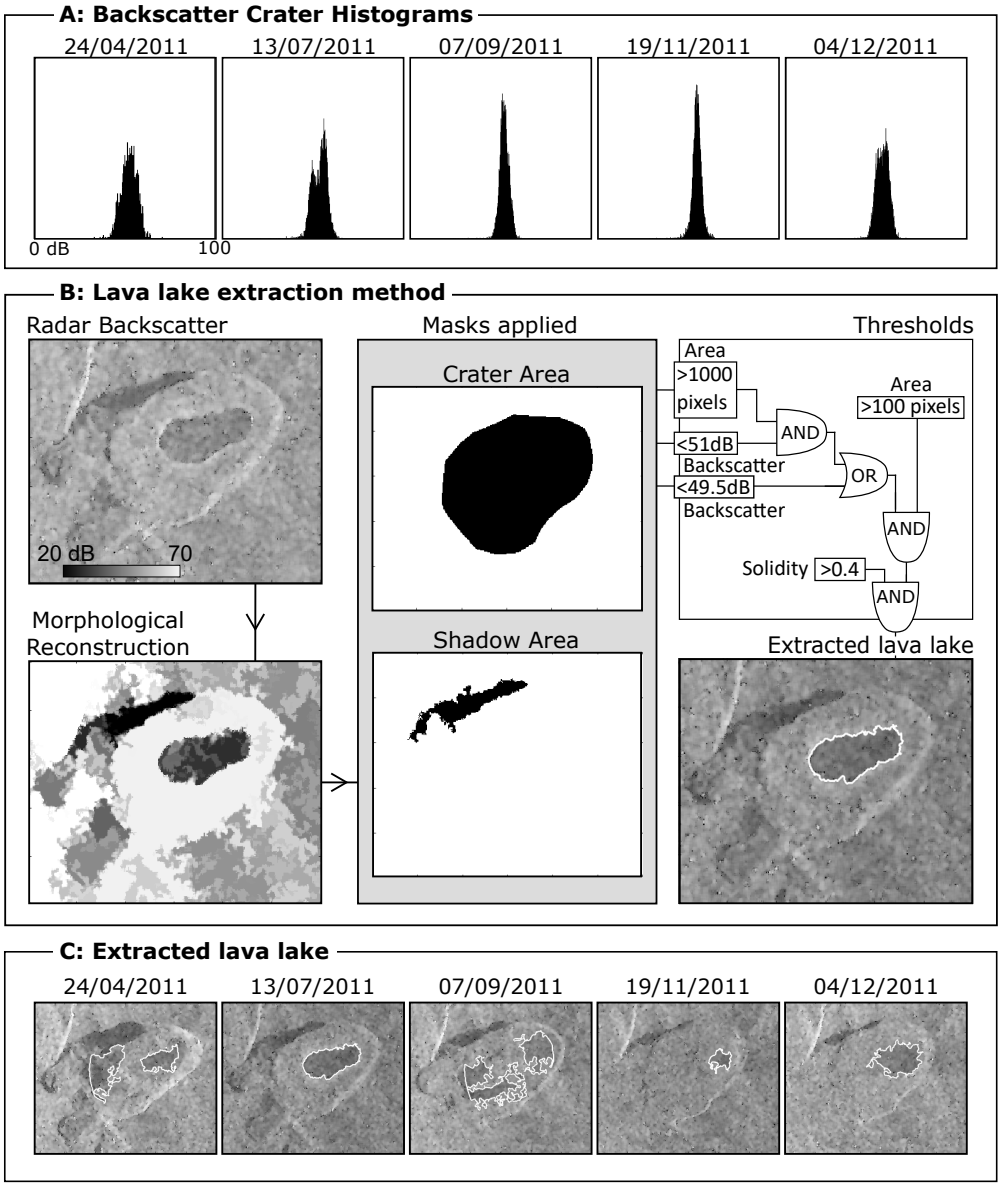

Figure 3.5: Pu‘u ‘Ō‘ō lava lake backscatter signal from CSK data in 2011. Section (a) shows the distribution of backscatter data for Pu‘u ‘Ō‘ō Crater. Section (b) is a flow diagram showing lava lake extraction using image segmentation and thresholds and section (c) presents example of automatically extracted lava lake (white outline) for the same images used in (a) using the method described in (b).

constraints as to include all groups with a very low mean SAR backscatter value. We determine this SAR backscatter threshold based on the average backscatter of the lava lakes in Pu‘u ‘Ō‘ō crater, and where present, we also use the bimodal distribution.

3. An area threshold
   Using the output from the threshold described in (1) and (2), we then apply another area threshold, this time much smaller, just to remove the clusters that slipped through the first two thresholds. We found that this threshold size worked best at removing the misidentified background noise without solely removing the lava lake.

4. A ‘roundness’ threshold
   The final threshold we applied is a measure of solidity of the lava lake. This is a measure signifies how much a shape has irregular boundaries (e.g., a circle has a solidity of 1). We expect a lava lake to generally have smooth boundaries. This threshold (> 0.4) therefore attempts to remove clusters with very rough edges. We keep it relatively low as Pu‘u ‘Ō‘ō crater can house irregular shaped lava lakes not constrained by a levees or walls.

These thresholds were calculated for the 2011 Pu‘u ‘Ō‘ō crater. The size and backscatter threshold would vary depending on parameters (i.e., wavelength, polarisation and resolution) of the SAR sensor. Therefore, further testing would be required to determine how these inputs vary for different sensors and whether the values are specific to a case study or could be applied to other lava lakes.

3.3.2 Lava lake Presentation in SAR Backscatter

In the single radar backscatter images, we were able to observe variations in the radar backscatter pattern related to different features within Pu‘u ‘Ō‘ō crater. We observed various signatures for lava lakes that included (1) both gradual and sharp lava lake boundaries depending the properties (e.g., perched, shallow) of the edges of the lava lake (e.g., 9 Oct. and 30 May 2011, Fig B.3), (2) a range of mean SAR backscatter values over the active lava lake (47.8–50.9 dB) that were not always distinguishable from the rest of the crater, (3) internal structure in backscatter within lava lake (e.g., 22 August 2011, Fig B.3) and (4) breaches and breakouts onto the surrounding crater floor (e.g., 5 July 2011, Fig. B.3). We determined the accuracy of our extracted lava lake areas through visual examination of the single radar backscatter image, and where available, with thermal and webcam images. We identified 39 SAR images out of 105 that potentially had a lava lake present (Fig. B.3). Out of these 39 images, 38 were correctly identified (Fig. 3.6, B.4). However, the method did miss 19 images where a lava lake was present (Fig. B.4), although most of these false negatives (13 SAR images)

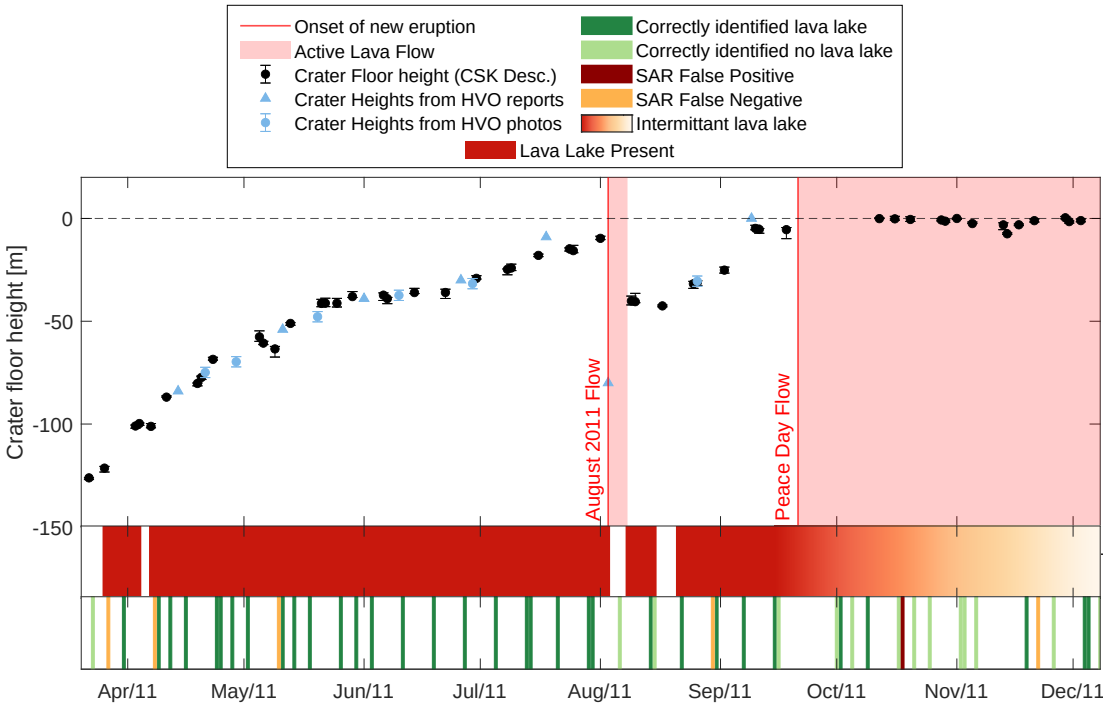

Figure 3.6: Identified lava lakes between 20 March and 31 December 2011. The scatter plot show the inflation and collapses at Pu‘u ‘Ō‘ō crater during this period of time. The first bar shows a red to yellow gradient that represents when there was a lava lake presenting in the crater. Following the Peace Day Flow (21 September) the lava lake stabilised and formed a crust with the occasional outbreak or exposed lava lake. The second bar chart shows the lava lake classification from the SAR backscatter extraction method. COSMO-SkyMed crater floor levels are discussed further in section 3.4

were for the same lava lake from mid-2012, which was a small lava pond approximately 30–40m in diameter. This lava pond is visible in the single SAR images, but the small size of the lake means that it gets removed by our size threshold during the automatic extraction. The other 6 images were either related to other small lava lakes (e.g., 22 Nov.), periods following the onset of a new eruption where the backscatter pattern of the crater was complex (e.g., 27 March) or to outbreaks (e.g., lava flows within the crater) that produced dendritic rather than circular patterns (e.g., 8 April). Our flagging method failed to identify lava lakes in two SAR images on the 10 May and 30 August 2011 (Yellow bar, Fig. 3.6), where the lava lakes only had slightly lower backscatter values than the surrounding area.

For the 1 false positive on the 18 October 2011 our approach identified a lava lake, but we did not observe a visible lava lake in the thermal imagery (Red bar, Fig. 3.6). Pu‘u ‘Ō‘ō crater was cooling after the crater being infilled by an earlier lava lake in early October and still had slightly elevated temperatures, dropping from approximately 260° to 60° in the 9 days up to 18 October. The changes in roughness of the cooling lava could be the reason for the false identification, resulting in a patchy radar backscatter

pattern as the signal increased while the surface cooled and increased in roughness.

The automatic extraction had a 67% success rate which rises to 87% when considering only lava lakes > 50 m in diameter. For the correctly flagged images, our method correctly extracted the total lava lake area approximately 85% of the time with the tendency being to underestimate area due to gradual transition in radar backscatter at the lava lake edges, possibly related to lava lake activity. The main limiting factors to the method were a minimum size of lava lake possible to identify and the crater geometry. We were only able to use the ascending track for this analysis as in the descending track geometry the lava lake was often covered by the radar shadow produced by the crater wall.

Backscatter and Lava Lake Morphology

To examine the variations in radar backscatter associated with changes to the lava lake surface, we compare our dataset to 45 thermal images, acquired within 5 minutest of SAR acquisition and webcam images. These images come from a thermal infrared camera that was installed at Pu‘u ‘Ō‘ō following the Kamoamoa Fissure Eruption in March 2011 by the HVO, with image spacing of an image every 2–5 minutes (Patrick et al., 2014). We aim to examine the correlation between the temperatures and patterns visible in the lava lake from these thermal images and the associated radar backscatter signals, (Fig. 3.7) and more generally to understand the sensitivity of the radar backscatter to morphological changes related to the formation of crusts and breakouts on an active lava lake.

Since such features are not apparent in individual backscatter images, we compare backscatter values from the automatically extracted lava lake and compare to temperature of the lava lake. We apply a simple threshold of 120° to the thermal imagery to identify the lava lake. However, most of the time the lava lake completely saturates the full temperature range (120–500°), as 500° is the upper limit for the thermal camera (Patrick et al., 2014). To get a better understanding of the temperature variations of the lava lake we calculated the 5–95^{th} percentile and do similar for the radar backscatter signal range for the lava lake. Overall, there was no visible correlation between the mean and range temperature with the radar backscatter values (Fig. 3.7).

We had hoped to observe lower radar backscatter values associated with high temperatures as higher temperatures would suggest more surface activity through overturning of the crust, and breakouts of fresh lava. These would produce smoother surfaces that would reflect more of the pulse away from the satellite, producing lower backscatter values. When the lava lake is less active, we would expect the surface to form a crust with less vigorous surface movement, which would translate to rougher surfaces observable in the radar backscatter as an increase. However, we do not observe a con-

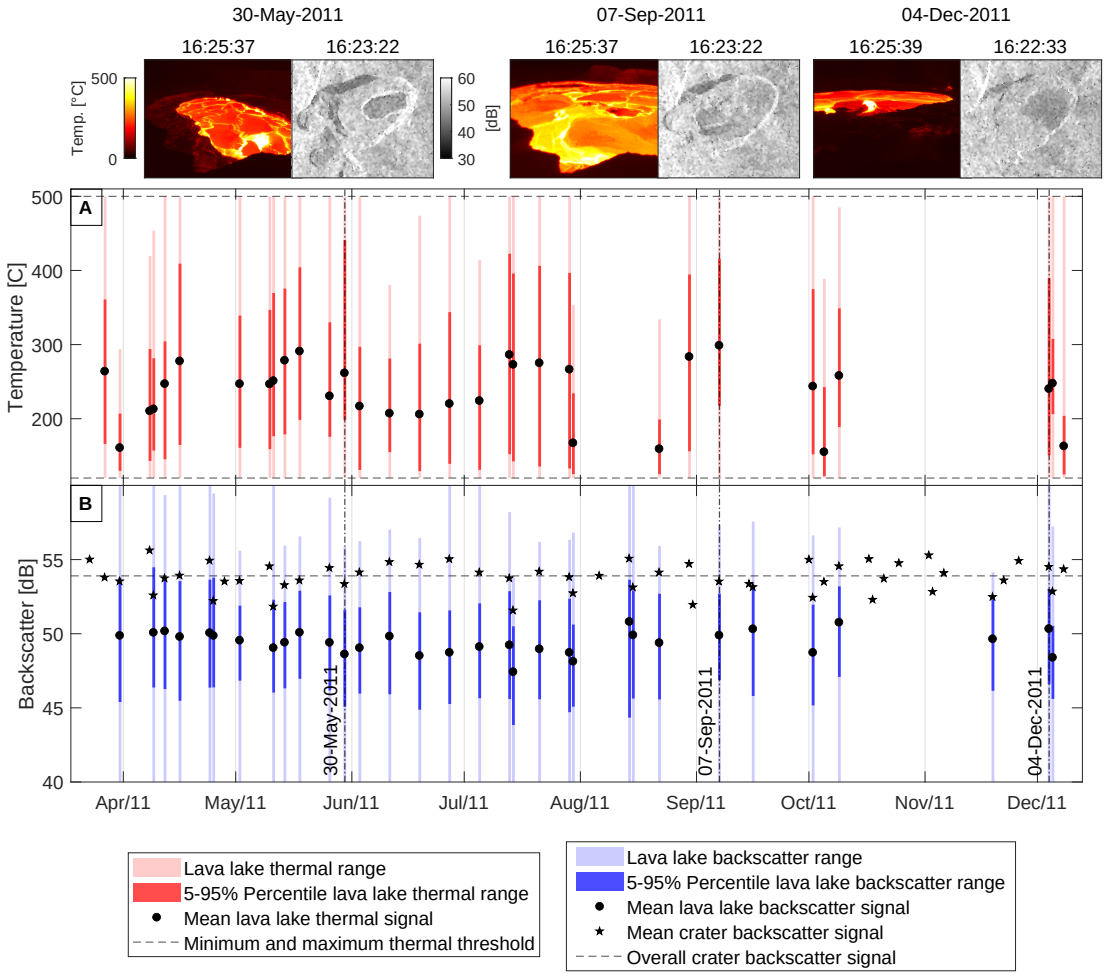

Figure 3.7: Temperature (a) and backscatter (b) range for the Pu‘u ‘Ō‘ō lava lake in 2011. When the lava lake is present the (a) light red bars represent the full range of lava lake temperature, red bars correspond to the 5^{th} to 95^{th} percentile range with the mean (black circle). Similarly, light blue bars in (b) represent lava lake backscatter range and blue bar the 5^{th} to 95^{th} percentile range with the mean (black circle) for when the lake is present. The stars and dashed black line represent the mean backscatter in Pu‘u ‘Ō‘ō crater. Dot-dash indicates the time of the example thermal and SAR images shown at top of the figure.

sistent trend between the two datasets. We further attempted to correlate the radar backscatter to the number of crustal plates that made up the lava lake surface (Fig. B.5). Based on the assumption that the number of plates present is a proxy of the lakes level of activity. Again, there was no clear correlation between this and the radar backscatter.

The reason we believe that we were not able to visualise these details for the Pu‘u ‘Ō‘ō lava lake are (1) the size of the lava lake and SAR sensor resolution, and (2) the location of the thermal camera. Pu‘u ‘Ō‘ō crater is 9.9×10^{-2} km^3, with a lava lake that can range from 0.38×10^{-2} km^3 to covering the whole crater. When using the

PCA corrected data in which we applied a boxcar filter, the small structural details and roughness variations in the lava lake would be lost. Even so we would expect the overall radar backscatter signal to remain the same. To examine whether, the lack of correlation was due to the loss of detail, we also use the full resolution SAR dataset, although would reintroduce of the satellite dependency. For both the corrected and uncorrected datasets we do not see a clear correlation to temperature. The lava lakes present in Pu‘u ‘Ō‘ō during 2011 are generally small and rapidly changing. We find that the size of the lava lake and with the resolution of the SAR sensor strongly effects the observations of possible patterns in the lava lake.

The position of the thermal camera could be considered another factor as to why we did not observe any correlation to the radar backscatter. The thermal camera at Pu‘u ‘Ō‘ō is located on the crater rim with an oblique view of the lava lake. When the crater is relatively deep (e.g., 30 May 2011) we can visualise the whole lake. However, later in the dataset, when the crater floor increased in height, the full extent of the lake lost due to the camera's field of view, which means that the temperature and number of plates are not representative.

We had the opportunity to do a qualitative analysis of the 2020 lava lake in Halema'uma'u crater in the summit caldera (Fig. 3.8). The 2020 lava lake began to infill the main crater that had formed following the 2018 eruption, covering the lake and rising rapidly over a few months into 2021. We are able to observe the partially active lake on the 8-9 February 2021 from a COSMO-SkyMed (2.6×4.5 m range by azimuth resolution, 2×2 multi-looked), Sentinel-1 (9.3×14.0 m, 4×1 multi-looked) and ICEYE (2.9×3.0 m, 7×6 multi-looked) image. In the high-resolution X-band imagery, we are able to observe changes in the radar backscatter across the lava lake. The western, more active, portion of the lava lake produced visible lower backscatter values than the central island and cooling eastern portion. This pattern in the radar backscatter matches the distribution of activity across the lava lake. Thermal imagery acquired on the 9 February 2021 (Fig. B.6), shows higher temperatures associated with the western section of the lava lake similar to the area of low radar backscatter. Further, in the high resolution ICEYE image it is possible to identify the source of new material (i.e., west vent, Fig. 3.8) and the direction material movement. Whilst the lava lake is also visible in the Sentinel-1 image, acquired on the 9 February 2021, the detail in the radar backscatter is lost. This all suggests that the 2011 Pu‘u ‘Ō‘ō lava lake may have been too small or rapidly changing to accurately correlate to surface temperature.

3.4 Measuring Pu‘u ‘Ō‘ō Crater Floor Height

Fluctuations in lava lake depth provide critical information about the shallow subsurface dynamics of the volcanic system (e.g., Patrick et al., 2015). Following the method

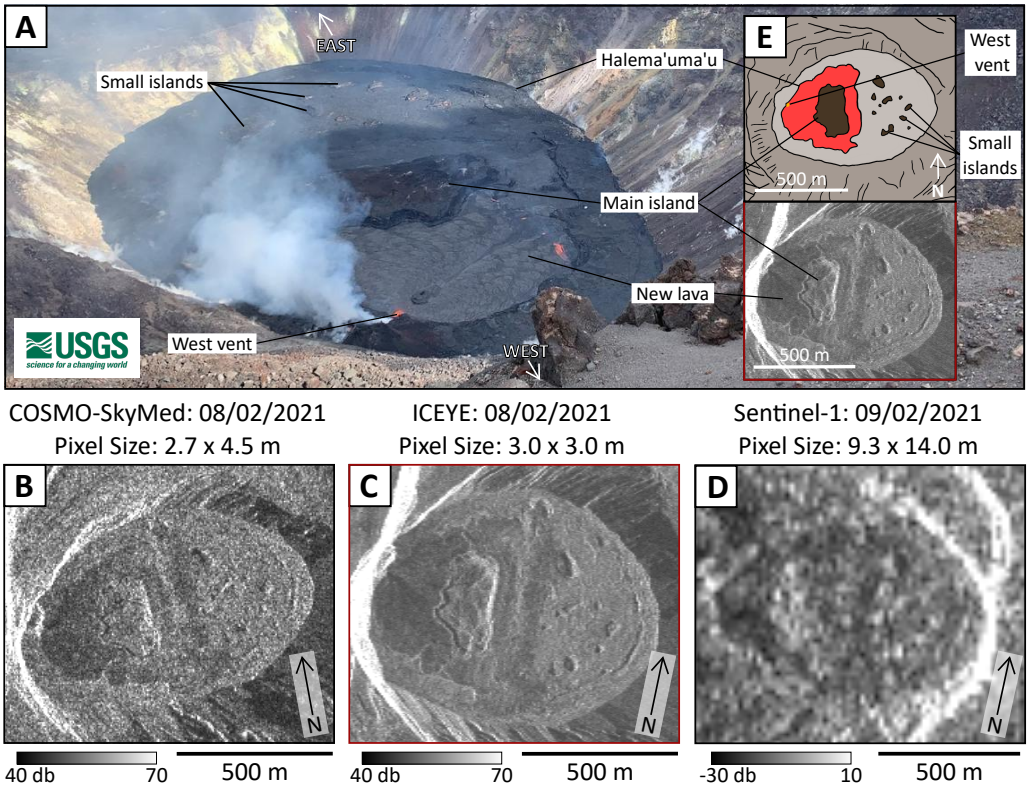

Figure 3.8: New lava lake in the summit crater, Halema’uma’u in 2020–2021. (a) photo of active portion the lava lake, showing vent location and inactive sections. SAR backscatter images from (c) COSMO-SkyMed, 8 February 2021, (d) ICEYE, 8 February 2021 and (e) Sentinel-1, 9 February 2021 showing the lava lake. Insert (e) shows a simple schematic of crater on the 8 February 2021 and Halema’uma’u crater from the ICEYE imagery (red box in d).

in Arnold et al. (2018), we calculate the depth of Pu‘u ‘Ō‘ō crater floor from the top of the crater rim using the radar shadows produced as the result of the radar viewing geometry. We use the crater floor as a proxy for the lava lake height. This assumption seems reasonable since webcam imagery, shows that the crater floor and lava lake are equal in depth or rise proportionally most of the time. The exception is the month before the August 2011 eruption where there was uplift of the crater floor causing bulging within Pu‘u ‘Ō‘ō Crater (HVO, 2011d). The height of the feature (h) casting the radar shadow in the SAR image can be calculated by,

$$h = W_{range} \cos\theta \tag{3.2}$$

where W_{range} is the width of the radar shadow in the range direction and θ is the satellite incidence angle. The method assumes that the crater floor in this particular situation is completely horizontal, which was not always the case during the 2011 period.

3.4.1 Inflation and Collapse of the Crater

Pu‘u ‘Ō‘ō crater is a relatively small oval shaped approximately 380×240 m. We use a northeast to southwest trending cross section over the radar shadow in CSK descending SAR data to calculate the changes in the crater depth, almost perpendicular to the satellite azimuth direction (Fig. 3.9a). At this point the crater is relatively narrow (∼325 m from rim to rim from optical imagery) and boarded by steep walls on either side. The crater floor depths extracted from the radar shadow method work well when using a well defined shadow, which occurred when the feature casting the shadow is perpendicular to the satellite's line of sight and the crater is steep-sided. We calculate uncertainties based on the maximum, mean and minimum radar shadow width over five sequential range lines. A crater depth of 0 m represents a crater floor that has reached the height of the crater wall for that particular cross-section.

To capture the slight increase in lava lake height that partially overtopped sections of the crater in 2013, we combine estimated heights from two cross-sections to construct an extended timeseries (blue dashed line, Fig 3.9a). Overall, we observe a good agreement between the SAR, HVO ground-based measurements and depths extracted from photos of the crater (Fig. 3.9a).

We validate our crater floor depths calculated from the radar shadow (Fig. 3.9a) using ground-based measurements from reported by the Hawaiian Volcano Observatory (HVO) and estimates from photos of Pu‘u ‘Ō‘ō crater from the HVO multimedia webpage (HVO, 2011a). The ground-based measurements were calculated using a laser rangefinder (Patrick et al., 2014). The photos we used to estimate crater floor depths, had to be taken directly facing the crater wall (no oblique views) with an object to scale the image (e.g., visible instruments or people). It is important to note that the frequency of SAR acquisition and sampling spacing determine how accurately and which small scale variations we are able to observe through this method. Rapid changes in height (e.g., collapse events), may be underestimated if either the pre- or post-collapse SAR acquisition occurs a few days away from the event.

From August 2010 to March 2011, we observed the transition from no activity, to periodic and then rapid inflation of Pu‘u ‘Ō‘ō crater leading up to the Kamoamoa fissure eruption and collapse of the crater. We estimate a collapse in the crater floor of 103±4 m (∼127±3 m below the east rim) during the Kamoamoa Fissure eruption (black cross-section Fig. 3.9). In comparison, ground based measurements made by HVO reported a drop of 115 m in the Pu‘u ‘Ō‘ō crater associated with the Kamoamoa Fissure eruption. Following the Kamoamoa Fissure eruption, we observed a build-up of the crater floor by 117±2 m to just under the east crater rim in the five months until August 2011. During this time, there were two distinct growth periods, initially from March to mid-May the crater grew rapidly at a rate of 1.36 m per day before it abruptly

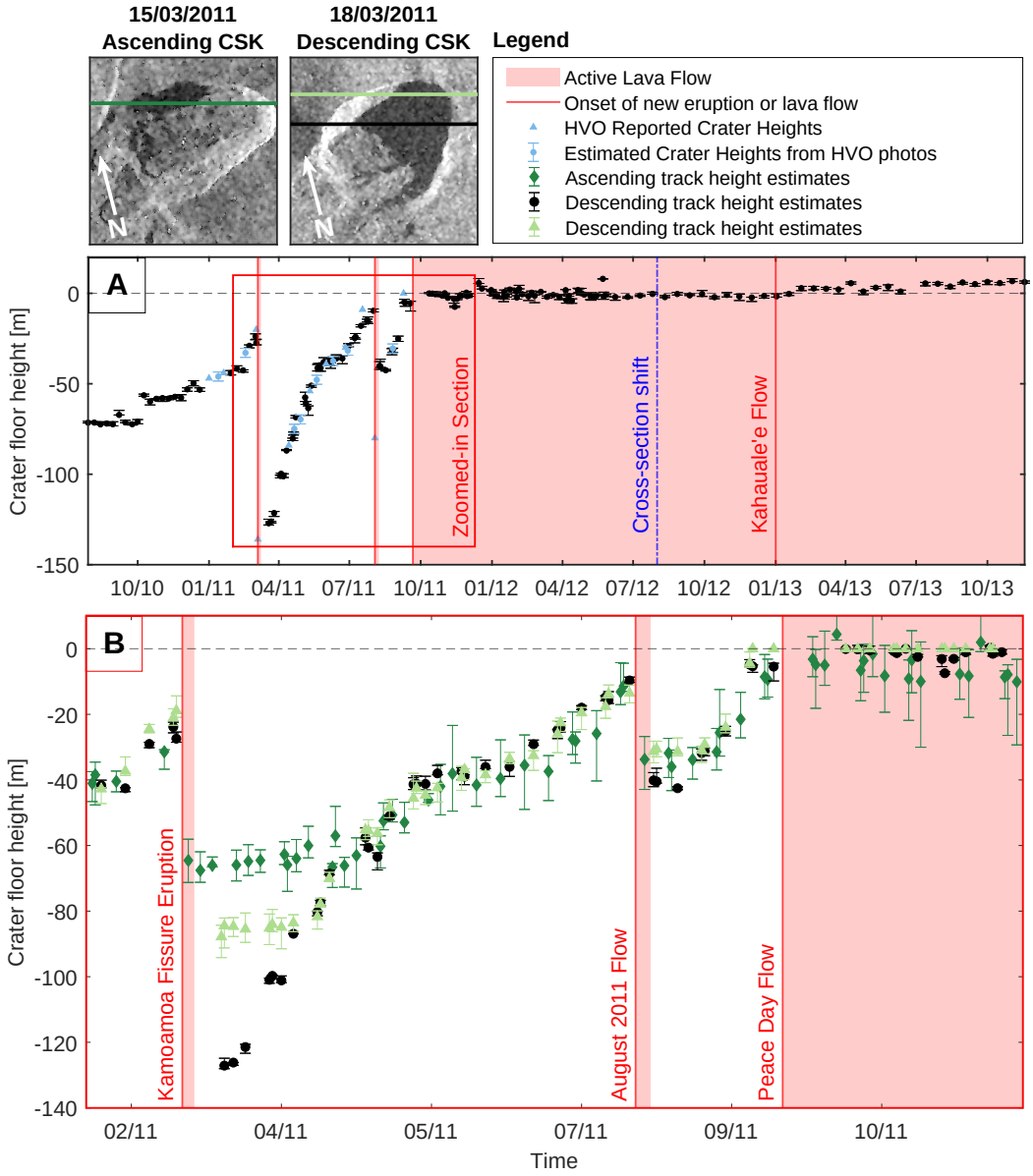

Figure 3.9: Pu‘u ‘Ō‘ō crater floor depths timeseries from (a) August 2010 to December 2013 calculated from SAR CSK descending data (black circles), depths reported by Hawaiian Volcano Observatory, HVO, (light blue triangle) and measured from photos taken by HVO (light blue circles). The zoomed in section shown in (b) shows the timeseries from the ascending (dark green cross-section) and descending (light green and black cross-sections) dataset for Jan 2011 to Jan 2012. The selection of different cross-sections show the various limitations in the radar shadow method. The start individual eruptions are marked by the red lines and the duration by the light red areas. Depths are relative to height of the crater rim in the cross-section.

decreased until mid-June to a rate of 0.17 m per day. From June until 3 August, the crater floor lifted at up to 0.66 m per day until the eruption when we observed a ∼30 m collapse of Pu‘u ‘Ō‘ō crater. Following the eruption, we observed a period where the crater floor appeared to level off around 40 m below the east rim until 25 August.

The start of the inflation that followed the August 2011 eruption coincided with reappearance of the lava lake in the crater on 21 August. The inflation during this period was very rapid (1.7 m per day), and reached the crater rim by early September. Unlike after the Kamoamoa fissure and August 2011 eruptions, the Peace Day Flow eruption (21 September 2011) did not result in a crater collapse. The crater floor remained high and relatively stable over for approximately 26 months. After the onset of eruption until June 2012, we observed variations in the crater depth estimates, with a standard deviation of 3 m. From June 2012 to January 2013 the Pu‘u ‘Ō‘ō crater floor remained relatively stable (i.e., standard deviation 0.5 m), before increased slightly (∼7 m) until December 2013. This change in height correlated with the transition of the eruptive vent from the one that fed the Peace Day Flow to a spatter cone on the crater floor that started feeding the Kahauale’a flows.

3.4.2 Limitations of Using Radar Shadows for Height Estimations

We found that the radar shadow technique works best when the feature casting the shadow is orientated parallel to the satellite heading direction or at least within 20°. When the feature is more obliquely situated to the radar shadow, the accuracy of the method declines. The overall trend of the fluctuations are still observable, however the magnitude of the changes are lost (dark green timeseries, Fig. 3.9b), with the oblique angle of the feature causing the shadow to be cast along the side of the crater wall rather than into the deeper sections of the crater. This results in an underestimation of the change in height.

When the feature casting the shadow is a crater wall there is potential of interaction between the radar shadow and the layover introduced by the opposite wall (slope steeper than incidence angle facing towards the satellite). When this occurs, the depth estimates will ‘plateau’ as the shadow width is reduced. This can be seen in the light green timeseries in Fig. 3.9b, where this plateau occurs at ∼85 m below the rim, until the crater floor rose high enough that the two satellite introduced distortions do not interact. For approximately symmetrical structures, such as craters, the maximum crater depth (D_{max}) that can be calculated using eq. 3.2 in this type of situation can be expressed as,

$$D_{max} = \frac{W_{total}}{\cos\theta + \sin(90 - \theta)} \tag{3.3}$$

where W_{total} is the total width of the structure (e.g. crater) including both shadow and layover, and θ is the satellite incidence angle, in radar geometry. At Pu‘u ‘Ō‘ō,

for the cross-section line we used to estimate the crater depth (black cross-section, Fig. 3.9) we calculated a maximum measurable depth of ∼160 m. This means that for this cross-section, if we were to calculate a depth of 160 m, this could mean that the crater floor was either at this depth or deeper (>160 m) as a result of the interaction between the crater and satellite geometry. The collapses of Pu‘u ‘Ō‘ō crater did not reach these depths.

The depth estimates calculated from the radar shadow captured the general trends of inflation and collapse events of Pu‘u ‘Ō‘ō crater in 2011, but we did observe discrepancies between estimates of changes in crater depth of ∼12 m for the Kamoamoa Fissure eruption and of ∼40 m for the August 2011 eruption (Fig. 3.9a) and the depths reported by HVO and calculated from photos HVO (2011a). The crater floor was uplifted for approximately a month prior to the Kamoamoa Fissure eruption (HVO, 2011d) resulting in a bulging topography. The radar shadow did not interact with the highest point of the bulge and underestimated the final depth of the crater floor before the Kamoamoa Fissure eruption.

The larger difference seen for the August 2011 eruption is related to the post-collapse crater geometry. The collapse of the crater during the Kamoamoa Fissure eruption occurred as a single large collapse resulting in an uniform bowl-shaped crater. In contrast, field photos of the August 2011 showed that this crater collapse produced terrace-like structures with a variety of different slope gradients. In the SAR imagery this results in multiple small shadows within the crater so that the large shadow from the crater wall did not reach into the deepest section of the crater but to an elevated ‘terrace’. While the crater floor remained lower than the height of that terrace, the backscatter shadow measurements underestimated the depth relative to the ground-based measurements.

An apparent lack of depth change from shadows indicate either (1) no volcanic activity, (2) that the collapse exceeded the potential radar shadow calculable depth or (3) the morphology of the crater was not uniform (e.g., formed shallow ledges or terraces).

At Kīlauea, frequent measurements of lava lake levels at Halema’uma’u and Pu‘u ‘Ō‘ō have been correlated with the elevation of the eruptive vent and with GNSS data and seismicity (e.g., Orr et al., 2015; Patrick et al., 2019a). These studies are able to constrain the geometry of the conduit and demonstrate the hydraulic connection between the craters suggesting a dynamic equilibrium between Kīlauea and the East Rift Zone (Patrick et al., 2019a). Monitoring long-term trends in lava lake levels are useful as they can capture changes to the magma supply rate and deviations from usual behaviour (Orr et al., 2015; Patrick and Orr, 2018). The Hawaiian lava lakes are well monitored (Patrick et al., 2014), most lava lakes do not have this continuous ground-

based monitoring. While we are starting to see similar measurements being made from SAR shadow measurements for more remote volcanoes (Barrière et al., 2018; Moore et al., 2019). It is currently still a case study and sensor dependent method. We demonstrated here the potential for this method, examining in detail the limitations of the method (e.g., feature geometry) and what to consider when interpreting the measurements (e.g., plateaus).

3.5 The 2011–2013 Pu‘u ‘Ō‘ō Flow Field

3.5.1 Modelling Lava Flows in Radar Backscatter

The emplacement of a lava flow causes a significant change to the ground surface altering the shape, and surface roughness (Cashman et al., 2013). We therefore, theoretically expect lava flow emplacement to be clearly visible in the radar backscatter. However, as a result of multiple scattering properties changing at the same time, the change in backscatter can actually be minimal and is not always discernible in single radar backscatter images. This is especially true for flows emplaced onto areas already with low radar backscatter signals. Interpreting backscatter for volcano monitoring is therefore challenging, as the signal represents multiple changes to ground surface between acquisitions and differentiating between and understanding what produced a signal is not always clear.

We develop an approach to map radar backscatter change associated with lava flow emplacement based on a simple theoretical model of how backscatter evolves (Fig. 3.10). Our model comprises (1) a stable pre-emplacement radar backscatter signal, σ_0^{pre}, (2) a sudden drop related to the emplacement of the lava flow, t_e, (3) the gradual recovery, k, as the lava flow cools, and (4) a stable post-emplacement radar backscatter signal, σ_0^{post}. First, we calculate the variance of each pixel for the whole time span of our dataset to identify pixels that have a high likelihood of being affected by the lava flow. We apply a variance threshold ($s^2 = 0.18$), which is calculated by determining the mean variance over a stable (i.e., known unchanged area), for the Pu‘u ‘Ō‘ō lava flows we use the vegetated area towards the northwest of Pu‘u ‘Ō‘ō crater.

Taking just the high variance pixels, we identify the time, t_e, when the radar backscatter first deviated from background levels (Fig. 3.10b). This is an unconstrained change that could either be an increase or decrease in radar backscatter depending on the previous land coverage and topography. Here, we expect a decrease in radar backscatter for most pixels, as the lava flow was initially emplaced on rough old lava flows. The fresh lava flow surface appears smooth in the X-band imagery relative to the older, weathered lavas, causing a drop in radar backscatter signal.

For the subset of pixels that have a significant, instantaneous decrease in radar

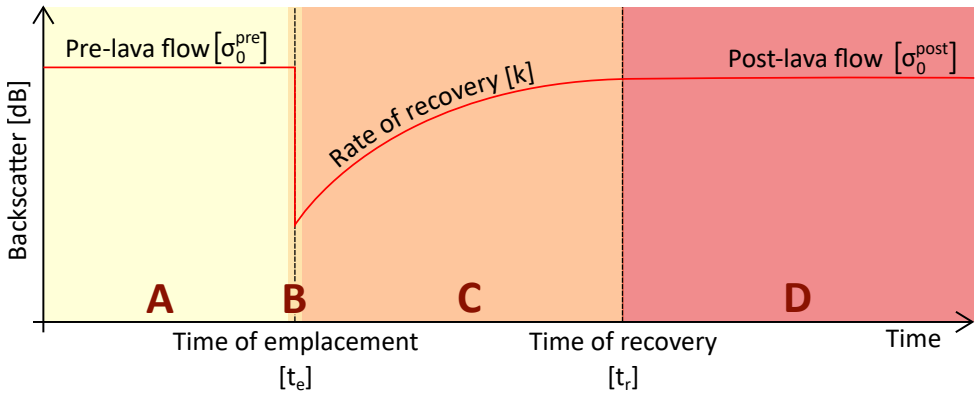

Figure 3.10: Schematic model of radar backscatter signal for lava flow emplacement and recovery divided into four categories: (a) stable backscatter signal pre-lava flow emplacement, σ_0^{pre}, (b) sudden increase or decrease in radar backscatter related the emplacement of a lava flow, t_e, (c) exponential recovery of lava flow, k, until it reaches a (d) stable backscatter signal post-lava flow emplacement, σ_0^{post}. This model is based pixel timeseries of a lava flow emplaced on the Pu‘u ‘Ō‘ō lava field.

backscatter, we quantify the lava flow the ‘recovery’ period from the backscatter values following the emplacement (Fig. 3.10c). We defined this ‘recovery’ period as the time it took for the radar backscatter signal over a lava flow to return to a stable level (t_r–t_e). Following the point when the radar backscatter drops, we apply a simple exponential function,

$$\sigma_{0(t)} = \sigma_0^{post}\left(1 - e^{-kt}\right) \tag{3.4}$$

where σ_0^{post} is the stable radar backscatter level post-lava flow emplacement, and k is the rate of lava flow recovery. Smaller values of k indicate a gentle recovery over a longer period, whilst larger values indicate rapid recovery. We solve for this equation using a non-linear least-square inversion for the timeseries for each pixel above our variance threshold.

3.5.2 Lava Flow Emplacement

We use the times of emplacement, t_e, to produce a flow field map for each COSMO-SkyMed image. When viewing the flow field maps altogether it clearly shows the progression of the flow over time (Fig. 3.11). We compare our extracted flow fields to maps produced by the USGS, SAR coherence maps (Fig. 3.11c) and other studies describing topography change over the same period (e.g., TanDEM-X, Poland, 2014). SAR coherence has previously been used to map the evolution of lava flows either using (1) various InSAR datasets (e.g., Piton de la Fournaise, La Réunion Island, Bato et al., 2016), (2) through a combination of radar and optical imagery (e.g., Volcán de Colima, Mexico, Carrara et al., 2019), or (3) only using SAR coherence (e.g., Hawai’i, Dietterich et al., 2012). The SAR coherence maps we produced here are made from

coherence images using SAR coherence mapping (SCM) described in Dietterich et al. (2012), which uses the decorrelation associated with lava flow emplacement. When a lava flow is emplaced it causes areas to become incoherent as it completely changes the scattering properties of the ground surface. SCM produces lava flow maps from coherence images by identifying the loss of coherence. The method can provide high spatial and temporal lava flow maps and produces accurate maps when the lava flow is emplaced on an area with previous high coherence. However, this approach loses detail when flows enter either vegetation or persistently decorrelated areas (Dietterich et al., 2012).

The Kamoamoa Fissure and August 2011 eruptions were both emplaced relatively rapidly over three and one CSK acquisition, respectively, so the final flow field maps are less detailed than the long emplacement period of the Peace Day Flow (compare D to E, Fig. 3.11). The total area covered for the Kamoamoa Fissure and August 2011 eruption from radar backscatter was 1.7 km^2 (Fig. 3.11g). We treat these two flows as a single entity because their flow fields intersect in areas, producing a SAR backscatter signature related to the emplacement of two lava flows. Our method only identified the first sudden change in backscatter. The total area calculated from the radar backscatter for these two flows is significantly smaller than the final flow field calculated of 3.6 km^2 from the HVO maps.

In September 2011, a new eruption began with activity focused around Pu‘u ‘Ō‘ō before localising on the eastern flank feeding lava towards the southeast (i.e., Peace Day Flow). For approximately 28 months activity was concentrated on this flow, with multiple ocean entries and small changes in the direction of the flow front (Fig. 3.11e). In January 2013, a new flow, the Kahauale’a flow, developed to the north of Pu‘u ‘Ō‘ō flowing towards the east (Fig. 3.11f), partially on the old flow field before entering into vegetation. During the first half of 2013, activity slowly decreased on the Peace Day Flow, as more lava was directed into the Kahauale’a flow to the north. From the radar backscatter maps, we estimated that the Peace Day Flow affected an area of 13.2 km^2 (Fig. 3.11g), approximately 17% smaller than the area calculated from the HVO flow fields. The Kahauale’a flows which were only partially emplaced in the timing of our dataset had an area of 1.9 km^2 in the radar backscatter (Fig. 3.11g). The main reason for this is that these flows were predominately emplaced on either vegetation, or in the case of the August 2011 flow, on to the recently emplaced Kamoamoa Fissure eruption (March 2011), meaning that the radar backscatter timeseries here have high levels of background noise. This high level of noise means that the new lava flows only produce a small change in radar backscatter from the background variation leading to the mislocation of the emplacement time (e.g., similar to Fig. B.7).

Timing of Emplacement

For the 2011 Peace Day Flow we observed that the SAR backscatter emplacement maps (Fig. 3.11f) corresponded well with both the SAR coherence (Fig. 3.12b) and HVO

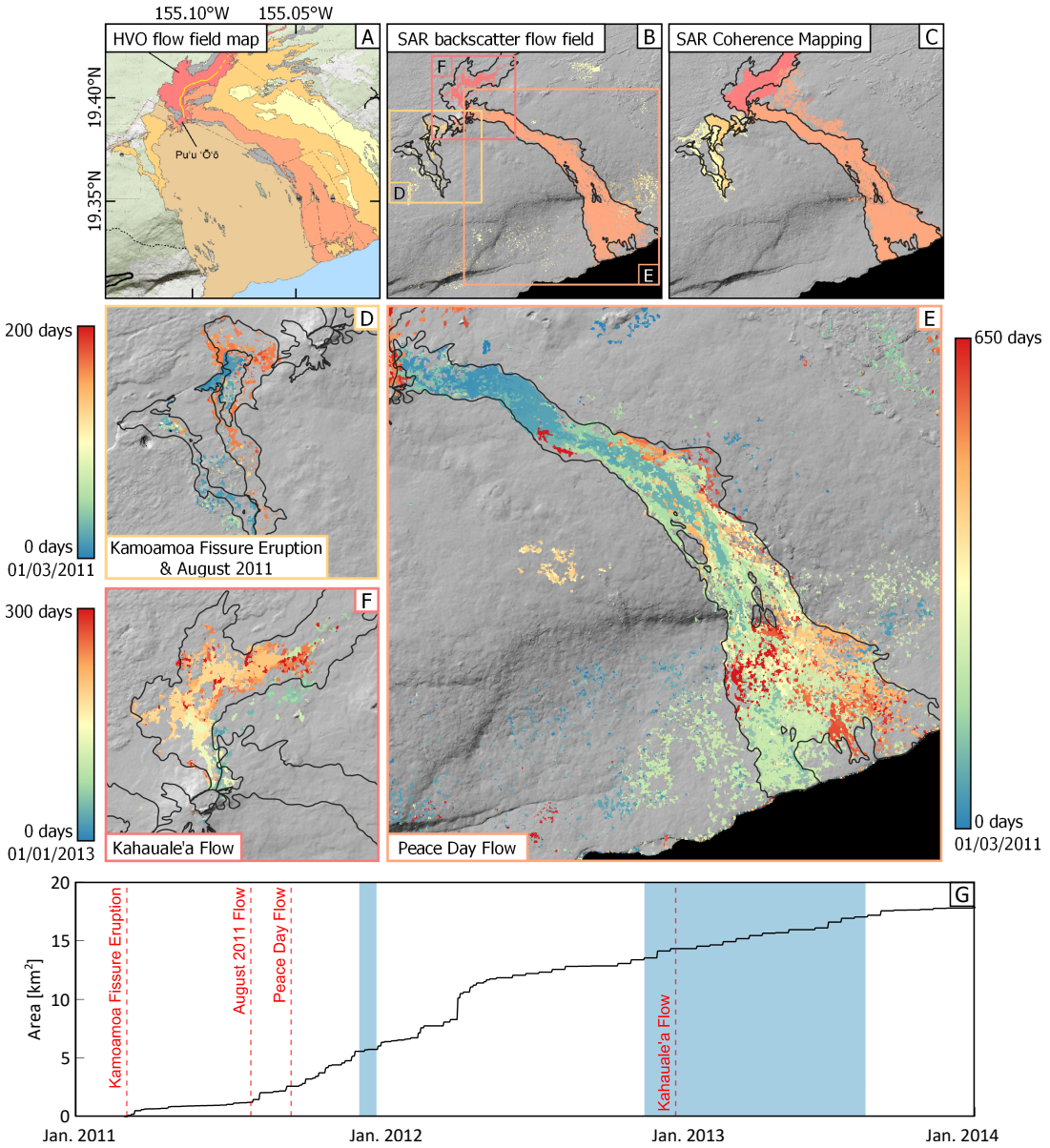

Figure 3.11: Flow maps summarizing the 2011–2013 lava flow activity from (a) USGS published maps (HVO, 2014), (b) calculated from SAR backscatter, and (c) SAR coherence. Panels (d-f) show the progression of various lava flows based on the time of emplacement, t_e, for the (d) Kamoamoa Fissure eruption and August 2011 eruption, (e) Peace Day Flow, and (f) start of the Kahauale’a Flow. Lava flows are coloured according to time of emplacement, older flows in blue and younger in red based on indicated start date (Location are shown in b). Black outlines represent flow shapes based on the HVO flow field map (HVO, 2014). (g) Cumulative area covered by lava flow extracted from the SAR backscatter flow field, with start of eruption (red dashed line) and ocean entries (blue) labelled.

flow maps. The SAR maps both managed to identify most of the Peace Day Flow although the SAR backscatter method did not capture the full extent of the eastern ocean entry point on the coastal plain as the backscatter change caused by lava flow emplacement here was similar to the overall timeseries variance (Fig. B.7).

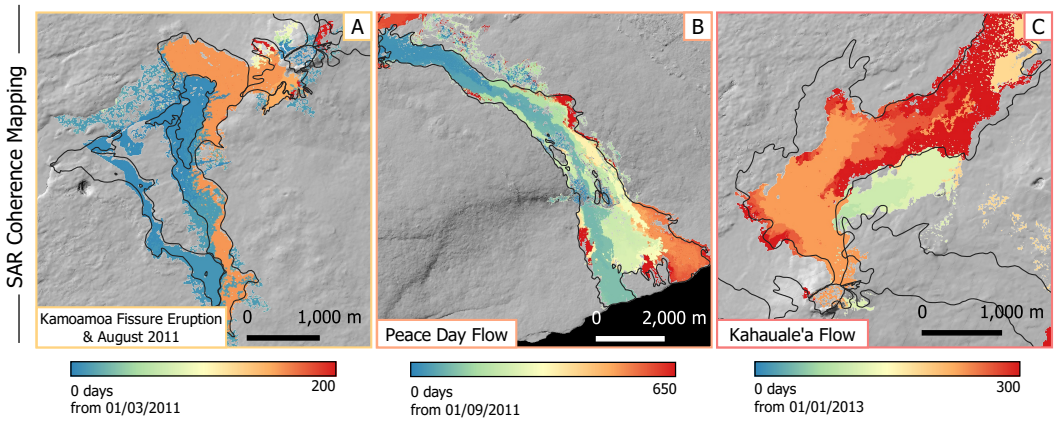

Figure 3.12: The equivalent SAR Coherence (a-c) lava flow emplacement maps of the 2011–2013 Pu‘u ‘Ō‘ō lava flows as the flow field maps produced from SAR backscatter (Fig. 3.11d-f). Note pixel spacing for coherence and SAR imagery was the same (∼5×5 m).

For the other flow there were more differences between the two SAR methods. The coherence maps better captured the flow field. However, for the area affected by and around the August 2011 flow, the coherence maps had problems correctly identifying the correct timing of the lava flow emplacement (Fig. 3.12a). We can see a large proportion of areas within and outside the August 2011 USGS flow outline indicating emplacement at the beginning of March 2011 (Fig. 3.12a). This misidentification of flow emplacement means that we completely lose the full extent of the August 2011 flow due to earlier decorrelation from vegetation.

Although, the SAR backscatter maps missed sections of these flows, there are fewer misidentified pixels (false positives, Fig. 3.11d). The sparse flow fields in the SAR backscatter maps area are due to deviations from the expected trends in the timeseries. Here, the new lava flow mainly resulted in increase in radar backscatter (Fig. 3.13). The change in variance associated with the emplacement of the new lava flow appears low, as the overall timeseries already had a higher variance due to the previous vegetation cover. Even though the SAR backscatter method has limitations, it has the potential to provide independent measurements for flow extent and could provide missing details or margin constraints for coherence maps when the flows enter vegetation. Backscatter can also provide data when the lava flow is emplaced on an already incoherent area.

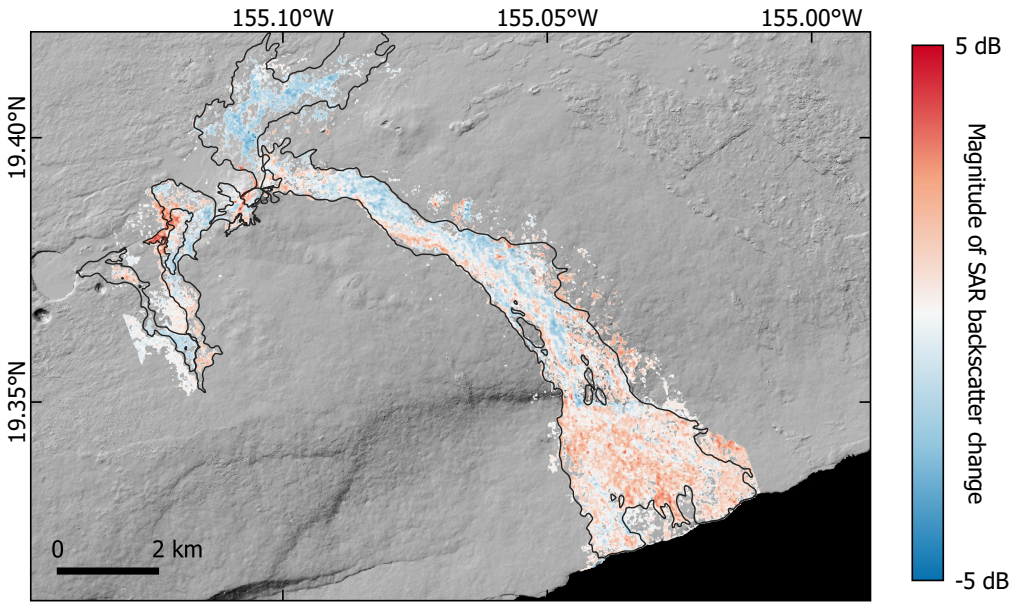

Figure 3.13: SAR backscatter magnitude change for the 2011–2013 Pu‘u ‘Ō‘ō lava flows. Map show the change in SAR backscatter calculated at t_e

3.5.3 Post-Emplacement Recovery

We produce a flow recovery map (t_r-t_e) for the Peace Day Flow (Fig. 3.14b) to visualise the changes in SAR backscatter pattern following the emplacement of a lava flow. We limited this analysis to the Peace Day Flow, as it was fully emplaced before the last acquisition in our dataset and allowed us to capture backscatter changes as the flow became inactive and cooled down at different rates (e.g., cooling directly or following lava tube formation).

We found that our model proved to be too simplistic to capture the full picture of the flow development. In the oldest section of the Peace Day Flow near Pu‘u ‘Ō‘ō crater we did observe systematic long recovery times (∼200 days). We expected to observe these longer recovery times over sections of the lava flow where activity was concentrated for an extended time before becoming inactive and cooling (e.g, through the formation of channels or tubes to insulate flow). In this upper section of the Peace Day Flow, it is easy to distinguish the emplacement and recovery of the lava flow. However, in the younger sections, especially on the Pali (i.e., cliffs) and coastal plain, where the emplacement of the lava flow becomes more widespread with frequent changes in flow front location, the recovery patterns are not captured by our model. Through a combination of multiple lava flow emplacement events (e.g., through redirection of the flow front or because of breakouts) and additional contributions to the SAR backscatter signal our model does not produce distinguishable patterns to proper capture the flow complexity.

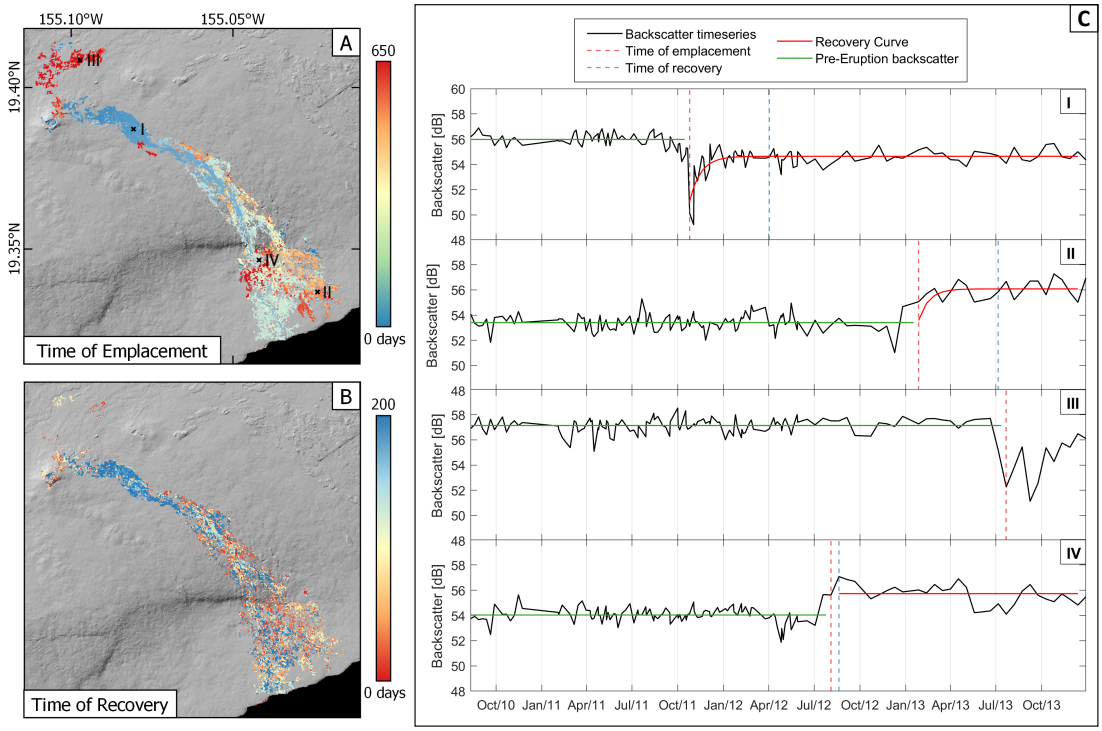

Figure 3.14: Flow maps of the 2011–2013 Pu‘u ‘Ō‘ō lava flows showing (a) the timing of the emplacement of the lava flow, (b) the modelled recovery time for each timeseries, and (c) individual pixel timeseries (location shown in a) showing pixel timeseries of where the model worked (i) and where it did not (ii-iv).

Complexity of Backscatter Variations

The main areas where our model failed to capture the lava flow recovery from the SAR backscatter signal were when there were deviations from the expected recovery pattern in the SAR backscatter and contributions to the signal from separate events. In our original model, we suggested a decrease in radar backscatter followed by an exponential increase until it reached a stable SAR backscatter value, σ_0^{post} (Fig. 3.14i). We did expect to see some deviation from this model and to observe increases in SAR backscatter when a lava flow was emplaced on vegetation. We did not expect to observe these variations in SAR backscatter trends for the Peace Day Flow, as it was completely emplaced on older lava flows. However, we found that these deviations from expectations were common throughout our dataset. For the Peace Day Flow, we observe frequent initial increases in radar backscatter on the coastal plain (Fig. 3.13). We assume this is because the older lava flows on the coastal plain have a smoother surface texture. The issue with an initial increase in SAR backscatter is that the recovery in backscatter is not exponential, but rather a period of high variability before stabilising around a similar backscatter level (Fig. 3.14iv). This step-like lava flow emplacement and recovery pattern is not captured by our model.

In addition to difference in the pre-emplacement surfaces, there are frequent breakouts along the length and edges of the Peace Day Flow. These breakouts can cause secondary or multiple changes in a single radar backscatter timeseries. In these situations, our model identifies the first change and depending on the timing of the second change, the shape of the recovery is distorted. Breakouts generally occurred later in the timeseries. Although, our method did not identify the breakouts that occurred on top of other recently emplaced lava flow, we did map out breakouts on the edge of the Peace Day Flow (∼600 days approximately $\frac{1}{4}$ along the flow from P'u O'o, Fig. 3.11e) and where lava infilled gaps as the flow went over the Pali onto the coastal plain (∼600 days following the break in slope where the flow spreads out, Fig. 3.11e). The Peace Day Flow also developed a complex lava flow channel network relatively soon following the start of eruption, with a lava tube formed by late October 2011, although we could not pick this out in the SAR backscatter data.

Another consideration we have to note is that from mid-2012 the frequency of acquisitions decreased from an average of 6 day between acquisition to 17-18 days. This decrease affected the accuracy of the times calculated from our model in comparison to those for the younger flows.

3.5.4 Possible Method Improvements

The initial method we showed here to model the recovery of a lava flow from the radar backscatter demonstrated the complexity of the backscatter signal related to emplacement and recovery of lava flows. Overall, we were able to identify the emplacement of the lava flow well, especially in on the old flow field. However, the method did struggle to correctly identify the change in radar backscatter when the initial change was an increase, since this was commonly also associated with high background variance (e.g., vegetation).

We found that our lava flow recovery model was too simple when applied to the various different backscatter timeseries patterns found across the whole flow field. A possible improvement to the method to better capture the period of lava flow recovery could be to use changes in variance through time to identify how long a lava flow remains active (Fig. 3.14i). This would allow for different types of recovery patterns (e.g., gradual increase or high levels of variation before stabilising) to be considered, assuming that the lava flows causes enough variation to the radar backscatter before returning to a stable level. However, this would also require consistent and frequent acquisitions across the timeseries. In the CSK dataset, the decrease in temporal resolution from mid-2012, which reduced the variance in radar backscatter (Fig. 3.14). This would be something to consider if we were to apply this method to other SAR sensors, the different temporal resolution would cause shifts in the estimates of emplacement time and rate of recovery (Fig. B.8).

Lastly, it would be beneficial to identify pixels where the lava flow is still active and ground has not returned to a stable state post-emplacement. Identifying these pixels would be useful to visualise where the flow is currently active, as well as where there may be large errors when examining the post-emplacement lava flow recovery.

3.6 Conclusion

We demonstrated a wide range of potential uses of SAR backscatter for monitoring, and have identified a set of considerations for applying SAR backscatter to effusive eruptions. At Pu‘u ‘Ō‘ō crater, we produce a dense timeseries of crater floor height, which captures the inflation and collapse events related to various eruptions. The temporal extent of this dataset allowed us to correct for the systematic pattern in COSMO-SkyMed SAR backscatter values related to the individual SAR satellites, massively increasing the signal to noise ratio of the dataset and allowing the detection of relatively subtle backscatter changes caused by lava flows.

We use this dataset to test the limitations of using radar shadows to estimate heights, and identify the satellite (i.e., LOS perpendicular to feature casting the shadow) and crater geometries (i.e., steep edge) where this method would be successful. This method could easily be automated for continuous height measurements for remote locations, after tailoring for local topography and satellite geometry. The automatic detection of lava lakes proved to be more complex since the Pu‘u ‘Ō‘ō lava lakes vary greatly in size and SAR backscatter values (47.8–50.9 dB), we did see evidence that for large lava lakes and high-resolution SAR imagery backscatter captures much more useful information across the surface of the lava lake.

In this chapter, we have demonstrated the possibility of tracking the progression of lava flows based solely on the changes to SAR backscatter. Although our lava flow model proved to be too simplistic to completely capture the post-emplacement development of the lava flows, we were able to show examples of the complexity of the long-term trends in SAR backscatter and the type of information there is within this dataset. As each SAR image can provide information about the eruption at a particular time, it has the potential to provide independent supplementary information to other datasets (e.g., optical or phase coherence). We further discuss the potential for backscatter methods to support volcano monitoring in Section 5.1.

Chapter 4

Dome Growth at La Soufrière, St. Vincent Quantified from Synthetic Aperture Radar Backscatter

The extrusion rate of a lava dome is a critical parameter for monitoring eruptions and forecasting their development. In this chapter, we present an approach for estimating volcanic topography from individual backscatter images. Using data from multiple SAR sensors we apply the method to the dome growth during the 2021 eruption at La Soufrière, St. Vincent. We measure an average extrusion rate of 1.8 m^3s^{-1} between December 2020 and March 2021 before an acceleration in extrusion rate to 17.5 m^3s^{-1} in the 2 days prior to the explosive eruption on 9 April 2021. We estimate a final dome volume of 19.4 million m^3, extrapolated from the SAR sensors, with approximately 15% of the total extruded volume emplaced in the last 2 days. A possible explanation for this could be the combined emptying of a conduit and reservoir of older material before the ascent of gas-rich magma in April 2021.

4.1 Introduction

After 41 years of quiet, La Soufrière Volcano, St. Vincent, began a new phase of extrusive dome growth on 27 December 2020. By the beginning of April 2021 the new dome had grown steadily around the southwest section of the 1979 dome (Fig. 4.1). Starting on 9 April 2021 the eruption suddenly transitioned into an explosive phase that lasted until 22 April 2021, completely reshaping the summit crater (Joseph et al., 2022). Understanding and forecasting such transitions from extrusive to explosive phases of

eruptions is critical for hazards assessment and mitigation (Fink and Anderson, 2000; Joseph et al., 2022) and relies on robust monitoring data (e.g., Griffiths and Fink, 1997; Pallister et al., 2013; Scharff et al., 2014).

Transition from an effusive to explosive eruption occurs when the overpressure in a conduit exceeds confining pressure and has been attributed to both shallow changes in a volcano's edifice ('top-down', depressurisation) and events deeper in the magmatic system ('bottom-up', increased overpressure). Some top-down triggers of explosive eruption, such as changes in the shallow stress regime caused by dome collapse (e.g., Pallister et al., 2013), high rainfall (e.g., Carn et al., 2004), or changes in extrusion direction (e.g., Watts et al., 2002) are detectable from ground- or satellite-based observations (e.g., Ryan et al., 2010; Pallister et al., 2013). Deeper triggers (Metcalfe et al., 2022), such as the crystallisation or degassing of an ascending magma, or an increase in conduit permeability, may not result in diagnostic changes at the surface. However, the resulting increases in magma ascent rate (e.g., Castro et al., 2012; Wang et al., 2015) can be inferred from (1) changes in seismicity (e.g., Nakada et al., 1999; Roman et al., 2016) or (2) increases in extrusion rate, if measurements are sufficiently frequent.

High-temporal-resolution measurements of dome growth are difficult to obtain from the ground, being limited by accessibility, resources, cloud coverage and rapidly changing hazards. Whilst optical aerial and satellite imagery can have sub-metre pixel resolution (e.g., Pléiades, WorldView), and can make Digital Elevation Model (DEM) directly with stereo optical imagery these datasets depend on daylight and low cloud coverage. Historical timeseries of dome extrusion (e.g., Zharinov and Demyanchuk, 2008; Ryan et al., 2010; Harnett et al., 2019) therefore tend to have large gaps or rely on measurements averaged over weeks to months.

Synthetic Aperture Radar (SAR) sensors has the benefit of being independent of the time of day and meteorological conditions. SAR backscatter has previously been used to observe dome stability and growth (e.g., Pallister et al., 2013; Plank et al., 2019) and to track changing morphology (e.g., Wadge et al., 2011; Walter et al., 2015). Structural information such as dome heights and volumes has been extracted from SAR backscatter through the use of radar shadows (El Reventador, Ecuador, Arnold et al., 2017), feature tracking (Mt. Cleveland, Alaska, Wang et al., 2015) and simulating SAR backscatter signals to construct synthetic domes (Shinmoe-dake, Japan, Ozawa and Kozono, 2013). The recent study by Angarita et al. (2022), demonstrates a similar method as we present here to quantify changes to Shishaldin Volcano.

Here, we present an analysis of the 2021 dome growth at La Soufrière volcano on the island of St. Vincent using radar backscatter from multiple sensors. We describe an approach to extract topographic profiles from SAR backscatter images. Using data

from multiple SAR satellite systems (i.e., TerraSAR-X, COSMO-SkyMed and Sentinel-1), we construct a timeseries of 32 dome volume estimates between December 2020 and April 2021. We show that the extrusion rate remained relatively constant until two days before the explosive eruption on 9 April 2021.

4.1.1 La Soufrière, St. Vincent

La Soufrière (1,234 m) is the current active volcanic centre on the main island of St. Vincent and is situated in the northern section of the island (Fig. 4.1). La Soufrière is considered one of the most active volcanoes in the Caribbean, with at least five explosive eruptions since the first recorded eruption in 1718 (Robertson, 1995).

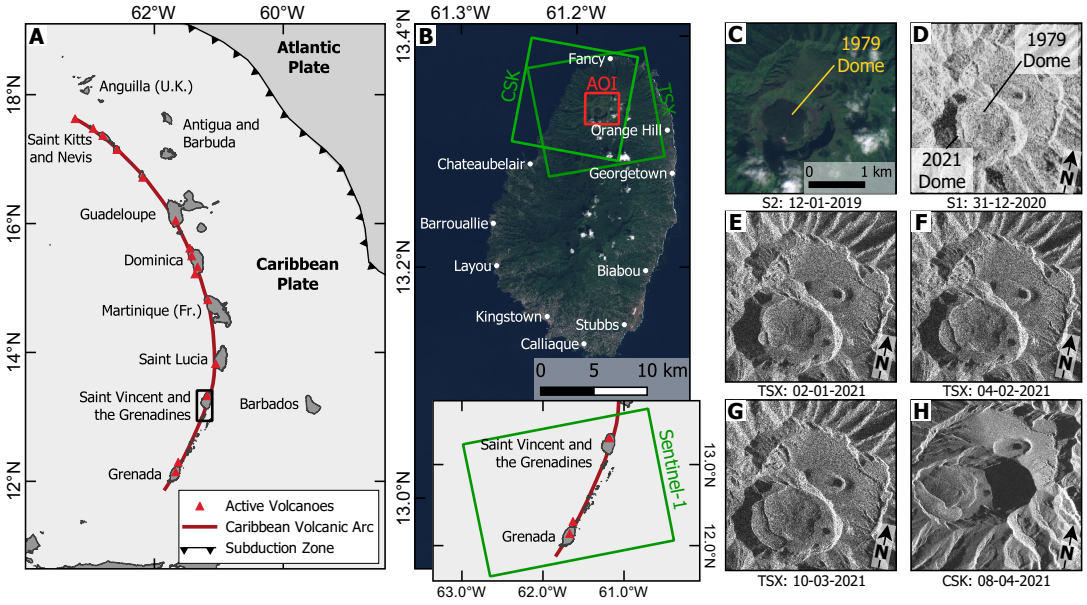

Figure 4.1: Location and overview of La Soufrière. (a) map of the Lesser Antilles arc and the Atlantic and Caribbean plate subduction zone, (b) Sentinel-2 (S2) image (29-12-2019) of island of St. Vincent with extent of SAR tracks shown in green and summit of La Soufrière in red, (c) optical and (d-h) SAR images in radar geometry showing the dome growth in La Soufrière crater between December 2020 to April 2021. SAR satellite abbreviation: CSK, COSMO-SkyMed; TSX, TerraSAR-X; S1, Sentinel-1.

La Soufrière is monitored by the University of the West Indies Seismic Research Centre (UWI-SRC), assisted by the Soufrière Monitoring Unit (SMU) of National Emergency Management Organisation (NEMO) of St. Vincent and the Grenadines. Historic eruptions were characterised by both explosive activity and effusive dome growth.

In December 2020, La Soufrière entered a new period of activity with a new dome growing on the edge of the 1979 dome first observed on 27 December 2020 (Joseph et al., 2022). The Government of St. Vincent raised the volcanic alert level in December to 'Orange' in response to the extrusive activity (NEMO, 2020a). By mid-February

2021 the dome had grown to approximately 90 m in height and had transitioned into an elongated coulee, curling around the southwest edge of the 1979 dome (Fig. 4.1). During the extrusive phase, 12 measurements of the 2021 lava dome were made by UWI-SRC and SMU through photogrammetry using ground-based (i.e., from the crater rim) and aerial (i.e., UAVs, helicopters and fixed-wing aircrafts) imagery. A volcano-tectonic (VT) earthquakes swarm was observed on 23–25 March 2021, marking a change in eruptive and suggesting movement of magma towards the surface (NEMO, 2020c; Joseph et al., 2022). The rate of earthquakes increased on the 5–6 April with the first banded tremor appearing on the 8 April (Joseph et al., 2022); the volcanic alert level was raised to 'Red', triggering an evacuation order for sections of the island (NEMO, 2020b; Joseph et al., 2022).

At 12:41 UTC on the 9 April 2021 La Soufrière started to erupt explosively, with multiple explosions occurring over the day. Over the following week the volcano continued to erupt, with pyroclastic flows, continuous venting, and ashfall over St. Vincent and on neighbouring Barbados (11 April 2021). Both the newly emplaced dome that had been growing since the beginning of the year and the 1979 dome and much of the previously existing crater floor were completely destroyed. This was confirmed by the first observations of the volcano summit from SAR images acquired on 10 April 2021 from ICEYE at 02:03 UTC (Fig. C.9) and Capella at 14:02 UTC (Joseph et al., 2022). Explosive activity ceased on 22 April 2021 at La Soufrière and the seismicity has remained low. The alert level was lowered to 'Orange' on 6 May 2021 (NEMO, 2020b; Joseph et al., 2022) and to 'Green' in March 2022.

4.2 Data and Methods

We develop a method that allows us to make measurements of new volcanic topography from single SAR backscatter images on the assumption that relative brightness derived from SAR backscatter range is proportional to the local topographic gradient. We make empirical estimations of the scaling factors and offsets required to map backscatter onto local slope and integrate along range lines to retrieve a relative height for each range pixel. We then apply a triangular mesh interpolation in radar geometry, including a smoothing factor and edge constraints, to estimate the full lava dome shape, before returning to geographic coordinates to calculate the dome volume and extrusion rates.

We exploit 32 SAR images from three sensors (TerraSAR-X, COSMO-SkyMed and Sentinel-1) acquired from Jan. 2021 to April 2021 (Table 4.1) to observe the dome growth at St. Vincent (Fig. 4.1). The acquisition of the high-resolution X-band data (i.e., CSK and TSX) was coordinated and supported by the CEOS Volcano Demonstrator, and output products were provided to UWI-SRC during the eruption to support monitoring efforts. For each sensor geometry we co-register the image to the first in the

dataset and multi-look to give the pixel range dimensions shown in Table C.2. Multi-looking reduces the contribution of speckle, which would otherwise introduce noise to our estimations of topography. We use the GAMMA-remote sensing software (Werner et al., 2000) to produce the backscatter images. We use a Digital Elevation Model (DEM) constructed from three 2014 Pleiades images (2 m pixels) and 2018 Copernicus DEM (30 m pixels) (Grandin and Delorme, 2021) to calibrate our estimations of relative brightness and act as reference points for the height profiles extracted from SAR cross sections.

Table 4.1: SAR acquisitions used to monitor St. Vincent Dome growth

Acquisition Date	Sensor	Acquisition Date	Sensor	Acquisition Date	Sensor
31 Dec. 20 22:19	[1]S1	24 Jan. 21 22:19	TSX_a	09 Mar. 21 22:19	TSX_a
02 Jan. 21 22:19	[2]TSX_a	30 Jan. 21 22:18	S1	13 Mar. 21 22:18	S1
08 Jan. 21 22:10	[3]TSX_b	04 Feb. 21 22:19	TSX_a	19 Mar. 21 22:18	S1
12 Jan. 21 22:19	S1	05 Feb. 21 22:19	S1	20 Mar. 21 22:19	TSX_a
13 Jan. 21 22:19	TSX_a	10 Feb. 21 22:10	TSX_b	25 Mar. 21 22:19	S1
17 Jan. 21 21:38	[4]CSK_a	11 Feb. 21 22:18	S1	31 Mar. 21 22:18	S1
18 Jan. 21 21:38	CSK_a	15 Feb. 21 22:19	TSX_a	31 Mar. 21 22:19	TSX_a
18 Jan. 21 22:18	S1	17 Feb. 21 22:18	S1	06 Apr. 21 22:19	S1
19 Jan. 21 22:10	TSX_b	23 Feb. 21 22:18	S1	07 Apr. 21 21:38	CSK_a
22 Jan. 21 21:32	[5]CSK_b	01 Mar. 21 22:18	S1	08 Apr. 21 21:38	CSK_a
24 Jan. 21 22:19	S1	07 Mar. 21 22:18	S1		

[1]Sentinel-1 Descending; [2]TerraSAR-X Descending 085; [3]TerraSAR-X Descending 039
[4]COSMO-SkyMed S2_17 Ascending; [5]COSMO-SkyMed S2_25 Ascending

The SAR backscatter (σ_0), describes the radar pulse scattered back towards the sensor by the ground surface and is affected by local gradient, surface roughness and dielectric properties. We use calibrated SAR backscatter intensity images, rather than the raw intensity images (I_0), these two quantities are related by $I_0 = k\sigma_0$, where k is the calibration constant of the SAR system. For our dataset, we assume that local incidence angle is the dominant contributor to the backscatter signal. Slopes facing towards the satellite are foreshortened, meaning there are more returns per ground unit, whereas slopes facing away are lengthened and have fewer ground returns. When the local incidence angle of slopes is greater than the satellite incidence angle, we observe layover for slopes facing away and shadows for slopes facing towards the sensor. In a SAR image a radar shadow appears as a gap in data where no returns are recorded. Regions of layover do return radar signals, but each radar unit receives returns from multiple locations at the same radar range, producing a layered image that results in ambiguity in the location of the reflectors.

4.2.1 Topographic Change from SAR Backscatter

Estimation of Relative Brightness

SAR backscatter is dependent on sensor parameters that vary between sensor.We therefore estimate scaling factors that describe how relative brightness relates to topography. We estimate this factor for each image by comparing an area where topography was unchanged to simulated backscatter (σ_s) calculated from the pre-eruptive DEM using a Lambertian backscatter model. For most datasets this was the 1979 dome, (Fig. 4.1) but for the lower-resolution Sentinel-1 we incorporated areas outside the 1979 dome to increase the number of data points. We then apply an iteratively reweighted least squares method to determine the best linear scaling factors (m, c) between the simulated backscatter, σ_s, and the real backscatter values, σ_0. These scaling factors vary between sensors due to different (1) levels of noise present, (2) calibrations of sensors, and (3) satellite geometry and parameters (i.e., wavelength). Finally, we apply these factors to the whole image (including where topography has changed) to estimate a relative backscatter ($\sigma_r = m\sigma_0 + c$).

Although no radiation is scattered back to the sensor from shadows, they still have non-zero σ_0 values introduced by thermal noise and residual radiation from sidelobes. We therefore mask out the data gaps caused by radar shadows using a threshold estimated from the maximum backscatter within a known shadow in each SAR dataset (e.g., from La Soufrière crater wall, Table C.2).

Retrieval of Topography along Range Lines

Based on the assumption that the local incidence angle is the dominant scattering property of the radar backscatter signal, we can express this in terms of the gradient of topography, h, in radar (slant range) geometry,

$$\sigma_r \propto h\delta \tag{4.1}$$

where δ the range pixel spacing. A relative brightness of 1 implies flat topography, while values > 1 are caused by slopes that face the satellite and < 1 are caused by slopes facing away (Fig. C.1).

To calculate h from σ_r we need to integrate along each range line. Explicitly, we calculate relative height (ε_i) with respect to the first point, set to 0, for the i^{th} point along a line in range by,

$$\varepsilon_i = \varepsilon_{i-1} + \delta(\sigma_r - 1) \tag{4.2}$$

following similar methods outlined by Taud and Parrot (1995) and Paquerault and Maitre (1998). This equation is valid provided there is no layover or radar shadows (Appendix Text C.1). To mitigate the gaps in data caused by radar shadows, we use

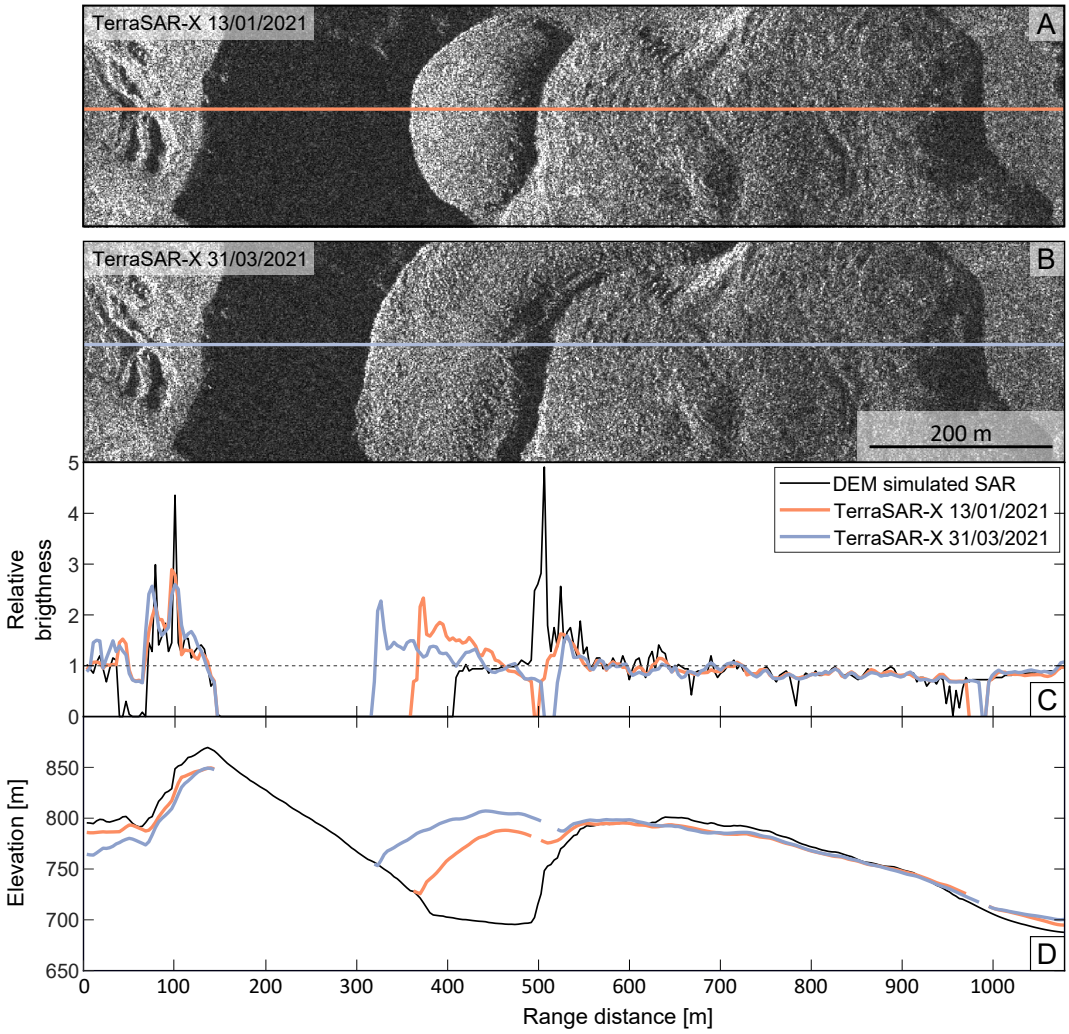

Figure 4.2: Topography extracted for radar backscatter range line. TSX images (a) 13/01/2021 and (b) 31/03/2021 with cross-section lines over the 2021 dome. The growth of the 2021 dome can be seen in (c) the radar backscatter range line cross-sections with the corresponding simulated SAR signal produced from the DEM (black line) and (d) the retrieved topography for all cross-sections shown in (c). Zero values (c) and gaps in data (d) correspond to radar shadow locations.

the width of the shadow in the SAR range line and calculate the corresponding shift in height, Δ_H, for each radar shadow present in the cross-section:

$$\Delta_H = W_{range} \cos\theta \tag{4.3}$$

where W_{range} is the width of the shadow in radar geometry and θ the incidence angle, (Fig. C.1d). We then apply this correction Δ_H to all of the heights following that radar shadow.

Because we apply the summation independently on each range line, inconsistencies

between consecutive range lines can give rise to apparent 'jumps', typical of topographic maps derived from radarclinometry methods (Wildey, 1986; Guindon, 1990). Differences between the shape of our relative height profile and the true topography can be introduced by layover, inadequate estimate of scaling factors, speckle or by changes in backscatter caused by differences in roughness or dielectric constant. We therefore estimate a best-fit vertical adjustment by masking out the 2021 dome and comparing the shape of the our relative height profile with the pre-eruption DEM along the same line in range. Until this point, we have not made any mitigation for the influence of layovers in our estimated profiles. To accurately calculate the vertical shift, we apply a layover mask constructed from the pre-eruption DEM. We then use the DBSCAN clustering algorithm (Ester et al., 1996) to determine the different clusters between the two profiles and then calculate the linear gradient, so that a value of 1 would indicate a perfect match between our estimations and DEM topography. We select the cluster with a linear gradient closest to 1 and use the corresponding y-intercept, y, to shift our relative height profiles, so that best estimate of the new topography, d_{topo}, takes the form $d_{topo(i)} = \varepsilon_{i-1} + \delta(\sigma_r - 1) + y$, neglecting corrections for any shadows.

Inversion for Dome Shape

	Shadow Threshold		Triangular Mesh size	
Sensor	Backscatter [σ_0]	Backscatter [dB]	Radar [m]	Geographic [m]
COSMO-SkyMed	5.5×10^4	47	15–28	25
TerraSAR-X	1.3×10^3	31	18–26	25
ALOS-2 (HH)	1.0×10^{-2}	-20	43–38	40
ALOS-2 (HV)	4.0×10^{-3}	-24	43–38	40
Sentinel-1 (Asc)	2.0×10^{-2}	-17	47–70	40

Table 4.2: Shadow threshold and triangular mesh size used for the various sensors applied to the 2021 St. Vincent dome.

To construct a complete dome surface from the multiple topographic profiles along range lines we divide the outline of the SAR dome into a regular triangular mesh and solve for the height of each node, assuming that the topography changes linearly across each triangle (Fig. 4.3). The resolution of the constructed mesh is lower than the original heights estimated from the SAR images so that multiple height estimations falls into a single triangle (Table 4.2). This smooths the small-scale variations originating in backscatter noise and bridges areas where there are gaps in height measurements (e.g., radar shadows). Using the topographic profiles in range, d_{topo}, and the DEM height values for the edge of the dome, d_{edges}, the system of equations for this model can be written as,

$$\left[h\right] = (G^T W^{-1} G)^{-1} G^T W^{-1} d \tag{4.4}$$

$$G = \begin{bmatrix} G_{sar} \\ K^2\nabla^2 \\ G_{edges} \end{bmatrix} W = \begin{bmatrix} r_1 & 0 & \cdots & 0 \\ 0 & r_2 & \cdots & 0 \\ \cdots & \cdots & \cdots & \cdots \\ 0 & 0 & \cdots & r_n \end{bmatrix} d = \begin{bmatrix} d_{topo} & 0 & d_{edges} \end{bmatrix} \tag{4.5}$$

where h are the unknown height observations for the triangular vertices; the design matrix (G) is constructed from G_{sar} (1×number of vertices), the matrix of interpolated kernels representing the shape function (Wang and Wright, 2012) for each height observation; ∇^2 is the Laplacian smoothing operator (1×number of vertices) with an umbrella smoothing factor, K^2; G_{edges} is the matrix that contains a weighted edge constraint (1×number of edge vertices). For the smoothing factor, K^2, used in our Laplacian operator, we apply a small value ($K^2 = 0.5$) to minimally smooth the structure but remove any large artifacts otherwise introduced over data gaps. Further to avoid smoothing of the dome beyond where we know its edges to be, we include edge constraints (G_{edges}) that indicate where we are confident about location the dome edge (d_{edges}), and elevations can be taken from the DEM in radar geometry. To reduce the contribution from range lines that were particularly distorted through radar layovers (e.g., large difference on stable topography, upper section of Fig. 4.3b), we apply a weighting matrix (W) to our system to reduce the influence from these particular lines. The weighting matrix is constructed using the RMSE between each range line and the corresponding pre-existing DEM line ($r_1, r_2, \ldots, r_n$), with the new dome masked out. Profiles that deviate from the known topography will produce larger values, which are then accordingly down weighted in Eq. 4.4.

After solving for a smooth continuous mesh of dome heights in radar geometry (Fig. 4.3c), we translate our new elevation maps back into geographic coordinates. To do this, we return our triangular mesh back into range lines and convert the coordinates of each line into Cartesian geometry (Text C.1, Eq. C.1). We use a look-up table to geographically locate the start and end of each line.

As we used multi-looked images for the SAR height extractions, when we translate the individual range line back into their geographic coordinates it results in gaps in heights between lines. We apply a second triangular mesh in geographic coordinates to bridge these data gaps and fully construct the dome geometry without any additional weighting, smoothing, or constraints. By comparison to the original pre-eruption DEM, we can then calculate the dome heights and bulk volumes for each SAR image (Fig. 4.3d-f, 4). We keep our final volumes as bulk volumes rather than calculate the dense-rock equivalent (DRE), as we do not have the appropriate information about the vesicularity and void space of the dome. For a more complete description of the method

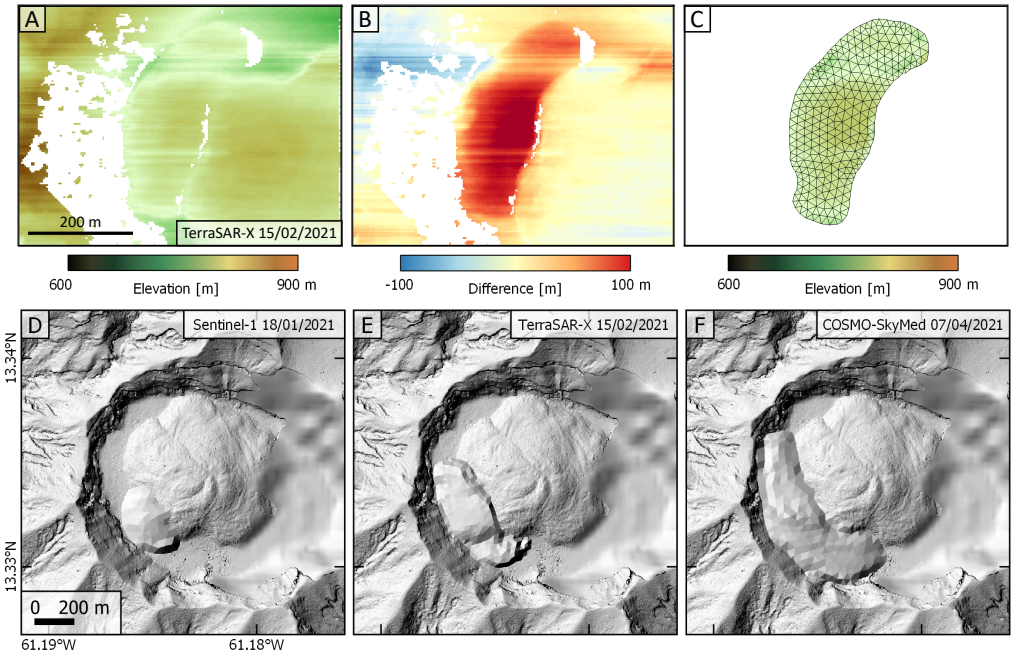

Figure 4.3: TerraSAR-X 15/02/2021 backscatter image showing (a) the range line retrieval of topography over the 2021 dome, (b) the difference between the extracted height from SAR and the pre-eruptive DEM. This clearly shows the emplacement of the new dome. (c) triangular mesh interpolation overlaying the range line in radar geometry. Examples of (d-f) the final dome shapes shown as shaded relief maps from various sensors between January and March 2021, and (g-i) the original SAR baskscatter images used to estimate the dome topography. Note (a-c) are shown in the original side-looking geometry of the satellite, radar geometry (range × azimuth), rather than in geographic coordinates (latitude and longitude)

see appendix text C.1 and figures C.1–C.3.

4.2.2 Estimation of Extrusion Rates and Uncertainties

Using our dome bulk volumes estimates, we calculate extrusion rates between pairs of images that have the same geometry. We do this separately for each sensor to avoid introducing uncertainties associated with combining different sensor resolutions and geometries. We consider the largest sources of uncertainty in our estimates to be the systematic effects of radar layover, which introduce distortions to the topographic profiles retrieved, and vary between satellite geometries. The error bars in Figure 4.4 therefore show the error in the final dome volumes estimated as the percentage of the new dome that we expect to be affected by layover (an estimate which depends on the accuracy and resolution of the pre-eruption DEM). While there are also uncertainties in our estimations of topography caused by noise in backscatter images, we are able to mitigate these to some extent by multi-looking and by smoothing our data during interpolation to a triangular mesh.

4.2.3 SAR Pixel Offset Tracking

We also make pixel offset tracking estimates of surface displacements in both range (i.e., perpendicular to the satellite track direction) and azimuth (i.e., parallel to the satellite track direction) using pixel-based cross-correlation. Whilst InSAR methods are able to measure surface displacements between acquisitions with centimetre accuracy (e.g., Delgado et al., 2017; Moore et al., 2021), they require stable ground surface scatterers, otherwise the data become completely decorrelated. In contrast, pixel offset tracking can measure larger surface movements (i.e., metre-scale) without the use of SAR phase (e.g., Wang et al., 2015; Schaefer et al., 2017) using pixel-based cross correlation between the backscatter signals of the two images. The two SAR images used are required to be precisely co-registered, as the accuracy of the pixel offset measurements are strongly dependent on the image co-registration. This method only works if changes are relatively small.

We apply pixel offset tracking to two 1-day X-band COSMO-SkyMed (CSK) pairs to detect short-term dome growth during the early phase and immediately before the eruption transitioned from extrusive to explosive. Based on the large perpendicular baseline between our 1-day CSK image pairs (564 m and 2411 m), we apply a co-registration that makes use of a look-up table formed between the SAR images and the DEM in radar geometry based on the primary SAR image. For higher-resolution systems with large baselines, this method has the advantage that it incorporates topography-related offsets in the lookup table and applies them during the co-registration. We use a small cross-correlation threshold of 0.05 to remove some of the obvious outliers from the offset results. We found that a large cross-correlation window with steps of about a third of the window size (i.e., 100×100 pixels window and 32×32 step size) maximises the spatial coverage of the dome offsets for CSK and returned appropriate offsets across the dome. Nevertheless, measurements were not possible over the centre of the dome, where surface changes were too large. Pixel offset maps produced from 7 pairs of TerraSAR-X (TSX) images were sparser, with a less-distinct offset pattern (Fig. C.8) and higher uncertainties. The difference between the TSX and CSK offset tracking quality is mainly the result of the longer time intervals for the TSX dates (11 days) that capture a longer growth period where the dome appears significantly different.

4.3 The 2021 Dome Growth at La Soufrière, St. Vincent

The gradual growth of the 2021 dome, including changes in morphology and surface texture, is observable directly from individual SAR images (Fig. C.4–C.6). The 2021 dome gradually changed from uniform central growth to laterally spreading around the 1979 dome. From February 2021 we can observe the development of fractures at either end of the 2021 dome (Fig. C.5-C.4) and visible bulging in the center in April 2021

(Fig. C.4).

Our analysis has enabled us to estimate dome volumes and extrusion rates from the 32 CSK, TSX and Sentinel-1 SAR images spanning the dome-growth phase (Fig. 4.4). This allows us to examine patterns in extrusion rates for the dome over the three and a half months in early 2021 before the eruption transitioned from extrusive to explosive on 9 April 2021.

4.3.1 The Dome Growth Phase

To characterise the main dome-growth phase at La Soufrière from Dec 2020 to March 2021, we use a total of 29 SAR backscatter images (Fig. 4.4). The dome at La Soufrière showed steady growth with extrusion rates of ∼0.5–5 m^3s^{-1} from December 2020 to March 2021 (Fig. 4.4b). There is some indication in our data that extrusion rate varied over short time scales, for example, with shorter timespan image pairs (e.g., CSK 1-day pair dates) recording the highest rates; however, the extrusion rate recorded over intervals > 10 days is remarkably consistent (Fig. 4.4). Our data are well explained with a constant rate of ∼1.8 m^3s^{-1} from the first appearance of the dome until 7 April 2021, two days prior to the eruption. Our independent measurements of extrusion rate are consistent with those presented by Stinton (In Prep.), who found extrusion rates that varied between 0.95 and 2.65 m^3s^{-1}, with a long term average of 1.85 m^3s^{-1} from 12 sets of photogrammetric measurements made from locations along the rim of the summit crater, UAVs, and helicopter and fixed-wing aircraft overflights.

4.3.2 Pre-explosive Phase Increase in Extrusion Rate

At the beginning of April 2021, the dome continued to grow laterally around the older 1979 dome without any significant change in rate. However, from the SAR data, we observed a major change in extrusion rate in the days prior to the transition from extrusive to explosive. There was a sudden increase in extrusion rate from ∼1.8 to 17.5 m^3s^{-1} some time between 21:38 UTC on 7 April and 21:38 UTC on 8 April, when the SAR images were acquired (Fig. 4.4c). The rapid increase in extrusion rate is confirmed by images of rapid inflation acquired by a remote camera on the crater rim (Joseph et al., 2022). If we assume this new, higher rate was constant during the few days prior to the onset of explosive activity, then the transition to higher-rate extrusion would have occurred on 7 April 2021, just after the onset of rapid dome inflation as observed by a remote camera (Joseph et al., 2022). Our final dome volume calculated from a CSK image acquired at 21:38 UTC 8 April, approximately 15h before the first explosions were recorded (12:41 UTC 9 April 2021), was 18.5 million m^3, slightly higher than the estimate of final dome volume made by Stinton (In Prep.) of 16 million m^3 by extrapolating a constant extrusion rate of 1.85 m^3s^{-1}. Using the increased extrusion rate from the 8 April CSK image, we extrapolate the dome volume from 8 April to the

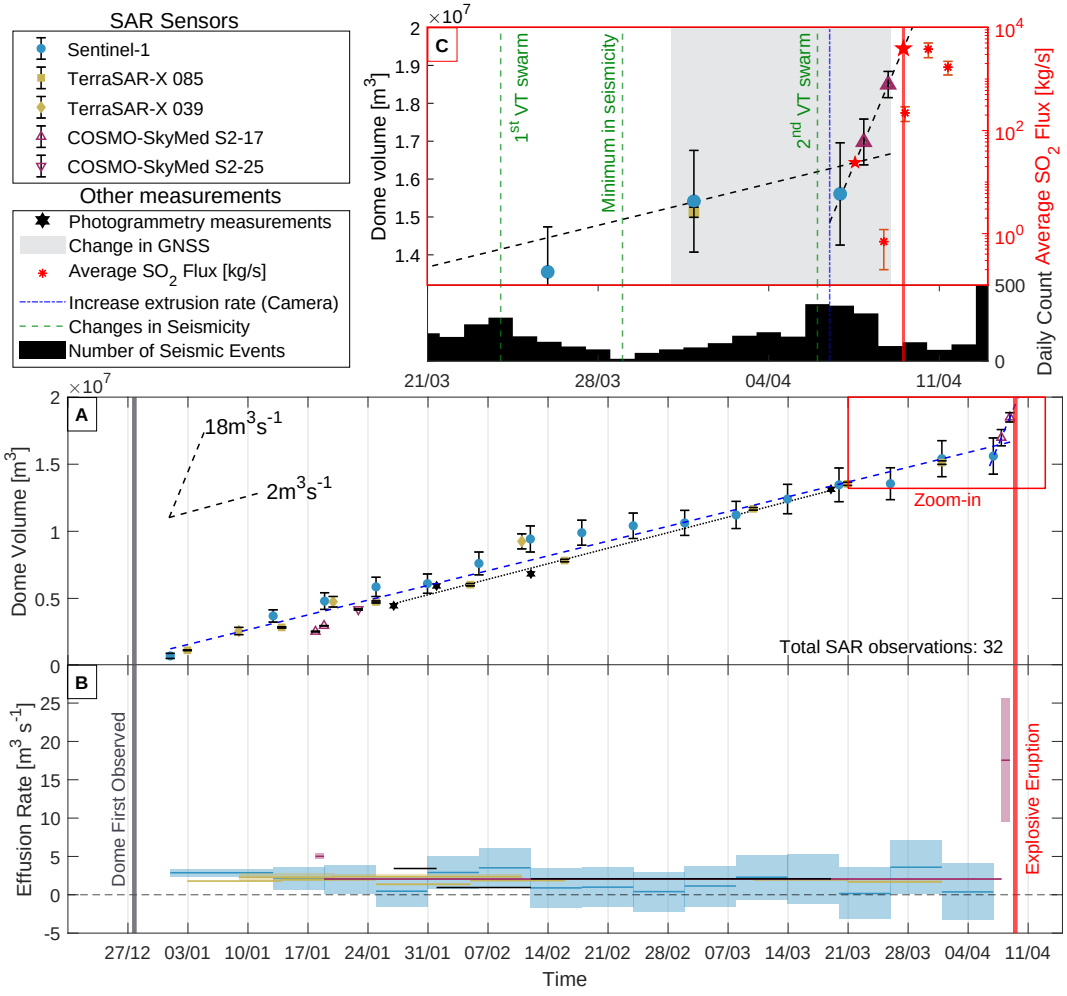

Figure 4.4: Timeseries of (a) cumulative bulk volumes (black dashed and blue dotted lines represent the average extrusion rate for SAR backscatter and photogrammetry respectively) and (b) time-averaged extrusion rates of the dome at La Soufrière between Dec 2020 to April 2021 extracted from SAR backscatter data. The SAR backscatter data extend the photogrammetry observations showing the sudden increase in dome volume and extrusion rate in the days prior to the transition from extrusive to explosive eruption. Insert (c) zoomed timeseries of the two weeks prior to the eruption, with important changes seen in other dataset (i.e., seismicity, SO_2 emissions, GNSS, visual observations). SO^2 fluxes measured by TROPOMI, from Esse et al. (In Press).

time of the first explosive eruption (12:41 UTC 9 April 2021), to estimate a final dome volume of 19.4 million m^3. The first post-explosion SAR image, acquired on 10 April 02:03 UTC by ICEYE, showed the complete destruction of the new dome (Fig. C.9).

The 1-day CSK pixel offset tracking over the 2021 dome showed displacements within the dome itself and no significant changes elsewhere in the summit crater (Fig. 4.5). During the initial dome growth phase from 17-18 January 2021, we observed localised movements (maximum offset of ~9m) centred around 13°19'56"N 61°11'08"W, which we estimated to be the location of the vent (Fig. 4.5c). The image from 8 April

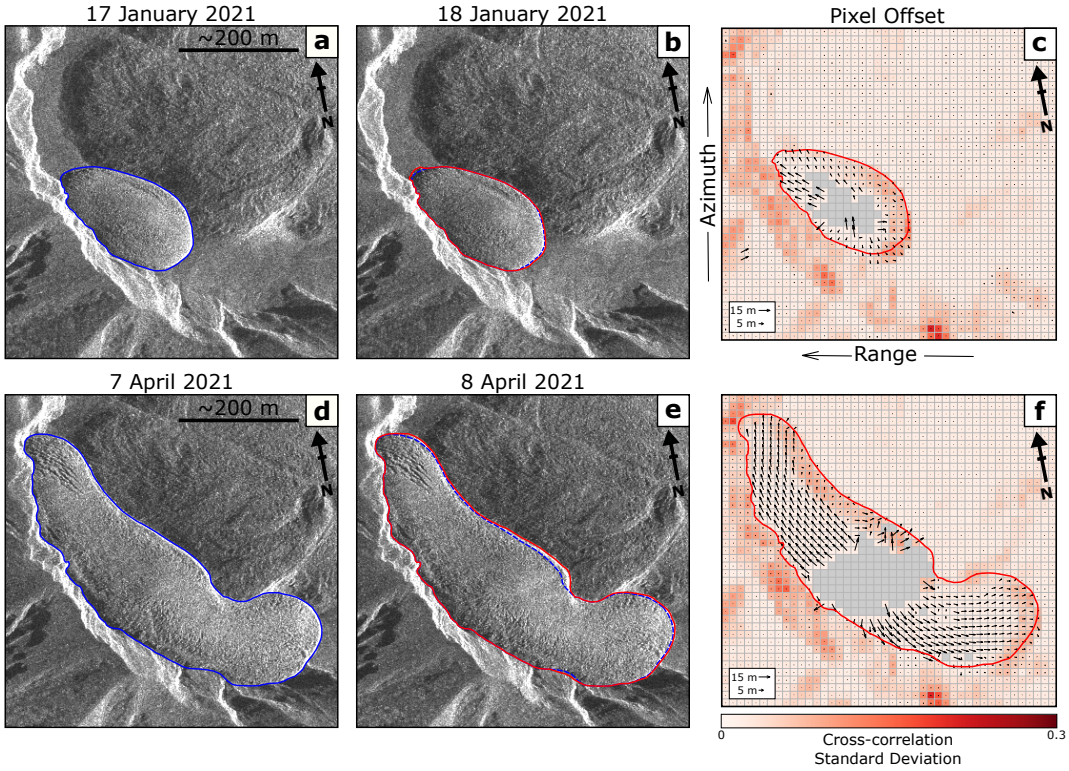

Figure 4.5: COSMO-SkyMed (CSK) pixel tracking maps. Radar backscatter images from (a) 17 January, (b) 18 January, (d) 7 April and (e) 8 April with dome outlines in blue (1^{st} date) and red (2^{nd} date). (c) and (f) Pixel tracking maps for (c) January and (f) April overlain on cross-correlation standard deviations. Arrows show the direction of surface displacement in range and azimuth direction, and grid represents the step window used (CSK, 32×32). Location of images is shown in Fig. 4.1H.

2021 showed displacements away from the same centre point and extending over whole dome (maximum measurable offsets of ∼15m, Fig. 4.5f). The order-of-magnitude increase in extrusion rate could not be accommodated by the continued growth of the dome along the central axis of the coulee (e.g., Fig. C.5) but can be seen bulging around the vent location on 7-8 April. Displacement in this area exceeds the threshold measurable with pixel offset tracking. From our dome measurements, the dome grew by 10 m in the central section of the dome during this 24 hour period.

4.4 Discussion

4.4.1 The Transition from Effusive to Explosive at St. Vincent 2021

The sudden increase in dome volume and extrusion rate seen at St. Vincent in the days prior to the start of the explosive phase suggests that the transition was driven by changes in the magmatic system (a 'bottom-up' process). We see no evidence in the pre-eruptive SAR imagery of dome collapse up to 15h before the eruption. However,

the sudden increase in dome volume between 7 and 8 April 2021 does correlate with other evidence of rapid dome inflation in backscatter images: (1) increased fracturing, (2) surface displacements > 15 m, and (3) a bulge surrounding the vent (Fig. 4.5).

Independent evidence of a magmatic change that preceded the transition to explosive activity on 9 April include (1) a change in volcano-tectonic earthquakes beneath the volcano on 5-6 April (Thompson et al., 2022) (2) a transition from only hydrothermal signatures in the plume to first detection of SO_2 on 8 April from both TROPOMI and a coastal traverse with UV Spectrometer and MultiGAS instruments (e.g., Joseph et al., 2022; Esse et al., In Press), (3) banded tremor and incandescence, both first observed on 8 April (Joseph et al., 2022), and (4) ash venting from fractures in the rapidly inflating region on the 2021 dome.

The high volume of extruded material (16.4 million m^3) up to 7 April and constant extrusion rate indicates the steady removal of older material from a combined conduit and established magma reservoir, where the loss of material does not result in a discernible pressure decay. The subsequent increase in extrusion rate to 17.5 m^3s^{-1} could be consistent either with the addition of new magma to the system in April 2022, or as proposed by Joseph et al. (2022)'s conceptual model, a gas-rich magma injected earlier in the eruption (between December 2021 and April 2022) that had been slowly pushing up older material from the 1979 eruption before finally breaking through this degassed, viscous cap. By the 7 April we observed changes in the SAR backscatter that indicated a sudden increase in dome volume as the last of the old, degassed material (we estimate 3 million m^3 between the 7-9 April, 15% of the total extruded volume) was erupted. Shortly after, the first detection of SO_2 on 8 April indicating that the SO_2 reached the critical threshold to force its way to the surface, finally triggering the 9 April eruption.

4.4.2 Potential for Application to Future Eruptions

Our method for extracting topographic profiles and thus extrusion rates from SAR backscatter has potential to be a powerful monitoring tool. Extrusion rate is typically one of most challenging geophysical parameters to obtain safely during an eruption, requiring either in-situ measurements near vents or clear conditions for overflights. Volume estimates made from radar satellites have important potential for densifying extrusion-rate timeseries where photogrammetry is possible when conditions allow (as for the 2021 St. Vincent eruption), and for tracking otherwise unobservable eruptions where it is not.

However, the usefulness of results depends on (1) the accuracy of our underlying assumption that σ_0 is primarily controlled by topography, (2) satellite radar image resolution and geometry relative to the new volcanic topography, and (3) the quality and resolution of the pre-eruption DEM used to identify areas of shadow and layover.

Our assumption that local topographic gradient was the primary control on backscatter is justified only where surface roughness and dielectric proprieties are relatively steady. We can correct for these effects where variations are uniform across the structure. For the lava dome at La Soufrière, we assumed that the surface roughness of the new dome was uniform across the dome and through time; however, this was not the case for other parts of La Soufrière's crater. For example, we observed that σ_0 on sections of the 1979 dome adjacent to the 2021 dome decreased over the course of the eruption a change that we attribute to the removal of vegetation caused by the emission of gases from the growing dome (Fig. C.7).

To explore the accuracy of our method, we use synthetic topographic cross-sections to test the impact of varying incidence angle and the local incidence angle (Fig. C.2). We found that radar layovers had a greater impact on the accuracy of the retrieved topography than radar shadows, which can be easily identified from backscatter images. The edges of regions of layover are harder to identify in backscatter, and since topographic change is unknown for real data, cannot be reliably predicted. In the synthetic models, a single section of radar layover would skew the final profile shape, but our correlations meant that the overall height estimations were similar to the original profile. When a layover interacted with a radar shadow, however the estimated topography would include distortions and differ significantly from the original synthetic cross-section (Fig. C.2). The distortion introduced by the layovers in our estimations of topography is under constrained and cannot be corrected. In this dataset, these effects are most significant during the early period of dome growth, when the edges are relatively steep and not constrained by the surrounding topography. Lower incidence angles produced greater areas affected by radar layovers, and we found that an ALOS-2 ascending track and the Sentinel-1 descending track (that ultimately did not contribute to our results) were less successful in retrieving the dome heights because of smaller incidence angles, 37° and 31° respectively. We consider layover to be the largest source of uncertainty in our results, especially for the descending tracks as the 2021 dome grew into the layover cast from the crater wall, concealing the backscatter signal from the dome (Fig. C.3).

4.4.3 Recommendations for SAR Acquisitions

The different SAR datasets covering the 2021 dome growth at St. Vincent allowed us to test how different sensor polarisations and resolutions affected our estimations of topography. We found that unmitigated speckle greatly increased the noise in our retrievals of topography. The higher-resolution sensors allowed us to multi-look and apply speckle corrections to the images while retaining high spatial resolution (CSK 1.5×2.8 m pixels at 4×4 looks, range by azimuth and TSX 3.6×5.1 m at 4×4 looks, range by azimuth). Although the multi-looked Sentinel-1 images (9.3×14.0 m at 4×1

looks, range by azimuth) were much lower resolution, the frequent acquisitions and multiple tracks covering the dome-growth period provided a denser temporal spacing for extrusion rate estimations and allowed a much denser timeseries than possible from X-band alone. We also found that the Sentinel-1 cross-polarisation images (i.e., VH) produced less accurate topographic estimations, presumably due to their greater sensitivity to volume scattering and therefore vegetation (Patel et al., 2006).

The ideal SAR imagery for estimation of topography from backscatter is therefore (1) single polarisation, (2) a geometry that minimises shadow and layover, and (3) acquired as frequently as possible. In practise, this is most likely to be achieved for any individual eruption by analysis of a constellation of different SAR instruments. The most appropriate geometry for tasking is especially hard to predict in advance of an eruption, as the shape of new topography determines to a major extent the locations of shadow and layover. Volcanic craters, domes with steep sides, and flows that fill steep valleys are all likely to be bounded by zones of shadow and layover, so although this source of uncertainty can be minimised by choice of geometry, it is unlikely to be eliminated.

4.5 Conclusion

Our approach to estimating topography directly from satellite radar backscatter was successful for 5 different geometries and has potential for future monitoring of volcanic topography and therefore extrusion rate. We found that high-resolution, single-polarisation imagery with small areas affected by layover (i.e., larger incidence angles) resulted in the most reliable dome-volume estimates.

By combining 32 SAR images from multiple sensors (TerraSAR-X, TSX; COSMO-SkyMed, CSK; and Sentinel-1), we were able to estimate a dense timeseries of dome volumes and extrusion rates for the 2021 dome growth at La Soufrière. Extrusion was relatively stable between December 2020 and March 2021, with an average extrusion rate of 1.8 m^3 s^{-1}. By 7 April 2021, extrusion rate increased by an order of magnitude to 17.5 m^3 s^{-1}, before the explosive phase on 9 April 2021, 15 hours after our last SAR measurement. The final dome volume measured from SAR data was 18.5 million m^3 with a maximum height of ∼140 m. This increase in extrusion rate is consistent with an incursion of gas-rich magma into the conduit, which then led to the explosive phase of the eruption.

Chapter 5

Discussion and Conclusions

This thesis has investigated through three different eruption settings the utility of SAR backscatter for detecting explosive deposits (e.g., pyroclastic density currents, lahars and ash), effusive processes (e.g., lava flows) and quantifying topographic changes (e.g., dome growth and lava lake levels). We examined different approaches to extract small magnitude changes in SAR backscatter, ranging from simple spatial filters (e.g., multi-looking and speckle filters), to using long-term SAR backscatter signals (e.g., step estimation maps, Fig. 2.6) and removing systematic sources of noise (e.g., PCA-correction, Fig. 3.2). In addition to observing changes in SAR backscatter, we demonstrate how it can be used to extract quantitative information about topography (e.g., dome growth, Fig. 4.4) and changes in deposit (e.g., pyroclastic density currents, Fig. 2.8) or feature (e.g., lava lake, Fig. 3.9) heights. Through this thesis, I hope to have demonstrated that SAR backscatter, although complex, can be an appropriate tool for monitoring a range of volcanic settings.

In this chapter, I first summaries the outcomes of each eruption case study I presented in thesis (Section 5.1), before discuss the possible future advancement of SAR backscatter (Section 5.2) for volcano monitoring, and how the methods here could be optimised for monitoring ongoing volcanic eruptions (Section 5.3).

5.1 Developments in Analysing SAR Backscatter

5.1.1 Monitoring Volcanic Eruptions

Observations of volcanic eruptions are crucial for monitoring as they provide information about the dynamics of an eruption and provide constraints for modeling behaviour. With the increase of SAR sensors in orbit, SAR backscatter is well situated for observing volcanic eruptions. I presented observations spanning a range of eruption styles to demonstrate potential tools for distinguishing different deposits through time from

high-resolution SAR backscatter.

For the explosive eruption at Volcán de Fuego in 2018, I found that producing the change difference maps by solving for a step change over multiple (>2) images allowed for better identification of explosive deposits and internal flow structures (e.g., surge deposits, overbanking). Further, by visualising the full dataset, through backscatter confusion grids, I was able to show temporal patterns that would be related to gradual post-eruption erosion processes (e.g., gradual drying of ground deposit) that were missed in other methods and the potential to identify periods of high lahar activity. The SAR backscatter dataset over Volcán de Fuego demonstrated the capability of SAR backscatter has for distinguishing between different explosive deposits (i.e., pyroclastic flow, lahar and ash), especially when other datasets are limited either by cloud coverage (e.g., optical) or vegetation coverage (e.g., phase coherence).

In contrast to explosive eruptions, effusive eruptions can last much longer periods of times. For lava flow mapping, SAR backscatter data can provide an independent supplement to optical imagery and flow maps from phase coherence. I found that SAR backscatter could map out the emplacement of lava flows well over the old flow field, with the potential to correctly identify the lava flow over vegetation. I also presented multiple timeseries that demonstrate the complexity of the SAR backscatter signals and the potential to examine flow recovery. Although, the methods presented here still require further work before being applied monitoring purposes, SAR backscatter could supply information about ongoing activity and cooling of flows, especially as the ground becomes incoherent when a lava flow is emplaced. SAR backscatter has the additional benefit that each acquisition can provide detail about how the ground surface look like at that point in time, rather than a sum of change from the previous image.

Having a snapshot of how the ground looked at a specific point in time, meant that I could examine activity for the 2011 Pu‘u ‘Ō‘ō lava lakes in detail. I found that automatic detection of lava lakes is challenging, as SAR backscatter signals show large variations over lava lakes. The 2011 lava lakes generally appeared as areas with low SAR backscatter with minimal internal variations. However, this is not the case for all lava lakes. The 2020 lava lake that infilled Halema’uma’u crater showed much more internal variations in SAR backscatter, which seemed to correlate with observed variations in the surface temperature. The primary difference between the these lava lakes is that the 2011 Pu‘u ‘Ō‘ō lava lakes was significantly smaller than the 2020 Halema’uma’u lava lake. This difference in affected area allows for more variation in activity across Halema’uma’u lava lake that result in discernible details in the surface structure.

It is important to note that all SAR imagery is limited by the sampling spacing of the acquisitions. For most of the eruption at Volcán de Fuego, I could not identify deposits related to a single process as on average there was 7 days between CSK ac-

quisitions. This meant that we were observing changes in SAR backscatter associated with the emplacement of multiple processes and how they settled or were reworked over time. High-temporal frequency and background missions are therefore desirable for monitoring ongoing eruptions where the ground surface is changing rapidly day-by-day. During the 2021 dome growth of La Soufrière, the 1-day CSK pair acquired in the days (7 and 8 April) leading up to the explosive eruption (9 April), was crucial for capturing the change in extrusion rate leading up to the transition in eruption, from extrusive to explosive. In addition to high-temporal frequency, it is important to have comparable pre-eruption imagery. This is something the Sentinel-1 mission has been able to provide with almost global coverage every 12 days. At St. Vincent, Sentinel-1 was the only dataset with systematic pre-dome growth imagery. The first acquisitions with CSK and TSX were both in January 2021 following a couple of weeks of dome growth. To address this problem, groups such as the CEOS Volcano Demonstrator (Pritchard et al., 2018) are working on determining optimal SAR acquisition intervals and acquiring high-resolution SAR (TSX) background data currently for volcanoes in Africa, Latin America, and Southeast Asia. Although, this work is mainly motivated for ground deformation purposes, which means that tasking decisions are influence by environmental factors (e.g., dense vegetation) since that affects phase coherence, it is also very beneficial for SAR backscatter methods.

5.1.2 Quantifying Topographic Change

In addition to being able to observe the emplacement and development of eruptive deposits, being able to quantify these changes would constrain the progression of an eruption (e.g., effusion rates) or understanding how an eruption could affect subsequent hazards (e.g., blocked drainages diverting later flows).

Using changes in radar shadow widths to estimate relative change in height have shown to be useful for various volcanic deposits (e.g., Wadge et al., 2012; Arnold et al., 2017; Barrière et al., 2018; Moore et al., 2019). By attempting to use this method across the different volcanic settings for the eruptions looked at, I was able to test the limitations of the method and determine where it could work well.

The first thing to consider is the geometry of the feature casting the radar shadow. In the simplest scenario, if the satellite line-of-sight (LOS) is parallel to the structure on the ground then this method is not suited to measure changes in height, as no shadow is cast. This was the case for the drainage systems around Volcán de Fuego, where the main drainages were orientated almost parallel to the satellite LOS. There were only a handful of shadows along the drainage, and most were close to parallel to the LOS, meaning that changes in these shadows did not accurately represent the accurate thickness of the deposit.

At Pu‘u ‘Ō‘ō crater, I was able to further examine the interplay between the satellite and crater geometry and how this affected the results from the radar shadow method. I found that the most accurate measurements were calculated when the feature casting the shadow was close to perpendicular to the satellite line of sight (within 45°, Arnold et al., 2017). When the crater rim was <45° from the radar LOS, the radar shadow was not cast into the deepest section of the crater but along the steep rim wall. Further, the morphology of the crater also determines the accuracy of estimate heights. During the August 2011 eruption, the terrace-like collapse of the crater meant that it was not possible to estimate the complete change in depth. The satellite LOS was not the only parameter to consider, the width of the crater, and the satellite incidence angle set the maximum depth that is possible to observe. For a deep crater or collapse, the radar shadow can interact with the layover and underestimate the crater depth. The maximum depth that can be observed from SAR backscatter for a crater can be calculated from eq. 3.3.

As with most SAR backscatter methods, having an understanding of what you are looking at is important for the interpretation. The radar shadow method assumes that the shadow is being cast onto a flat piece of ground. In most situations this is not the case and by having an understanding of the ground morphology helps determine the accuracy of the estimates. For example, the uplift in the crater floor before the August 2011 eruption at Pu‘u ‘Ō‘ō crater and then the staggered collapse produces an underestimate in the calculated crater depth. While this bulging at Hawai‘i resulted in slight underestimation, in other settings this could produce completely inaccurate results. This is the case for the 2021 La Soufrière dome. I initially attempted to estimate dome heights from TSX data at St. Vincent using radar shadows. The 2021 La Soufrière dome interacted with two radar shadows; its own shadow that it was casting on the 1979 dome and intersecting the crater wall shadow on the other side. When using its own shadow, the height estimates were completely incorrect and not representative of the complete dome height, as the shadow is never complete and interacts with different sections of the 1979 dome. By measuring the interaction between the dome and the crater wall shadow, I was able to systematically underestimate the dome height. Similar to the bulging at Hawai‘i, the crater wall shadow here did not interact with the highest section of the 2021 dome. These estimates managed to capture the correct trend in dome growth but by overestimating the difference in height between the crater rim and the top of the dome, I was underestimating the true height of the dome. For a crater or lava lake with consistent geometry (no large collapses or overflows), this method could easily be automated to regularly calculate height measurements. I discuss the potential to make this method operational in section 5.3.2.

To estimate more accurate dome heights, I demonstrated in chapter 4, the capability of SAR backscatter for extracting quantitative measurements for a volcanic eruptions.

The method developed here successfully estimated the topography from individual SAR images, which could then be used to calculate extrusion rate for dome growth from five different radar geometries for the 2021 eruption of La Soufrière, St. Vincent. I found that by using multiple geometries, and comparing our volumes estimates to other datasets, that our method accurately estimated dome growth.

While the method was able to capture the overall 2021 dome growth of La Soufrière, there are a few assumptions and limitations to the method. I found that changes in the scattering properties and the setting of the target feature (e.g., lava dome) contributed the most to distortions in the retrieved topography profiles. This method is based on the assumption that the dominant scattering property was the local incidence angle with minimal changes to the other scattering properties (i.e., surface roughness and dielectric properties). Therefore, any changes in these other scattering properties would produce distortions in the topography retrieved from individual SAR profiles. A dome that grows on bare rock would be a simpler target to retrieve accurate topography from, compared to a dome in or next to a crater lake, where moisture contributes to the SAR signal.

If the target feature meets these conditions and the local incidence angle is the dominant scattering property, then the satellite geometry and the surface morphology become the main source of error when retrieving the topography. Artefacts introduced by the geometry of the satellite (e.g., layovers), produce gaps and distorted in the topography profiles based on SAR backscatter. For example, a steep-sided dome on a flat surface would produce its own radar shadow and layover. The same dome within a crater, which is a more typical location for a lava dome, would also interact with the distortions produced from the crater walls. At St. Vincent, I found that radar layovers introduced larger distortions in the retrieved profiles than the radar shadows. Therefore, imagery with minimal areas affected by layovers (i.e., large incidence angles) produce the most reliable dome-volume estimates.

Through the comparison between the different sensors, I showed that high resolution, single polarisation SAR backscatter imagery, ideally with large incidence angles, were best able to capture realistic dome shapes. This method is well situated to retrieve topography for lava domes as these are generally dominated by the local gradient with minimal influences from the surface roughness and dielectric properties but it could also be applied to retrieve height measurements for other volcanic processes such as cinder cones and andesitic or rhyolitic lava flows (e.g., Bagana or Sinabung). I discuss further possible developments and potential automation for this method in section 5.3.1.

5.1.3 Methods to Increase the Signal-to-Noise Ratio

SAR backscatter is an inherently complex and noisy dataset. The signal is the result of the strength of the surface scattering properties, and satellite parameters (e.g., wavelength and polarisation), along with contributions from speckle and influences from the satellite geometry. Depending on the eruption deposits examined, I found that applying different corrections and filters help to mitigate the noise signals unrelated to the changes scattering properties.

For large deposits (e.g., pyroclastic flows), I was able to spatially average the data, either simply by multi-looking the data (e.g., 4×4 multi-looked TSX data at La Soufrière) or applying a speckle filter (e.g., gamma_*MAP* filter for the CSK at Volcán de Fuego). These spatial filters are able to increase the strength of the signal at the cost of the spatial resolution of the data. Therefore, it is not always advisable to apply these types of filters when observing volcanic deposits. At Pu‘u ‘Ō‘ō crater, I decided to prioritise the resolution of the data, as the target signals related to the lava lake covered small spatial extent. The application of a spatial filter would have smoothed out, possibly removed, the detail I was trying to observe in the lava lake surface.

The side-looking nature of the satellite not only introduces distortions in the SAR imagery, but also causes the over- and under-saturation of slopes facing towards and away from the satellite. For volcanoes that have high relief, such as is common for stratovolcanoes, this can make it difficult to compare different flanks of the volcano. Doing a radiometric terrain correction (Small, 2011) using an accurate DEM, reduces this trend in the data and means that when looking at changes between SAR backscatter acquisition there is less contribution from variations in the local incidence angle. This would therefore help highlight the contribution of the surface roughness and dielectric properties.

Following the application of spatial filters, and doing a radiometric terrain correction, the strength of SAR backscatter signal is suitable to accurately differential changes between acquisitions with more certainty, especially for large magnitude changes (e.g., major pyroclastic density currents in Barranca Las Lajas, Volcán de Fuego, Fig. 2.6). However, for more subtle changes (e.g., ashfall or gradual edges of deposits), I found there was still a lot of variation in the SAR backscatter between acquisitions masking these signals. I demonstrated that by solving for a step change in a SAR backscatter pixel timeseries, with even as little as four images (Fig. 2.5) was able to improve the signal sufficiently to observe low magnitude changes and reduce the variance of the background signal.

Even following after filtering and correcting the SAR dataset, the patterns in the changes of SAR backscatter through time can be complex. I showed for the 2018 deposits at Volcán de Fuego (Fig. 2.4) that understanding the pre-eruptive land cover is

important to correctly interpret how the deposit has changed the ground. For example, ash deposits on Volcán de Fuego produced opposite change directions over vegetation and agricultural fields, as a result how the scattering properties were changed (e.g., increased or decreased the surface roughness).

Specifically for COSMO-SkyMed, I observed a repetitive signal in the SAR backscatter related to the satellite that acquired the image. This particular signal was clearly visible in the Hawai‘i dataset due to the high-temporal resolution of all four CSK satellites and the relatively steady climate.

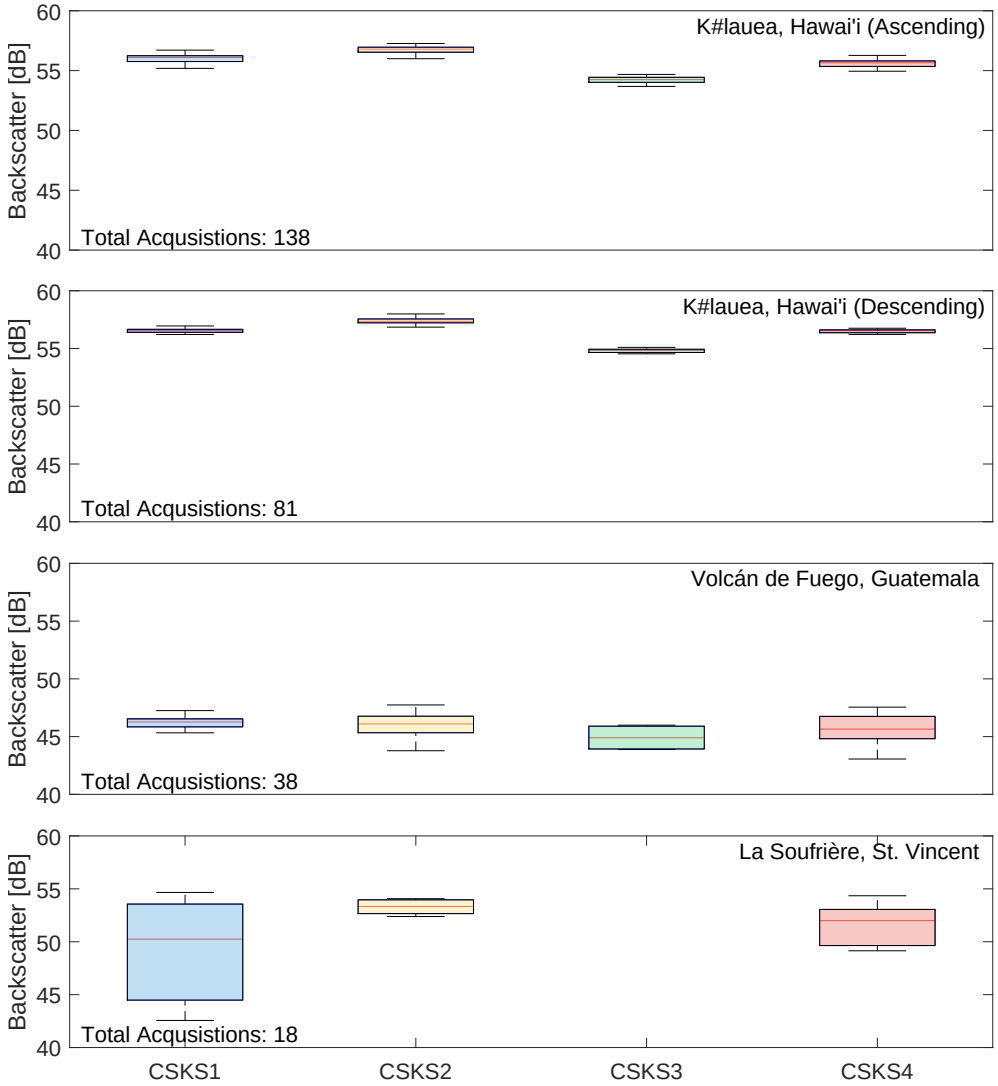

Figure 5.1: COSMO-SkyMed (CSK) SAR backscatter ranges corresponding to which satellite acquired the data for (a) Hawai‘i 2010 - 2013 ascending data, (b) Hawai‘i 2010 - 2013 descending data, (c) Volcán de Fuego ascending data and (e) La Soufrière, St. Vincent ascending data.

I observed similar but less pronounced satellite trends for the CSK datasets over

Volcán de Fuego, Guatemala and La Soufrière, St. Vincent (Fig. 5.1). In comparison to Hawai'i these both have much larger contributions from other systematic (e.g., seasonal influences) variations in the local scattering properties. The Fuego CSK dataset shows a slightly lower overall mean in SAR backscatter signals for CSK3 correlating with the trends observed over Hawai'i. However, while the St. Vincent dataset did not have any CSK3 imagery, I do observe larger SAR backscatter variations, which I assume are introduced by external scattering properties and hide the satellite pattern. While I do observe this satellite dependency in other CSK datasets (Fig. 5.1), I can not comment on whether this is a common trend for constellation satellite. It would be interesting to see whether other constellations, such as Sentinel-1, RADARSAT Constellation Mission (RCM), COSMO-SkyMed Second Generation (CSG), also observe this dependency.

For the comprehensive and stable CSK dataset over Hawai'i, it was straightforward to identify and correct this satellite dependency. However, for smaller datasets, quick analysis or when a PCA correction is not suitable, I found that a quick work around is to comparing dates acquired from the same CSK satellite to avoid the satellite introduced variation. For large magnitude changes this is generally not needed as the change in SAR backscatter is greater than the average difference between sensors. Similarly, a comparison between CSK1 and CSK4 would be adequate as they share comparable backscatter ranges (Fig. 3.2a, 5.1). Although, both these solutions would limited the number of acquisition that could be used.

In May 2022, the Italian Space Agency (L'Agenzia Spaziale Italian, ASI) decommissioned CSK3 after 14 years and the first COSMO-SkyMed Second Generation (CSG) satellite became operational in January 2022 (Fig. 5.2). The 1^{st} and 2^{nd} generation satellite operate on the same orbit, meaning that the data should be compatible between the generations. Archive CSK data will need to consider the satellite dependency in the backscatter data. As the other CSG satellites are launched (2022, 2024 and ∼2027) and become operational, we will be able to determine how the two generations work together and whether this satellite dependency is a systematic contribution to the CSK constellations.

5.2 Future of SAR Backscatter for Volcano Monitoring

Over the last three decades, there has been an increase of earth observation satellites, in particular for SAR sensors (Fig. 5.2). Accompanying this increase in data, SAR backscatter has slowly been used more frequently for volcano remote sensing.

5.2.1 The New SAR Generation

We entered a new era of earth observation satellites, with the launch of Sentinel-1 constellation in 2014 by the European Space Agency (ESA), providing frequent (6–12 days

after Sentinel-1b came online), open-access global data. This dataset produced significant advancement for long-term and frequent volcano monitoring. However, due to the relatively low resolution the SAR backscatter is still not routinely used in volcano monitoring. Throughout this thesis, I have considered the capability of using the respective Sentinel-1 data. Even with the lower resolution, I found that for the large magnitude changes or deposits the Sentinel-1 data was comparable. During the 2018 eruption at Volcán de Fuego, the Sentinel-1 data clearly visualised the major pyroclastic density current in the individual drainage and for the 2021 dome growth on St. Vincent the high frequency of acquisitions increased the temporal density of volume estimates from

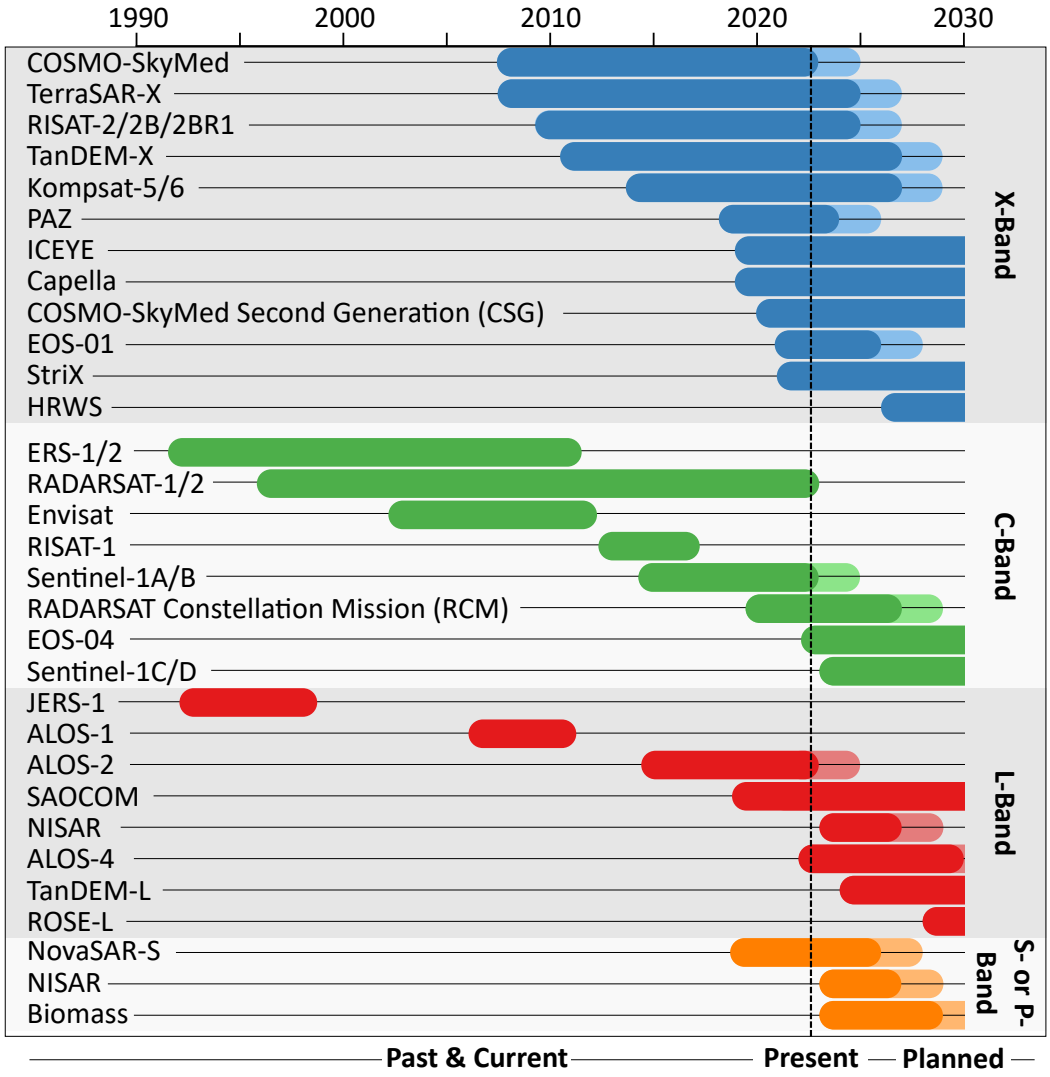

Figure 5.2: Timeline of past, present and future SAR missions between 1990 and 2030. Colours represent the wavelength of the SAR sensor, with the anticipated launch and end dates provided by operators. Lighter colours indicate the potential for system to remain active beyond its designed lifespan. Further, it is important to note that future dates are tentative as upcoming missions are often subject to delay or errors.

the high resolution dataset. However, the lower resolution meant that the smaller and more subtle signals were missed (e.g., ashfall from the 2018 Volcán de Fuego eruption).

In recent years there has been an increase in commercial small-constellation satellites (i.e., ICEYE and Capella Space) that have long-term missions planned (up until 2040) with fleets of satellites (Fig. 5.2). This new wave of SAR sensors has the potential to change the way that we observe volcanic eruption using SAR data. These satellites have the capability for rapid tasking at high resolution for a wide range of satellite geometries (e.g., large range of incidence angles, and right- or left-looking). This means that methods that can compare multiple geometries will be important to maintain temporal frequency. The multiple geometries will also allow for observations of volcanic deposits from different directions. This would provide more observations and details of process than would be possible from a single sensor.

The flexibility in data acquisition of these satellites has shown significant advantages during volcanic unrest. During the 2021 eruption of La Soufrière, St. Vincent the first observations of the new crater following the first eruption came from ICEYE and Capella imagery. Further, the high resolution of these new sensors allowed us to observe small details of the ground surface, for example surface variations in the 2020 Kīlauea lava lake (Fig. 3.8d).

Further, the anticipated launch of the high-resolution (3–10 m depending on mode) NASA-ISRO SAR (NISAR) in 2023 (Fig. 5.2), will provide new opportunities for monitoring volcanic eruptions using SAR data. The dual-frequency (L- and S-band; 23 and 10 cm wavelength), fully polarmetric nature of this satellite has a planned repeat interval of 12 days (Rosen et al., 2017) and should be freely available. The Japan Aerospace Exploration Agency's (JAXA) ALOS-PALSAR sensors have shown the benefit of long wavelength and dual-polarisation for monitoring volcanic activity (e.g., Solikhin et al., 2015), especially in the tropics where volcanoes have a dense vegetation cover.

5.2.2 SAR Wavelength and Polarisation

The increase in availability of SAR data for multiple satellites, means that there is more possibility for comparing singles measured using different wavelengths and polarisation. As the ground scattering properties are a function of the radar wavelength and polarisation, the resulting SAR backscatter signal will vary for a given wavelength and polarisation.

When comparing SAR backscatter images acquired with different wavelengths, large changes, such as crater collapse, can be easily visualised and compared between sensors. However, as the strength of the scattering properties is influenced by the wavelength, a direct comparison of backscatter signals is not possible. For recent lava flow eruptions, I

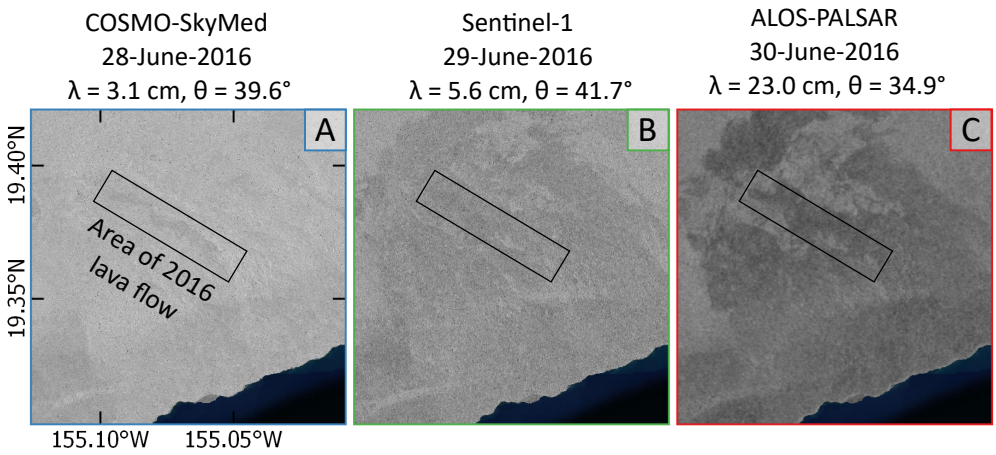

Figure 5.3: SAR backscatter images of 2016 Puʻu ʻŌʻō lava flow emplaced on older flows (Puʻu ʻŌʻō flow field) from (a) COSMO-SkyMed (CSK), X-band, (b) Sentinel-1, C-band, and (c) ALOS-2, L-band. Lava flow is easily discernible in the CSK image as an area (shown in black rectangle) of low SAR backscatter again the brighter SAR backscatter of the surrounding flow field. Modified Appendix C figure B.8.

observed how lava flows were not always visible in all wavelengths. A quick comparison between COSMO-SkyMed (X-band), Sentinel-1 (C-band), and ALOS-2 (L-band) over a lava flow on Hawaiʻi in 2016 demonstrated how different the ground surface is imaged from different wavelengths (Fig. 5.3). In the CSK imagery, the lava flow was clearly visible against a bright flow field. Using the Rayleigh criterion (Eq. 1.12), I estimate the degree of surface roughness (Δh) for each sensor (Table 5.1).

	COSMO-SkyMed	Sentinel-1	ALOS-2
Wavelength [cm]	3.1	5.6	23.0
Incidence Angle [°]	39.6	41.7	34.9
Rayleigh Criterion [cm]	0.5	0.9	3.5

Table 5.1: Sensor wavelength and incidence angle required to estimate the height of the surface variation for a surface to be considered smooth. Smaller surface variation values will appear appear rough and produce low SAR backscatter values.

For the CSK image, the new flow would have to have a variation in surface roughness less than 0.5 cm for it to appear dark in SAR, while the rest of the flow field would have a Δh>0.5 cm, to appear bright (higher values) in the SAR backscatter. For the longer wavelengths, it is not possible to differentiate between the 2016 lava flow and the other old flows on the Puʻu ʻŌʻō flow field based on their differences in surface roughness, especially visible in the ALOS-2 data (Fig. 5.3c). Based on the Rayleigh criterion for the three sensors and how the SAR backscatter values vary, I can estimate that generally speaking the Puʻu ʻŌʻō flow field has a surface roughness between 0.6–0.9 cm for it to appear rough in CSK (Δh > 0.5 cm) but smooth in both Sentinel-1 (Δh > 0.9 cm) and ALOS (Δh > 0.5 cm). This type of analysis would benefit from

ground-based observations to validate distinctions made in surface roughness.

Although a direct comparison between signal may be challenging it could provide boundary parameters for the scattering properties and help distinguish between different mechanisms of change in the SAR backscatter. For example, for a lava flow for which we assume the dominate scattering property is the surface roughness, we could potentially use the SAR backscatter signal and the Rayleigh criterion to say something about the roughness of the flow surface morphology as demonstrated above.

In this thesis, I showed single polarisation SAR imagery as I was concentrating on the high-resolution sensors (CSK and TSX) and these dataset were available only in HH mode. However, dual and fully polarimetric SAR has been shown to yield good results to map and characterise variations within lava flows (e.g., Poland, 2022) and explosive volcanic deposits (e.g., Saepuloh et al., 2012; Solikhin et al., 2015). The differences in the ground scattering properties, especially surface roughness, are better captured by polarimetric SAR imagery, as the sensor is able to capture more of the scattering characteristics of the target. For example, over vegetation an incoming wave will interact with multiple randomly orientated elements (i.e., volume scattering from branches, leaves, stems) and the resulting scattered wave is unpolarised, or depolarized (Palmann et al., 2008). The influence of volume scattering produces different SAR backscatter signals, with dual-polarisation (HV) producing higher backscatter values than the same pixel from a single-polarisation (HH) image. This difference can be used to distinguish between variations in surface roughness across volcanic deposits (e.g., Solikhin et al., 2015).

In the St. Vincent case study presented here, I had two dual-polarisation datasets from Sentinel-1 and ALOS-2 data. However, I found that in this case the dual-polarisation signal was not suitable to accurately retrieve topography from the SAR backscatter. I believe this is because the underlying assumption of the SAR topography extraction is that the dominant scattering property is the local incidence angle. Any variations in the other scattering properties (i.e., surface roughness and dielectric properties) in a range line would lead to distortions in the profile. As dual-polarimetric imagery is sensitive to variations in these scattering properties, especially over vegetated areas on the shrub covered 1979 dome, I observed many more distortions across profiles estimated from HV imagery than HH.

5.3 Potential for Operational SAR Backscatter in Volcanology

In this thesis, I presented three case studies of different volcanic eruptions and examined the potential of SAR backscatter data for monitoring purposes. As currently these are

three independent case studies, the obvious next step would be to assess the usefulness of each output for monitoring volcanic eruptions and produce operational tools that could be applied to other eruptions. To finish, I outline here a few examples of how the work from this thesis could be expanded and possibly be made operational.

5.3.1 Topographic Extraction from SAR Backscatter

The extraction of topography from SAR backscatter showed to be extremely useful in observing the progression of the eruption. However, to make the retrieval of topography from SAR backscatter operational, the method applied to the St. Vincent dataset would require more testing to determine how well it can be applied to a different datasets and possibly a different type of eruption. Currently, the method is relatively automated, with the only manual input being the identification of a radar shadow (used to determine the shadow threshold), location of a stable area (used to calculate the scaling factors), selecting the dome outline (used in triangular mesh interpolation), and size of triangular mesh in both radar and real geometry. By testing the method using different case studies, it could be determined whether it is possible to simplify the required inputs and associated background knowledge (e.g., temporal surface scattering trends) so that it could be applied quickly elsewhere, or whether this is a case-by-case method that requires initial setup depending on the setting.

An interesting next case study would be the 2021 dome growth at Great Sitkin volcano, Alaska. Similarly to St. Vincent, this dome rapidly grew within the summit crater with a uniform scattering pattern across the dome (Fig. A.4). However, unlike at St. Vincent, the dome has continued to grow and transitioned into a lava flow and due to its high latitude has interacted with surrounding snow and ice. These differences would help determine the constraints of the method with regards to less regular geometries (e.g., unconstrained flows) and influences from other scattering properties (e.g., change to the dielectric properties and surface roughness over ice). Additionally, another next step could be to identify an appropriate case study that has bi-static TanDEM-X imagery, which can be used to make direct measurements of the topography (e.g., Poland, 2014; Albino et al., 2020). Using TanDEM-X data would allow us to make a direct comparison between two different methods using the same input data.

To calibrate the method it would be useful to either examine past or inactive lava domes (e.g., Shinmoedake, Japan, or Mount St. Helens, U.S.A) where dome growth has either been previously studied or has a well observed existing dome (e.g., with LiDAR). Or to model different dome growth scenarios (e.g., Harnett et al., 2018) and uses these to simulate SAR backscatter. This type of modelling would help determine what situations this method would work in and what trends could be visualised from the SAR backscatter and through this method.

In addition to lava dome studies, the method could also be to other volcanic structures (e.g., well defined lava flows) to determine the limitations of the method with respect to influences from surface roughness. By applying it to various areas would hopefully allow me to make improvements to the method and make it easier for others to apply it to different volcanic settings and SAR sensors.

5.3.2 Automatic Lava Lake Height Estimates

The work on the 2011 Pu‘u ‘Ō‘ō crater demonstrated how radar shadow estimates have the potential to densify a timeseries. Currently, these measurements from radar shadow are being made case-by-case for individual sensors. However, the method has the potential for continuous automatic height retrieval over stable features. In addition, it would be possible to combine multiple sensor to increase acquisition frequency. It would be interesting to determine which currently active lava lakes could be monitored using this method using Sentinel-1 data. This would depend on the size of the lava lake, the geometry of the crater, the satellite geometry, and whether there is continuous acquisitions. As I am writing this, there are six permanent lava lakes:

1. Ambrym, Vanuatu
2. Erebus, Antarctica
3. Erta Ale, Ethopia
4. Kīlauea, Hawai‘i
5. Masaya, Nicaragua
6. Nyiragongo, Democratic Republic of the Congo

The lava lakes levels at Nyiragongo and Erta Ale already have been measured using changes to the radar shadow (Barrière et al., 2018; Moore et al., 2019; Barrière et al., 2022). I demonstrated here that the past lava lake at Pu‘u ‘Ō‘ō crater are possible to measure with high-resolution SAR backscatter imagery, there has not been enough variation in crater levels at Pu‘u ‘Ō‘ō crater during the Sentinel-1 era to test this dataset. Further, the current lava lake in Halema’uma’u crater is slowly infilling the crater and is not interacting with any radar shadows. Therefore, this method cannot be applied. For the other three lava lakes, they are all covered to different extents by Sentinel-1 (e.g., 226 acquisition of Erebus, 354 of Ambrym and 589 of Masaya between June 2014 and Aug. 2022), and are all situated within complex craters. A comprehensive study would be needed of the different view geometries covering these craters to determine whether (1) the lava lake is visible, and (2) if there is an appropriate geometry that could be used to measure fluctuations in lava lake height. The limitations and considerations that I outlined throughout the thesis would be helpful in determining where this method is suitable.

5.3.3 Flow Mapping from SAR Backscatter

The focus of this thesis was to use SAR backscatter as the sole or main dataset for monitoring volcanic activity. SAR backscatter proved to be capable for mapping volcanic flow deposits. I showed that for explosive and effusive deposits, the SAR backscatter images contains useful information about both the initial emplacement and the alteration over time. The temporal complexity following the emplacement of a deposit, can add information about what is happening to the ground surface when we lose coherence. Optimising flow mapping from SAR backscatter really depends on what deposits are being monitored. It can easily be used to quickly visualise large magnitude changes (e.g., pyroclastic density currents) through analysis of single or pairs of images (e.g., RGB change difference maps), which would not be difficult to implement in existing monitoring systems (Meyer et al., 2015). However, there is more information to be gained from longer timeseries. Therefore, optimising the calculation of the step in backscatter signal, and the timing of lava flow emplacement could provide continuous tracking of eruption progression. I suspect that this type of implementation would have to be specific to a volcano and the type of deposit being mapped. At Hawai'i, I was able to completely automate the method to extract the time of emplacement. Along with further improvements to the extraction method, it would need to be tested on a rolling dataset, rather than a complete dataset.

5.4 Conclusion

In this thesis, I have shown the potential of using high-resolution SAR backscatter to detect spatial and temporal changes of volcanic deposits. SAR backscatter is a complex dataset which potentially contains useful information about how an eruption has changed the earth's surface. I believe that I have shown how SAR backscatter can be best applied to different types of volcanic eruptions (e.g., long timeseries analysis for small magnitude changes, such as ash), and what influences need to be considered while interpreting the data (e.g., pre-eruption land cover). SAR data is currently mainly used to monitoring volcanic ground deformation. However, with the increase of current and future SAR missions (e.g., ICEYE, NISAR) with different wavelengths, and easier access to data for observatories, there is room for SAR backscatter to be incorporated into monitoring strategies. A SAR backscatter image captures the ground surface as it was at the time of acquisition, it is not dependent on the surface remain coherent between images or meteorological conditions. Further, in addition to SAR backscatter being able to used independently for hazard assessment there is the additional benefit of interrogating it with other SAR datasets (e.g., coherence) and ground-based observations to gain a more detail interpretation of changes in signal.

Bibliography

Albino, F., J. Biggs, R. Escobar-Wolf, A. Naismith, I. M. Watson, J. C. Phillips, and G. A. C. Marroquin (2020). "Using TanDEM-X to measure pyroclastic flow source location, thickness and volume: Application to the 3rd June 2018 eruption of Fuego volcano, Guatemala". In: *Journal of Volcanology and Geothermal Research*, p. 107063.

Angarita, M., R. Grapenthin, S. Plank, F. J. Meyer, and H. Dietterich (2022). "Quantifying large-scale surface change using SAR amplitude images: Crater morphology changes during the 2019-2020 Shishaldin Volcano eruption". In: *Journal of Geophysical Research: Solid Earth*, e2022JB024344.

Arnold, D. W. D., J. Biggs, K. Anderson, S. Vallejo Vargas, G. Wadge, S. K. Ebmeier, M. F. Naranjo, and P. Mothes (2017). "Decaying Lava Extrusion Rate at El Reventador Volcano, Ecuador, Measured Using High-Resolution Satellite Radar". In: *Journal of Geophysical Research: Solid Earth* 122.12, pp. 9966–9988.

Arnold, D. W. D., J. Biggs, H. R. Dietterich, S. V. Vargas, G. Wadge, and P. Mothes (2019). "Lava flow morphology at an erupting andesitic stratovolcano: A satellite perspective on El Reventador, Ecuador". In: *Journal of Volcanology and Geothermal Research* 372, pp. 34–47. DOI: 10.1016/j.jvolgeores.2019.01.009.

Arnold, D. W. D., J. Biggs, G. Wadge, and P. Mothes (2018). "Using satellite radar amplitude imaging for monitoring syn-eruptive changes in surface morphology at an ice-capped stratovolcano". In: *Remote Sensing of Environment* 209, pp. 480–488. DOI: 10.1016/j.rse.2018.02.040.

AVO (2021). *Great Sitkin TanDEM-X: IMAGE 175841*. https://avo.alaska.edu/images/image.php?id=175841. Accessed: 2022-07-15.

Babu, A. and S. Kumar (2019). "InSAR coherence and backscatter images based analysis for the Anak Krakatau volcano eruption". In: *Multidisciplinary digital publishing institute proceedings* 24.1, p. 21.

Barrière, J., N. d'Oreye, A. Oth, H. Geirsson, N. Mashagiro, J. B. Johnson, B. Smets, S. Samsonov, and F. Kervyn (2018). "Single-Station Seismo-Acoustic Monitoring of Nyiragongo's Lava Lake Activity (DR Congo)". In: *Frontiers in Earth Science* 6, p. 82.

Barrière, J., N. d'Oreye, B. Smets, A. Oth, L. Delhaye, J. Subira, N. Mashagiro, D. Derauw, D. Smittarello, A. M. Syavulisembo, and Kervyn F. (2022). "Intra-Crater Eruption Dynamics at Nyiragongo (DR Congo), 2002–2021". In: *Journal of Geophysical Research: Solid Earth* 127.4, e2021JB023858.

Bato, M. G., J. L. Froger, A. J. L. Harris, and N. Villeneuve (2016). "Monitoring an effusive eruption at Piton de la Fournaise using radar and thermal infrared remote sensing data: insights into the October 2010 eruption and its lava flows". In: *Geological Society, London, Special Publications* 426.1, pp. 533–552.

Bignami, C., S. Corradini, L. Merucci, M. de Michele, D. Raucoules, G. De Astis, S. Stramondo, and J. Piedra (2014). "Multisensor satellite monitoring of the 2011 Puyehue-Cordon Caulle eruption". In: *IEEE journal of selected topics in applied earth observations and remote sensing* 7.7, pp. 2786–2796.

Bignami, C., J. Ruch, M. Chini, M. Neri, M. F. Buongiorno, S. Hidayati, and D. S. Sayudi (2013). "Pyroclastic density current volume estimation after the 2010 Merapi volcano eruption using X-band SAR". In: *Journal of Volcanology and Geothermal Research* 261, pp. 236–243.

Bürgmann, R., P. A. Rosen, and E. J. Fielding (2000). "Synthetic aperture radar interferometry to measure Earth's surface topography and its deformation". In: *Annual review of earth and planetary sciences* 28.1, pp. 169–209.

Burrows, K., R. J. Walters, D. Milledge, and A. L. Densmore (2020). "A systematic exploration of satellite radar coherence methods for rapid landslide detection". In: *Natural Hazards and Earth System Sciences* 20.11, pp. 3197–3214.

Carn, S. A. (1999). "Application of synthetic aperture radar (SAR) imagery to volcano mapping in the humid tropics: A case study in East Java, Indonesia". In: *Bulletin of Volcanology* 61.1–2, pp. 92–105. DOI: 10.1007/s004450050265.

Carn, S. A., R. B. Watts, G. Thompson, and G. E. Norton (2004). "Anatomy of a lava dome collapse: the 20 March 2000 event at Soufrière Hills Volcano, Montserrat". In: *Journal of Volcanology and Geothermal Research* 131.3-4, pp. 241–264.

Carr, M. J., L. C. Patino, and M. D Feigenson (2007). "Petrology and geochemistry of lavas". In: *Central America: geology, resources and hazards*. Ed. by J. Buntschuh and G. E. Alvarado. Taylor and Francis London. Chap. 22, pp. 565–590. ISBN: 978-0-203-94704-3.

Carrara, A., V. Pinel, P. Bascou, E. Chaljub, and S. De la Cruz-Reyna (2019). "Post-emplacement dynamics of andesitic lava flows at Volcán de Colima, Mexico, revealed by radar and optical remote sensing data". In: *Journal of Volcanology and Geothermal Research* 381, pp. 1–15.

Cashman, K. V., S. A. Soule, B. H. Mackey, N. I. Deligne, N. D. Deardorff, and H. R. Dietterich (2013). "How lava flows: New insights from applications of lidar technologies to lava flow studies". In: *Geosphere* 9.6, pp. 1664–1680.

Castro, J. M., B. Cordonnier, C. I. Schipper, H. Tuffen, T. S. Baumann, and Y. Feisel (2016). "Rapid laccolith intrusion driven by explosive volcanic eruption". In: *Nature Communications* 7.1, pp. 1–7.

Castro, Jonathan M, Benoit Cordonnier, Hugh Tuffen, Mark J Tobin, Ljiljana Puskar, Michael C Martin, and Hans A Bechtel (2012). "The role of melt-fracture degassing in defusing explosive rhyolite eruptions at volcán Chaitén". In: *Earth and Planetary Science Letters* 333, pp. 63–69.

Chaussard, E. (2017). "A low-cost method applicable worldwide for remotely mapping lava dome growth". In: *Journal of Volcanology and Geothermal Research* 341, pp. 33–41.

Chorowicz, J., E. Lopez, F. Garcia, J-F. Parrot, J-P. Rudant, and R. Vinluan (1997). "Keys to analyze active lahars from Pinatubo on SAR ERS imagery". In: *Remote Sensing of Environment* 62.1, pp. 20–29.

Corradino, C., E. Amato, F. Torrisi, S. Calvari, and C. Del Negro (2021). "Classifying Major Explosions and Paroxysms at Stromboli Volcano (Italy) from Space". In: *Remote Sensing* 13.20, p. 4080.

Dean, K. G., K. Engle, J. Groves, J. Dehn, and K. Partington (2002). "Analysis of surface processes using SAR data: Westdahl Volcano, Alaska". In: *International Journal of Remote Sensing* 23.21, pp. 4529–4550.

Delgado, F., M. E. Pritchard, S. Ebmeier, P. González, and L. Lara (2017). "Recent unrest (2002–2015) imaged by space geodesy at the highest risk Chilean volcanoes: Villarrica, Llaima, and Calbuco (Southern Andes)". In: *Journal of Volcanology and Geothermal Research* 344, pp. 270–288.

Di Traglia, F., T. Nolesini, A. Ciampalini, L. Solari, W. Frodella, F. Bellotti, A. Fumagalli, G. De Rosa, and N. Casagli (2018). "Tracking morphological changes and slope instability using spaceborne and ground-based SAR data". In: *Geomorphology* 300, pp. 95–112. DOI: 10.1016/j.geomorph.2017.10.023.

Dietterich, H. R. and K. V. Cashman (2014). "Channel networks within lava flows: Formation, evolution, and implications for flow behavior". In: *Journal of Geophysical Research: Earth Surface* 119.8, pp. 1704–1724.

Dietterich, H. R., M. P. Poland, D. A. Schmidt, K. V. Cashman, D. R. Sherrod, and A. T. Espinosa (2012). "Tracking lava flow emplacement on the east rift zone of Kılauea, Hawai 'i, with synthetic aperture radar coherence". In: *Geochemistry, Geophysics, Geosystems* 13.5. DOI: 10.1029/2011GC004016.

Dualeh, E. W., S. K. Ebmeier, T. J. Wright, F. Albino, A. Naismith, J. Biggs, P. A. Ordoñez, R. M. Boogher, and A. Roca (2021). "Analyzing Explosive Volcanic Deposits From Satellite-Based Radar Backscatter, Volcán de Fuego, 2018". In: *Journal of Geophysical Research: Solid Earth* 126.9, e2021JB022250.

Dumont, S., F. Sigmundsson, M. M. Parks, V. J. P. Drouin, G. B. M. Pedersen, I. Jónsdóttir, Á. Höskuldsson, A. Hooper, K. Spaans, M. Bagnardi, M. T. Gudmunds-

son, S. Barsotti, K. Jónsdóttir, T. Högnadóttir, E. Magnússon, Á. R. Hjartardóttir, T. Dürig, C. Rossi, and B. Oddsson (2018). "Integration of SAR Data Into Monitoring of the 2014–2015 Holuhraun Eruption, Iceland: Contribution of the Icelandic Volcanoes Supersite and the FutureVolc Projects". In: *Frontiers in Earth Science* 6, p. 231. DOI: 10.3389/feart.2018.00231.

Ebmeier, S. K., B. J. Andrews, M. C. Araya, D. W.D. Arnold, J. Biggs, C. Cooper, E. Cottrell, M. Furtney, J. Hickey, J. Jay, R. Lloyd, A. L. Parker, M. E. Pritchard, E. Robertson, E. Venzke, and J. L. Williamson (2018). "Synthesis of global satellite observations of magmatic and volcanic deformation: implications for volcano monitoring & the lateral extent of magmatic domains". In: *Journal of Applied Volcanology* 7.1, pp. 1–26. DOI: 10.1186/s13617-018-0071-3.

Ebmeier, S. K., J. Biggs, C. Muller, and G. Avard (2014). "Thin-skinned mass-wasting responsible for widespread deformation at Arenal volcano". In: *Frontiers in Earth Science* 2, p. 35. DOI: 10.3389/feart.2014.00035.

EMS (2021). *[EMSR546] La Palma: Grading Product, Monitoring 47, version 1, release 1, RTP Map #01*. https://emergency.copernicus.eu/mapping/ems-product-component/EMSR546_AOI01_GRA_MONIT47_r1_RTP01/1. Accessed: 2022-07-15.

EOS-RS (2022). *OS-RS_202112_Indonesia_Semeru_Volcano*. https://eos-rs-products.earthobservatory.sg/EOS-RS_202112_Indonesia_Semeru_Volcano/. Accessed: 2022-07-15.

ESA (2022). *Level-1 Single Look Complex*. https://sentinels.copernicus.eu/web/sentinel/user-guides/Sentinel-1-sar/resolutions/level-1-single-look-complex. Accessed: 2022-08-20.

Escobar Wolf, R. and Ferres, D. (2018). "Informe Tecnico: Volcan de Fuego." In: *Technical Report* Cooperacion Espanola. URL: http://bibliotecadigital.aecid.es/bibliodig/i18n/consulta/registro.cmd?id=8751.

Esse, B., M. Burton, C. Hayer, R. Contreras-Arratia, T. Christopher, E. P. Joseph, M. Varnam, and C. Johnson (In Press). "SO2 emissions during the 2021 eruption of La Soufrière St. Vincent, revealed with back-trajectory analysis of TROPOMI imagery". In.

Ester, M., H-P. Kriegel, J. Sander, and X. Xu (1996). "A density-based algorithm for discovering clusters in large spatial databases with noise." In: *kdd*. Vol. 96. 34, pp. 226–231.

Fink, J. H. and S. W. Anderson (2000). "Lava domes and coulees". In: *Encyclopedia of volcanoes*, pp. 307–319.

Fournier, T. J., M. E. Pritchard, and S. N. Riddick (2010). "Duration, magnitude, and frequency of subaerial volcano deformation events: New results from Latin America using InSAR and a global synthesis". In: *Geochemistry, Geophysics, Geosystems* 11.1. DOI: 10.1029/2009GC002558.

Frey, O., M. Santoro, C. L. Werner, and U. Wegmuller (2012). "DEM-based SAR pixel-area estimation for enhanced geocoding refinement and radiometric normalization". In: *IEEE Geoscience and Remote Sensing Letters* 10.1, pp. 48–52.

Frost, V. S., J. Abbott Stiles, K. S. Shanmugan, and J. C. Holtzman (1982). "A Model for Radar Images and Its Application to Adaptive Digital Filtering of Multiplicative Noise". In: *IEEE Transactions on Pattern Analysis and Machine Intelligence* PAMI-4.2, pp. 157–166. DOI: 10.1109/TPAMI.1982.4767223.

Global Volcanism Program (2005). "Report on Fuego (Guatemala) (Wunderman, R., ed.)" In: *Bulletin of the Global Volcanism Network* 30:8. Smithsonian Institution. DOI: 10.5479/si.GVP.BGVN200508-342090.

Goitom, B., C. Oppenheimer, J. O. S. Hammond, R. Grandin, T. Barnie, A. Donovan, G. Ogubazghi, E. Yohannes, G. Kibrom, J. M. Kendall, S. A. Carn, D. Fee, C. Sealing, D. Keir, A. Ayele, J. Blundy, J. Hamlyn, T. Wright, and S. Berhe (2015). "First recorded eruption of Nabro volcano, Eritrea, 2011". In: *Bulletin of Volcanology* 77.10, p. 85. DOI: 10.1007/s00445-015-0966-3.

Grandin, R. (2021). *Soufriére Saint Vincent: Capella Space Imagery*. https://twitter.com/RaphaelGrandin/status/1381930061570392066. Accessed: 2022-07-15.

Grandin, R. and A. Delorme (2021). *La Soufriere volcano (Saint Vincent) – Fusion of Pleiades (2014, 2 m) and Copernicus (2018, 30 m) digital elevation models*. Dataset on Zenodo. DOI: 10.5281/zenodo.4668734.

Griffiths, R. W. and J. H. Fink (1997). "Solidifying Bingham extrusions: a model for the growth of silicic lava domes". In: *Journal of Fluid Mechanics* 347, pp. 13–36.

Guindon, B. (1990). "Development of a shape-from-shading technique for the extraction of topographic models from individual spaceborne SAR images". In: *IEEE Transactions on Geoscience and Remote Sensing* 28, pp. 654–661.

Hanssen, R. F. (2001). *Radar interferometry: data interpretation and error analysis*. Vol. 2. Springer Science & Business Media.

Harnett, C. E., M. E. Thomas, E. S. Calder, S. K. Ebmeier, A. Telford, W. Murphy, and J. Neuberg (2019). "Presentation and analysis of a worldwide database for lava dome collapse events: the Global Archive of Dome Instabilities (GLADIS)". In: *Bulletin of Volcanology* 81.3, pp. 1–17.

Harnett, C. E., M. E. Thomas, M. D. Purvance, and J. Neuberg (2018). "Using a discrete element approach to model lava dome emplacement and collapse". In: *Journal of Volcanology and Geothermal Research* 359, pp. 68–77.

Head, E. M., A. L. Maclean, and S. A. Carn (2013). "Mapping lava flows from Nyamuragira volcano (1967–2011) with satellite data and automated classification methods". In: *Geomatics, Natural Hazards and Risk* 4.2, pp. 119–144.

HVO (2011a). *Hawaiian Volcano Observatory Multimedia*. https://www.usgs.gov/observatories/hvo/multimedia. Accessed: 2022-08-09.

HVO (2011b). *Photo and Video Chronology - Kīlauea - August 8, 2011*. https://www.usgs.gov/volcanoes/kilauea/news/photo-and-video-chronology-kilauea-august-8-2011. Accessed: 2022-08-19.

— (2011c). *Photo and Video Chronology - Kīlauea - June 29, 2011*. https://www.usgs.gov/volcanoes/kilauea/news/photo-and-video-chronology-kilauea-june-29-2011. Accessed: 2022-08-19.

— (2011d). *The active lava lake in Pu'u 'Ō'ō and its levee*. https://www.usgs.gov/volcanoes/kilauea/news/photo-and-video-chronology-kilauea-june-23-2011. Accessed: 2022-08-05.

— (2014). *Small-scale map of Kīlauea's ERZ flow field*. https://www.usgs.gov/media/images/small-scale-map-k-laueas-erz-flow-field-4. Accessed: 2022-08-19.

— (2021). *February 09, 2021—Kīlauea summit eruption thermal map*. https://www.usgs.gov/node/278854. Accessed: 2022-08-19.

INSIVUMEH (2018a). "Descenso de Flujos Piroclásticos". In: *Bolentín Vulcanólogico Especial* Volcán de Fuego.36.

— (2018b). "Erupcion con Flujoc Piroclásticos". In: *Bolentín Vulcanólogico Especial* Volcán de Fuego.27.

— (2018c). "Finaliza la erupcion". In: *Bolentín Vulcanólogico Especial* Volcán de Fuego.33.

— (2018d). "Flujos Piroclásticos Barranca Las Lajas y Jute". In: *Bolentín Vulcanólogico Especial* Volcán de Fuego.38.

— (2018e). "Lahares Moderados en la Barranca: Las Lajas Y Honda". In: *Bolentín Vulcanólogico Especial* Volcán de Fuego.127.

Joseph, E. P., M. Camejo-Harry, T. Christopher, R. Contreras-Arratia, S. Edwards, O. Graham, M. Johnson, A. Juman, J. L. Latchman, L. Lynch, and V. L. Miller (2022). "Responding to eruptive transitions during the 2020–2021 eruption of La Soufrière volcano, St. Vincent". In: *Nature Communications* 13.1, pp. 1–15.

Jousset, P., J. Pallister, M. Boichu, M. F. Buongiorno, A. Budisantoso, F. Costa, S. Andreastuti, F. Prata, D. Schneider, L. Clarisse, and H. Humaida (2012). "The 2010 explosive eruption of Java's Merapi volcano—a '100-year'event". In: *Journal of volcanology and geothermal research* 241, pp. 121–135.

Keysight Technologies (2018). *A Framework for Understanding: Deriving the Radar Range Equation*. Accessed: 2022-08-20.

Kubanek, J., M. Westerhaus, and B. Heck (2017). "TanDEM-X time series analysis reveals lava flow volume and effusion rates of the 2012-2013 Tolbachik, Kamchatka fissure eruption". In: *Journal of Geophysical Research: Solid Earth* 122.10, pp. 7754–7774.

Lazecký, M., K. Spaans, P. J. González, Y. Maghsoudi, Y. Morishita, F. Albino, J. Elliott, N. Greenall, E. Hatton, A. Hooper, and D. Juncu (2020). "LiCSAR: An

automatic InSAR tool for measuring and monitoring tectonic and volcanic activity". In: *Remote Sensing* 12.15, p. 2430.

Lee, J-S., L. Jurkevich, R. Dewaele, P. Wambacq, and A. Oosterlinck (1994). "Speckle filtering of synthetic aperture radar images: A review". In: *Remote sensing reviews* 8.4, pp. 313–340.

Lei, T., X. Jia, Y. Zhang, L. He, H. Meng, and A. K. Nandi (2018). "Significantly fast and robust fuzzy c-means clustering algorithm based on morphological reconstruction and membership filtering". In: *IEEE Transactions on Fuzzy Systems* 26.5, pp. 3027–3041.

Lev, E., P. Ruprecht, C. Oppenheimer, N. Peters, M. Patrick, P. A Hernández, L. Spampinato, and J. Marlow (2019). "A global synthesis of lava lake dynamics". In: *Journal of Volcanology and Geothermal Research* 381, pp. 16–31.

Lopes, A., E. Nezry, R. Touzi, and H. Laur (1993). "Structure detection and statistical adaptive speckle filtering in SAR images". In: *International Journal of Remote Sensing* 14.9, pp. 1735–1758. DOI: 10.1080/01431169308953999.

Loughlin, S. C., C. Vye-Brown, R. S. J. Sparks, S. K. Brown, J. Barclay, E. Calder, E. Cottrell, G. Jolly, J-C. Komorowski, C. Mandeville, and et al. (2015). "An introduction to global volcanic hazard and risk". In: *Global Volcanic Hazards and Risk*. Ed. by S. C. Loughlin, R. S. J. Sparks, S. K. Brown, S. F. Jenkins, and C. Vye-Brown. Cambridge University Press, pp. 1–80. DOI: 10.1017/CBO9781316276273.003.

Lu, Z., R. Rykhus, T. Masterlark, and K. G. Dean (2004). "Mapping recent lava flows at Westdahl Volcano, Alaska, using radar and optical satellite imagery". In: *Remote Sensing of Environment* 91.3-4, pp. 345–353.

Lyons, J. J., G. P. Waite, W. I. Rose, and G. Chigna (2010). "Patterns in open vent, strombolian behavior at Fuego volcano, Guatemala, 2005-2007". In: *Bulletin of Volcanology* 72.1, pp. 1–15. DOI: 10.1007/s00445-009-0305-7.

Mania, R., T. R. Walter, M. Belousova, A. Belousov, and S. L. Senyukov (2019). "Deformations and morphology changes associated with the 2016–2017 eruption sequence at Bezymianny Volcano, Kamchatka". In: *Remote Sensing* 11.11, p. 1278.

Martin, D. P. and W. I. Rose (1981). "Behavioral patterns of Fuego volcano, Guatemala". In: *Journal of Volcanology and Geothermal Research* 10.1-3, pp. 67–81. DOI: 10.1016/0377-0273(81)90055-X.

Massonnet, D., P. Briole, and A. Arnaud (1995). "Deflation of Mount Etna monitored by spaceborne radar interferometry". In: *Nature* 375.6532, pp. 567–570.

Metcalfe, A., S. Moune, J-C. Komorowski, and R. Moretti (2022). "Bottom-up vs top-down drivers of eruption style: Petro-geochemical constraints from the holocene explosive activity at La Soufrière de Guadeloupe". In: *Journal of Volcanology and Geothermal Research* 424, p. 107488.

Meyer, F., A. I. Flores-Anderson, K. E. Herndon, R. B. Thapa, and E. Cherrington (2019). *The SAR Handbook: Comprehensive Methodologies for Forest Monitoring*

and Biomass Estimation. Huntsville, AL, USA: SERVIR Global. DOI: 10.25966/nr2c-s697.

Meyer, F. J., D. B. McAlpin, W. Gong, O. Ajadi, S. Arko, P. W. Webley, and J. Dehn (2015). "Integrating SAR and derived products into operational volcano monitoring and decision support systems". In: *ISPRS Journal of Photogrammetry and Remote Sensing* 100, pp. 106–117. DOI: 10.1016/j.isprsjprs.2014.05.009.

Moore, C., T. Wright, A. Hooper, and J. Biggs (2019). "The 2017 Eruption of Erta'Ale Volcano, Ethiopia: Insights Into the Shallow Axial Plumbing System of an Incipient Mid-Ocean Ridge". In: *Geochemistry, Geophysics, Geosystems* 20.12, pp. 5727–5743.

Moore, C., T. J. Wright, and A. Hooper (2021). "Rift Focussing and Magmatism During Late-Stage Rifting in Afar". In: *Journal of Geophysical Research: Solid Earth*, e2020JB021542.

Naismith, A. K, I. M. Watson, R. Escobar-Wolf, G. Chigna, H. Thomas, D. Coppola, and C. Chun (2019). "Eruption frequency patterns through time for the current (1999–2018) activity cycle at Volcán de Fuego derived from remote sensing data: Evidence for an accelerating cycle of explosive paroxysms and potential implications of eruptive activity". In: *Journal of Volcanology and Geothermal Research* 371, pp. 206–219.

Naismith, A. K., M. T. Armijos, E. A. B. Escobar, W. Chigna, and I. M. Watson (2020). "Fireside tales: understanding experiences of previous eruptions and factors influencing the decision to evacuate from activity of Volcán de Fuego". In: *Volcanica* 3.2, pp. 205–226.

Nakada, S., H. Shimizu, and K. Ohta (1999). "Overview of the 1990–1995 eruption at Unzen Volcano". In: *Journal of Volcanology and Geothermal Research* 89.1-4, pp. 1–22.

Neal, C. A., S. R. Brantley, L. Antolik, J. L. Babb, M. Burgess, K. Calles, M. Cappos, J. C. Chang, S. Conway, L. Desmither, and P. Dotray (2019). "The 2018 rift eruption and summit collapse of Kılauea Volcano". In: *Science* 363.6425, pp. 367–374.

NEMO (2020a). *Effusive Eruption at the La Soufrière Volcano alert level raised to orange*. http://nemo.gov.vc/nemo/index.php/news-events/news-release/568-volcano-alert-level-raised-to-orange. Accessed: 2021-08-11.

— (2020b). *La Soufrière Bulletin #50 April 08, 2021 5:30 PM*. http://nemo.gov.vc/nemo/index.php/news-events/news-release/638-la-soufriere-bulletin-50-april-08-2021-5-30-pm1. Accessed: 2021-08-11.

— (2020c). *Scientists have noted a change in seismic activity associated with the ongoing eruption of the La Soufrière Volcano*. http://nemo.gov.vc/nemo/index.php/news-events/news-release/628-scientists-have-noted-a-change-in-seismic-activity-associated-with-the-ongoing-eruption-of-the-la-soufriere-volcano. Accessed: 2021-08-11.

NOAA Office for Coastal Management (2022). *Hawaii IfSAR Digital Terrain Model (DTM)*. https://www.fisheries.noaa.gov/inport/item/48377. Accessed: 2022-08-19.

Ordoñez, M., C. Laverde, and M. Battaglia (2022). "The new lava dome growth of Nevado del Ruiz (2015–2021)". In: *Journal of Volcanology and Geothermal Research* 430, p. 107626.

Orr, T. R., M. P. Poland, M. R. Patrick, W. A. Thelen, A. J. Sutton, T. Elias, C. R. Thornber, C. Parcheta, and K. M. Wooten (2015). "Kılauea's 5–9 March 2011 Kamoamoa fissure eruption and its relation to 30+ years of activity from Pu 'u 'O 'o". In: *Hawaiian Volcanoes: From Source to Surface* 208, p. 393.

Ozawa, T. and T. Kozono (2013). "Temporal variation of the Shinmoe-dake crater in the 2011 eruption revealed by spaceborne SAR observations". In: *Earth, Planets and Space* 65.6, pp. 527–537.

Pallister, J. S., D. J. Schneider, J. P. Griswold, R. H. Keeler, W. C. Burton, C. Noyles, C. G. Newhall, and A. Ratdomopurbo (2013). "Merapi 2010 eruption-Chronology and extrusion rates monitored with satellite radar and used in eruption forecasting". In: *Journal of Volcanology and Geothermal Research* 261, pp. 144–152. DOI: 10.1016/j.jvolgeores.2012.07.012.

Palmann, C., S. Mavromatis, M. Hernández, J. Sequeira, and B. Brisco (2008). "Earth observation using radar data: an overview of applications and challenges". In: *International Journal of Digital Earth* 1.2, pp. 171–195.

Paquerault, S. and H. Maitre (1998). "New method for backscatter model estimation and elevation map computation using radarclinometry". In: *SAR Image Analysis, Modeling, and Techniques*. Vol. 3497. SPIE, pp. 230–241.

Pardini, F., M. Queißer, A. Naismith, M. Watson, L. Clarisse, and M. R. Burton (2019). "Initial constraints on triggering mechanisms of the eruption of Fuego volcano (Guatemala) from 3 June 2018 using IASI satellite data". In: *Journal of Volcanology and Geothermal Research* 376, pp. 54–61.

Patel, P., H. S. Srivastava, S. Panigrahy, and J. S. Parihar (2006). "Comparative evaluation of the sensitivity of multi-polarized multi-frequency SAR backscatter to plant density". In: *International Journal of Remote Sensing* 27.2, pp. 293–305.

Patrick, M., T. Orr, K. Anderson, and D. Swanson (2019a). "Eruptions in sync: Improved constraints on Kılauea Volcano's hydraulic connection". In: *Earth and Planetary Science Letters* 507, pp. 50–61.

Patrick, M., T. Orr, G. Fisher, F. Trusdell, and J. Kauahikaua (2017). "Thermal mapping of a pāhoehoe lava flow, Kılauea Volcano". In: *Journal of Volcanology and Geothermal Research* 332, pp. 71–87.

Patrick, M., D. Swanson, and T. Orr (2019b). "A review of controls on lava lake level: insights from Halema 'uma 'u Crater, Kılauea Volcano". In: *Bulletin of Volcanology* 81.3, p. 13.

Patrick, M. R., K. R. Anderson, M. P. Poland, T. R. Orr, and D. A. Swanson (2015). "Lava lake level as a gauge of magma reservoir pressure and eruptive hazard". In: *Geology* 43.9, pp. 831–834.

Patrick, M. R., A. J. L. Harris, M. Ripepe, J. Dehn, D. A. Rothery, and S. Calvari (2007). "Strombolian explosive styles and source conditions: Insights from thermal (FLIR) video". In: *Bulletin of Volcanology* 69.7, pp. 769–784. DOI: 10.1007/s00445-006-0107-0.

Patrick, M. R., T. Orr, L. Antolik, L. Lee, and K. Kamibayashi (2014). "Continuous monitoring of Hawaiian volcanoes with thermal cameras". In: *Journal of Applied Volcanology* 3.1, pp. 1–19.

Patrick, M. R., T. Orr, D. A. Swanson, and E. Lev (2016). "Shallow and deep controls on lava lake surface motion at Kılauea Volcano". In: *Journal of Volcanology and Geothermal Research* 328, pp. 247–261.

Patrick, M. R. and T. R. Orr (2018). *Operational tracking of lava lake surface motion at Kılauea Volcano, Hawai 'i*. Tech. rep. US Geological Survey.

Pedersen, G. B. M., A. Höskuldsson, T. Dürig, T. Thordarson, I. Jónsdóttir, M. S. Riishuus, B. V. Óskarsson, S. Dumont, E. Magnusson, M. T. Gudmundsson, F. Sigmundsson, V. J.P.B. Drouin, C. Gallagher, R. Askew, J. Gudnason, W. M. Moreland, P. Nikkola, H. I. Reynolds, and J. Schmith (2017). "Lava field evolution and emplacement dynamics of the 2014–2015 basaltic fissure eruption at Holuhraun, Iceland". In: *Journal of Volcanology and Geothermal Research* 340, pp. 155–169. DOI: 10.1016/j.jvolgeores.2017.02.027.

Pinel, V., M. P. Poland, and A. Hooper (2014). *Volcanology: Lessons learned from Synthetic Aperture Radar imagery*. DOI: 10.1016/j.jvolgeores.2014.10.010.

Plank, S., F. Marchese, N. Genzano, M. Nolde, and S. Martinis (2020). "The short life of the volcanic island New Late'iki (Tonga) analyzed by multi-sensor remote sensing data". In: *Scientific reports* 10.1, pp. 1–15.

Plank, S., T. R. Walter, S. Martinis, and S. Cesca (2019). "Growth and collapse of a littoral lava dome during the 2018/19 eruption of Kadovar Volcano, Papua New Guinea, analyzed by multi-sensor satellite imagery". In: *Journal of Volcanology and Geothermal Research* 388, p. 106704.

Poland, M. P. (2014). "Time-averaged discharge rate of subaerial lava at Kılauea Volcano, Hawai 'i, measured from TanDEM-X interferometry: Implications for magma supply and storage during 2011–2013". In: *Journal of Geophysical Research: Solid Earth* 119.7, pp. 5464–5481.

— (2022). "Synthetic aperture radar volcanic flow maps (SAR VFMs): a simple method for rapid identification and mapping of volcanic mass flows". In: *Bulletin of Volcanology* 84.3, pp. 1–11.

Pritchard, M. E., J. Biggs, C. Wauthier, E. Sansosti, D. W.D. Arnold, F. Delgado, S. K. Ebmeier, S. T. Henderson, K. Stephens, C. Cooper, K. Wnuk, F. Amelung,

V. Aguilar, P. Mothes, O. Macedo, L. E. Lara, M. P. Poland, and S. Zoffoli (2018). "Towards coordinated regional multi-satellite InSAR volcano observations: results from the Latin America pilot project". In: *Journal of Applied Volcanology* 7.1, pp. 1–28. DOI: 10.1186/s13617-018-0074-0.

Raney, R. K., T. Freeman, R. W. Hawkins, and R. Bamler (1994). "A plea for radar brightness". In: *Proceedings of IGARSS'94–1994 IEEE International Geoscience and Remote Sensing Symposium*. Vol. 2. IEEE, pp. 1090–1092.

Robertson, R. E. A. (1995). "An assessment of the risk from future eruptions of the Soufrière volcano of St. Vincent, West Indies". In: *Natural Hazards* 11.2, pp. 163–191.

Roman, D. C., M. Rodgers, H. Geirsson, P. C. LaFemina, and V. Tenorio (2016). "Assessing the likelihood and magnitude of volcanic explosions based on seismic quiescence". In: *Earth and Planetary Science Letters* 450, pp. 20–28.

Rosen, P. A., Y. Kim, R. Kumar, T. Misra, R. Bhan, and V. R. Sagi (2017). "Global persistent SAR sampling with the NASA-ISRO SAR (NISAR) mission". In: *2017 IEEE radar conference (RadarConf)*. IEEE, pp. 0410–0414.

Rowland, S. K., G. A. Smith, and P. J. Mouginis-Mark (1994). "Preliminary ERS-1 observations of Alaskan and Aleutian volcanoes". In: *Remote Sensing of Environment* 48.3, pp. 358–369.

Ryan, G. A., S. C. Loughlin, M. R. James, L. D. Jones, E. S. Calder, T. Christopher, M. H. Strutt, and G. Wadge (2010). "Growth of the lava dome and extrusion rates at Soufrière Hills Volcano, Montserrat, West Indies: 2005–2008". In: *Geophysical Research Letters* 37.19.

Saepuloh, A., K. Koike, and M. Omura (2012). "Applying Bayesian decision classification to Pi-SAR polarimetric data for detailed extraction of the geomorphologic and structural features of an active volcano". In: *IEEE Geoscience and Remote Sensing Letters* 9.4, pp. 554–558.

Saepuloh, A., K. Koike, M. Omura, M. Iguchi, and A. Setiawan (2010). "SAR- and gravity change-based characterization of the distribution pattern of pyroclastic flow deposits at Mt. Merapi during the past 10 years". In: *Bulletin of Volcanology* 72.2, pp. 221–232. DOI: 10.1007/s00445-009-0310-x.

Saepuloh, A., K. Koike, M. Urai, and J. T. S. Sumantyo (2015a). "Identifying surface materials on an active volcano by deriving dielectric permittivity from polarimetric SAR data". In: *IEEE Geoscience and Remote Sensing Letters* 12.8, pp. 1620–1624. DOI: 10.1109/LGRS.2015.2415871.

Saepuloh, A., M. Urai, N. Aisyah, C. Widiwijayanti, and P. Jousset (2013). "Interpretation of ground surface changes prior to the 2010 large eruption of Merapi volcano using ALOS/PALSAR, ASTER TIR and gas emission data". In: *Journal of Volcanology and Geothermal Research* 261, pp. 130–143.

Saepuloh, A., K. Wikantika, and M. Urai (2015b). "Observing lava dome roughness on synthetic aperture radar (SAR) data: Case study at Mt. Sinabung and Merapi–Indonesia". In: *2015 IEEE 5th Asia-Pacific Conference on Synthetic Aperture Radar (APSAR)*. IEEE, pp. 645–648.

Schaefer, L. N., T. Wang, R. Escobar-Wolf, T. Oommen, Z. Lu, J. Kim, P. R. Lundgren, and G. P. Waite (2017). "Three-dimensional displacements of a large volcano flank movement during the May 2010 eruptions at Pacaya Volcano, Guatemala". In: *Geophysical Research Letters* 44.1, pp. 135–142.

Scharff, L., M. Hort, and A. Gerst (2014). "The dynamics of the dome at Santiaguito volcano, Guatemala". In: *Geophysical Journal International* 197.2, pp. 926–942.

Scharrer, K., C. Mayer, T. Nagler, U. Münzer, and Á. Gumundsson (2007). "Effects of ash layers of the 2004 Grımsvötn eruption on SAR backscatter in the accumulation area of Vatnajökull". In: *Annals of Glaciology* 45, pp. 189–196.

Scharrer, K., O. Spieler, C. Mayer, and U. Münzer (2008). "Imprints of sub-glacial volcanic activity on a glacier surface—SAR study of Katla volcano, Iceland". In: *Bulletin of Volcanology* 70.4, pp. 495–506.

Scott, C. P., R. B. Lohman, and T. E. Jordan (2017). "InSAR constraints on soil moisture evolution after the March 2015 extreme precipitation event in Chile". In: *Scientific Reports* 7.1, pp. 1–9.

Sherwin, C. W., J. P. Ruina, and R. D. Rawcliffe (1962). "Some early developments in synthetic aperture radar systems". In: *IRE Transactions on Military Electronics* 2, pp. 111–115.

Shevchenko, A. V., V. N. Dvigalo, E. U. Zorn, M. S. Vassileva, F. Massimetti, T. R. Walter, I. Y. Svirid, S. A. Chirkov, A. Y. Ozerov, V. A. Tsvetkov, and I. A. Borisov (2021). "Constructive and Destructive Processes During the 2018–2019 Eruption Episode at Shiveluch Volcano, Kamchatka, Studied From Satellite and Aerial Data". In: *Frontiers in Earth Science*, p. 457.

Small, D. (2011). "Flattening gamma: Radiometric terrain correction for SAR imagery". In: *IEEE Transactions on Geoscience and Remote Sensing* 49.8, pp. 3081–3093. DOI: 10.1109/TGRS.2011.2120616.

Solikhin, A., V. Pinel, J. Vandemeulebrouck, J. C. Thouret, and M. Hendrasto (2015). "Mapping the 2010 Merapi pyroclastic deposits using dual-polarization Synthetic Aperture Radar (SAR) data". In: *Remote Sensing of Environment* 158, pp. 180–192. DOI: 10.1016/j.rse.2014.11.002.

Sparks, R. S. J., J. Biggs, and J. W. Neuberg (2012). "Monitoring volcanoes". In: *Science* 335.6074, pp. 1310–1311.

Stinton, A. J. (In Prep.). "Growth and evolution of the lava dome and coulée during the 2020-21 eruption of La Soufrière, St Vincent". In: *Geological Society London (GSL) Memoirs*.

Taud, H. and J-F. Parrot (1995). "Qualitative digital elevation model from sar data". In: *Synthetic Aperture Radar and Passive Microwave Sensing*. Vol. 2584. SPIE, pp. 226–233.

Terunuma, T., K. Nishida, T. Amada, T. Mizuyama, I. Sato, and M. Urai (2005). "Detection of traces of pyroclastic flows and lahars with satellite synthetic aperture radars". In: *International Journal of Remote Sensing* 26.9, pp. 1927–1942. DOI: 10.1080/01431160512331326576.

Thompson, J. O., R. Contreras-Arratia, K. S. Befus, and M. S. Ramsey (2022). "Thermal and seismic precursors to the explosive eruption at La Soufrière Volcano, St. Vincent in April 2021". In: *Earth and Planetary Science Letters* 592, p. 117621.

Tilling, R. I. (1987). "Fluctuations in surface height of active lava lakes during 1972–1974 Mauna Ulu eruption, Kilauea volcano, Hawaii". In: *Journal of Geophysical Research: Solid Earth* 92.B13, pp. 13721–13730.

— (2008). "The critical role of volcano monitoring in risk reduction". In: *Advances in Geosciences*.

Tolometti, G. D., C. D. Neish, C. W. Hamilton, G. R. Osinski, A. Kukko, and J. R. C. Voigt (2022). "Differentiating Fissure-Fed Lava Flow Types and Facies Using RADAR and LiDAR: An Example from the 2014–2015 Holuhraun Lava Flow-field". In: *Journal of Geophysical Research: Solid Earth*, e2021JB023419.

Tomiyasu, K. (1978). "Tutorial review of synthetic-aperture radar (SAR) with applications to imaging of the ocean surface". In: *Proceedings of the IEEE* 66.5, pp. 563–583.

Vincent, L. (1993). "Morphological grayscale reconstruction in image analysis: applications and efficient algorithms". In: *IEEE transactions on image processing* 2.2, pp. 176–201.

Wadge, G., P. Cole, A. Stinton, J. C. Komorowski, R. Stewart, A. C. Toombs, and Y. Legendre (2011). "Rapid topographic change measured by high-resolution satellite radar at Soufriere Hills Volcano, Montserrat, 2008-2010". In: *Journal of Volcanology and Geothermal Research* 199.1–2, pp. 142–152. DOI: 10.1016/j.jvolgeores.2010.10.011.

Wadge, G. and M. Haynes (1998). "Cover Radar images growth of Soufriere Hills Volcano, Montserrat". In: *International Journal of Remote Sensing* 19.5, pp. 797–800. DOI: 10.1080/014311698215720.

Wadge, G., S. Saunders, and I. Itikarai (2012). "Pulsatory andesite lava flow at Bagana Volcano". In: *Geochemistry, Geophysics, Geosystems* 13.11, 2012GC004336. DOI: 10.1029/2012GC004336.

Wadge, G., B. Scheuchl, and N. F. Stevens (2002). "Spaceborne radar measurements of the eruption of Soufrière Hills Volcano, Montserrat". In: *Geological Society Memoir* 21.1, pp. 583–594. DOI: 10.1144/GSL.MEM.2002.021.01.27.

Walter, T. R., M. H. Haghighi, F. M. Schneider, D. Coppola, M. Motagh, J. Saul, A. Babeyko, T. Dahm, V. R Troll, F. Tilmann, and S. Heimann (2019a). "Complex hazard cascade culminating in the Anak Krakatau sector collapse". In: *Nature communications* 10.1, pp. 1–11.

Walter, T. R., C. E. Harnett, N. Varley, D. V. Bracamontes, J. Salzer, E. U. Zorn, M. Bretón, R. Arámbula, and M. E. Thomas (2019b). "Imaging the 2013 explosive crater excavation and new dome formation at Volcán de Colima with TerraSAR-X, time-lapse cameras and modelling". In: *Journal of Volcanology and Geothermal Research* 369, pp. 224–237. DOI: 10.1016/j.jvolgeores.2018.11.016.

Walter, T. R., J. Subandriyo, S. Kirbani, H. Bathke, W. Suryanto, N. Aisyah, H. Darmawan, P. Jousset, B-G. Luehr, and T. Dahm (2015). "Volcano-tectonic control of Merapi's lava dome splitting: The November 2013 fracture observed from high resolution TerraSAR-X data". In: *Tectonophysics* 639, pp. 23–33.

Wang, H. and T. J. Wright (2012). "Satellite geodetic imaging reveals internal deformation of western Tibet". In: *Geophysical Research Letters* 39.7.

Wang, T., M. P. Poland, and Z. Lu (2015). "Dome growth at Mount Cleveland, Aleutian Arc, quantified by time series TerraSAR-X imagery". In: *Geophysical Research Letters* 42.24, pp. 10, 614–10, 621. DOI: 10.1002/2015GL066784.

Watts, R. B., R. A. Herd, R. S. J. Sparks, S. R. Young, and T. H. Druitt (2002). "Growth patterns and emplacement of the andesitic lava dome at Soufriere Hills Volcano, Montserrat". In: *Memoirs-Geological Society of London* 21, pp. 115–152.

Werner, C., U. Wegmüller, T. Strozzi, and A. Wiesmann (2000). "Gamma SAR and interferometric processing software". In: *Proceedings of the ers-envisat symposium, Gothenburg, Sweden*. Vol. 1620. Citeseer, p. 1620.

Wiart, P. A. M., C. Oppenheimer, and P. Francis (2000). "Eruptive history of Dubbi volcano, northeast Afar (Eritrea), revealed by optical and SAR image interpretation". In: *International Journal of Remote Sensing* 21.5, pp. 911–936.

Wildey, R. L. (1986). "Radarclinometry". In: *Earth Moon Planet* 36, pp. 217–247. DOI: https://doi.org/10.1007/BF00055161.

Wiley, C. A. (1985). "Synthetic aperture radars". In: *IEEE Transactions on Aerospace and Electronic Systems* 3, pp. 440–443.

Williams, R., P. Rowley, and M. C. Garthwaite (2019). "Reconstructing the Anak Krakatau flank collapse that caused the December 2018 Indonesian tsunami". In: *Geology* 47.10, pp. 973–976.

Woodhouse, I. H., A. Marino, and I. Cameron (2011). "A standard index of spatial resolution for distributed targets in synthetic aperture radar imagery". In: *International journal of remote sensing* 32.23, pp. 7929–7938.

Wright, R., L. P. Flynn, H. Garbeil, A. J. L. Harris, and E. Pilger (2004). "MODVOLC: near-real-time thermal monitoring of global volcanism". In: *Journal of Volcanology and Geothermal Research* 135.1-2, pp. 29–49.

Xiang, J., S. Guo, X. Shi, D. Yu, G. Wei, N. Wen, C. Chen, and K. Dai (2022). "Revealing the Morphological Evolution of Krakatau Volcano by Integrating SAR and Optical Remote Sensing Images". In: *Remote Sensing* 14.6, p. 1399.

Yu, C., Z. Li, N. T Penna, and P. Crippa (2018). "Generic atmospheric correction model for interferometric synthetic aperture radar observations". In: *Journal of Geophysical Research: Solid Earth* 123.10, pp. 9202–9222.

Zebker, H. A., P. Rosen, S. Hensley, and R. J. Mouginis-Mark (1996). "Analysis of active lava flows on Kilauea volcano, Hawai'i, using SIR-C radar correlation measurements". In: *Geology* 24.6, pp. 495–498.

Zebker, H. A. and J. Villasenor (1992). "Decorrelation in interferometric radar echoes". In: *IEEE Transactions on geoscience and remote sensing* 30.5, pp. 950–959.

Zharinov, N. A. and Y. V. Demyanchuk (2008). "The growth of an extrusive dome on Shiveluch Volcano, Kamchatka in 1980–2007: geodetic observations and video surveys". In: *Journal of Volcanology and Seismology* 2.4, pp. 217–227.

Appendix A:

Supporting information for Chapter 2: Introduction

Contents of this file

1. Figures A.1 to A.4

Introduction This appendix contains supporting material referenced the introduction. It includes examples of SAR images and products used in near-real time monitoring during volcanic eruptions.

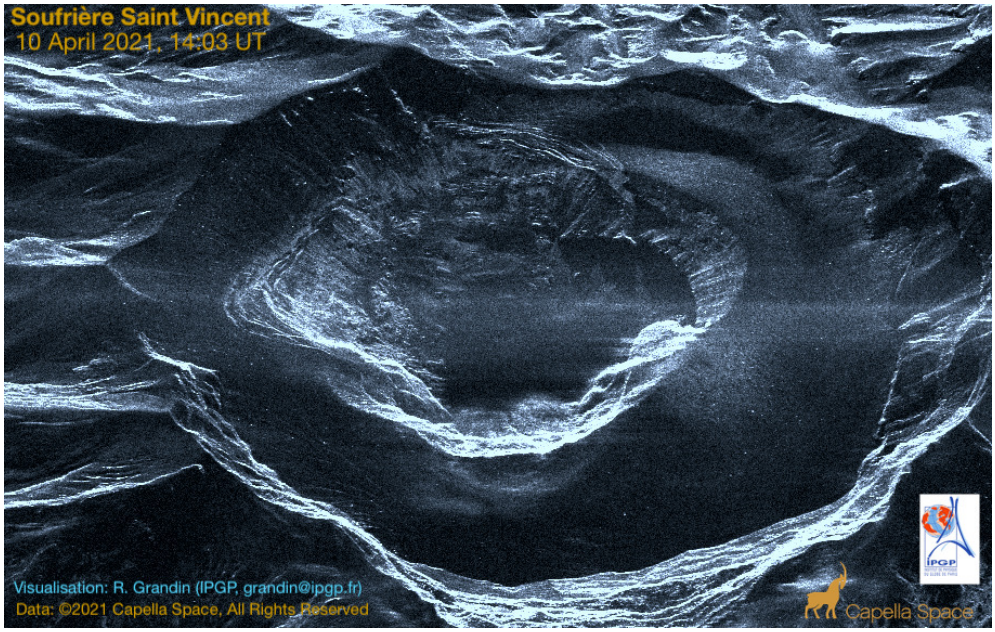

Figure A.1: Capella Space image from 10 April at 14:02 UTC, capturing the first observations of the La Soufrière crater following the 9 April 2021 explosive eruption. Data was supplied by Capella Space to and processed by R. Grandin. (Posted to twitter, Grandin, 2021).

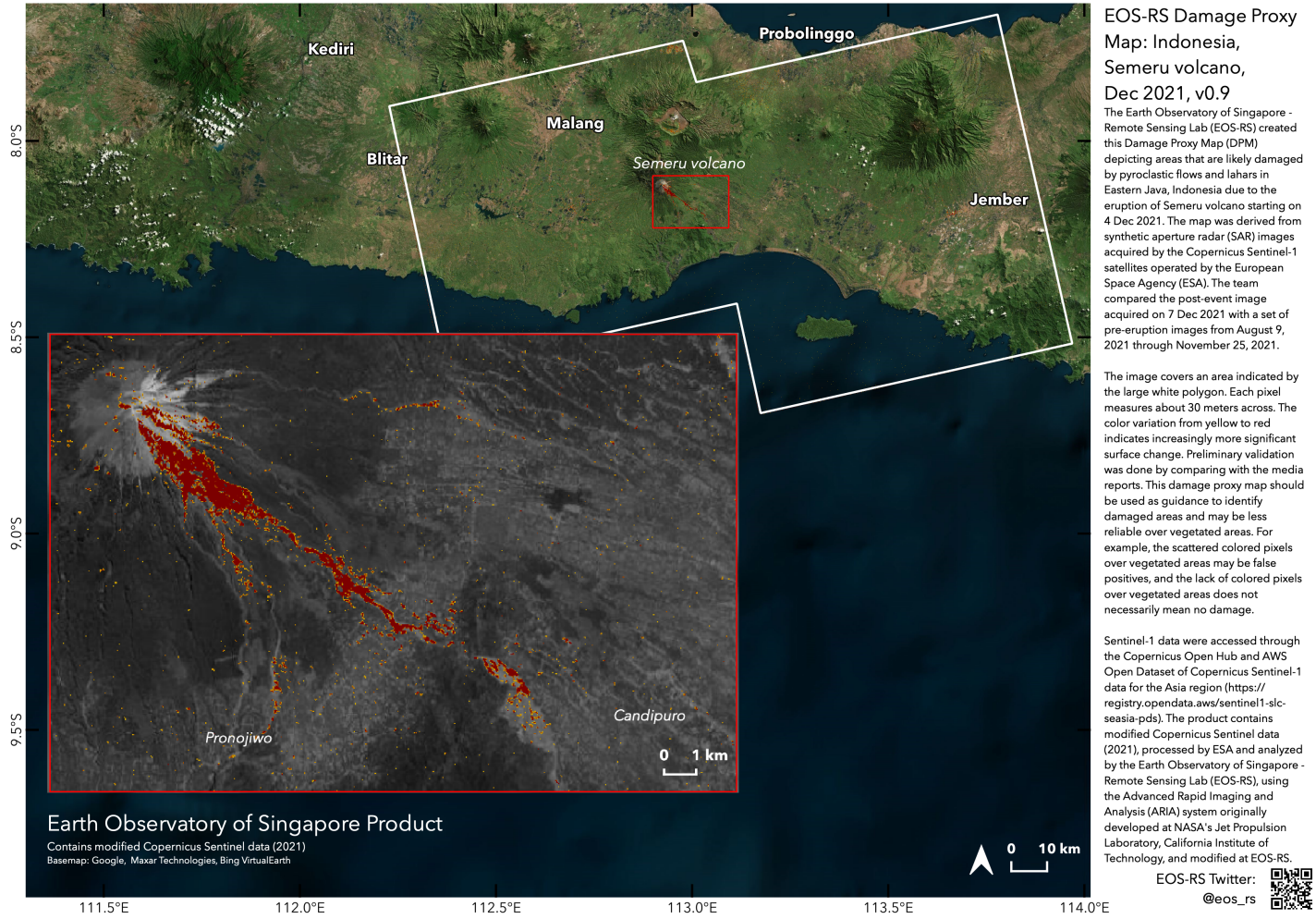

Figure A.2: Damage proxy map produced by the Earth Observatory of Singapore - Remote Sensing (EOS–RS) showing areas likely damaged by pyroclastic flows and lahars associated with the Dec. 2021 eruption of Semeru volcano, Indonesia. Map was produced using Sentinel-1 data. Damage proxy map can be found in the Advanced Rapid Imaging and Analysis Singapore (ARIA–SG) Products Repository (EOS-RS, 2022)

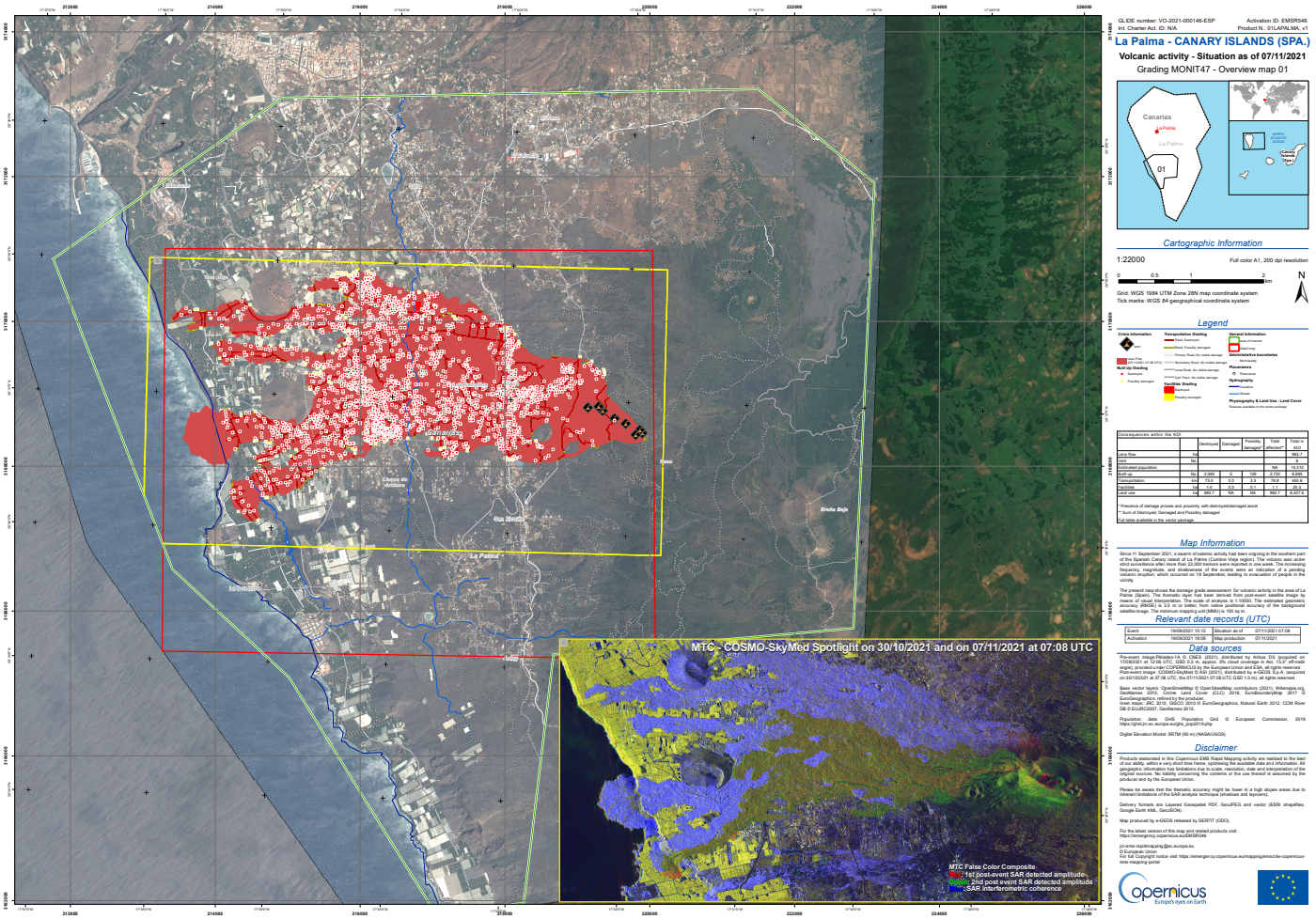

Figure A.3: Eruption map of the La Palma 2021 eruption. Published product shows a damage map produced from SAR data and a false colour composite map from COSMO-SkyMed data showing changes in the flow field. The product was published on 07-11-2021 as part of the Copernicus Emergency Management Service (EMS) - Rapid Mapping activity. (EMS, 2021).

Figure A.4: TerraSAR-X image of the 2021 lava dome at the summit of Great Sitkin, Alaska from the 16-08-2021. Image courtesy of AVO/USGS. Data processed by Simon Plank (German Aerospace Center). (AVO, 2021).

Appendix B:

Supporting information for Chapter 3

Contents of this file

1. Figures B.1 to B.9

Introduction This supplementary material includes figures covering details on the PCA-correction of the COSMO-SkyMed dataset, the complete results of the automatic extraction of the lava lakes in Pu‘u ‘Ō‘ō crater, additional comparison to thermal data, examples problems extracting lava flow noise based on high levels of SAR backscatter variance, and variations in SAR backscatter based on different wavelengths.

Figure B.1: COSMO-SkyMed (CSK) satellite parameters timeseries showing (a) incidence angle, and (b) perpendicular baseline correlated to CSK satellite that acquired the first date.

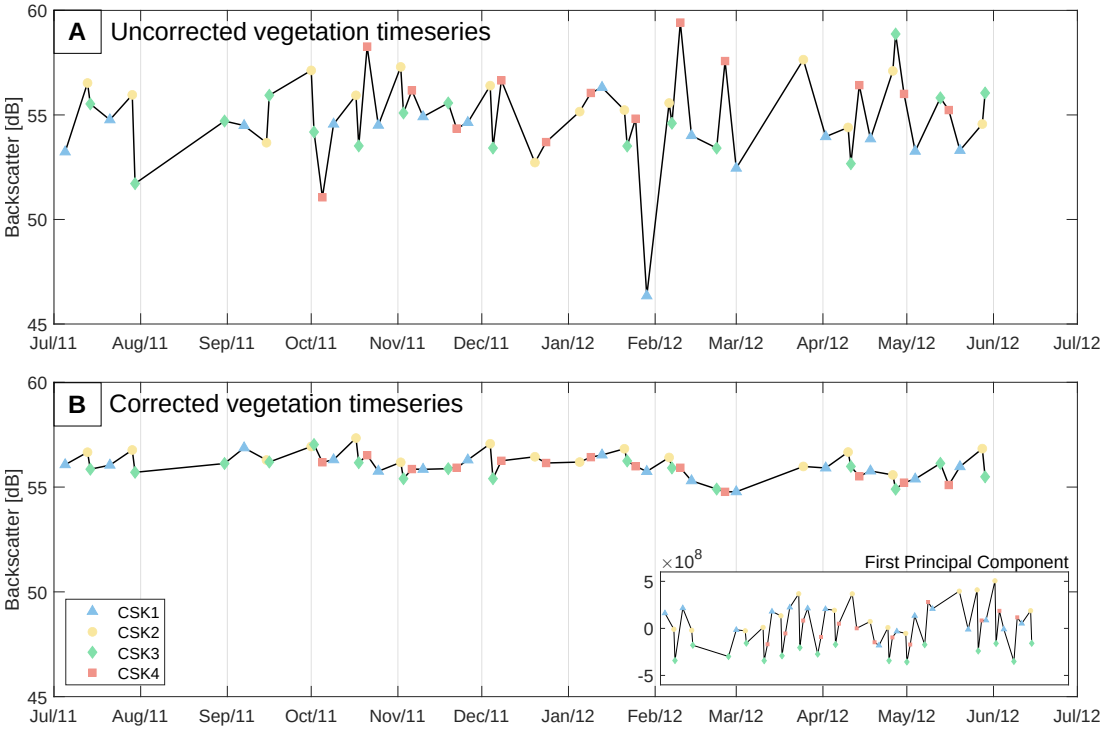

Figure B.2: Timeseries for the same single pixel for (b) uncorrected, and (d) PCA-corrected radar backscatter over unchanged vegetation towards the northwest of Pu‘u ‘Ō‘ō crater, showing the improvement in the signal following the removal of the first principal component (PC1) from the dataset (PC1 shown in insert on b).

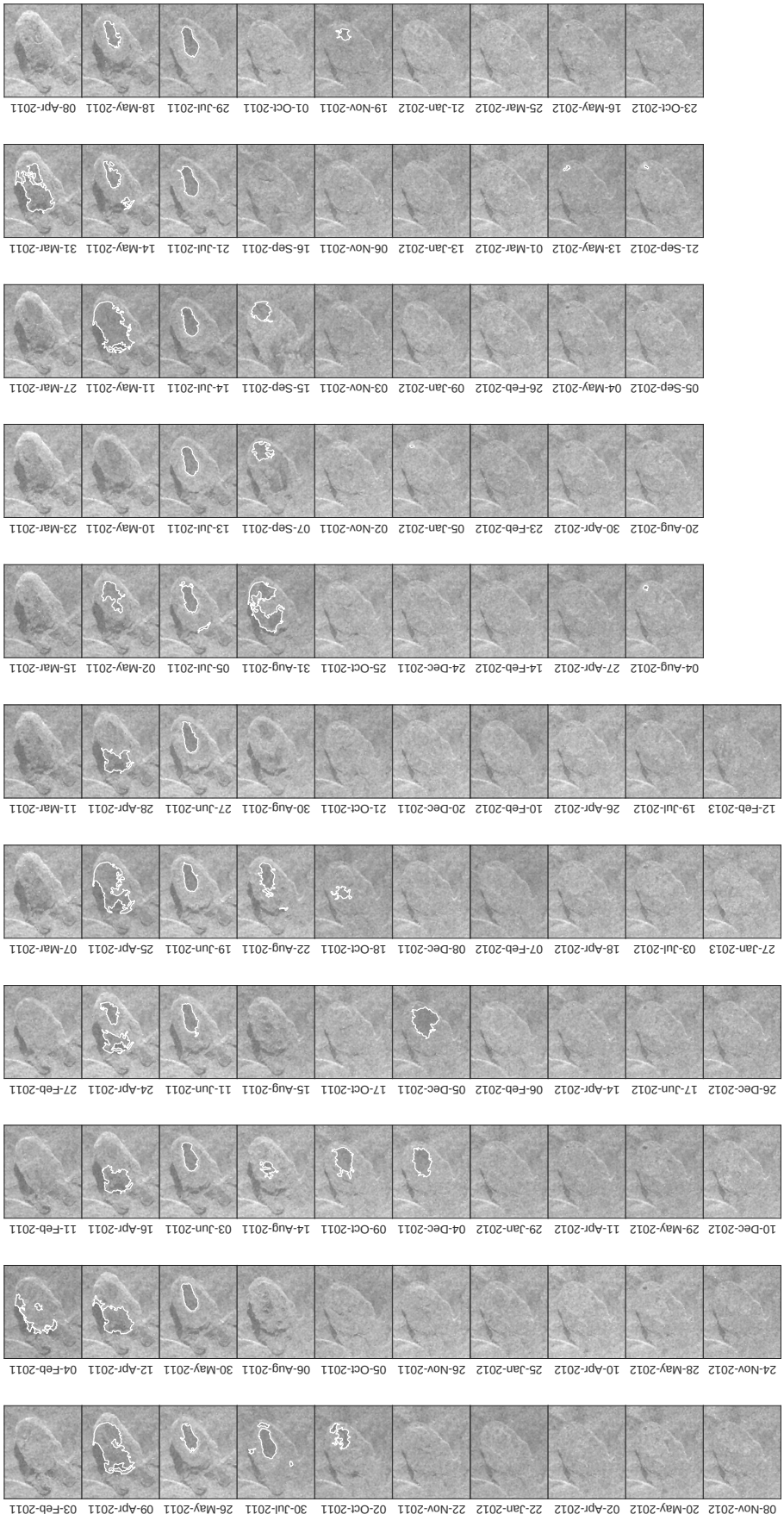

Figure B.3: Complete results from the automatic identification and extraction of the lava lake in Pu'u 'Ō'ō crater from SAR backscatter imagery between 2010–2013. White outlines represent the area identified as a lava lake by this method.

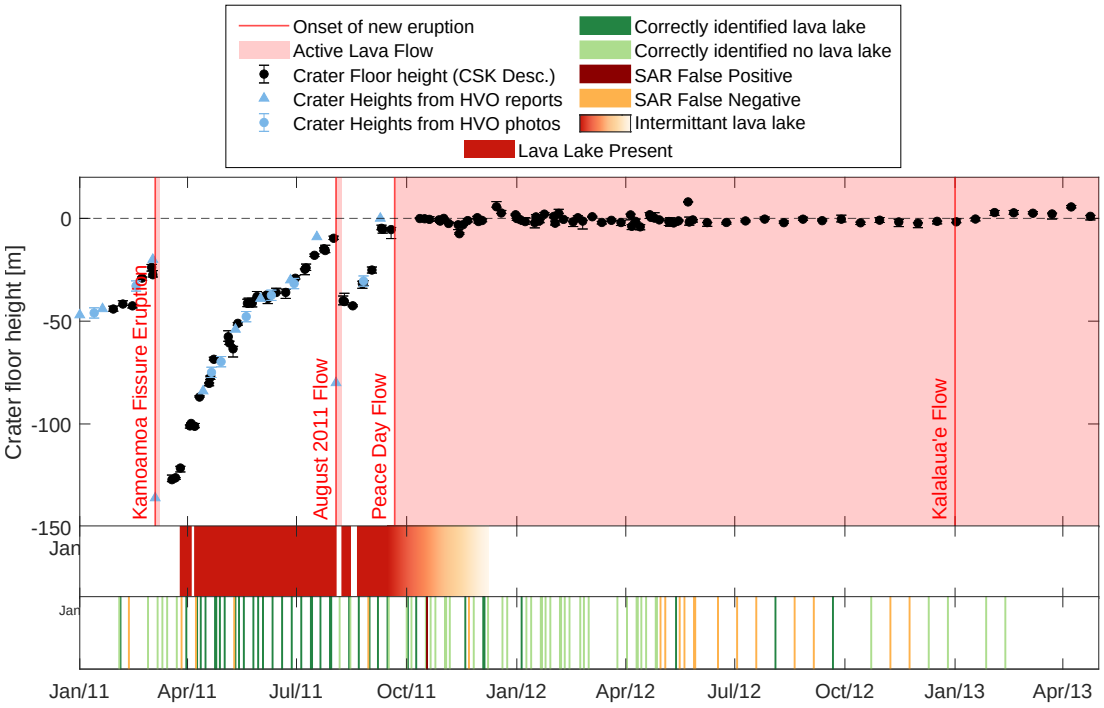

Figure B.4: Identified lava lakes between 01 Jan. and 31 April 2013. The scatter plot show the inflation and collapses at Pu‘u ‘Ō‘ō crater during this period of time. The first bar shows a red to yellow gradient that represents when there was a lava lake presenting in the crater. Following the Peace Day Flow (21 September) the lava lake stabilised and formed a crust with the occasional outbreak or exposed lava lake. The second bar chart shows the lava lake classification from the SAR backscatter extraction method.

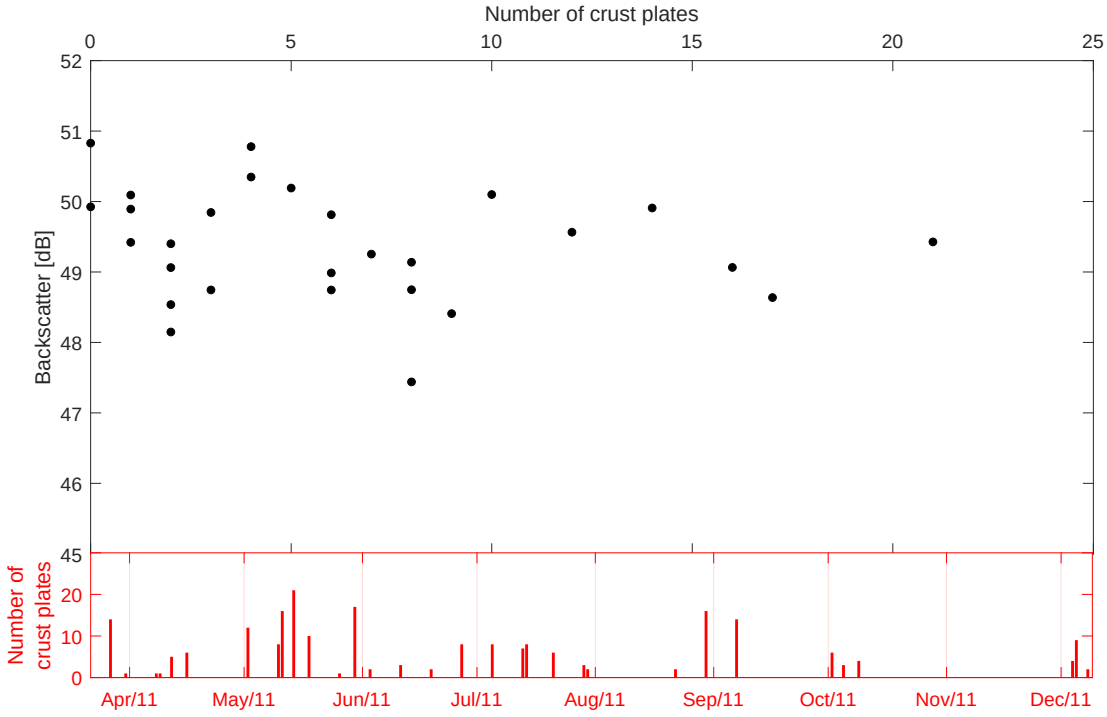

Figure B.5: Comparison between the mean SAR backscatter of Pu‘u ‘Ō‘ō lava lake and the number of crustal plates present on the lava lake surface. The number of crustal plates are identified from the thermal imagery using a thermal threshold (300°), applying a dilation and erosion operator to separate plates for easier identification. This is based on the methods described in Patrick et al. (2016) and Lev et al. (2019)

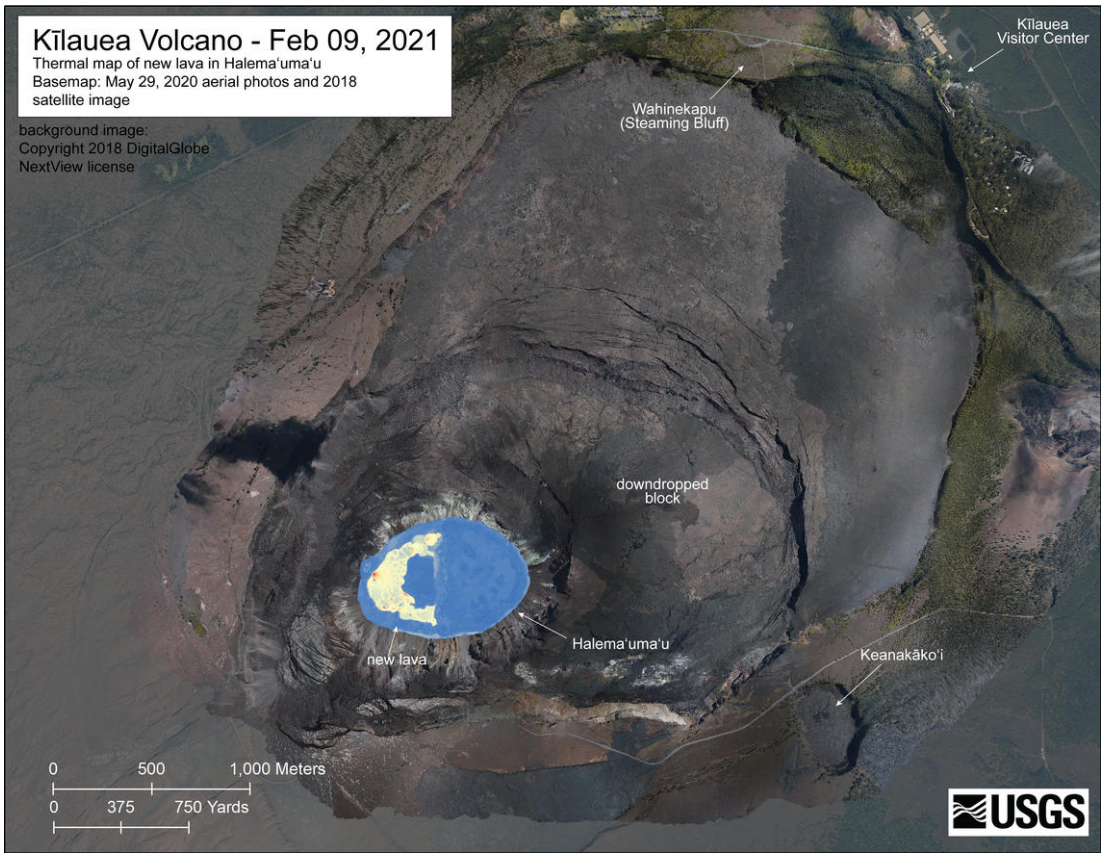

Figure B.6: 9 February 2021 map published by the Hawaiian Volcano observatory HVO, 2021 of the 2020 lava lake in Halema'uma'u crater. Thermal imagery during a helicopter overflight, showing the surface activity pattern of the infilling lava lake. Blue indicates cooler temperatures and red indicates warmer.

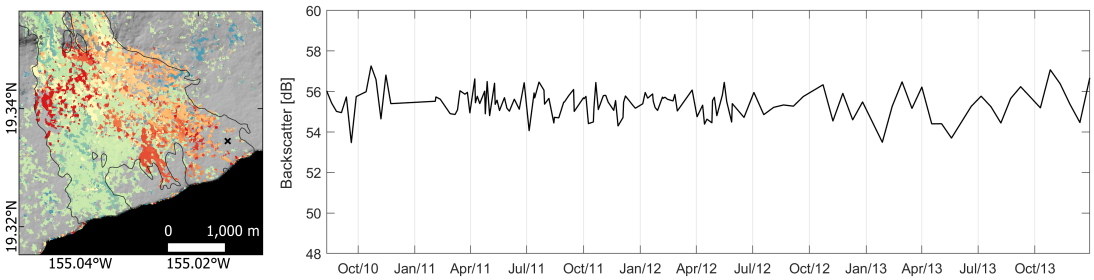

Figure B.7: Single pixel timeseries using the PCA-corrected COSMO-SkyMed dataset showing a the high variability in the SAR backscatter signal covering the time of lava flow emplacement and recovery. Map shows the location of timeseries (black cross) and the timing of lava flow emplacement of the Peace Day Flow on the coastal plain.

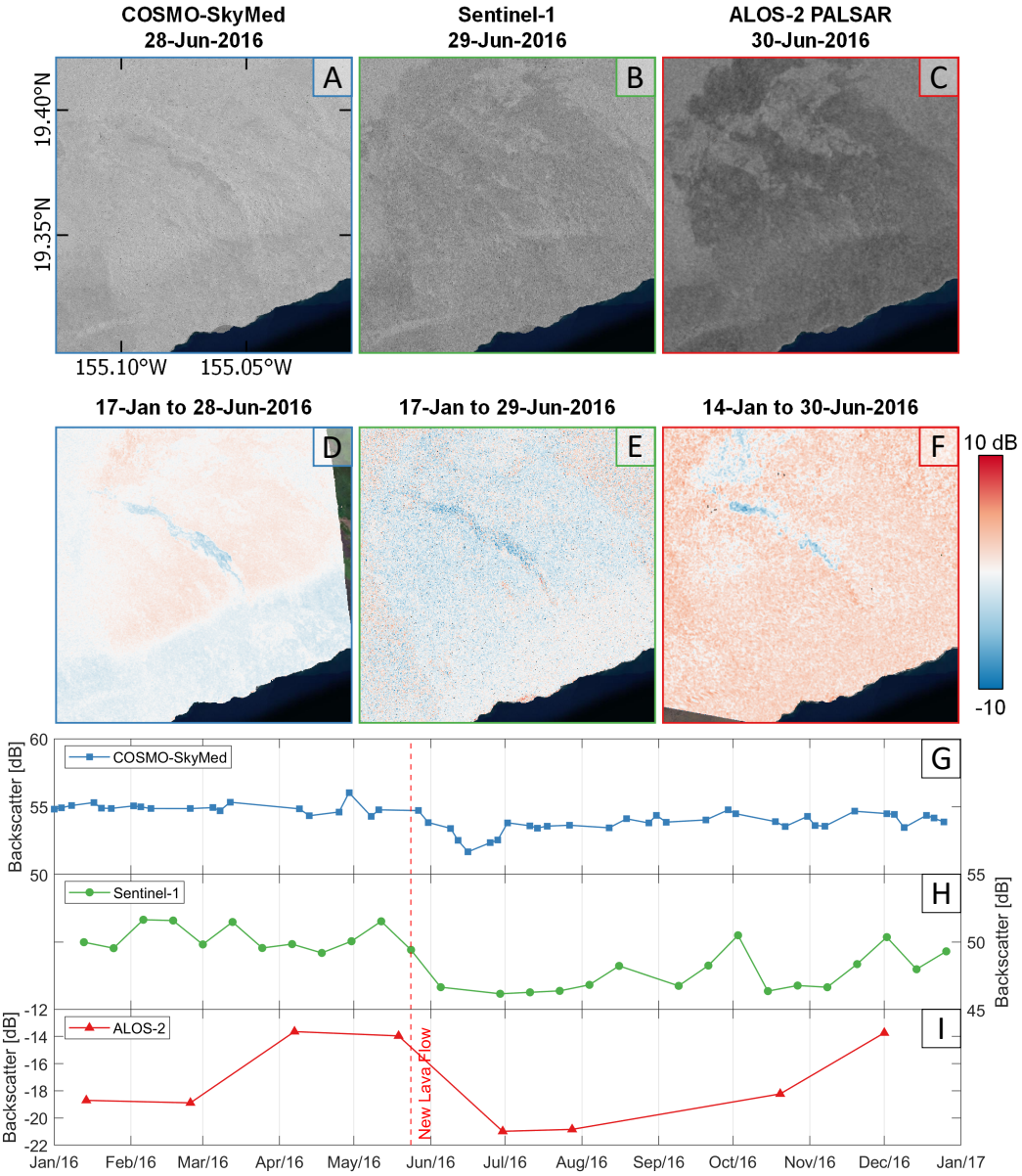

Figure B.8: Comparison of SAR backscatter signals for a lava flow in 2016 on Hawai'i for X-band (COSMO-SkyMed), C-band (Sentinel-1), and L-band (ALOS-2). (a-c) show a single SAR backscatter image, (d-f) are step estimation maps for the same time span, and (g-i) the corresponding pixel timeseries for a single pixel affected by the lava flow showing the difference in the temporal frequency of the different sensors. We corrected the COSMO-SkyMed dataset for the satellite dependency (example of correction in Fig. C.9).

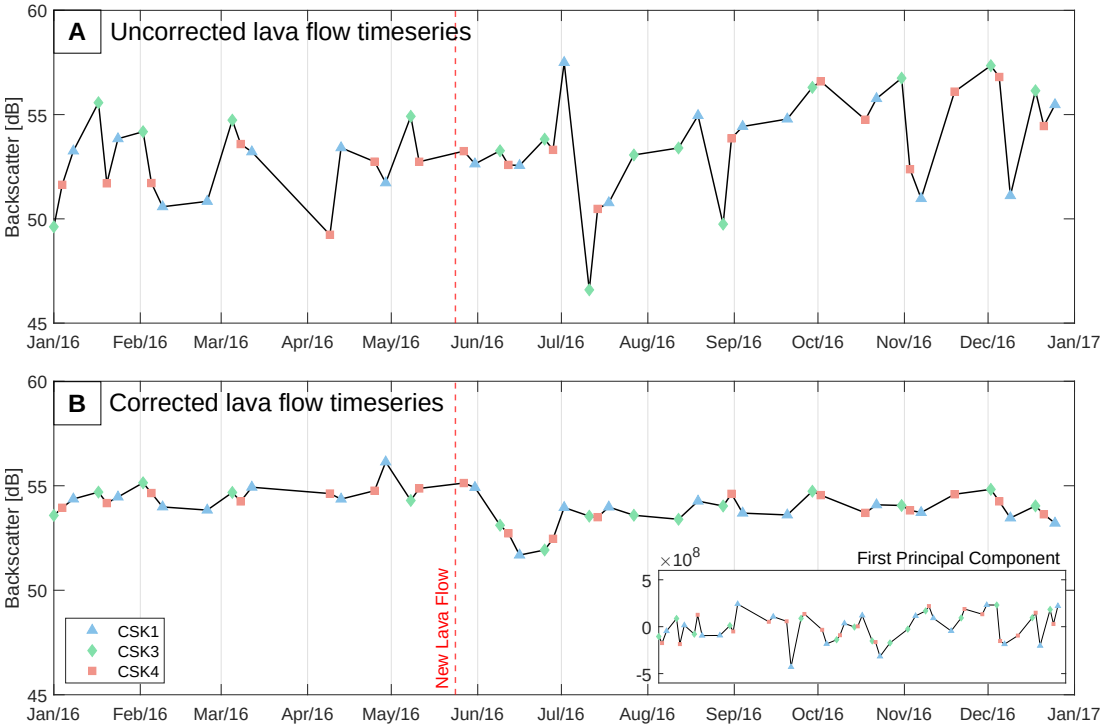

Figure B.9: Timeseries for the a single pixel for the (b) uncorrected, and (d) PCA-corrected radar backscatter over a lava flow in 2016 on Hawai'i, showing the improvement in the signal following the removal of the first principal component (PC1) from the dataset (PC1 shown in insert on b).

Appendix C:

Supporting information for Chapter 4

Contents of this file

1. Text C.1;
2. Figures C.1 to C.9
3. Tables C.2 to 4.2

Introduction This appendix contains material referenced to in Chapter 4 and includes the text and figures detailing the synthetic method to convert topography into simulated radar backscatter signals (i.e., relative 'brightness'). We also included a synthetic example of method limitations, the complete SAR dataset as single images, non-local gradient changes in radar backscatter associated with the eruption and the pixel offset tracking for the TerraSAR-X images, and tables summarising the SAR sensor parameters and triangular mesh input variables

Text C.1. Topography to radar backscatter (and vice versa)
We developed a simple method that allowed us to produce simulated SAR cross-sections based on topographic cross sections and then retrieve the topography from the simulated SAR (Fig. C.1). We assume that the majority of variations in the SAR backscatter signal are dominated by variations in the local gradient.

To test our method we can either produce a synthetic cross-section or extract a cross-section from the DEM that corresponds to a range line in the SAR image (Fig. C.1a). We divide each 'pixel' in the the topography cross-section into equally spaced sub-units. We use the cross-section in geographic geometry to locate the radar shadow and layovers before translating it into radar geometry. The pixels affected by a radar shadow are determinate by the gradient of each pixel. Slopes where the gradient is steeper than the incoming incidence angle are extracted and then for each of these sections we identify which subsequent pixels are covered by that particular radar shadow. The pixel spacing

in radar geometry, xr, is given by

$$xr = \left(x - \frac{h}{\tan\theta} \right) \frac{1}{R} \tag{C.1}$$

where h is the topographic height, x the original pixel spacing, R the pixel size in range direction and θ the satellite incidence angle. The radar layover in the cross-sections are identified by where the topography now either has a zero or negative gradient.

To calculate the relative brightness of the DEM cross section. We divided the DEM cross section in radar geometry into equal bins and sum the number of sub-units present in each bin (Fig. C.1b). From the simulated SAR we can reverse the process to retrieve the topography by integrating along the simulated SAR profile. We cannot retrieve the topography that is covered by a radar shadow. However, using the width of the radar shadow we can calculate the shift in topography (Fig. C.1d) and then correct the height of the topography following that radar shadow.

We transform our final cross-sections back from radar into geographic geometry and compare the extracted profile against the equivalent cross-section from the original DEM (Fig. C.1e). We do this to examine how the different correction we applied and the overall accuracy of our method affect the extracted topography. We also examine how well the method works for different satellite geometries and different types of topography.

In this paper we incorporate a scaled SAR cross-section into the method at stage Fig. C.1c and are able to use this to retrieved the topography.

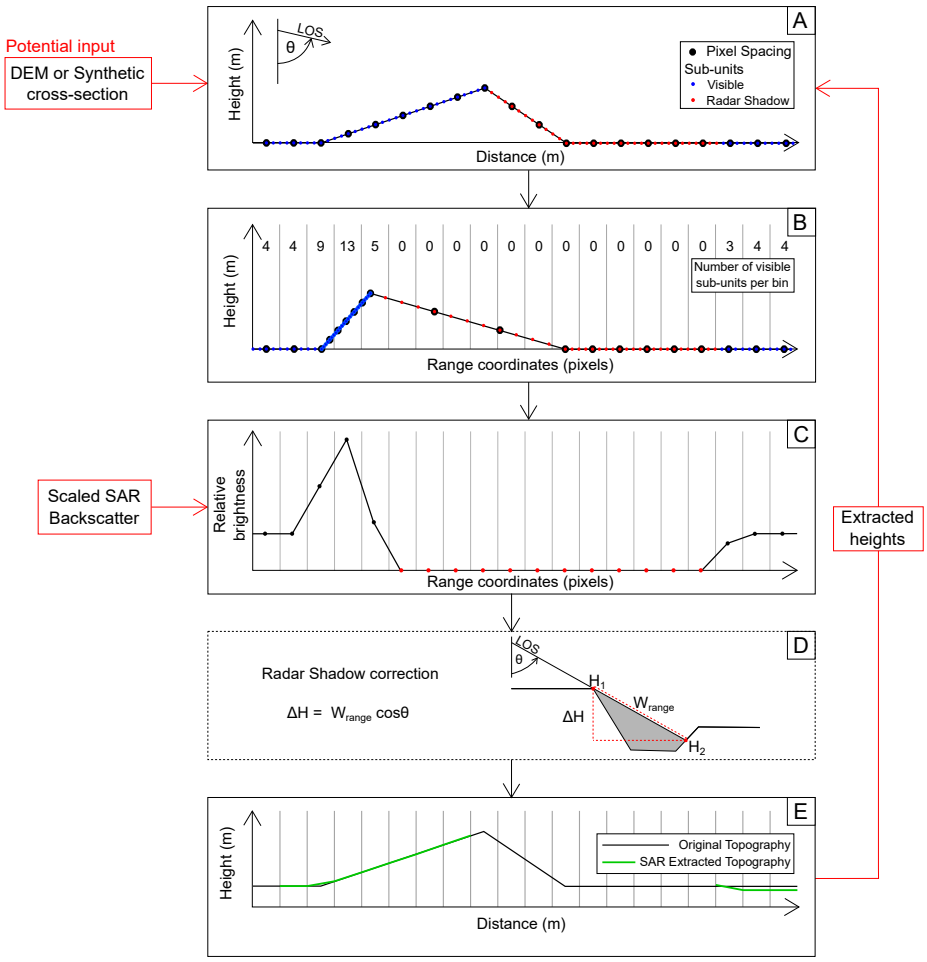

Figure C.1: Schematic flowchart outlining the main stages of the SAR topography extraction method. (a) Topographic cross-section in geographic geometry, with sub-units showing what sections are visible or covered by a radar shadow. (b) Topographic cross-section translated into radar geometry. The numbers indicate the number of sub-units per bin. (c) Relative brightness calculated from cross section. Radar shadow areas are indicated by red points. (d) Corrections applied to extracted topography. Stretching profile based on a constant (a) and the incidence angle (θ). Radar shadow elevation Change (ΔH) based on range width, W_{range}. (e) Topography extracted from backscatter. Various potential inputs are indicated in red.

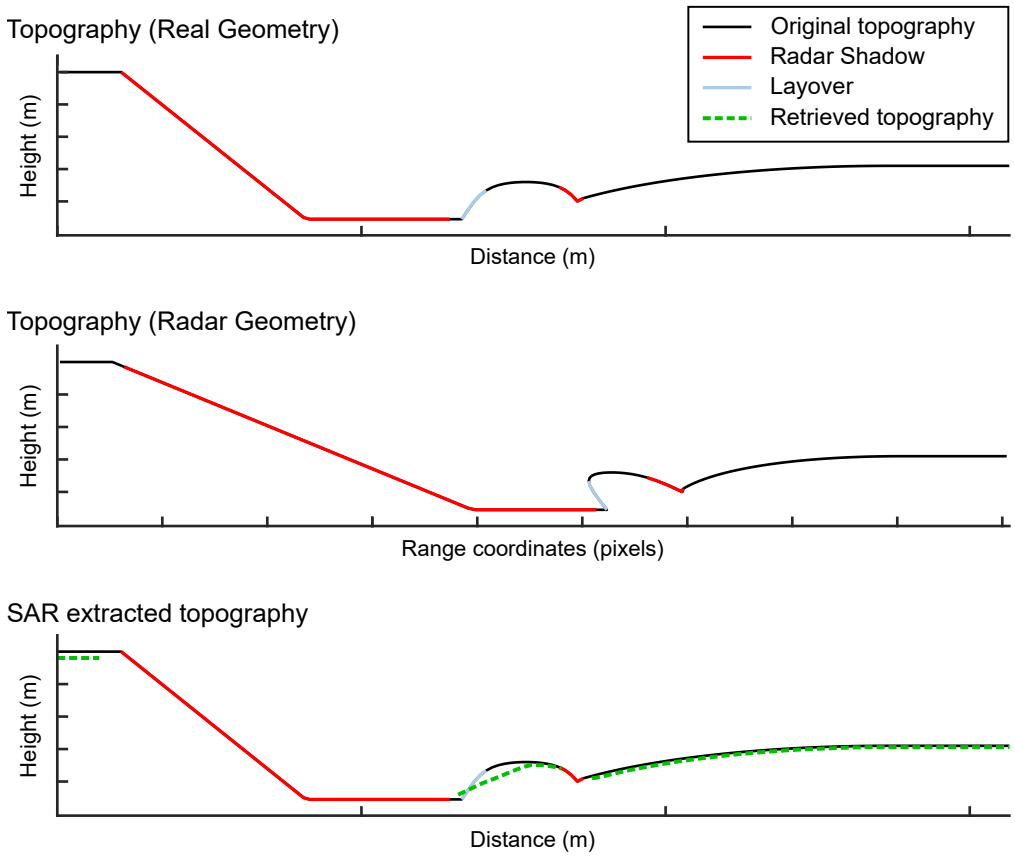

Figure C.2: Synthetic cross-section showing the interaction of radar layover and shadow, (a) shows a simple synthetic topgraphic profile in geographic geometry with red and blue lines representing radar shadows and layovers respectively. (b) shows the same profile in transformed into radar geometry, and (c) shows in green the extracted SAR topography for this synthetic profile that demonstrates the underestimate and distorted dome shape where the radar shadow and layover interacted in the profile.

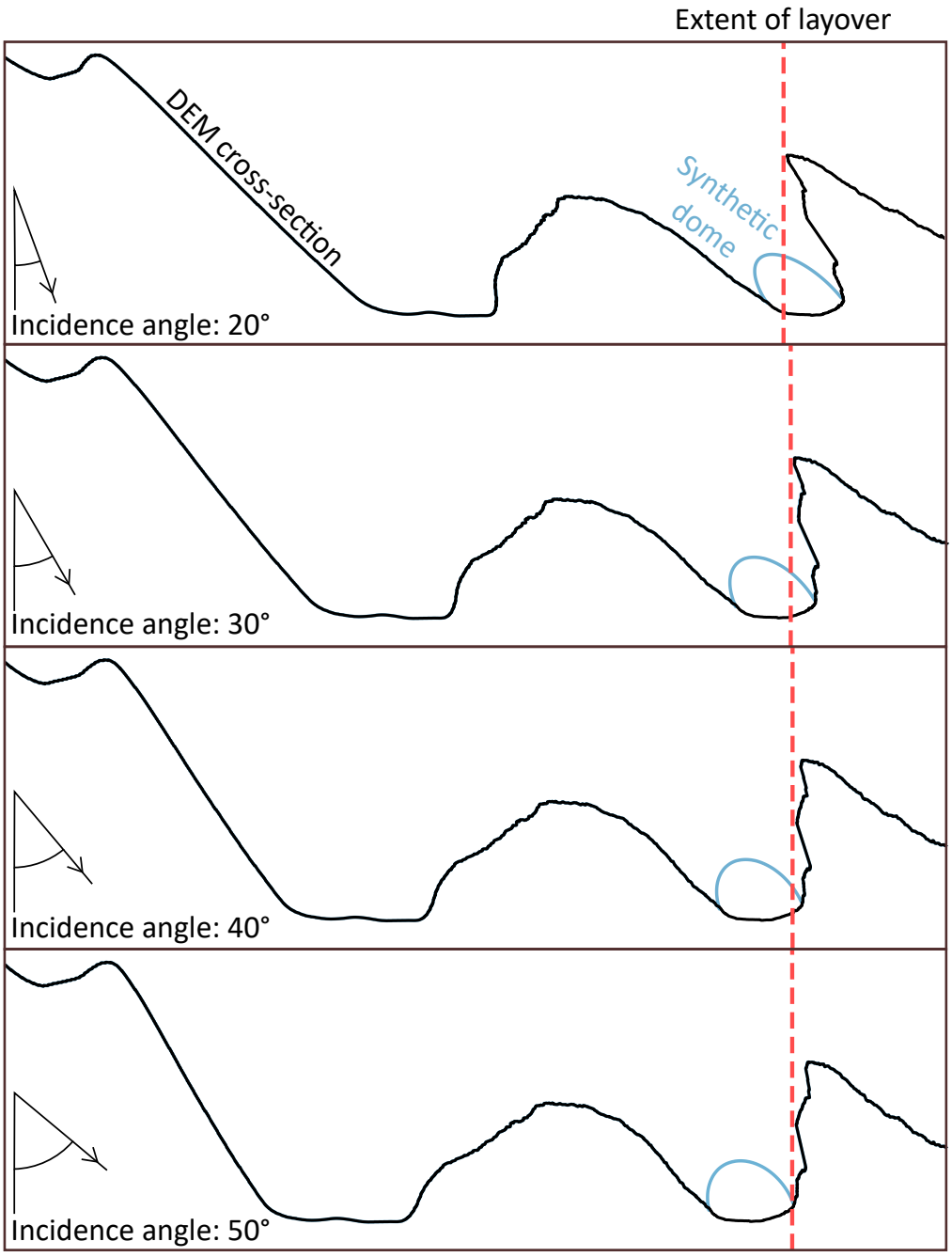

Figure C.3: DEM cross-section in radar geometry (black line) with synthetic dome (blue line) similar to descending SAR imagery profiles. Panels show extent of radar layover with increasing incidence angle. Smaller incidence angles showed much larger overlap between dome and crater wall, reducing our ability to extract accurate topography in these areas.

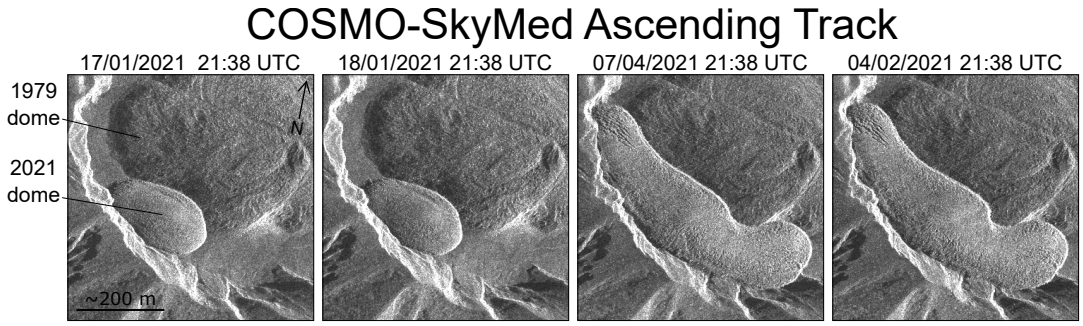

Figure C.4: COSMO-SkyMed radar backscatter images showing dome growth at La Soufrière, St. Vincent between 17 January and 8 April 2021.

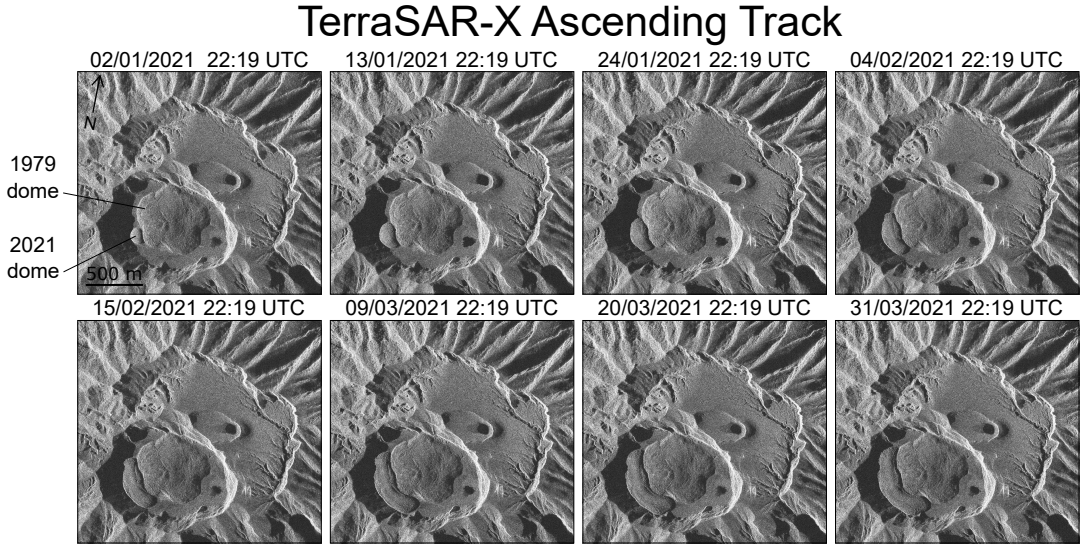

Figure C.5: TerraSAR-X radar backscatter images showing dome growth at La Soufrière, St. Vincent between 2 January and 31 March 2021.

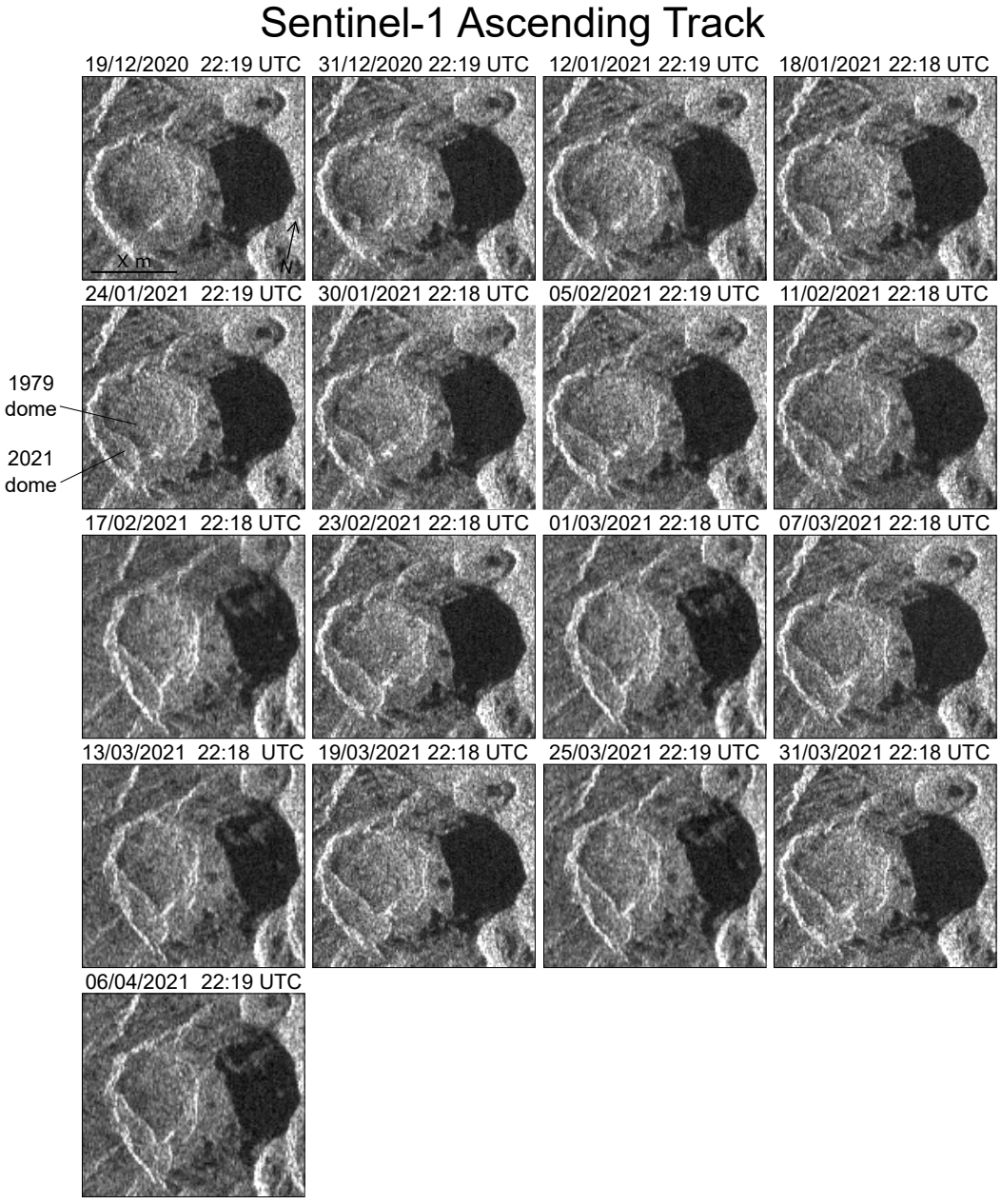

Figure C.6: Sentinel-1 ascending track radar backscatter images showing dome growth at La Soufrière, St. Vincent between 19 December 2020 and 6 April 2021.

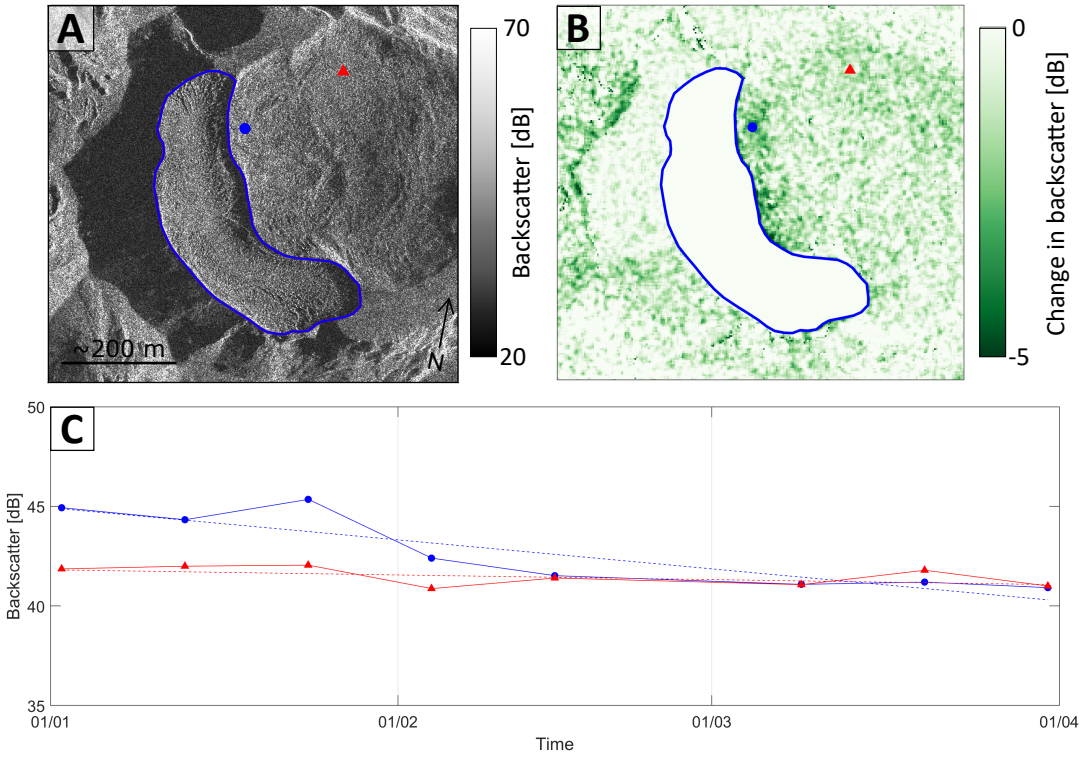

Figure C.7: Changes to radar backscatter signal in TerraSAR-X imagery adjacent to the 2021 St. Vincent dome associated to eruption. Panel (a) 31-03-2021 TerraSAR-X image, with 2021 dome outlined, (b) average changes in SAR backscatter for the 1979 dome adjacent to newly emplaced 2021 dome, and (c) SAR backscatter timeseries showing the stable background radar backscatter (blue points and linear fit) and the decrease in backscatter associated with the dome growth (red points and linear fit).

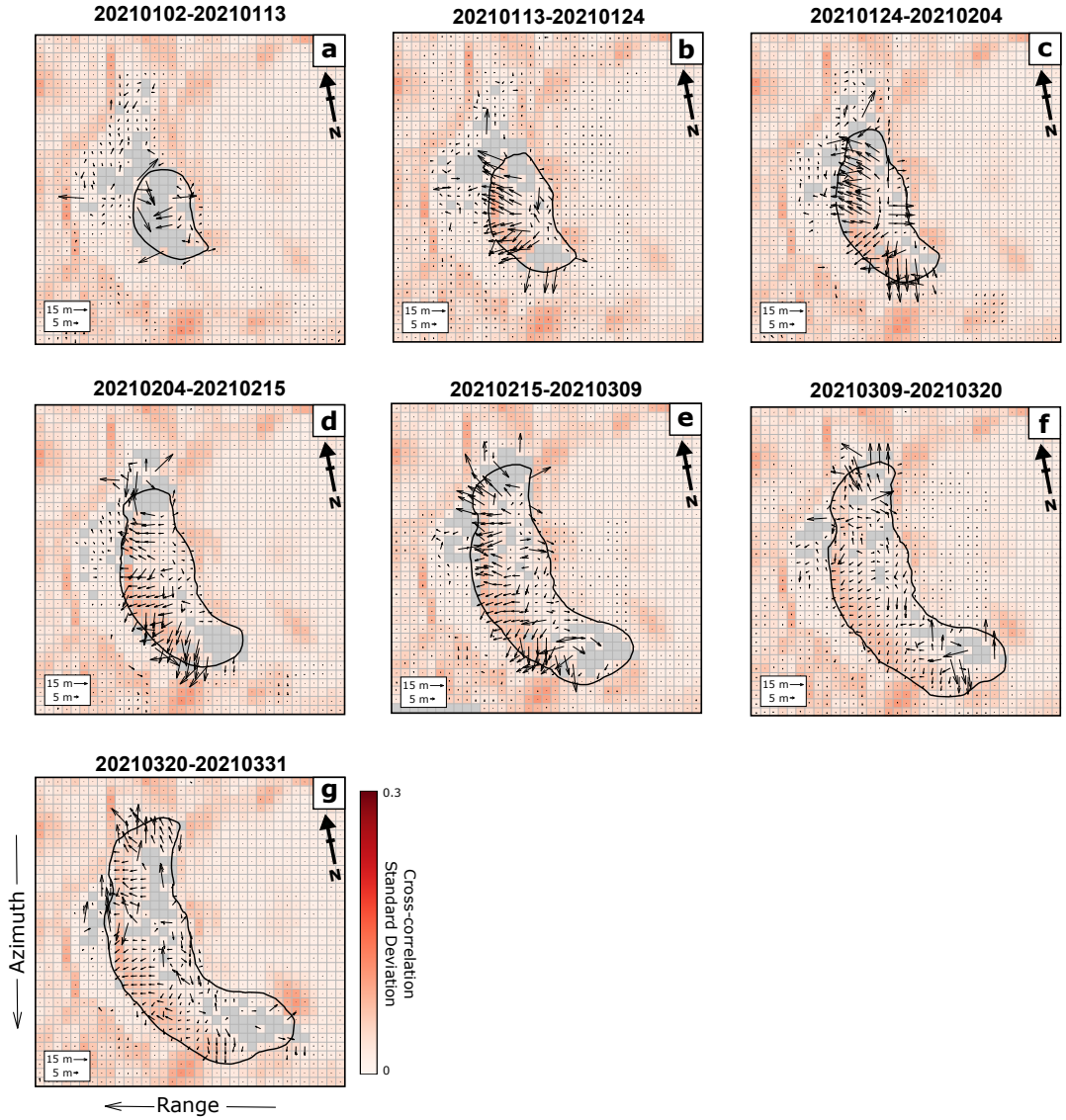

Figure C.8: TerraSAR-X (TSX) pixel tracking maps between January and March 2021 overlain on cross-correlation standard deviations. Arrows show the direction of surface displacement in range and azimuth direction and grid represents the step window used (TSX, 24 x 24). Maps produced using cross-correlation 96 x 96 pixels window and 24 x 24 step sizes.

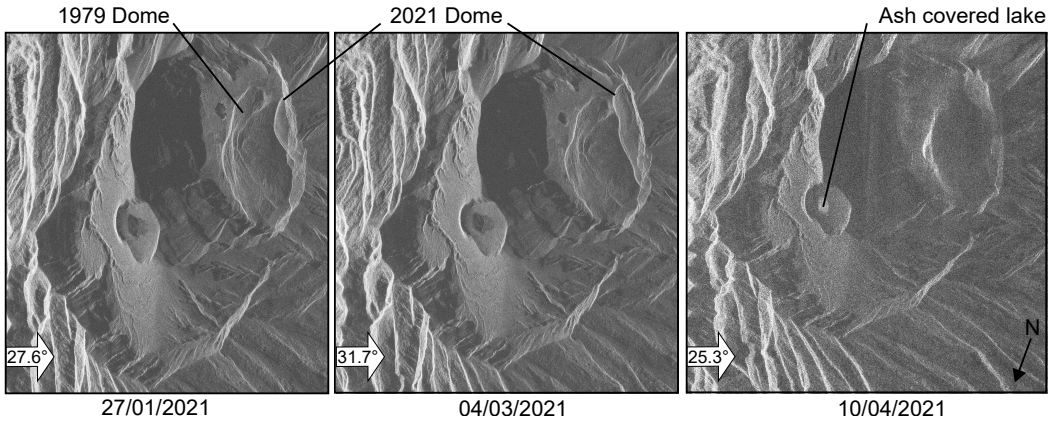

Figure C.9: Two pre- and first post-explosive eruption ICEYE SAR image showing 2021 dome growth and destruction during the explosive eruption. Data provided to SRC through the CEOS Volcano Demonstrator and acquired through an ESA TPM account to S. Ebmeier

Sensor	Band	Incidence Angle	Polarisation	Multi-look Factor	Resolution Range×Azimuth [m]
COSMO-SkyMed	X	44.2-44.4	HH	4×4	1.5×2.8
TerraSAR-X	X	50.9	HH	4×4	3.6×5.1
Sentinel-1 (Asc)	C	43.0	VV & VH	4×1	9.3×14.0
Sentinel-1 (Desc)	C	31.0	VV & VH	4×1	9.3×14.0
ALOS-2	L	36.3	HH & HV	2×2	4.3×3.8

Table C.2: SAR sensor parameters used to examine the St. Vincent dome growth.